Doctoral Dissertation
Doctoral Program in Materials Science and Technology (32th Cycle)

Study of heat treatments for the Inconel 625 and process optimization for the Inconel 939 produced by Laser Powder Bed Fusion

Simone Parizia

* * * * * *

Supervisors
Prof. P. Fino
Prof. D. Manfredi
Prof. S. Biamino (co-supervisor)
Doc. G. Marchese (co-supervisor)

Doctoral Examination Committee:
Prof. A.B. , Referee, University of….
Prof. C.D. , Referee, University of…
Prof. E.F. , Referee, University of….
Prof. G.H. , Referee, University of…
Prof. I.J. , Referee, University of….

Politecnico di Torino
April 30, 2020

I hereby declare that, the contents and organisation of this dissertation constitute my own original work and does not compromise in any way the rights of third parties, including those relating to the security of personal data.

…………………………………......

Simone Parizia

Turin, April 30, 2020

Summary

Among Additive Manufacturing (AM) technologies, Laser Powder Bed Fusion (LPBF) is attracting a lot of interest from both university and industry, thanks to the capability to produce in a single step near net shape components. This possibility is particularly interesting for the production of complex components in alloys which are expensive to process with traditional technologies, such as Ni-based superalloys.

However, the LPBF technology is a relatively new technology, that produces alloys with a really peculiar microstructure thus presenting challenges in the alloys processing as well as up to now a quite limited portfolio of materials. So the potential of this technology is twofold. On the already processed materials, more knowledge of the process is required, in term of effect of the process parameters, properties of the LPBF produced alloys as well as the effect of the standard or optimized heat treatments. Contemporary there is free space to optimize the process parameters for a great number of new alloys.

In this thesis work, I followed exactly this twofold line.

On one side I focused the attention on the already known Inconel 625 (IN625) produced by LPBF as well as on the other side I started to work by LPBF with the Inconel 939 (IN939).

IN625 is a superalloy that already proved to be very compatible with the LPBF process, thanks to its high weldability, so a lot of studies are already available in the literature. However, the effect of the commonly suggested heat treatments is still not clear, and there is a lack of literature on the oxidation behaviour for the LPBF IN625.

The first part of this thesis is focused on the investigation of as-built LPBF IN625 and the effect on standard annealing treatments on the microstructure and mechanical properties. The results show that the as-built condition possesses an anisotropic grain structure with fine dendrites, segregations and a high Low Angle Grain Boundaries (LAGB) content, that result in high Yield Stress (YS), Ultimate Tensile Strength (UTS) and a marked anisotropy in the mechanical properties. Appling low temperature annealing temperature causes precipitation and a partial segregation dissolution. Higher annealing temperatures remove the segregations

but remain carbides, and from 1030 °C causes recrystallization. To increase the annealing temperature gradually reduces the LAGB content, reducing YS, UTS and the mechanical anisotropy, improving the elongation.

In the second part, the oxidation performance at 900 °C of the as-built IN625 and the solutionized alloy are evaluated. The chosen temperature is comprised in the application temperature range of this alloy, and produces microstructural changes during the thermal exposure. The results show a superior oxidation resistance for the as-built condition, that develops a compact and continuous oxide layer. The solutionzed alloy inferior resistance is caused by defects in the oxide layer, that reduce the passivating effect and lead to the formation of mixed oxides.

At the end of the thesis, the effect of the process parameters in the production of the Inconel 939 is evaluated. Unlike the IN625, this alloy is prone to cracking during the process due to the presence of γ' formation elements. However, the results show that some parameter combinations allow the production of dense samples with an extremely low cracks content. The resulting microstructure is characterized by elongated grains and a fine dendritic structure, with the presence of nanometric precipitates that play a role in the cracking mechanism.

Acknowledgment

I would like to express my gratitude to my supervisors Prof. Paolo Fino, Prof. Sara Biamino and Prof. Diego Manfredi, for the opportunity of start this Ph.D journey on such innovative and interesting topic and for the important advices.

I would like to sincerely thank Doc. Giulio Marchese for the help, advices and really big support given to me since from my master thesis.

I would like to express my special appreciation to the researchers and of the Istituto Italiano di Tecnologia (IIT) di Torino, Dr. Flaviana Calignano and Dr. Massimo Lorusso for supporting me in the research activities.

Thanks to the Professors and researchers of Chalmers University of Technology, especially Prof. Eduard Hryha and Masoud Rashidi, for the opportunity of work abroad.

I would like to express my gratitude to all my colleagues: Alberta, Hamed, Antonio, Fabrizio, Luca, Daniel, Alessandra, Alessandra, Cristian, Federico, Gloria, Elisa, Bosio, Mario and Oxana for their contribution to a funny work environment and for their help during my work.

Special thanks to the PhD students of IIT, who gave me a lot of support and advices during my first year: Francesco, Giulio, Luisa and Umberto.

Thanks to all my friends, especially Lorenzo, Paolo, Sisca, Gullo, Luisa and Leonardo that sustained me during this journey.

At least, I would like to thank my family, that gave me the opportunity to arrive at this day, supporting me during all my life, and my girlfriend Rosy, who is always on my side and I love so much.

I’m arrived here today thanks to all of you!

Contents

List of Tables

List of Figures

List of Symbols & Abbreviations

Symbol	Meaning	Unit	Page
γ	Austenitic matrix		1
YS	Yield Stress	MPa	1
UTS	Ultimate Tensile Strength	MPa	1
SFE	Stacking Fault Energy	J/m^2	2
hcp	Hexagonal Closed-Packed		2
γ’	Ordered fcc [$Ni_3(Al,Ti)$], strengthening phase in Ni-superalloys		5
γ’’	Metastable coherent btc [Ni_3Nb], strengthening phase in Ni-superalloys		5
fcc	Face Centered Cubic		7
η	Hcp [Ni_3Ti]		7
bct	Body Centered Tetragonal		11
δ	Stable coherent orthorombic [Ni_3Nb], detrimental phase in Ni-superalloys		12
MC	Carbides, “M” is a metallic element and “C” is carbon		13
M_6C	Carbides, “M” is a metallic element and “C” is carbon		13
$M_{23}C_6$	Carbides, “M” is a metallic element and “C” is carbon		13
M_7C_3	Carbides, “M” is a metallic element and “C” is carbon		14
M_3B_2	Borides, “M” is a metallic element and “B” is boron		14
TPC	Topological Closed Packed phases, family of detrimental phases in Ni-superalloys		14
σ	Tetragonal TPC phase		14
μ	Rhombohedral TPC phase		14
ODS	Oxide-Dispersion Strengthened superalloys		15
HIP	Hot Isostatic Pressing		15
L	Laves phases, a hexagonal TPC phase		24
TTT	Time-Temperature Transformation diagram		24
FHT	4 stage heat treatmet of the Inconel 939		27
AM	Additive Manufacturing		27

CAD	Computer Aided Drafting		27
FDM	Fused Deposition Modeling		28
LPBF	Laser Powder Bed Fusion		28
EBM	Electron Beam Melting		28
BJ-3DP	Binder Jetting 3D Printing		28
DED	Direct Energy Deposition		28
LOM	Lamination Object Manufacturing		28
SLM	Selective Laser Melting		29
DMLS	Direct Metal Laser Sintering		29
t	Powder Layer thickness	mm	30
P	Laser power	W	30
v	Laser scan speed	mm/s	30
$\mathbf{h_d}$	Hatching distance (distance between two laser scans)	mm	30
SC	Solidification Cracking		33
LC	Liquation Cracking		33
SAC	Strain Age Cracking		34
PWHT	Post Weld Heat Treatment		34
DDC	Ductility Dip Cracking		34
BD	Building Direction		36
VED	Volumetric Energy Density	J/mm^3	45
SEM	Scanning Electron Microscopy		48
OM	Optical Microscopy		48
EDS	Energy Dispersive X-Ray Spectrometry		48
EBSD	Electron BackScattered Diffaction		49
XRD	X-Ray Diffraction		51
$\boldsymbol{\lambda}$	X-ray wavelenght in the XRD analysis	Å	51
$\mathbf{d_{h,k,l}}$	Interplanar distance	Å	51
WQ	Water Quench		53
TMA	TermoMechanical Analysis		54
CTE	Coefficient of Thermal Expansion		54
TGA	Thermal Gravimeteric Analysis		54
EDM	Electro Discarge Machining		55
PDAS	Primary Dendritic Arm Spacing	µm	62
SDAS	Secondary Dendritic Arm Spacing		62
$\boldsymbol{\varepsilon}$	Cooling rate	°C/s	62

TEM	Transmission Electron Microscopy		63
LAGB	Low Angle Grain Boundary		65
HAGB	High Angle Grain Boundary		65
TGB	Twinning Grain Boundary		65
El	Elongation to break	%	68
SOFC	Solid oxide fuel cells		109
K_p	Oxidation Parabolic Constant	$mg^2/(cm^4*h)$	110

Chapter 1

Introduction

The first section of this chapter is meant to give the basic concepts of the metallurgy of Nickel based superalloys, with focus on the alloys Inconel 625 and Inconel 939, object of study in this thesis.

The second part is about the Additive Manufacturing technologies used in the production of metals, with particular attention to the Laser Powder Bed Fusion technology, used in this work.

In the third section is reported the state of the art of the production of Nickel based superalloys produced by Laser Powder Bed Fusion and the challenges in their production with this kind of technology.

1.1 Categories of superalloys

Superalloys have been developed mostly for being applied in the hot sections of gas turbine engines for energy production and aerospace engines, but thanks to their outstanding mechanical properties and corrosion resistance in high temperature condition they have found space in other sectors, such as military, nuclear, chemical, petrochemical, automotive and biomedical [1].

The superalloy family can be divided in three main groups:

- Ni-based superalloys;
- Ni-Fe-based superalloys;
- Co-based superalloys.

All those superalloy groups usually possess a face centred cubic crystal structure (austenitic structure, γ), thanks to the addition of γ-stabilizer elements in the case of Fe and Co. The Ni possess always a fcc crystal structure at all temperature instead.

Ni-based superalloys are used when highest strength at high-temperature is required. They can be used in the wrought condition when high yield stress (YS), ultimate tensile strength (UTS) and fatigue resistance are demanded, for example in turbine disks and rotors. When creep resistance is the main characteristic the choice falls on the cast condition, which possess bigger grains and consequently less grain boundaries. Typical application in this case are the turbines blades, that according to the operative conditions can require a traditional equiaxial microstructure or to go to directionally solidified or even single crystal superalloys [2].

For this family of superalloys reinforcement mechanism are solid solution strengthening, precipitation strengthening or oxides dispersion [1–4].

Ni-Fe-based superalloys possess high YS, UTS and fatigue resistance at moderate temperature and they found application in components such as turbine discs or forged rotors. This kind of superalloys is used in the wrought condition, since during the manufacturing process is possible to control both grain size and morphology, reaching good properties [2].

Ni-Fe-superalloys can be solid solution strengthened and precipitation-hardened. When the application requirements are relative low temperature and strength, Ni-Fe-based superalloys is more used that the other types, also thanks to their lower cost caused by the high Fe content. [1,2].

Ni and Ni-Fe superalloys possess a long production process, that require melting in vacuum and multiple remeltings in order to remove impurities and avoid the formation of Ti and Al oxides.

Co-based alloys are mostly used in applications where the most important characteristic is the hot corrosion or when the requirement of the component allow a low-stress at moderate-to-high temperatures. Typical applications for Co-based superalloys are stationary components such as combustors and injectors. The strengthening mechanisms are carbide formation and solid-solution strengthening. Compared to Ni-based superalloys, Co-based possess more Cr that provide superior corrosion resistance, higher melting temperature and they do not require a melting in vacuum for the component production [1,2].

Table.1 and Table.2 provide an overview on the composition of common superalloys used in wrought and the cast condition respectively, and Fig.1 shows a graphical representation of the resistance in temperature for different alloy classes.

Table 1: Composition of some commercial wrought superalloys [5]

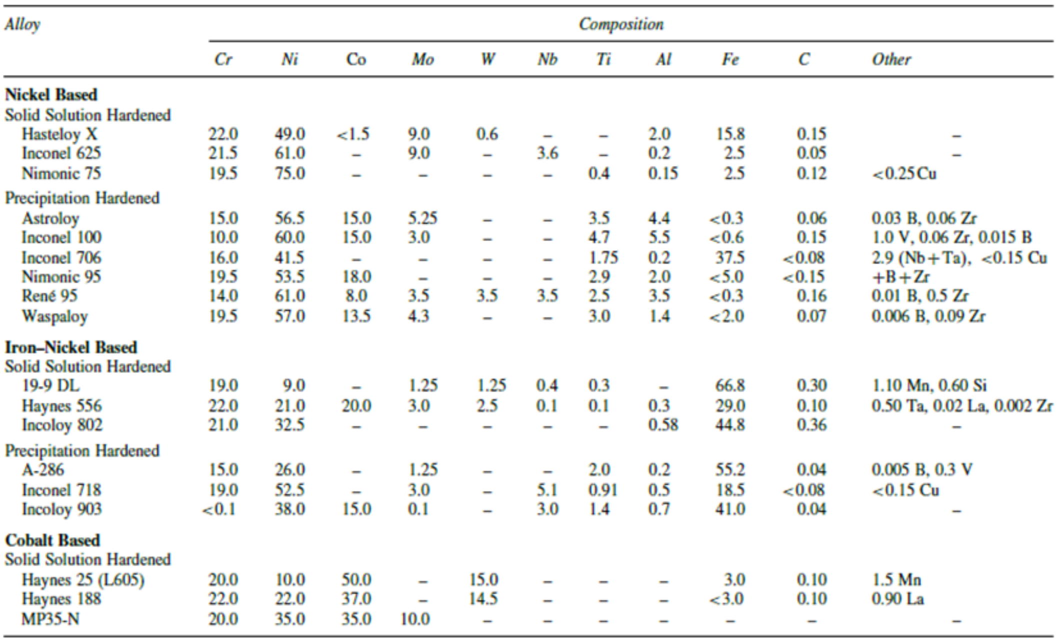

Alloy	Composition										
	Cr	Ni	Co	Mo	W	Nb	Ti	Al	Fe	C	Other
Nickel Based											
Solid Solution Hardened											
Hasteloy X	22.0	49.0	<1.5	9.0	0.6	–	–	2.0	15.8	0.15	–
Inconel 625	21.5	61.0	–	9.0	–	3.6	–	0.2	2.5	0.05	–
Nimonic 75	19.5	75.0	–	–	–	–	0.4	0.15	2.5	0.12	<0.25 Cu
Precipitation Hardened											
Astroloy	15.0	56.5	15.0	5.25	–	–	3.5	4.4	<0.3	0.06	0.03 B, 0.06 Zr
Inconel 100	10.0	60.0	15.0	3.0	–	–	4.7	5.5	<0.6	0.15	1.0 V, 0.06 Zr, 0.015 B
Inconel 706	16.0	41.5	–	–	–	–	1.75	0.2	37.5	<0.08	2.9 (Nb+Ta), <0.15 Cu
Nimonic 95	19.5	53.5	18.0	–	–	–	2.9	2.0	<5.0	<0.15	+B+Zr
René 95	14.0	61.0	8.0	3.5	3.5	3.5	2.5	3.5	<0.3	0.16	0.01 B, 0.5 Zr
Waspaloy	19.5	57.0	13.5	4.3	–	–	3.0	1.4	<2.0	0.07	0.006 B, 0.09 Zr
Iron–Nickel Based											
Solid Solution Hardened											
19-9 DL	19.0	9.0	–	1.25	1.25	0.4	0.3	–	66.8	0.30	1.10 Mn, 0.60 Si
Haynes 556	22.0	21.0	20.0	3.0	2.5	0.1	0.1	0.3	29.0	0.10	0.50 Ta, 0.02 La, 0.002 Zr
Incoloy 802	21.0	32.5	–	–	–	–	–	0.58	44.8	0.36	–
Precipitation Hardened											
A-286	15.0	26.0	–	1.25	–	–	2.0	0.2	55.2	0.04	0.005 B, 0.3 V
Inconel 718	19.0	52.5	–	3.0	–	5.1	0.91	0.5	18.5	<0.08	<0.15 Cu
Incoloy 903	<0.1	38.0	15.0	0.1	–	3.0	1.4	0.7	41.0	0.04	–
Cobalt Based											
Solid Solution Hardened											
Haynes 25 (L605)	20.0	10.0	50.0	–	15.0	–	–	–	3.0	0.10	1.5 Mn
Haynes 188	22.0	22.0	37.0	–	14.5	–	–	–	<3.0	0.10	0.90 La
MP35-N	20.0	35.0	35.0	10.0	–	–	–	–	–	–	–

Table 2: Composition of some commercial cast superalloys [5]

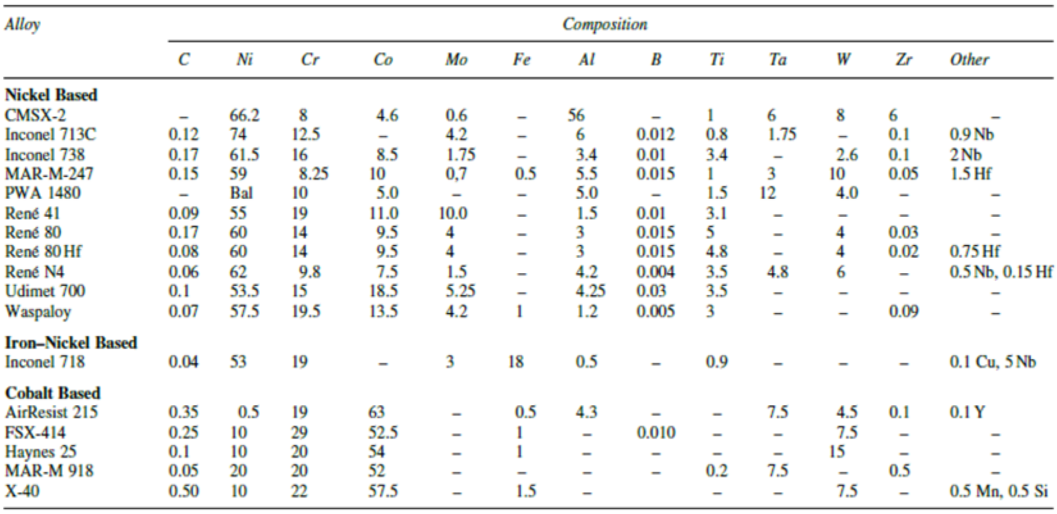

Alloy	Composition												
	C	Ni	Cr	Co	Mo	Fe	Al	B	Ti	Ta	W	Zr	Other
Nickel Based													
CMSX-2	–	66.2	8	4.6	0.6	–	56	–	1	6	8	6	–
Inconel 713C	0.12	74	12.5	–	4.2	–	6	0.012	0.8	1.75	–	0.1	0.9 Nb
Inconel 738	0.17	61.5	16	8.5	1.75	–	3.4	0.01	3.4	–	2.6	0.1	2 Nb
MAR-M-247	0.15	59	8.25	10	0,7	0.5	5.5	0.015	1	3	10	0.05	1.5 Hf
PWA 1480	–	Bal	10	5.0	–	–	5.0	–	1.5	12	4.0	–	–
René 41	0.09	55	19	11.0	10.0	–	1.5	0.01	3.1	–	–	–	–
René 80	0.17	60	14	9.5	4	–	3	0.015	5	–	4	0.03	–
René 80 Hf	0.08	60	14	9.5	4	–	3	0.015	4.8	–	4	0.02	0.75 Hf
René N4	0.06	62	9.8	7.5	1.5	–	4.2	0.004	3.5	4.8	6	–	0.5 Nb, 0.15 Hf
Udimet 700	0.1	53.5	15	18.5	5.25	–	4.25	0.03	3.5	–	–	–	–
Waspaloy	0.07	57.5	19.5	13.5	4.2	1	1.2	0.005	3	–	–	0.09	–
Iron–Nickel Based													
Inconel 718	0.04	53	19	–	3	18	0.5	–	0.9	–	–	–	0.1 Cu, 5 Nb
Cobalt Based													
AirResist 215	0.35	0.5	19	63	–	0.5	4.3	–	–	7.5	4.5	0.1	0.1 Y
FSX-414	0.25	10	29	52.5	–	1	–	0.010	–	–	7.5	–	–
Haynes 25	0.1	10	20	54	–	1	–	–	–	–	15	–	–
MAR-M 918	0.05	20	20	52	–	–	–	–	0.2	7.5	–	0.5	–
X-40	0.50	10	22	57.5	–	1.5	–		–	–	7.5	–	0.5 Mn, 0.5 Si

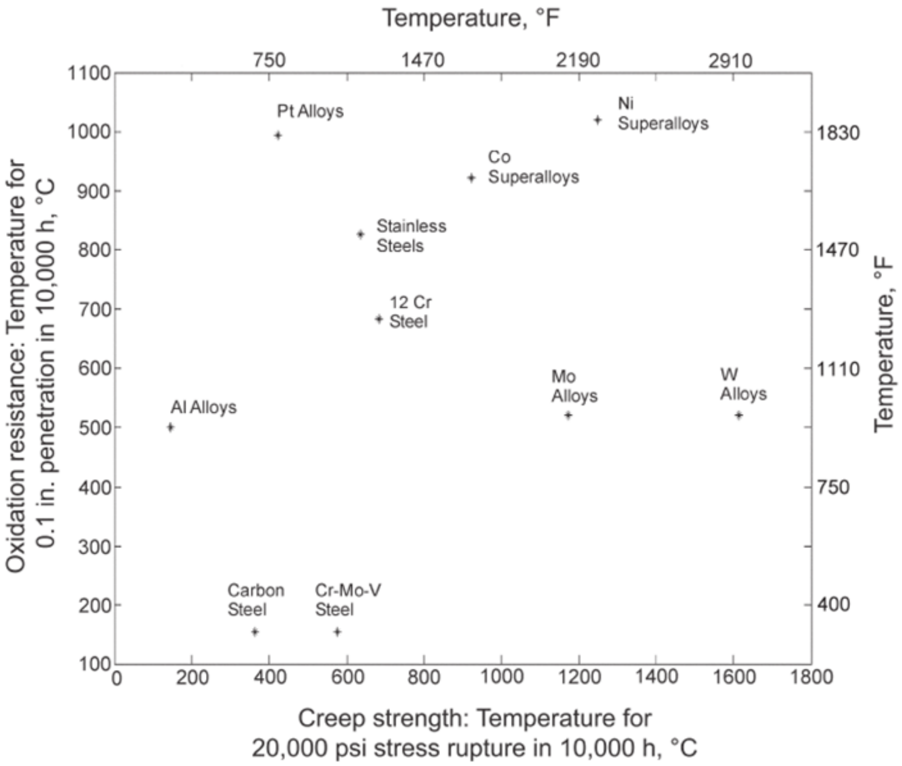

Figure 1: Creep strength and oxidation resistance of different materials classes [1]

1.1.1 Solid solution strengthened Ni-based superalloys

The first reinforcement mechanisms in Ni-based superalloys is the solid solution hardening. This hardening is given to an alloy adding in the alloy composition different soluble elements. This addition cause a misfit in the crystal lattice structure of the base alloy, inhibiting the dislocations movement of an amount proportional to the difference in the atomic radius, up to a misfit of 10 % of the atomic radius [1].

Moreover, elements characterized by a high melting point provide to the alloy a reduction of the diffusion coefficient and an increased lattice cohesion, also in high-temperature conditions [1].

This kind of reinforcement provides a reduction in the Stacking Fault Energy (SFE), which results in an inhibition of the dislocation cross slip, the most important deformation mechanism at high temperatures for imperfect crystals. The reduction of the SFE makes harder for dislocations change the slip plane, increasing the efficiency of metallurgical barriers such as grain boundaries and precipitates.

Reducing the SFE in alloys with fcc lattices causes the following effects:

- dislocations are dissociated into partials
- development of hexagonally close-packed (hcp) stacking fault ribbons
- inhibition of the dislocations passage from fcc matrix to hcp fault

The last effect that contributes in the solid solution hardening is called atomic clustering or short-range order. This hardening effect is due to electronic orbitals activity and is stronger for certain elements, such as Mo, W, Cr, Al, and Re, meanwhile is weaker for Fe, Ti, Co, or V. The beneficial effect of the atomic clustering is reduced by the diffusion, and becomes irrelevant for temperature higher than the 60% of the melting temperature of the alloy [1].

The addition of heavy chemical elements (Re, W, Mo, etc) in the alloy leads to lower diffusion rates, but at the same time bring an increase density and enhances the precipitation of weakening phases at the grain boundaries and in the interdendritic areas [1].

1.1.2 Precipitation strengthened Ni-based superalloys

A significant enhancement of the mechanical properties and the creep properties at high temperature in Ni-based superalloys can be obtained thanks to the precipitation strengthening mechanism.

The additions of elements in the alloy, such as Ti, Al, and Nb allow the formation of intermetallic compounds, usually coherent with the matrix, such as **γ'** [$Ni_3(Al,Ti)$] and **γ''** [Ni_3Nb]. The solubility in the matrix of these elements is not great, and it is further reduced lowering the temperature. Considering this behaviour, it is possible to form fine precipitates well dispersed in the alloy performing solution treatments followed by aging treatments [1,2].

The presence of precipitates has the beneficial effect of limiting the dislocations movements, which have to outflank or pass inside the particles using more energy.

There are different factors that influence the strengthening effectiveness of a precipitate:

- the coherency strains presence between the matrix alloy (γ) and the precipitates (such as **γ'** and **γ''**) caused by the misfit of their lattice parameters
- the antiphase-boundary (APB) energy present when there are ordered precipitates (such as **γ'** or **γ''**). This is the energy required by a dislocation in order to pass inside the ordered precipitate, since passage may result in disordering between the matrix and precipitate.
- the volume fraction of the precipitate.
- the precipitates particle size.
- the homogeneity of the precipitate distribution.

However, the reinforcement brought by ordering and coherent strains raises increasing the particle size, because in order to activate these two mechanisms the dislocations have to cut through the precipitate.

However, the stress required to cut through a particle increases with the particle dimension, and passed a limit value the dislocations change the movement mechanism. In order to overcome the precipitate, the dislocation starts to bend around the particle. The process continues until dislocation passes leaving a dislocation ring around the particle, and it is known as Orowan mechanism. This strengthening mechanism is also the one provided by incoherent precipitates [6]. An example of Orowan mechanism and its graphical representation are reported in Fig.2 and Fig.3.

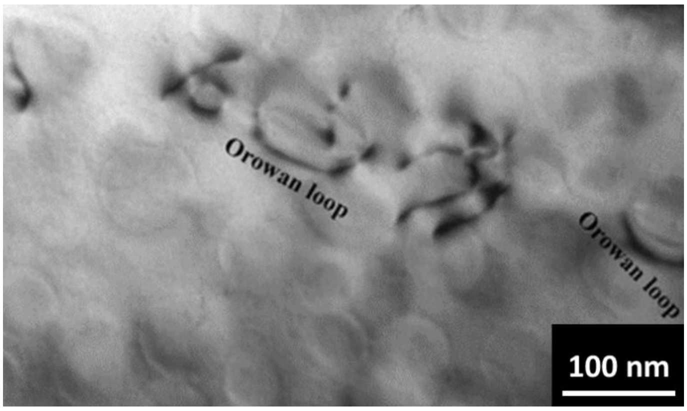

Figure 2: TEM image of the Orowan loop in the superalloy GH4037 [7]

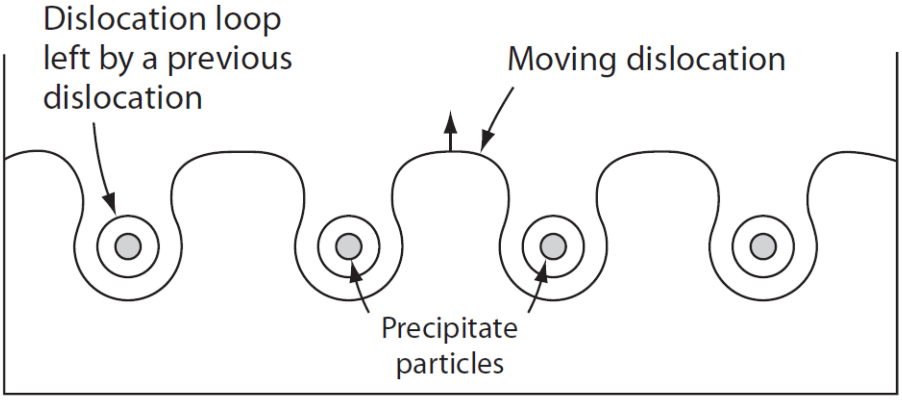

Figure 3: Orowan looping mechanism representation [6]

Part of the strengthening in superalloys is provided by carbides.

Carbides behaviour in superalloys is not simple; depending by their shape, composition, dimension and location they can be associated to improved or reduced properties [1,2].

Carbides can be formed in many ways in a superalloy, based on the composition and on the thermal history. They can form during solidification, from eutectic reaction, directly in the molten alloy, from precipitation and from decomposition of other carbides [2,3,8].

Most of the times they form along the grain boundaries, increasing the creep properties. Not cohesive, small and globular carbides are able to provide the best reinforcement in this case [1,2].

However, the carbides precipitation can subtract Cr from the alloy, leading to a reduction in the corrosion resistance [1].

The same event can happen for elements such as Mo and W, but in this case the reduction of solid solution strengthening elements can be an advantage, since it provides soft areas that can help in stress dissipation [1].

Moreover, in some alloy compositions the formation of carbides is desirable because it subtracts elements that otherwise can participate to the formation of detrimental phases [2].

Carbide levels in wrought alloys always have been below those in cast alloys, but some carbide is needed in order to achieve optimal mechanical properties, and in wrought alloy they can be used as grain refiner [2].

Carbides directly impact on stress rupture strength and tensile strength, pinning dislocations and reducing the grains movement [1,8].

Both shape and quantity of carbide located at the grain boundaries are critical for the alloy properties, since they can enhance crack propagation, but a reduced content of carbides is not able to reduce the grains sliding, which lead to short creep life [1,2,8].

The melting temperature of the alloy can be reduced by the presence of carbides, due to the high carbon [1].

In order to overcome this problem, it is possible insert carbides through mechanical alloying instead of make them precipitate. In this way the carbon content in the alloy is reduced, but the carbides possess a lower coherency with the matrix, and the resulting reinforcement is reduced [1].

1.1.2.1 Typical phases in superalloys

In the matrix (γ) of a superalloy a lot of secondary phases can be formed, based on the chemical composition and the thermal history. The phases normally found are reported in the following list:

- γ’: is an ordered, fcc precipitate with chemical formula Ni_3Al, in which Al can be substitute by Ti and/or Nb up to a 60% so the more appropriate chemical formula is $Ni_3(Al, Ti)$ [1,8].

  In Ni-Fe-based alloys this phase can transform in **η** phase over time, which is a detrimental phase, as will be treated in a following paragraph. This phase allows the strengthening of the alloy for high themperatures. In particular the strenghtening effect becomes more marked up to 800°C. However, this phase can provide a good strenghtening effect also for higher temperatures. This effect is related, in some extent, to the mechanism of interaction between **γ’** and the dislocations [1,3].

  The dislocations passage mechanism required for cut through a γ’ precipitate is explained in Fig.4 and an example is shown in Fig.5. A first dislocation forms the antiphase boundary (APB) in the slip plane used for moving, leaving a chain of incorrect bonds. In order to restore the order of γ′ a second dislocation is needed. In this way dislocations are forced to move in pairs, in order to preserve the **γ’** order [3].

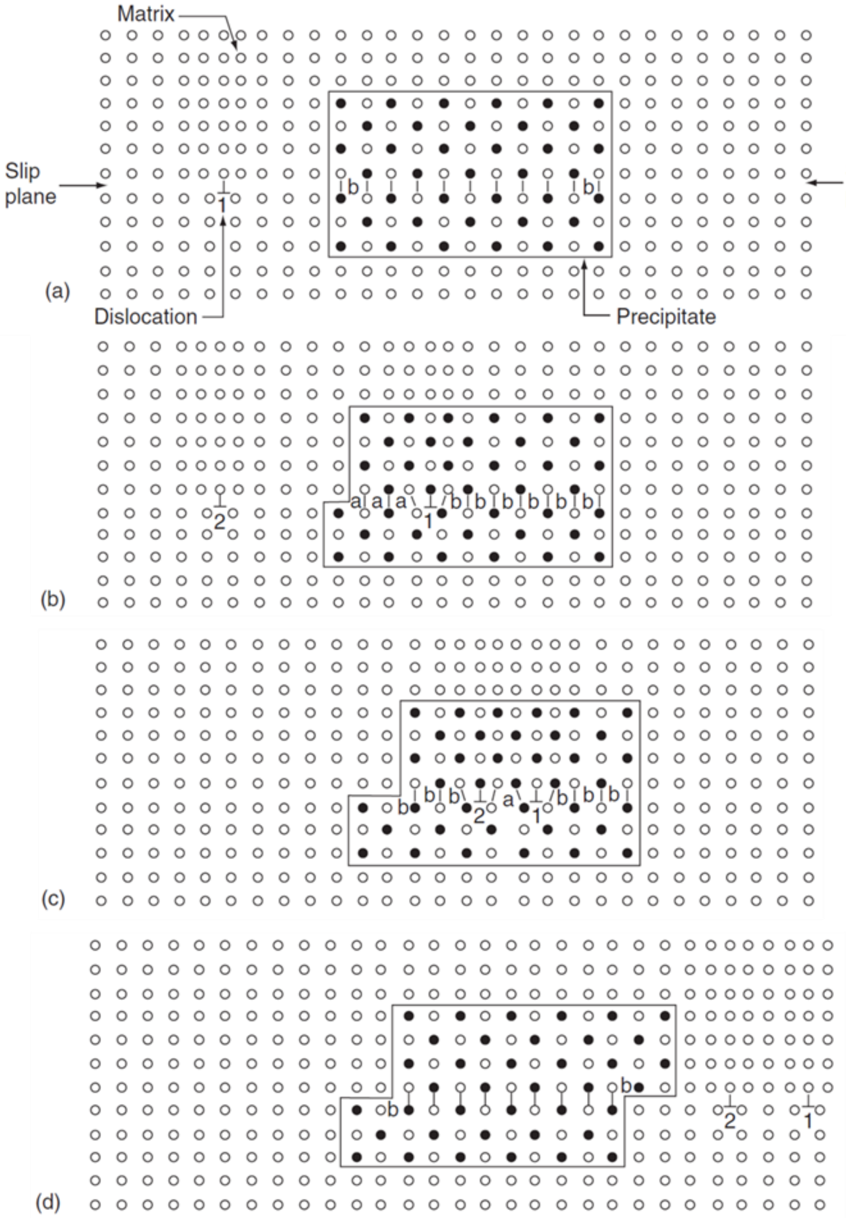

Figure 4: dislocations passage mechanism in an ordered γ’ structure [3]

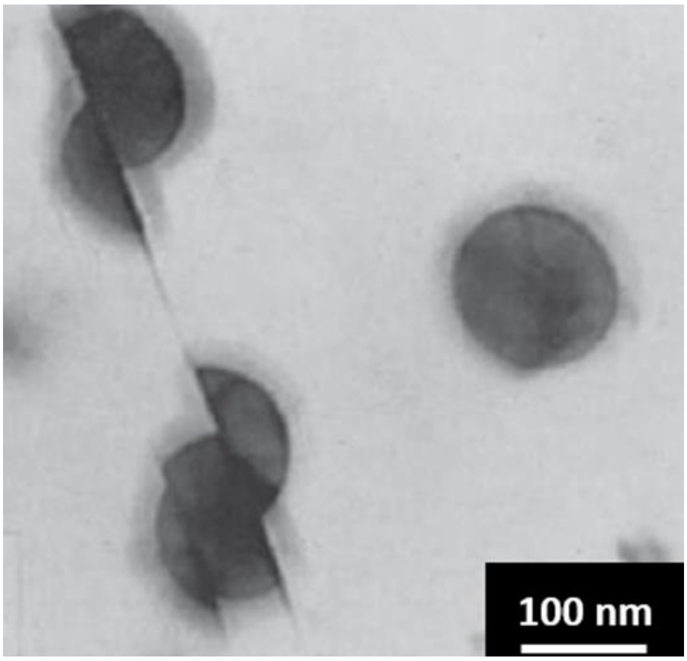

Figure 5: TEM image of some γ' precipitate cut by dislocations passage in a nickel superalloy [3]

The interface between **γ** and **γ'** act as a barrier to the moving of dislocations and increasing the **γ/γ'** lattice mismatch increase the strength of this barrier [1].

Increasing the service temperature leads to an increase of the lattice parameter of the alloy matrix and **γ'**, but for the latter the increase is lower, leading to an increasingly negative lattice mismatch by raising the temperature. This result in improved creep performance [1].

γ′ is usually disperses in the alloy matrix, but sometimes **γ'** can form film structure at the grain boundaries locations, normally after high-temperature exposure, and this behaviour is probably useful in the improvement of the creep-rupture properties [1].

γ' can appear with different shapes based on the lattice mismatch with the **γ** matrix: between 0 and 0.2% it appears as a spherical precipitate, between 0.5 and 1.0% as a cubic precipitate and a plate-like precipitate for mismatch above the 1.25% [1]. An elevated mismatch value, coupled with a long thermal exposure can cause the formation of the phases **η** and **σ**, both undesirable [2]. An example of different shapes of **γ'** based on the lattice mismatch is reported in Fig.6. Some experiments have shown that changing the Mo content and the Al/Ti ratio have an effect on the morphology of **γ'** [2].

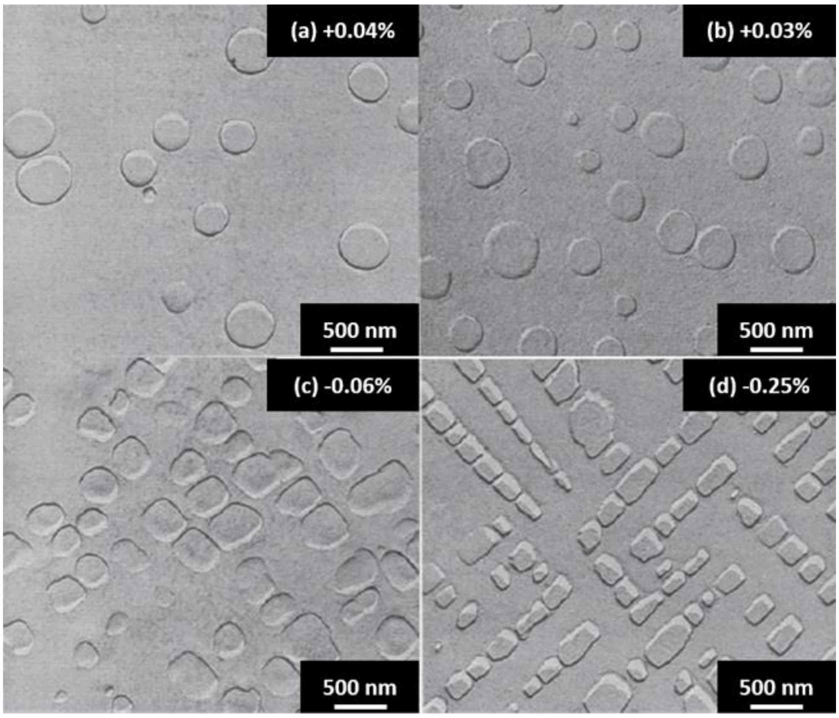

Figure 6: SEM images of γ' in a Ni - Al - Mo alloy with different levels of lattice mismatches [3]

A last factor that can modify γ' shape and dimension is the entity of the aging, as explained in Fig.7 [3].

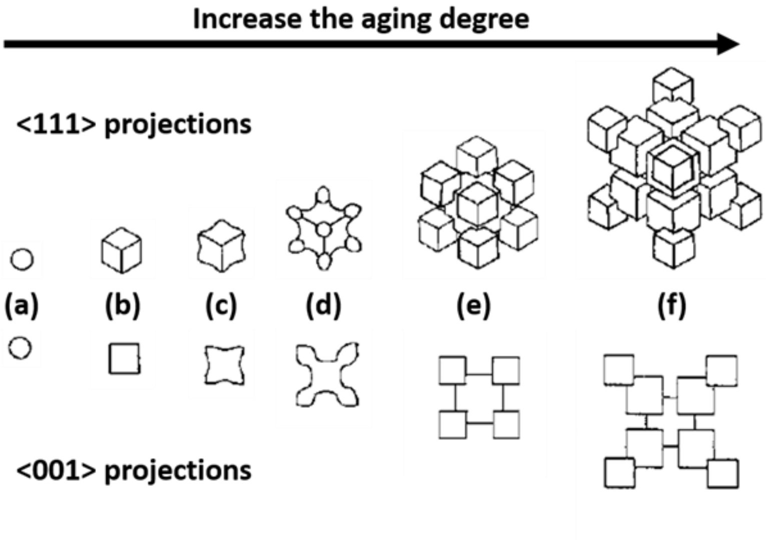

Figure 7: Evolution of strain-induced, from (a) to (f), γ' dimension and morphology during ageing [8]

As the Fig.7 shows, long time in temperature limits the life of a component through the coarsening (or sometimes the dissolution) of γ' [1]. In the coarsening case, when a critical dimension is reached, the dislocations movement mechanism changes from the cutting to the bypass mode, reducing the strength of the alloy [1].

- η is a phase with hcp lattice and chemical formula Ni_3Ti, without possibility of substitution for other elements. It is usually found in superalloys characterized by high Ti/Al ratios after long exposure at high temperatures. It can be identified as intergranular precipitates or in a Widmanstätten pattern with acicular or plates particles, and it is an undesirable phase [1,3].

- **γ''**: is a coherent, metastable precipitate used as strengthening phase in superalloys such as IN625 and IN718 [1,2].

  This precipitate is characterized by the chemical formula Ni_3Nb [1,2,8] and a bct lattice structure. The γ'' precipitation orientation is strictly related to the matrix orientation, since the plane <001> of **γ''** is parallel to the <001> plane of **γ** and the plane <100> of **γ''** is parallel to the plane <100> of **γ** [8].

  The morphology is dick-shaped, with the thickness down to 10 nm and the diameter around 50 nm, for instance an example of its shape is displayed in Fig.8 [8].

  The reinforcement brought by γ'' is caused by the large mismatch between the precipitate and the matrix lattice parameter, which is around the 3%.

  This high difference provides really high strength at low temperatures [3,8].

  Compared to **γ'**, **γ''** possess a lower solvus temperature, so the strengthening effect is limited to temperatures up to 750 °C [1].

  Moreover, superalloys **γ''** reinforced tend to lose their strength during the time when exposed at temperature higher than 650 °C, since the metastable **γ''** phase start to transforms in the undesired **δ** phase, and this evolution is associated to a lowering in the creep properties [1,3,8]. Alloys hardened forming γ'' precipitate are not subject to strain age cracking, since the **γ''** precipitate is formed at a much slower rate than **γ'** [8].

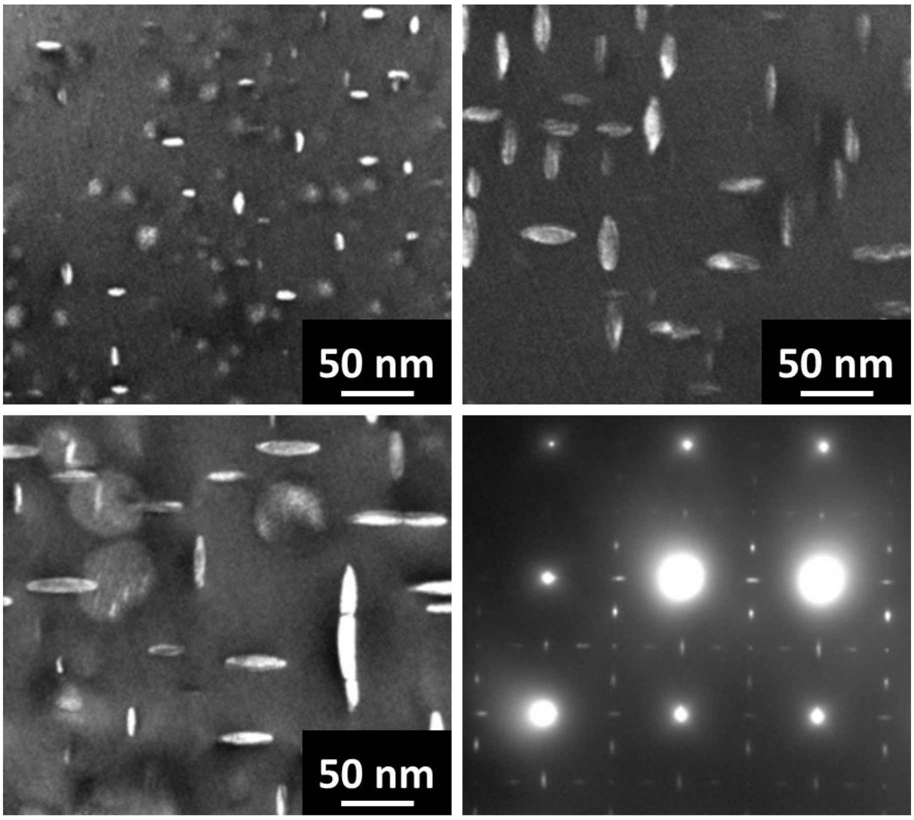

Figure 8: TEM image of the γ'' phase in IN625 aged at 650 °C for (a) 100 h (b) 200 h (c) 1000 h and (d) diffraction pattern [9]

- **δ**: incoherent, orthorhombic precipitate with chemical formula Ni_3Nb [1,3]. The common appearance of this phase is shown in Fig.9. This is a stable phase that forms in overaged **γ''** reinforced alloys at the grain boundaries, consuming the metastable **γ''**, below 700 °C, and also inside the grains, in a temperature range from 700 °C to 885 °C, forming by the coarsening of **γ''**, as summarized in Fig.10 [7,10]. Higher temperatures plates of **δ** directly precipitates faster than 24 h. The **δ** solvus temperature is tipically around 1000 °C [2,3,8].
  δ stability is increased in an alloy with high levels of Al and Ta, but can also be suppressed adding a 6% atomic of Ru [1].
  The formation of this phase is detrimental in terms of properties, since it is incoherent. It fails in provide a significant reinforcement even if present in large quantity, and it is associated to a reduction in ductility, creep performances and a severe worsening of the weldability, so its present is not desired [1,3,8].
  However, the **δ** formation kinetics can be accelerated performing forging below the **δ** solvus temperature; the **δ** phase precipitate in this condition can be used to refine the grain size. This is possible because small amounts of **δ** can be used exploiting its grain boundaries pinning effect, resulting in improved tensile properties, fatigue resistance, and creep rupture ductility [1,8].

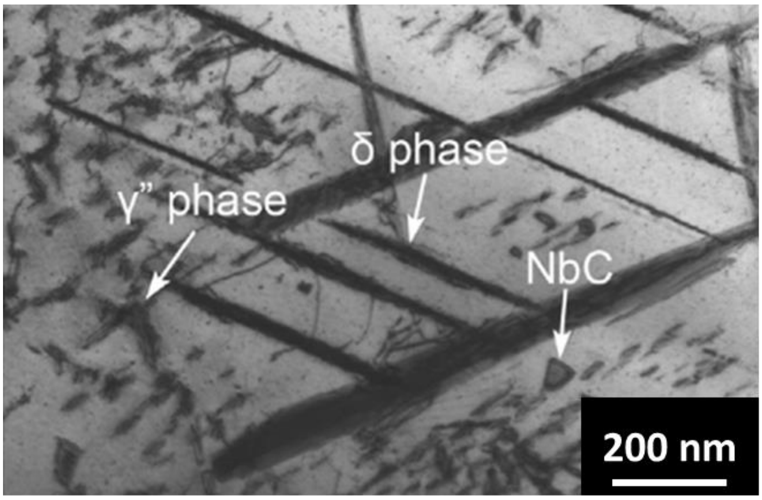

Figure 9: TEM image of δ phase [7]

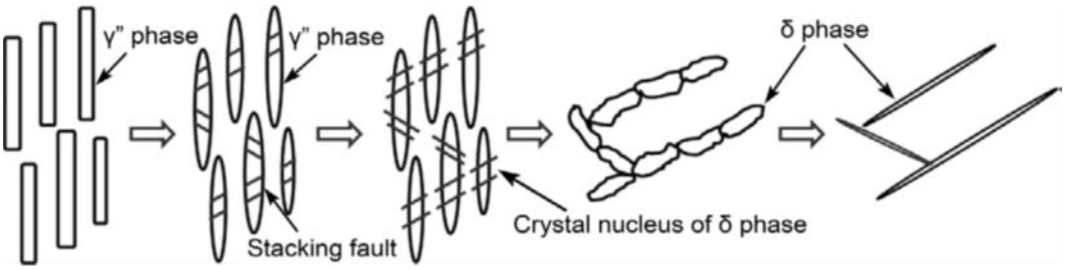

Figure 10: representation of the γ'' coarsening followed by the δ phase formation [7]

- **carbides**: primary carbides are usually in the form of MC and M_6C, where "M" is a metallic element [1].
  MC carbides possess a cubic lattice structure, and they can appear with globular, blocky and script morphology [8]. In this kind of carbides, the "M" can be Ti, Ta, Nb, Hf, Th, or Zr [1]. Usually they are formed by eutectic reaction during solidification in the interdendritic areas and along grain boundaries [1–3,8]. Precipitation from solid solutionized alloys is possible at temperature higher than 1038 °C and during cooling [2]. Their presence is beneficial mostly if they are used as source of carbon for precipitation of secondary carbides, but in continuous appearance they are detrimental [1]. During thermal exposure, MC carbides can decompose forming $M_{23}C_6$ and M_6C type carbides [1–3,8].
  M_6C carbides are characterized by a fcc lattice structure. They can have chemical formulas such as Fe_3Mo_3C, Fe_3W_3C and Fe_4W_2C, but they can have solubility also for elements such as Ta, Nb, Cr, Ni, and Co [1,2].
  This type of carbides form in a temperature range from 815 to 980 °C, and thanks to their stability are used as grain controller during processing [1–3].
  M_6C carbides tend to appears in alloys with level of Mo and/or W greater than 6 – 8% [3], and their formation can be caused by the decomposition of primary MC carbides [1], precipitate with a blocky shape at grain

boundaries, or sometimes they can assume a Widmanstätten morphology [2].
$M_{23}C_6$ carbides possess a fcc structure and usually $Cr_{23}C_6$ composition, But Cr can be in part changed with Ni, Fe, Co, W and Mo [1,2]. They possess a strict coherence with σ phase and can nucleate **σ** phase formation [2,8]. The shape of precipitation is crucial for the effect on mechanical properties [1]. It usually forms at grain boundaries in form of globules, platelets, in a temperature range between 760 and 980 °C, but also from decomposition of MC and M_6C carbides with reactions such as $MC + \boldsymbol{\gamma} \rightarrow M_{23}C_6 + \boldsymbol{\gamma}'$. The $M_{23}C_6$ [1–3,8].
They occasionally appear along twin bands, twin ends and stacking faults [2]. When this type of carbide grows along grain boundaries as a film leads to a reduction of both resistance and ductility, and when assumes cellular or Widmanstätten pattern morphology reduce ductility and rupture life [1–3,8].
At last, M_7C_3 carbides are characterized by hexagonal lattice structure. They are usually found with a blocky shape at the grain boundary [1,2]. Increasing the content of Co, Mo, W, and/or Nb in Ni-based superalloys can inhibit the formation of M_7C_3 [2].

- **borides**: borides possess a M_3B_2 structure with a tetragonal crystallattice. M can be Ta, V, Nb, Hf, Mo, Ti, Cr, Ni or Fe. Can be found in alloys with at least 0.03% of B. They appear similar to carbides, but they resist to chemical etching solution that attacks carbides [2]. The impact on the mechanical properties is also similar to the carbides effect, but they tend to form only at the grain boundaries, increasing the creep properties of the material [2,8].
  However, borides reduce the weldability because they precipitate at low temperatures and make the solidification temperature range wider [3].
- **nitrides** and **carbonitrides**: nitrides possess a generic formula of MN and a cubic crystallin lattice, and are insoluble in the alloy up to the melting temperature. M can be Ti, Nb, Hf, or Zr based on the alloy composition. They can be identified from shape (square or rectangular), and from the colour (yellow or orange colour). They form in the melt alloy and usually become nucleation sites for carbides, forming carbonitrides in some case, that possess similar properties to the MC carbides [1–3].
  Nitrides act like inclusions and reduce the forgeability in wrought nickel-base superalloys [2].
- **Detrimental Topological Closed Packed (TCP) phases σ, μ and Laves phases**:
  σ, **μ**, and **Laves** phases are defined as topologically close-packed phases, that usually show a brittle behaviour resulting in a reduction of the mechanical properties of the alloy, and they are detrimental also from the welding point of view, since their presence make wider the solidification temperature range and enhance the alloy cracking susceptibility [2,3].

They are usually located in the interdendritic area, indicating that they can forms thanks to eutectic mechanism, with a wide compositional range [3,8].

However, TCP phases are not dangerous every time: some study reveals that small amounts of σ may improve the creep-rupture strength [2]. The common undesirable effects of these phases are depending by several factors, such as the phase morphology, volume fraction and by the quantity of strengthening elements subtracted by the matrix and reinforcing phases [2]. Tensile strength is not reduced by TCP phase presence, meanwhile notch strength and ductility are more sensitive. Creep strength can be improved at the beginning of TCP phase precipitation, but in case of significant TCP phases formation the stress-rupture strength is greatly reduced [2]. Superalloys are usually designed in order to avoid the TCP phases formation, but in some cases minor composition changes can results in TCP precipitation, or, as discussed in the carbides section, other phases can act as nucleus for TCP development [2].

σ phase is formed by tetragonal FeCr, FeCrMo, CrFeMoNi, CrCo and CrNiMo. This phase shape is usually globular, irregular and elongated. It forms for long services between 540 and 980 °C.

μ is a rhombohedral phase with composition Co_2W_6, $(Fe, Co)_7(Mo, W)_6$ generally present in alloys rich in Mo and/or W. The appearance is coarse, irregular forming Widmanstätten platelets. It tends to form during exposure at high temperatures.

Laves phases usually is composed by globules with irregular shapes, elongated or by platelets when the alloy experience high temperature for long periods. The crystal structure is hexagonal and the possible compositions are Fe_2Nb, Fe_2Ti, Fe_2Mo, Co_2Ta and Co_2Ti [2].

1.1.3 Dispersed oxides strengthened Ni-based superalloys

The Oxide-Dispersion-Strengthened (ODS) superalloys are a special class of materials where oxides are insert in the alloy matrix by design, in order to be able to sustain very harsh operative conditions, where creep and corrosion resistance are crucial properties [1,3].

Generally, oxides can be introduced into alloy only through a mechanical alloying process, since oxide particles are insoluble in the matrix [1,3].

The oxide particles are usually characterized by a particle dimensional range from 25 to 50 nm [3]. During mechanical alloying process a composite of metal and oxide powder is produced, reaching a value of distance between two particles around 500 nm [3]. After this passage is common proceed with a post processing route where the consolidation is reached using Hot Isostatic Pressing (HIP) and the component shape is obtained through hot working. If needed, a high temperature annealing is performed in order to achieve recrystallization and grain growth [3].

The matrix of ODS superalloys is commonly Ni or Ni-Cr, sometimes Fe, and almost never Co [1,2].

The first generation of ODS superalloys used ThO_2 as strengthening oxide, than this practice was abandoned since Th is radioactive, so it was replaced with Y_2O_3 [1,2]. Other oxides applied in the ODS superalloys production are La_2O_3, Al_2O_3, CeO_2 and Sm_2O_3 [2]. The oxides presence in the matrix enhance mechanical resistance and creep properties of the alloy, providing stable properties for long times, since oxide particles are insoluble in the matrix and almost immune to coarsening, that limits the performance of γ' and γ'' strengthened alloys [1,3]. Moreover, oxides are found to be beneficial for the oxidation resistance of the alloy, since they act as nucleation agents for protective oxides and make the formed oxide layer smoother compared with the oxide formed in the same condition in the alloy without dispersed oxides [1].

In order to maximize the high temperature creep resistance, grains are preferred to be big and with a high aspect ratio parallel to the working direction [2,3]. This condition can be achieved choosing the correct post processing, obtaining high creep-rupture strengths for temperatures up to 90 % of their melting temperature [1].

ODS superalloys applications are components such as vane airfoils and platforms, nozzles, and combustor, engine glow plugs, heat treatment fixtures, burner hardware for power stations, gas sampling tubes and thermocouple tubes. They are also applied in aerospace components when are required high temperature strength properties and oxidation and sulfidation resistance [2].

1.2 Composition effects

Superalloys usually possess a really complex composition. The content of every element is related to the requirement of determined mechanical properties, surface stability or production costs [1,8].

Properties such as yield strength, toughness, ductility, low-cycle fatigue and creep life can be calibrated varying the alloy composition. Even small changes can impact on features such as **γ/γ’** lattice mismatch, **γ’** and carbides volume fraction, antiphase-boundary energy, stacking fault energy, elements diffusion rate and phases stability [1,8].

The effects of different elements in Ni-based superalloys is reported in the following list [1,3]:

- **Cr** is added in order to improve oxidation and corrosion resistance of the alloy, forming a protective Cr_2O_3 layer. Its presence is cause of $M_{23}C_6$ and M_7C_3 carbide formation. It provides to the alloy a moderate hardening through solid solution mechanism. It enhances the **γ’** volume fraction, but also the TCP phases formation.
- **Al** is added mostly for **γ’** precipitation. It has also the effect of improving the high temperature oxidation resistance forming Al_2O_3, that can

withstand to higher temperature compared to Cr_2O_3. Provides a moderate solid-solution hardening.

- **Ti** can moderately contribute to the solid-solution hardening of the alloy, but it is usually added in order to participate in the **γ'** precipitation and to form TiC carbides. During solidification it has a strong tendency to segregate in the liquid phase.
- **Ta** enhances the **γ′** volume fraction formation, the oxidation resistance and the solid-solution hardening of the alloy. It forms MC type carbides.
- **Nb** is a strong solid-solution strengthener of the alloy, allows the precipitation of **γ''** and **δ** phases and it improves the **γ'** volume fraction. It possesses a strong tendency to segregate in the liquid phase and forms NbC carbides.
- **Mo** is a strong solid-solution hardener and MC and M_6C carbides former. It helps to increase the **γ'** volume fraction. It has the drawbacks of increasing the alloy density and promoting the TCP phases formation.
- **W** provides a high solid-solution hardening to the alloy thanks to the high atomic radius. W additions are useful for increasing the **γ'** volume fraction and participate in the M_6C development. Similarly, to the Mo it increases the alloy density and promotes the TCP phases formation.
- **Fe** additions in the alloy enhance the workability and weldability of the alloy and it reduces the alloy cost. Unfortunately it reduces the oxidation resistance and promotes the formation of TCP phases.
- **Co** additions have the effect of raising the **γ** solidus temperature and the **γ'** solvus temperature. In some alloys it leads to an increased **γ'** volume fraction.
- **Re** brings to the alloy a contained solid-solution hardening and increase the lattice mismatch between the matrix and **γ'**. It has the effect of slowing down the diffusion, retarding the coarsening of reinforcing phases.
- **C** is added in order to form carbides that reduce the grains sliding. It also provides solid-solution hardening to the alloy.
- **B** provides a moderate solid-solution hardening to the alloy. It increases the grain-boundary strength, creep strength and ductility forming intragranular borides. It also inhibits the carbide coarsening.
- **Zr** provides similar beneficial effect of the B, but together with it possess a negative synergic effect that leads to hot tearing cracking, since their tendency to segregate in the liquid phase change the amount of eutectic liquid during solidification.
- **Hf** increases the grain-boundary strength, creep strength and ductility forming intragranular very stable borides and carbides. It also enhances the formation of eutectic γ/**γ'.**
- **Si** is seldom added in the composition just in order to enhance the alloy fluidity during casting. Keeping its level under a certain limit seems to reduce liquation cracking susceptibility.

- **Mn** is seldom added. It may be beneficial since it ties up S, which otherwise segregates at the grain boundaries with harmful effects. It loses this ability if Si is present because of a strong Si-Mn interaction. Keeping its level under a certain limit seems to reduce liquation cracking susceptibility.
- **Mg** in limited amount is beneficial, since limits sulfur segregation thank to its high affinity with S. However, outside this effect is detrimental, so its content is always very low.
- **S** and **P** are impurities that forms segregations at grain boundaries, causing grain boundary wetting and increasing the liquation cracking susceptibility.

1.3 Typical superalloy heat treatments

Heat treatments are a crucial post processing for many alloys, because they can be used for control the microstructural features, the precipitates shape, distribution and volume content and adjust the mechanical response of the material [2,11].

Usually superalloys production involves a singular or a combination of several heat treatments.

Heat treatments can be divided in 4 types, according to the time and temperature condition and to the objective of the treatment.

1) **Stress Relieving treatments**

Stress relieving treatment is performed on superalloys in order to reduce the stress carried by the material after the fabrication process. This heat treatment is usually performed at lower temperatures compared to the annealing or recrystallisation temperatures, in order to avoid microstructural changes. However the final result is often a compromise between the complete removal of stresses and the possible grain growth or phases evolution [2].

Usually the stress relief optimization for an alloy is the result of empirical studies of the stress reduction applying temperature for a certain time, evaluating it through nondestructive analysis such as X-ray diffraction.

However, the stress evaluation alone can be not enough for superalloys, since the effect of a heat treatments can modify also properties such as fatigue, creep and crack formation.

Stress relieving treatment is applied for both wrought and cast alloys, reducing the internal tension and avoiding shape and dimensional changes, and after welding. They are usually not performed on alloys that can be precipitation hardened, since these alloys have to be treated with solution heat treatment, that guarantees a drastic stress reduction [1,2,11].

Some typical stress reliving treatment conditions are reported in Table.3.

Table 3: Typical stress reliving treatment conditions [2]

Alloy	Stress relieving temperature (°C)	Holding time for inch of section (h)
	Ni & Ni-Fe-based superalloys	
19-9 DL	675	4
Incoloy 800	870	1.5
Inconel 600	900	1
Inconel 625	870	1

2) Annealing treatments

Annealing treatment is generally applied to a superalloy at a temperature that start grain growth and recrystallization mechanism, leading to a lower hardness of the material.

The annealing temperature range can be very wide, and the choise depends by the alloy treated, the mechanical properties required and the application conditions.

An annealing treatment can lead to different results based on the condition:

- Reduction of the internal stress of the alloy
- Homogenization of a cast microstructure
- Improvement of the ductility and reduction of the hardness, improving the workability
- Dissolving part of the phases
- Optimizing some microstructural features

Annealing treatments are often used during the components production in order to simplify the forming process. In this case, in order to limit grain growth during the hot work, the temperature is limited to value that not solubilize all the secondary phases at the grain boundaries, preserving their pinning effect [2,11].

Some typical annealing treatment condition is reported in Table.4.

Table 4: Typical annealing treatment conditions [2]

Alloy	Annealing treatment temperature (°C)	Holding time for inch of section (h)
	Ni & Ni-Fe-based superalloys	
19-9 DL	980	1
A-286	980	1
Discaloy	1035	1
Astroloy	1135	4
Hastelloy X	1175	1
Incoloy 800	870	0.25
Incoloy 901	1095	2
Inconel 600	1010	0.25
Inconel 625	980	1
Inconel 690	1040	0.5

Inconel 718	955	1
Inconel X-750	1035	0.5
Nimonic 80A	1080	2
Nimonic 90	1080	2
Renè 41	1080	2
Udimet 500	1080	4
Udimet 700	1135	4
Waspaloy	1010	4
	Co-based superalloys	
L-605 (HS-25)	1230	1
S-816	1205	1

3) Solution treatments

Solution heat treatment is performed at higher temperatures compared to stress reliving and annealing treatments, arriving near to the incipient melting temperature of the alloy.

The main goal of this treatment is the complete removal of secondary phases from the matrix, leaving a clean matrix decorated only with insoluble phases such as MC carbides and nitrides.

The high temperature needed to the precipitate dissolution creates also the condition for the maximum elemental diffusion, homogenizing the alloy composition and removing the segregations present after the solidification.

Moreover, it causes a complete recrystallization of the alloy, removing all the internal stresses and dendritic structures.

An alloy treated with this treatment reach the maximal ductility possible with a heat treatment, and the grain size results higher compared to the annealed condition.

Some typical solution treatment condition is reported in Table.5.

Table 5: Typical solution treatment conditions [2]

Alloy	Solution treatment temperature (°C)	Treatment time (h)	cooling
	Ni-Fe-based superalloys		
A-286	980	1	Oil quench
Discaloy	1010	2	Oil quench
N-155	1175	1	Water quench
Inconel 718	980	1	Air cooling
	Ni-based superalloys		
Astroloy	1175	4	Air cooling
Hastelloy S	1065	0.5	Rapid quench
Incoloy 901	1095	2	Water quench
Inconel 600	1120	2	Air cooling
Inconel 601	1150	1	Air cooling
Inconel 617	1175	2	Water quench
Inconel 625	1150	2	Rapid water quench
Inconel 939	1160	4	Furnace cooling
Inconel X-750	1150	2	Air cooling

Nimonic 80A	1080	8	Air cooling
Nimonic 90	1080	8	Air cooling
Renè 41	1065	0.5	Air cooling
Udimet 500	1080	4	Air cooling
Udimet 700	1175	4	Air cooling
Waspaloy	1080	4	Air cooling
	Co-based superalloys		
L-605 (HS-25)	1230	1	Rapid air cooling
Haynes 188	1175	0.5	Rapid air cooling
Haynes 556	1175	0.5	Rapid air cooling
S-816	1175	1	Rapid water quenching

4) Precipitation hardening (aging) treatments

Precipitation hardening treatments, also knew as aging treatments, are performed on alloys in which composition allows the formation of secondary phases when exposed to temperature.

The common phases desirable for develop optimal mechanical properties are precipitates such as **γ’**, **γ’’** and secondary carbides.

In order to achieve better properties, the formation of detrimental phases must be avoided during the aging.

Commonly a solution treatment is performed before the aging, in order to maximize the phases formation during aging.

An aging treatment can be long and complex, including multiple aging steps preformed at different temperature and for different times.

These complex treatments have been developed in order to stabilize some phases and give them size and distribution the results in properties perfect for a target application.

During service at high temperature the aging process goes on, usually coarsening precipitates and promoting transformation such as **γ’** → **η**, **γ’’** → **δ** and $M_{23}C_6$ growth. This process deteriorates the mechanical and corrosion properties of the alloy and it is called overaging [2,11].

Some typical aging treatment route is reported in Table.6.

Table 6: Typical aging route for superalloys [2][12][11]

Alloy	Aging treatment temperature (°C)	Treatment time (h)	cooling
	Ni-Fe-based superalloys		
A-286	720	16	Air cooling
Discaloy	730	24	Air cooling
N-155	815	4	Air cooling
Inconel 718	720 620	8 8	Furnace cooling+ Air cooling
	Ni-based superalloys		
Astroloy	845	24	Air cooling

Incoloy 901	790	2	Air cooling
Inconel 706	720	8	Furnace cooling+
	620	8	Air cooling
Inconel 939	1000	6	Furnace cooling+
	900	24	Air cooling+
	700	16	Air cooling
Inconel X-750	845	24	Air cooling
Nimonic 80A	705	16	Air cooling
Nimonic 90	705	16	Air cooling
Renè 41	760	16	Air cooling
Udimet 500	845	24	Air cooling
Udimet 700	845	24	Air cooling
Waspaloy	845	24	Air cooling
	Co-based superalloys		
S-816	760	12	Air cooling

1.4 Inconel 625 and Inconel 939 characteristics

1.4.1. IN625 properties

IN625 was developed to be a simple solid-solution strengthened superalloy, for application below 700 °C [13]. However, the content of Nb allows the age hardening for this alloy, making **γ’’** phase precipitate at temperatures between 649 and 871°C, increasing the alloy mechanical resistance. The service temperatures range for this alloy spaces from cryogenic up to 980 °C. Thanks to the high content in Cr and Mo this alloy possesses outstanding corrosion resistance in harsh conditions, and also an impressive fatigue and corrosion-fatigue life when the impurities are limited. The applications range of IN625 includes aerospace, aeronautic, marine, chemical, petrochemical, and nuclear industries.

It is one of the few alloys allowed by the ASME Boiler and Pressure Vessel Code to operate in pressure vessels for temperatures up to 982 °C.

Its peculiar resistance at cracking and easy weldability make this alloy popular as welding material for both superalloys and stainless steels. Thanks to the compatibility with stainless steels is frequently used as corrosion and heat resistant coating in order to reduce costs [13–18].

UNS N06625 summarize the chemical composition specifications for this alloy, showed in Table.7.

Table 7: Elemental composition limits in Inconel 625 according to UNS N06625 specification

Element Weight percent (wt %)	Element Weight percent (wt %)
Ni	58.0 min
Cr	20.0-23.0
Mo	8.0 -10.0
Nb + Ta	3.15-4.15
Fe	5.0 max
Co	1.0 max

Si	0.50 max
Mn	0.50 max
Ti	0.40 max
Al	0.40 max
C	0.10 max
S	0.015 max
P	0.015 max

This material is usually commercially available in two conditions, that are defined in the ASTM B443. According to the specification, IN625 is called:

- Grade 1 IN625 when the alloy is annealed at temperatures between 870 and 980 °C
- Grade 2 IN625 when the alloy is solution annealed at least at 1093 °C.

Since heat treated at lower temperature, Grade 1 IN625 possess smaller grains compared to the Grade 2 alloy. This microstructure provides superior tensile strength, stress-corrosion resistance in chloride presence and corrosion resistance in general. This condition is meant for application temperatures up to 600 °C. The high strength and corrosion resistance of this alloy condition make it perfect for marine applications such as submarines and boats components.

The higher temperature used for the Grade 2 IN625 have the effects of dissolving secondary phases and allowing a more consistent grain growth compared to the condition treated before. The resulting microstructure provides to the alloy extreme ductility and enhanced creep performances, making this condition more interesting for high temperatures applications. For these reasons this alloy condition finds common application in the aerospace sector for component of engines, exhaust and hydraulic systems [10,12,14,18].

Common mechanical properties of IN625 alloys found in literature are reported in Table.8 compared with the ASTM B443 specification.

Table 8: Typical mechanical properties of commercially available IN625

IN625	**YS (MPa)**	**UTS (MPa)**	**El (%)**
Cast [2]	350	710	48
Wrought IN625 [19]	517	930	40
As-rolled rod [18]	414 - 758	827 - 1103	30 - 60
Annealed rod [18]	414 - 655	827 - 1034	30 - 60
Solution annealed rod [18]	290 - 414	724 - 896	40 - 65
Wrought IN625 grade 1*	>414	>827	>30
Wrought IN625 grade 2**	>276	>690	>30

**ASTM B443 (minimum annealing temperature 871 °C)*

***ASTM B443 (minimum solution annealing temperature 1093 °C)*

The metallurgy of IN625 is quite complex considering that was designed for be a solid solution strengthened superalloy.

During solidification, different eutectic reactions can happen based on the Si and C content of the alloy, even if those composition are inside the alloy specification limits [16]. Some examples of solidification path, varying the Si and C content is reported below in Table.9 (L, γ, NbC and Laves indicate respectively the melt alloy, the matrix, Nb carbide and Laves phase) [3].

Table 9: different IN625 solidification paths as fuction of the alloy composition

IN625 (0.03 Si, 0.009 C) (low Si, low C) **L → L + γ → L + γ + NbC → L + γ + NbC + Laves →** **→ γ + NbC + Laves**
IN625 (0.03 Si, 0.038 C) (low Si, high C) **L → L + γ → L + γ + NbC → γ + NbC**
IN625 (0.38 Si, 0.008 C) (medium Si, low C) **L → L + γ → L +γ + NbC → L + γ + NbC + M_6C →** **→ L + γ + NbC + M_6C + Laves → γ + NbC + M_6C + Laves**
IN625 (0.46 Si, 0.035 C) (high Si, high C) **L → L + γ → L + γ + NbC → L + γ + NbC + Laves →** **→ γ + NbC + Laves**

As anticipated in previous sections, the Laves phases are TCP precipitates with very detrimental effect on the alloy ductility, so their presence must be avoided. If they are formed during solidification it is possible dissolve them in the matrix performing a solution annealing at temperature higher than 1093 °C.
The removal of NbC carbides is more challenging, since they can withstand temperatures up to 1190 °C, (the alloy melting range is between 1290 and 1350°C [18]), but when they are well dispersed in the microstructure with small dimensions are not detrimental for the properties, so usually is not mandatory their [13,16].

Many other phases can be present in the alloy, as reported in time-temperature transformation (TTT) diagram shown in Fig.11.

Between them γ’’ is often added into the microstructure performing a precipitation hardening treatment. Moreover, during the thermal exposures and the service the microstructure evolves, presenting multiple types of carbides, such as MC, M_6C, $M_{23}C_6$ that can be beneficial or detrimental based on their shape, morphology and distribution, and **δ** phase. The latter is the stable form of Ni_3Nb, and forms from γ’’ coarsening or precipitates at high temperatures. Its presence is usually detrimental because reduces the ductility without improvement of the tensile strength [2,11,13,14,16].

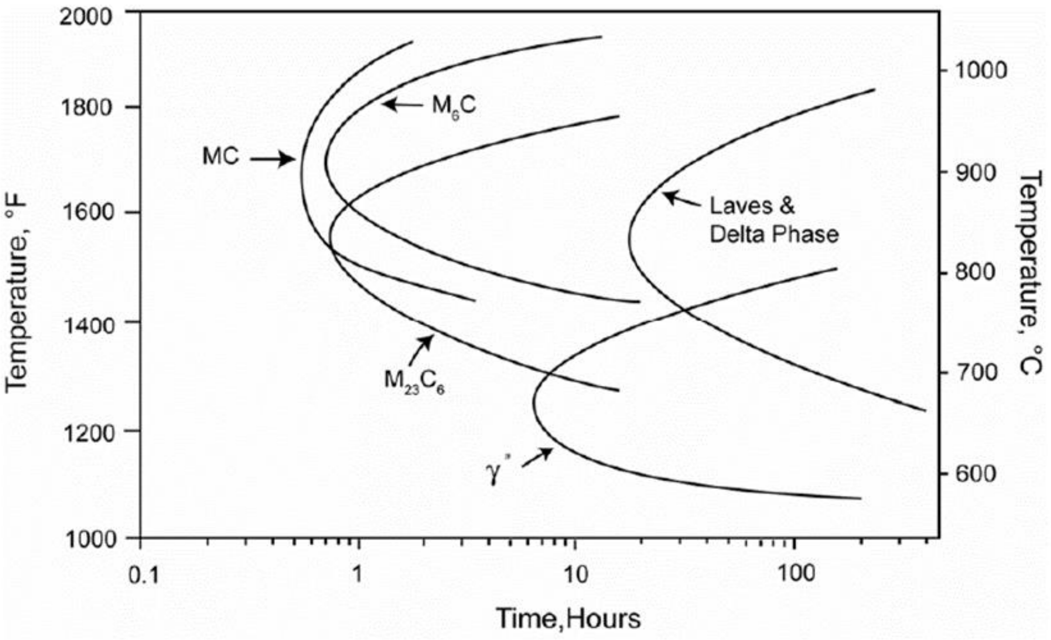

Figure 11: TTT diagram for the IN625 superalloy [14]

1.4.2. IN939 properties

IN939 is an age-hardenable superalloy reinforced through γ' precipitation characterized by a good corrosion resistance.

The chemical composition is reported in Table.10.

Table 10: Inconel 939 composition range [20]

Element	Weight percent (wt %)
Ni	Bal
Cr	20.0-22.6
Co	18.5-19.4
Ti	3.6-3.8
Ta	3.6-3.8
W	1.9-2.2
Al	1.8-2.1
Nb	0.8-1.8
C	0.13-0.165
Zr	0.08-0.12
B	0.008-0.012

It can operate for long service times at the temperature of 850 °C, and it is usually applied in the production of component such as vanes and blades for land-based and marine gas turbines [20–28].

In such application the repairing cost are elevated, and the possibility of repairing through welding is desirable. However, is well known that γ' age-hardenable superalloy are really difficult to be welded, especially when containing high content of γ' forming elements. Also IN939 suffer micro fissuring in the heat affected zone after welding, but several studies pointed out the performing a prewelding heat treatment results in a good weld results, especially when possess a low impurities content [22,26,29].

This alloy can be heat treated obtaining high volume fraction of γ’, and the common heat treatment route consists in a 4 step heat treatment in order to achieve good properties [2,11,20,23], but 3 step and 2 step routes were also proposed [24,28]. A list of possible treatments with the resulting mechanical properties at room temperature is reported in Table.11, and the creep properties at 816 and 870 °C are reported in Table.12. The most used treatments are the four stages heat treatment and the two stages heat treatment.

Table 11: Room temperature tensile properties of IN939 treated in different ways [28]

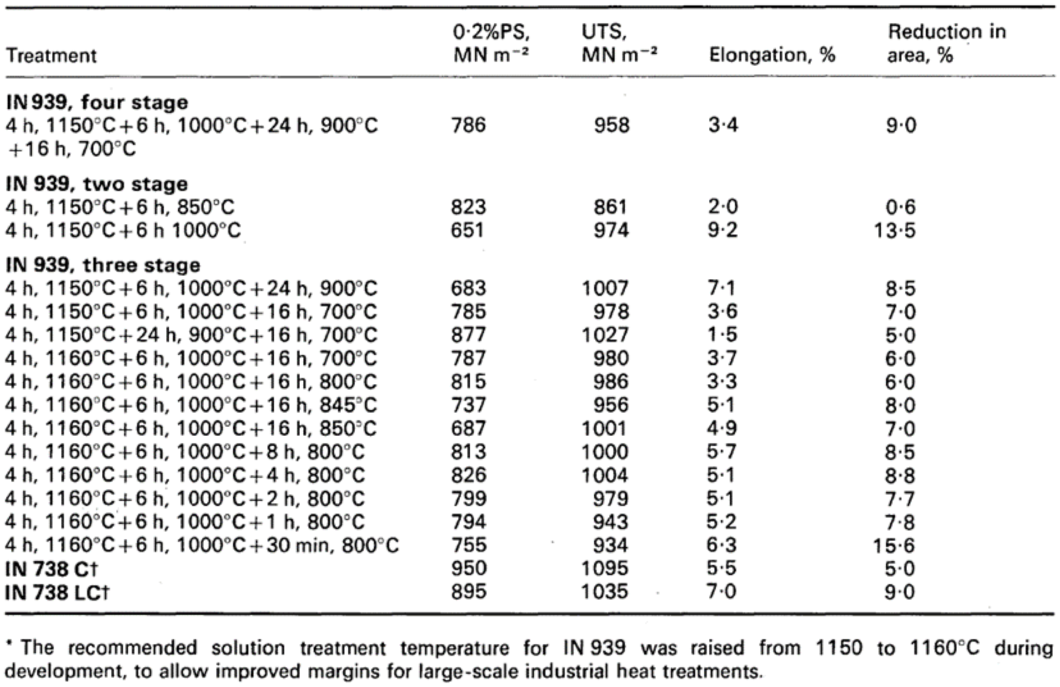

Treatment	0·2%PS, $MN\ m^{-2}$	UTS, $MN\ m^{-2}$	Elongation, %	Reduction in area, %
IN 939, four stage				
4 h, 1150°C+6 h, 1000°C+24 h, 900°C +16 h, 700°C	786	958	3·4	9·0
IN 939, two stage				
4 h, 1150°C+6 h, 850°C	823	861	2·0	0·6
4 h, 1150°C+6 h 1000°C	651	974	9·2	13·5
IN 939, three stage				
4 h, 1150°C+6 h, 1000°C+24 h, 900°C	683	1007	7·1	8·5
4 h, 1150°C+6 h, 1000°C+16 h, 700°C	785	978	3·6	7·0
4 h, 1150°C+24 h, 900°C+16 h, 700°C	877	1027	1·5	5·0
4 h, 1160°C+6 h, 1000°C+16 h, 700°C	787	980	3·7	6·0
4 h, 1160°C+6 h, 1000°C+16 h, 800°C	815	986	3·3	6·0
4 h, 1160°C+6 h, 1000°C+16 h, 845°C	737	956	5·1	8·0
4 h, 1160°C+6 h, 1000°C+16 h, 850°C	687	1001	4·9	7·0
4 h, 1160°C+6 h, 1000°C+8 h, 800°C	813	1000	5·7	8·5
4 h, 1160°C+6 h, 1000°C+4 h, 800°C	826	1004	5·1	8·8
4 h, 1160°C+6 h, 1000°C+2 h, 800°C	799	979	5·1	7·7
4 h, 1160°C+6 h, 1000°C+1 h, 800°C	794	943	5·2	7·8
4 h, 1160°C+6 h, 1000°C+30 min, 800°C	755	934	6·3	15·6
IN 738 C†	950	1095	5·5	5·0
IN 738 LC†	895	1035	7·0	9·0

* The recommended solution treatment temperature for IN 939 was raised from 1150 to 1160°C during development, to allow improved margins for large-scale industrial heat treatments.

Table 12: Creep properties at 816 and 870 °C of IN939 treated in different ways [28]

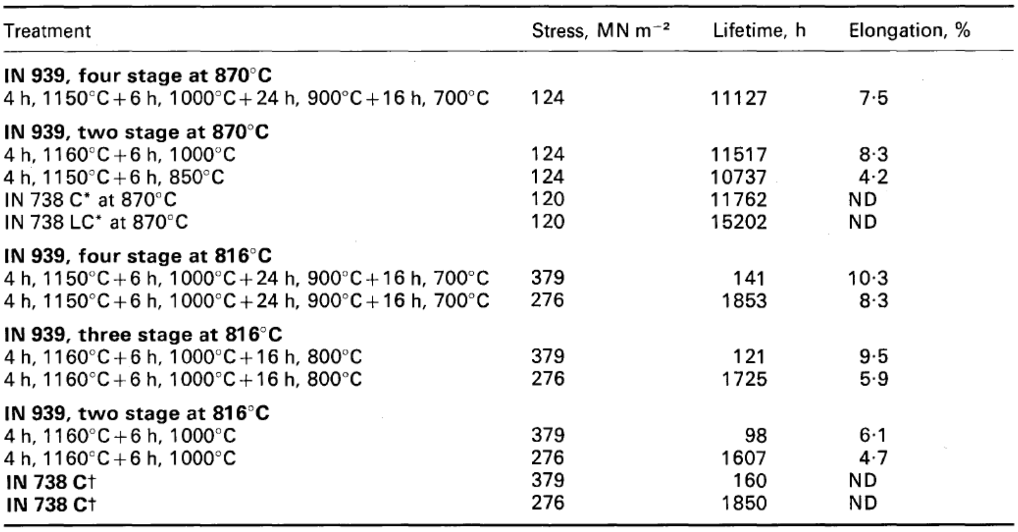

Treatment	Stress, $MN\ m^{-2}$	Lifetime, h	Elongation, %
IN 939, four stage at 870°C			
4 h, 1150°C+6 h, 1000°C+24 h, 900°C+16 h, 700°C	124	11127	7·5
IN 939, two stage at 870°C			
4 h, 1160°C+6 h, 1000°C	124	11517	8·3
4 h, 1150°C+6 h, 850°C	124	10737	4·2
IN 738 C* at 870°C	120	11762	ND
IN 738 LC* at 870°C	120	15202	ND
IN 939, four stage at 816°C			
4 h, 1150°C+6 h, 1000°C+24 h, 900°C+16 h, 700°C	379	141	10·3
4 h, 1150°C+6 h, 1000°C+24 h, 900°C+16 h, 700°C	276	1853	8·3
IN 939, three stage at 816°C			
4 h, 1160°C+6 h, 1000°C+16 h, 800°C	379	121	9·5
4 h, 1160°C+6 h, 1000°C+16 h, 800°C	276	1725	5·9
IN 939, two stage at 816°C			
4 h, 1160°C+6 h, 1000°C	379	98	6·1
4 h, 1160°C+6 h, 1000°C	276	1607	4·7
IN 738 C†	379	160	ND
IN 738 C†	276	1850	ND

As in the case of the IN625, also for this alloy there are several phases that can be formed in the alloy, during heat treatments and during the service in temperatures. They are summarized in Table.13.

Table 13: Phases observed in IN939 in different conditions [20] **(FHT is the traditional 4 stage heat treatment)**

Phase	**Observed in**	**Composition**	**Crystal structure**
Eutectic γ/γ'	As cast		
γ	All conditions	Solid solution (**Ni**, **Cr**, **Co**, Al, Ti, W, Ta, Nb)	fcc
γ'	FHT*	Ni_3Al (**Ni**, **Al**, **Ti**, Co, Cr, W, Nb, Ta)	fcc
MC	As cast and FHT*	MC (**Ti**, **Nb**, **Ta**, W)(**C**, N, Si, S, Zr)	fcc
$M_{23}C_6$	FHT*+service	Cr_{21}(**Mo**, **W**, Ni, Co, Ti, Zr)$_2$(**C**, B)$_6$	fcc
σ	FHT*+service	(**Ni**, **Co**, **Cr**, Al, Ti, W, Ta, Nb)	btc
η	As cast	Ni_3Ti	cph

** FHT is the traditional 4 stage heat treatment*

Some of those phases are detrimental and they tend to appear after long service periods (**σ**), others such as **η** are present in the as cast alloy and can be removed performing a solution treatment. However long service times tend to transform phases, coarsening **γ'** and carbides, and eventually making them toevolve into other phases [21,23], but at the moment the literature that cover this reduction of properties in service is limited [21,23].

1.5 Metals additive manufacturing

Additive Manufacturing (AM) technologies received a lot of attentions in the last ten years, thanks to advantages such as the unique design freedom and the short production line [30]. Differently than traditional fabrication process, based on subtractive methods, AM production is based on subsequent addition of material, following the instructions of a CAD project, in order to obtain components [30,31]. Metal AM technologies use metals in form of powder, wire or sheets as feedstock, which is consolidated through different ways, based on the selected AM technology [30,31]. It is more than 20 years that those technologies are known, but initially they were applied only in the rapid production of prototypes and porous structures [30]. After years of development the properties obtained improved enough to allow AM produced components application as tool inserts with complex internal cooling channels and customized prostheses [30].

Today some AM technologies can produce reliable, dense component with materials such as steels, Al and Ti alloys [30].

A list of the application fields for AM products of different alloys are summarized in Table.14.

Table 14: Application fields of different alloy classes [32]

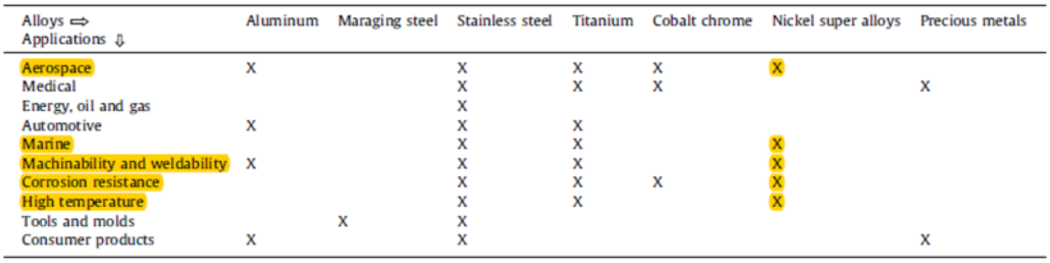

Alloys ⇨ Applications ⇩	Aluminum	Maraging steel	Stainless steel	Titanium	Cobalt chrome	Nickel super alloys	Precious metals
Aerospace	X		X	X	X	X	
Medical			X	X	X		X
Energy, oil and gas			X				
Automotive	X		X	X			
Marine			X	X		X	
Machinability and weldability	X		X	X		X	
Corrosion resistance			X	X	X	X	
High temperature			X	X		X	
Tools and molds		X	X				
Consumer products	X		X				X

There are many different metals AM technologies, as reported in Fig.12:

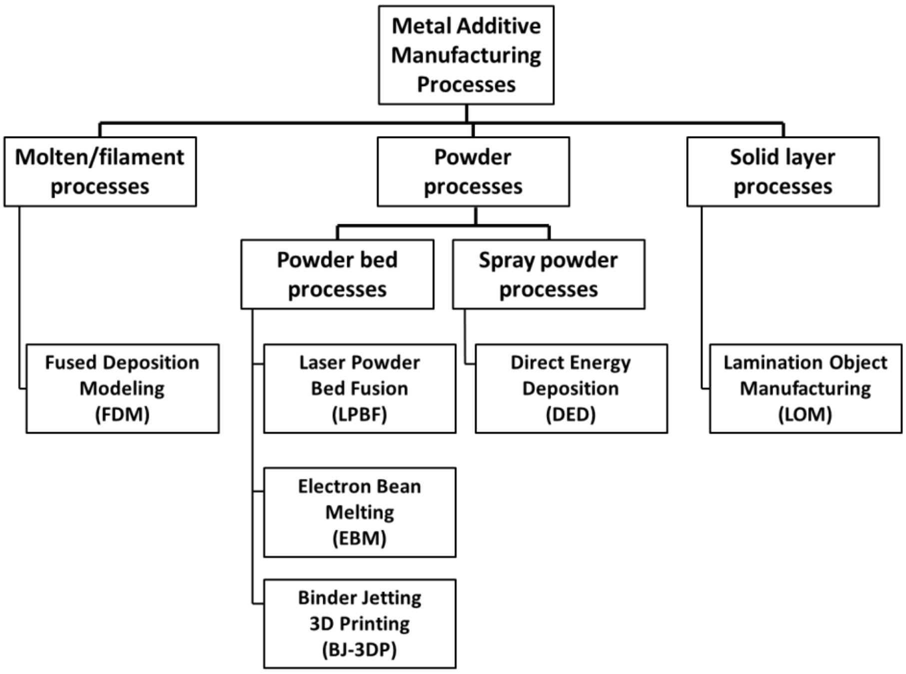

Figure 12: List of different metal additive manufacturing technologies [31]

- Fused Deposition Modeling (FDM): is an AM process in which the feedstock material, typically in wire form, is melted and deposited according to the CAD project layer by layer, up the complete replication of the CAD object. The feedstock can be a metal wire or a polymer filled with metal powder. In the second case, additional steps are required for production (polymer removal and sintering). This technology provides components with poor dimensional accuracies and surface finish [31].
- Laser Powder Bed Fusion (LPBF): is an AM process, conducted in inert gas atmosphere, in which a powder layer is selectively melted by a laser source, according to a CAD project, then a new layer is created and the process repeated until the complete object is created. Further details on this technology are present in the following thesis section [30–32].
- Electron Bean Melting (EBM): is a technology similar to the LPBF, but it is conducted in void and instead of a laser the powder densification is obtained using an electron beam, controlled through electromagnetic fields. This technology allows faster productions compared to LPBF, since

can use higher beam power and higher scanning speed. However, this technology is more expensive and complex then LPBF, gives final components with higher roughness and, because of the void, is not suitable for low melting point alloys [30–32].

- Direct Energy Deposition (DED): with this technology the CAD project is replicated using a robotic arm that end with a nozzle that emits a flux of powder that is melted outside using a laser or a plasma system located at the nozzle exit. This process is really versatile, and allows the repair of damaged components or can be used for coating deposition. The process can be conducted in air or with a presence of a shielding gas, in order to reduce oxidation during the melting process [30–32].
- Binder Jetting 3D Printing (BJ-3DP): this technology requires the production of powder layers as in the LPBF and EBM cases, but instead of melt the powder the consolidation is reached selectively injecting a liquid polymeric glue. In order to reach densification the components need a debinding process followed by a sintering one [31,33].
- Lamination Object Manufacturing (LOM): is a solid state AM technology that consists in cutting from a sheet each object layer using a laser system and then consolidate them applying high heat and pressure or ultrasonic vibrations This process is considerably faster compared to other AM processes, but the geometric accuracy, surface finish and material properties are often very poor as well as the part of each sheet which is cut away has to be considered a scrap. [31].

The advantages of this kind of technologies, compared to traditional processes are:

- Cutting the pre-processing time (from CAD to object)
- Material waste reduction (material added where is needed)
- High design freedom, with internal shapes not obtainable with other technologies
- Production of near net shape components that require limited post-process.

On the other hands there are some drawback to be aware of:

- High feedstock material cost (especially for powders)
- Anisotropy of the properties
- Maximum size limitation (depends by the system)
- Components have to be removed from the building platform and in some case also support structures have to be removed
- Long processing time in the AM machine

1.5.1. LPBF technology

As anticipated in the preview section, Laser Powder Bed Fusion (LPBF) is an AM technology in which powder layers are consolidated by a laser obtaining dense part.

In literature and commercially this technology is also known with different names, such as Selective Laser Melting (SLM), Direct Metal Laser Sintering (DMLS), Laser-cusing, that varies with the machine producer [34].

The entire building process is conducted in inert atmosphere, commonly obtained filling the machine with Ar and N_2.

Once the CAD file is processed with the machine software and the dispenser chamber is filled with powder, the building steps for create an object in the LPBF machine are:

- The dispenser platform raises
- A recoater system (typically a blade) moves from the dispenser to the collecting chamber, creating a uniform powder layer on the building platform
- The laser starts to scan, moved by a mirrors system, according to the CAD project, melting the powder in order to obtain a slice of the object
- When the slice is created, the building platform is lowered of an amount higher than a layer thickness and the recoater returns in position on the dispenser chamber
- At this point the building platform raises exactly at a height equal to the previews level minus a single layer thickness
- The dispenser platform raises and the recoater spread a new powder layer
- The process is repeated until the complete object is densified

A graphical overview of the process is reported in Fig.13.

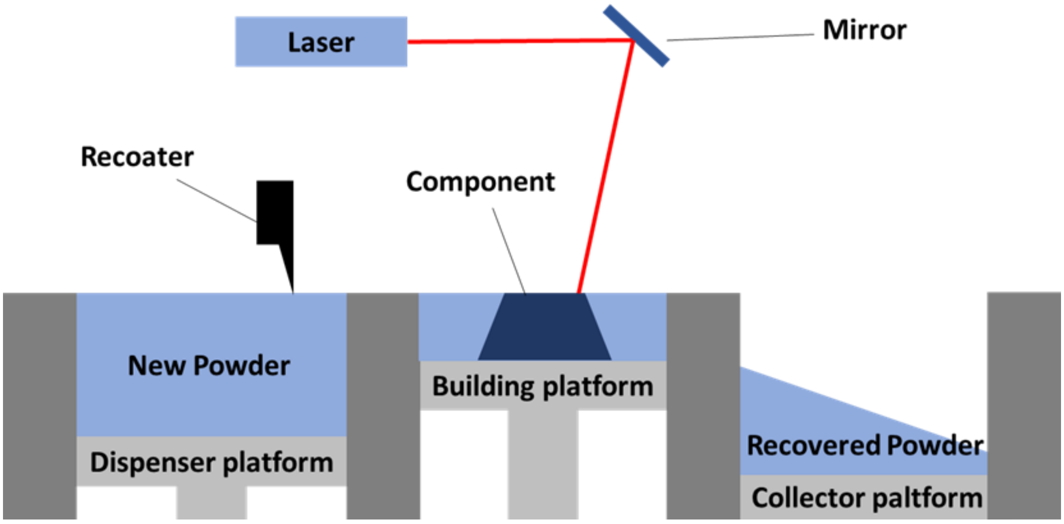

Figure 13: Graphical representation of the LPBF process

Depending by the machine used, there are many parameters that can be changed in the LPBF process:

- Building platform temperature;
- Layer thickness
- Laser power (**P**)
- Laser scanning speed (**v**)
- Hatching distance ($\mathbf{h_d}$), which is the distance between two laser scans

- Scanning strategy, that define route followed by the laser for densify a slice.

Scanning strategies can be very different form one to another, as illustrated in Fig.14. The laser can follow the same direction for all the scans (a), go back and forward (b) or follow fractal paths (c,d). Moreover, for each layer the laser can simply cover all the slice using the strategies a, b, c and d for the entire slice of dived the slices in islands (e) or stripes (f). In the end, between each slide the path followed can be the same, rotated (usually by 90° or 67° (the last suggested by EOS)) and translated of a certain distance [35–39].

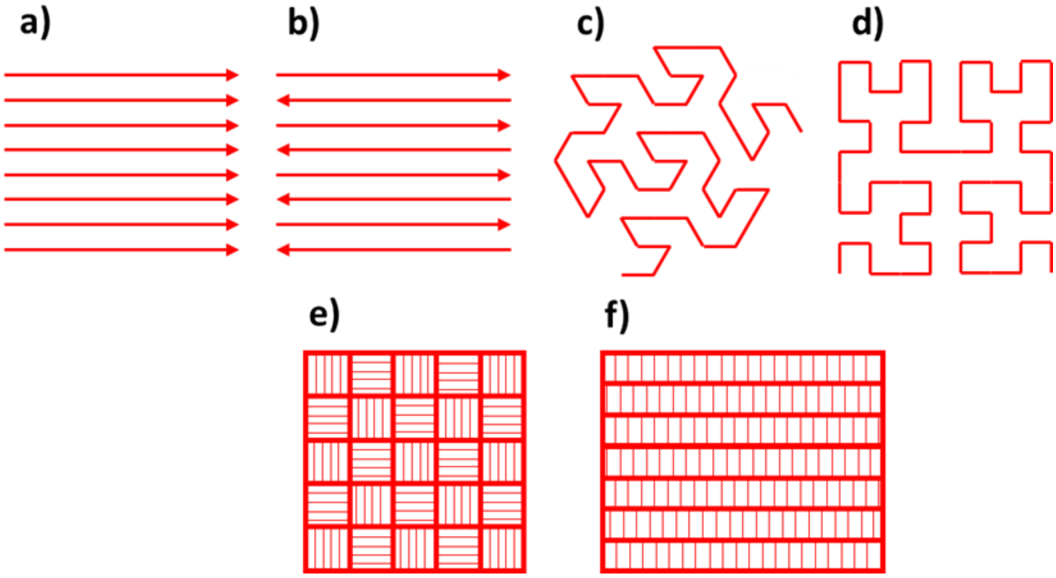

Figure 14: Scanning strategies examples

The choise of determined parameter sets, scanning strategy and building platform temperature determines the thermal history experienced by the alloy during the process, changing the resulting density, mechanical resistance, hardness and residual stresses [40].

1.5.1.1 LPBF produced Ni-based superalloys

The powder used for LPBF processes are commonly gas atomized powder obtained using an inert gas such as Ar or N_2, in order to reduce the risk of oxidation. Other powders production technologies utilize water, air, and plasma in the atomization process (the last two give better powder quality but are more expensive).

Good powders for LPBF should possess the following requirement:

- Spherical shape
- Smooth surface
- Absence of satellites particles
- Absence of external oxidation
- Low oxygen and humidity content

- Particle size distribution between 10 and 63 μm with a Gaussian distribution
- High skeletal density (absence of internal pores generated in the atomization process)
- Good flowability (in order to form a compact and uniform powder layer)
- Good apparent density (in order to form a compact powder layer)

The presence of defects such as rough surface, presence of satellites particles, bad particle size distribution and also humidity content tends to reduce the flowability of the powder, increasing the risk of inhomogeneities in the powder layer, that leads to porosity and lack of fusion defects.

The porosity in the powder can survive to the melting and remain inside the printed alloy.

The presence of high oxygen content can lead to oxides formation during the process, that together with pre-existing powder surface oxidation can remain as inclusions or prevent the melting of the powder particle [41–43].

1.6 LPBF produced Ni-based superalloys

The production of Ni-based superalloys using LPBF technology gained a lot of attention in the last ten years, as testified by the graph in Fig.15, where the number of publications specific for LPBF produced Ni-based superalloys is reported (obtained considering papers (241), reviews (7), proceedings (31) and reports (4) available on Scopus) as function of the pubblication year starting from 2008. It is clear that more than half of this material has been published in the last two years, proving the importance of this topic in both academic and industrial worlds. The main reasons of this interest are probably the difficulties of machining and forming alloys with such high properties in high temperature conditions, the possibilities of overcome the high weight of these alloys through new components design and create internal cooling channels customized for each design [4,24,44,45].

In the graph in Fig.16 is also reported the provenance of the papers, reveling where this topic is more investigated.

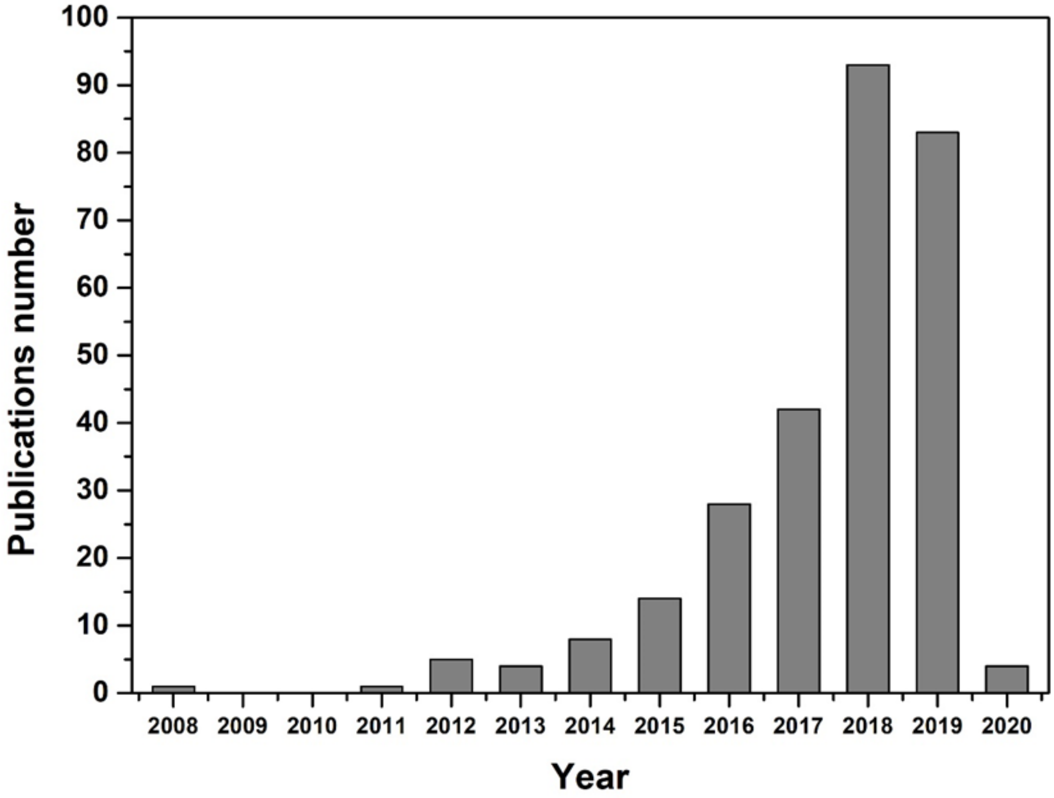

Figure 15: Publications on Ni-based superalloys LPBF produced

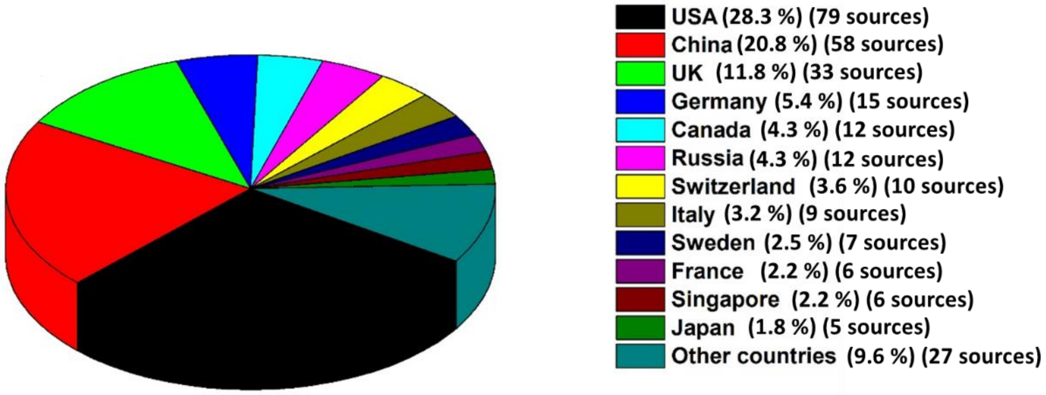

Figure 16: LPBF produced Ni-based superalloys publications percentage for various country

Processing Ni-based superalloys with LPBF technology is a big challenge, since most of them possess a very low weldability and are prone to several cracking mechanism, such as:

- Solidification Cracking (SC): this mechanism is also known as “hot tearing”. It can happen during the solidification process. The dendrites formation traps the interdendritic liquid in the interdendritic regions. The trapped liquid can become a crack initiation point, because of the stress associated to solidification. Elements such as boron and zirconium increase the SC of nickel-base superalloys [1]
- Liquation Cracking (LC): this mechanism, reported after welding process, interest the alloy in a location away from the melt pool. The rapid heating, caused from the weld, results in the melting of phases

located at the grain boundaries, wich have a low melting point or an eutectic composition. The liquid film formed can act as crack starting point under the thermal stresses of the welding.

- Strain Age Cracking (SAC): often associated with the Post Weld Heat Cracking (PWHT). During this treatment two effects have place: a stress relaxation and the precipitation of phases with a fast kinetics as **γ'** or **carbides**. This fast precipitation develops an extra stress and reduces the ductility of the alloy and its capability of accommodate stresses. If the relaxation effect results insufficient cracks can be nucleated near to intragranular carbides.
- Ductility Dip-cracking (DDC): this mechanism is associated to a drop in the ductility of Ni-based superalloys at intermediate temperatures.
  Young et al. attributed this phenomena to the formation of carbides at the grain boundary, that imposing stress to the surrounding alloy can lead to the develops of voids [46], meanwhile Collins et al. proposed a creep-like mechanism in which the temperature allows grain sliding but not dynamic recrystallization, leading to voids formation at the triple grain boundaries point.
  A way for reduce DDC seems to have tortuous grain boundaries and presence of grain boundaries particles that reduce the grain boundary sliding [3,45,47–49].

In a process such as LPBF, that can be seen as a repeated welding, all this mechanism can happen, resulting in alloys full of cracks.

In Fig.17 it is reported a graph where the weldability and the PWHT are evaluated as function on the **γ'** forming elements content in the alloy [2,3], and in Fig.18 a similar graph is proposed, but it uses a criteria in which also carbide forming elements (Cr and Co) content is considered [45]. Co can take part in the formation of the carbide (M_6C) and Cr is responsible of the $M_{23}C_6$ and M_7C_3 carbides.

From both of these graphs can be deduced that alloys with high **γ'** forming elements are considered not weldable, but these are the alloys that provide the best properties in high temperature applications [2,3,45].

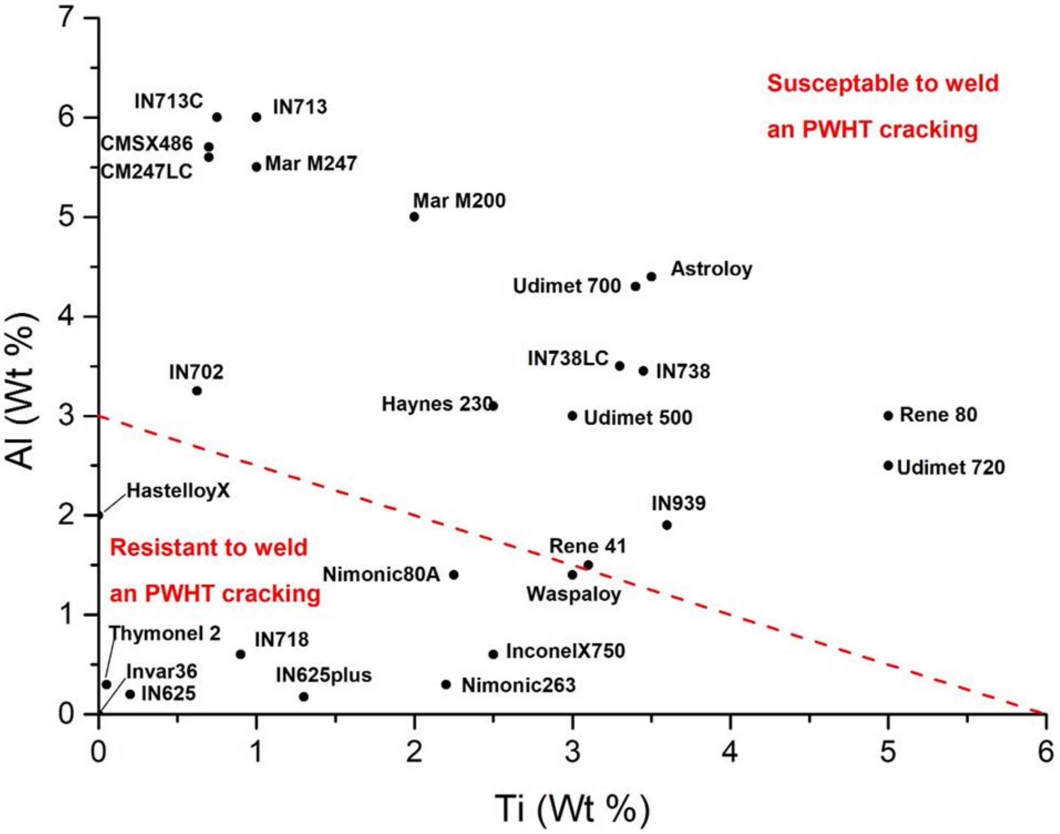

Figure 17: Weldabilty graph of Ni-based superalloys, considering γ' forming elements content [3]

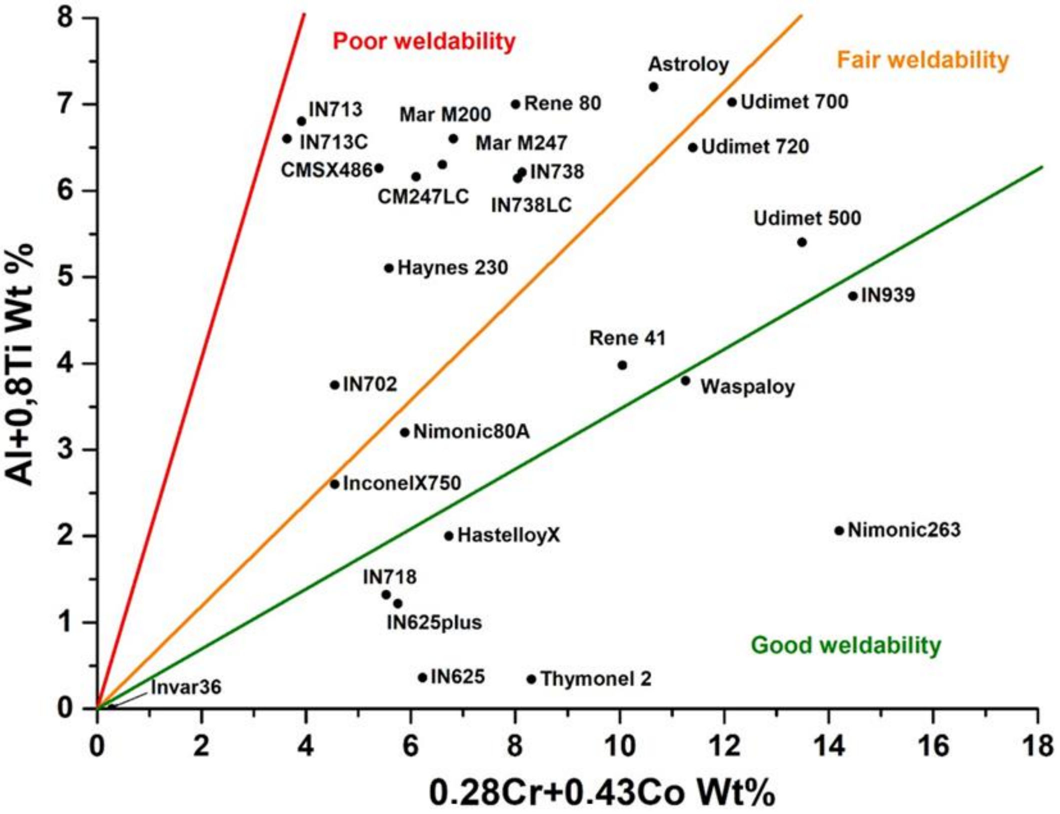

Figure 18: Weldabilty graph of Ni-based superalloys, considering γ' and carbides forming elements content [45]

These reasons explain why almost half of the publication on LPBF produced superalloys are about the IN718 alloy (as shown in Fig. 19), which provides good mechanical properties and possess a good weldability.

As reported in Fig.19 the second alloy most studied is the IN625, that is also easy to be welded and possess excellent corrosion resistance. Both IN718 and IN625 are γ'' reinforced, that possess a slow kinetic formation, avoiding SAC risk.

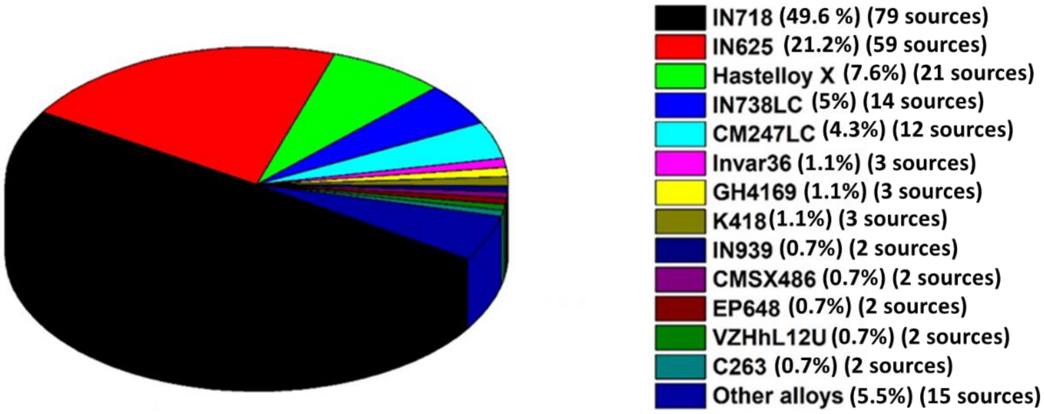

Figure 19: Publications on Ni-based superalloys percentage for various alloy

The remaining alloys are more interesting from the mechanical properties at high temperatures point of view, but are also prone to cracks formation during the LPBF process, and the studies performed on those alloy mostly focus on the cracks removal performing HIP or the mitigation of the cracking formation during the LPBF process [35,48,50–52].

The LPBF system commonly used in literature for the production of LPBF Ni-based superalloys are summarized in Fig.20.

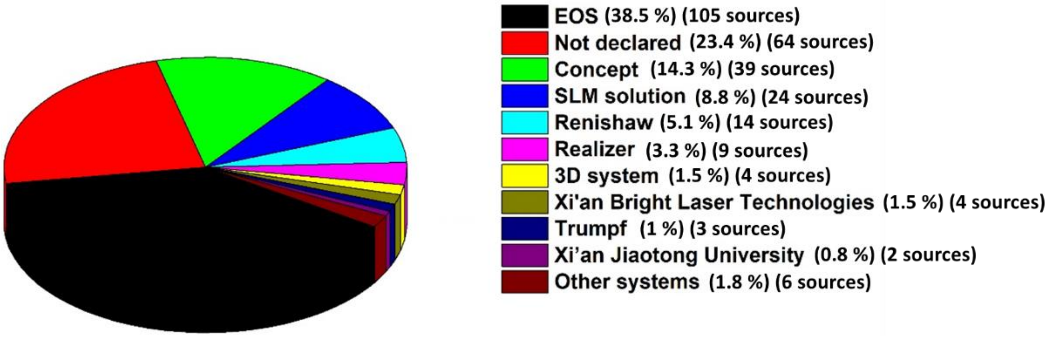

Figure 20: Publications on Ni-based superalloys percentage for various LPBF systems used

1.7 LPBF Ni-based superalloys microstructure and typical defect

As mentioned before, the LPBF process consist in multiple laser scanning. The process generates a microstructure in which the laser tracks can be identified in the XY plane (perpendicular to the building direction (BD)). These tracks, when seen on planes parallel to the BD (ZX and ZY) appears as melt pools. Dimensions, shape and position of the melt pools can vary changing the process parameters, as reported in Fig.21, and the scanning strategy [39,53].

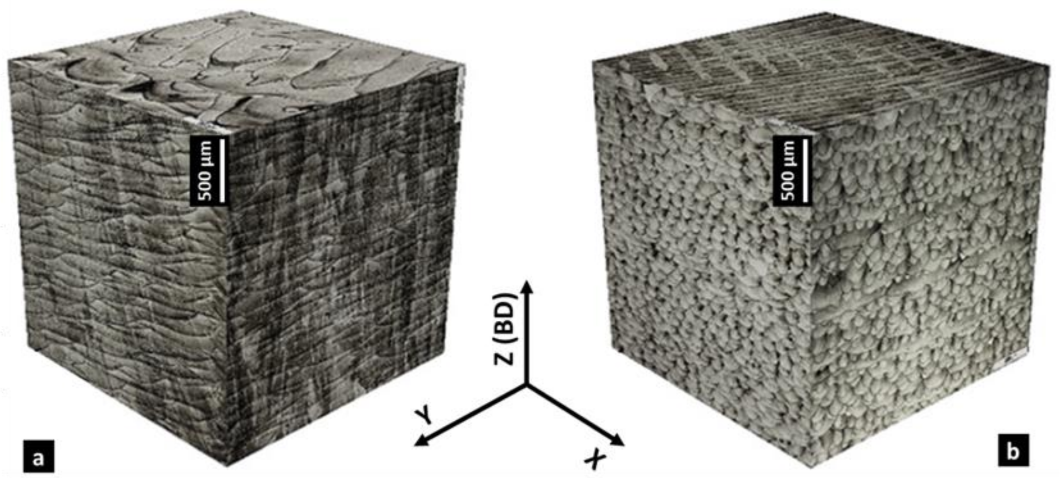

Figure 21: 3D representation of LPBF produced IN718 printed with lase power a) 950 W and b) 250 W [53]

During the solidification in the LPBF process, a strong thermal gradient is developed parallel to the BD (Z axes), and that results in the generation of columnar grains, that grow epitaxially following the heat flux. As results the obtained microstructure present a strong anisotropy, with columnar grains without particular crystallographic orientation in the planes parallel to the BD and mostly equiaxial and aligned along the <100> crystallographic direction in the case of Ni-based superalloys [38,39,54]. An example of the different grain appearance of the ZX and XY planes for the LPBF produced IN718 is reported in Fig.22 [55].

Popovich et al. found that the microstructural texturing can be modified by the process parameters and the scan strategy, and become stronger increasing of the energy density [53].

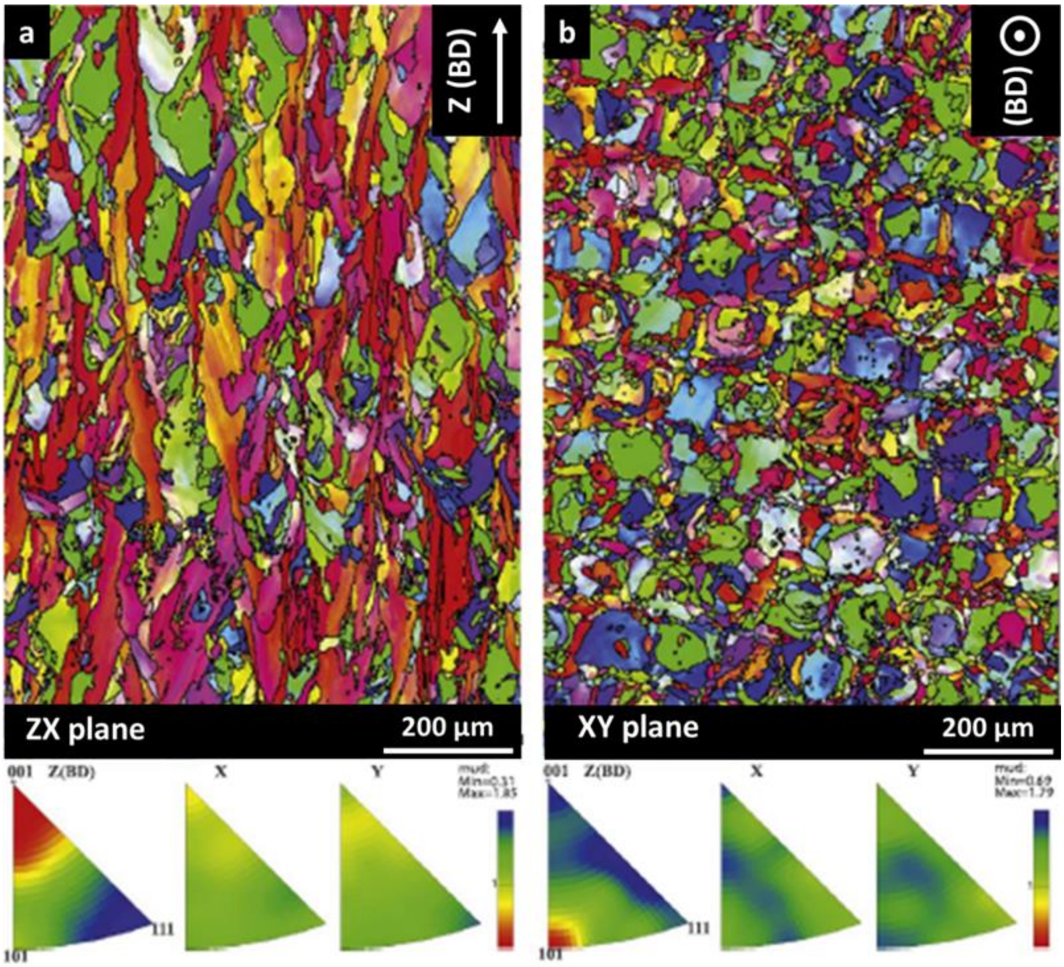

Figure 22: EBSD maps of LPBF produced IN718 on the a) ZX plane and b) XY plane [55]

The melt pools and grains structure is composed by really fine dendrites (see Fig.23), organized in zones with cellular or columnar dendrites with dimensions from sub-micrometric to around 1 µm [56–58]. The extremely small dimension of these dendrites is caused by the extremely high cooling rate experienced by the alloy during the LPBF process (10^4 to 10^6 K/s) [58–60].

The high mechanical properties of the LPBF produced Ni-based superalloys are mainly associated to these fine dendrites and the high dislocation density [58,61–63].

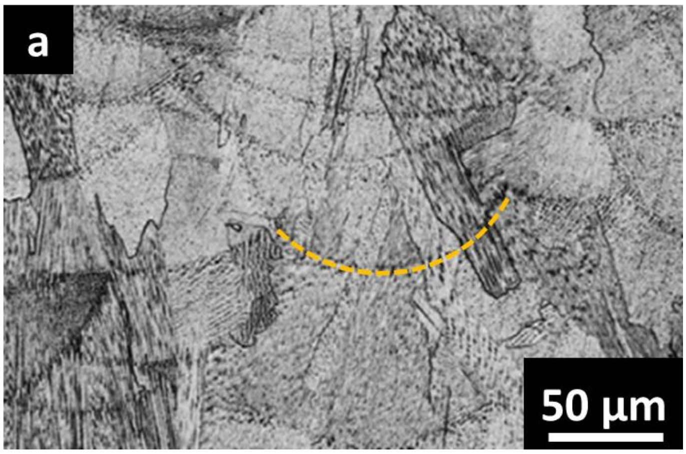

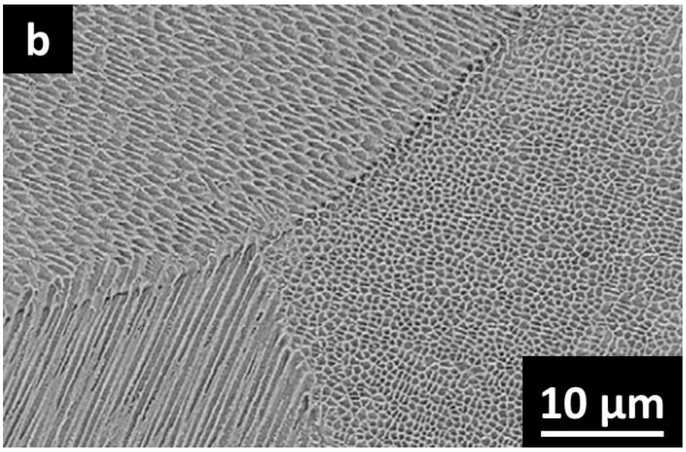

Figure 23: (a) Melt pool (highlighted with yellow line) [63] **and (b) fine dendritic structure** [64] **in LPBF produced IN625**

After the LPBF production of Ni-based superalloys different defects can be found in the alloy, such as porosity, cracks and residual stresses.

Porosity can be present with pores shape spherical or irregular.

The spherical pores are commonly caused by gas that remain trapped in the molten alloy, when the solidification gives no enough time for the gas releasing. Those gas bubbles can be already present in the powder as atomization defect or can be caused by atmosphere gas enveloped by the molten alloy due to melt pool instability [65].

The irregular porosity is often caused by instabilities in the molten pool shape, lack of fusion or balling effect [66,67].

This last effect happens when the wettability of the substrate and the melt alloy is too low for insure a good covering, and it is caused by low laser energy input [66].

However increasing the energy given to the powder is not always beneficial, since high energy input can lead to material evaporation and melt pool instability, raising the porosity content of the produced components [39,68].

The effect of different energy input in the LPBF production of the TiAl6V4 alloy is reported in Fig.24. It is easy to observe that low energy input (Fig.24a) are insufficient for the complete densification of the alloy, leaving lack of fusion defects and unmelted powder particles inside the alloy. In Fig.24b an optimal energy input is used, and is able to remove the porosity, providing a good densification. In the last figure (Fig.24c) an excessive energy density is used, and the result is an alloy full of irregular pores, caused by effects such as evaporation and melt instability [39].

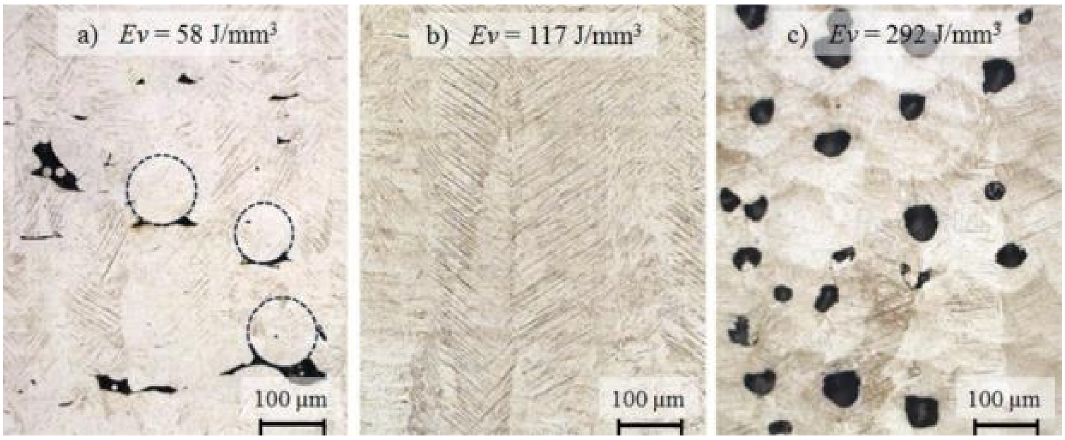

Figure 24: Volumetric energy density effect on the porosity content in LPBF produced TiAl6V4 alloy [39]

The cracks often present in Ni-based superalloys can be explained with the concepts explored in the previous section, when the weldability of Ni-based superalloy has been discussed.

Typically, the cracks found in Ni-based superalloys are located at the grain boundary locations, parallel to the building direction [52,69,70].

Rickenbacher et al. found cracks in the IN738LC produced by LPBF, and they identified the cracks origin as solidification or liquation cracking since no precipitates were present in the cracks location [71].

Studying the LPBF production of the alloy CM247LC, Carter and Wang found cracks located on high angle grain boundaries, with presence of carbides characterized with TEM analysis, indicating that the cracking mechanism may be ductility dip cracking in this case [48,72].

In the case of LPBF Hastelloy-X alloy, Harrison et al . [52] tried to change the alloy composition in order to raise the thermal shock resistance. In order to reach that goal, he increased the solid solution strengthening elements content of the alloy, raising the ultimate tensile strength of the alloy and achieving a marked reduction of the cracks content.

On the other hand, Tomus et al. studied the effect of the minor elements content in the Hastelloy-X, such as Si, C and Mn, finding that the cracks formation is related to the precipitation of intergranular carbides coupled with the cyclic thermal stress, and a reduction of Si and C can have a positive effect in the cracks mitigation [51].

Due to the rapid heating and cooling cycling experienced by the alloy during LPBF process, residual stresses are developed into the material, that can result in in defects such as delamination, distortions or cracks in the microstructure (Fig.25). The stress is accumulated layer after layer, since the material right below the melt pool is rapidly heated up by the laser irradiation and tends to expand, but is limited by the colder alloy under itself. This restriction of the thermal expansion develops residual compressive stresses, that can result in plastic deformation or cracking if the stress intensity results higher than the yield strength of the alloy.

Moreover, during the cooling step, the melt track solidifies and contracts because is lowering its temperature, but also in this case the underlying alloy limits the contraction, leading to tensile stresses in the upper layer and compression stresses in the lower alloy [43,62].

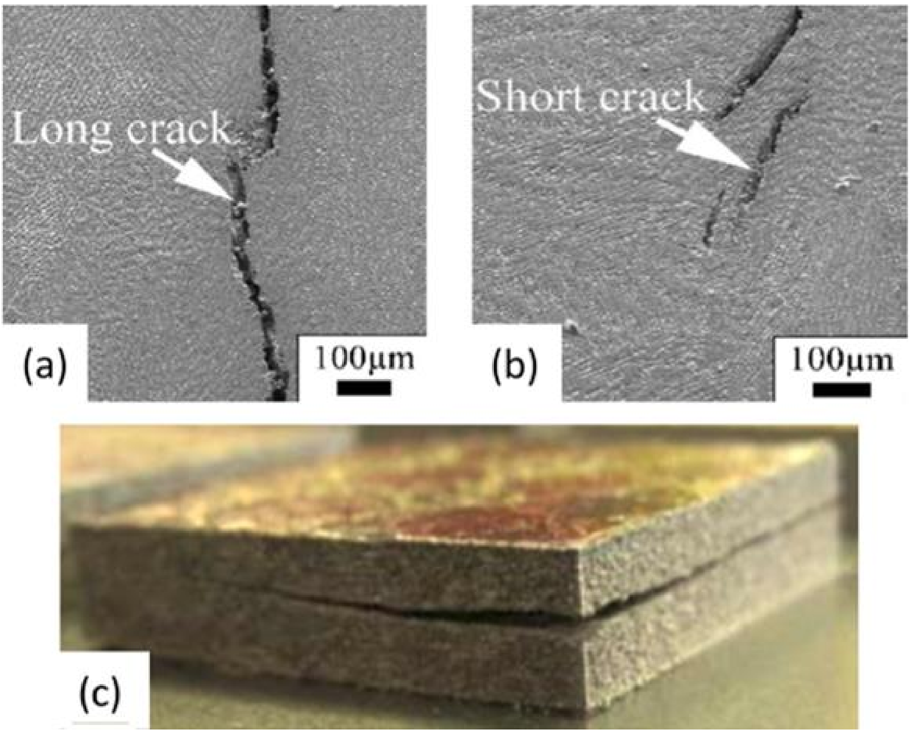

Figure 25: a) long crack, b) short cracks and delamination in a LPBF produced alloy [62]

Chapter 2

Materials and methods

This chapter presents the materials and methods applied in the fabrication, sample preparation and characterization of Ni-based superalloys studied in this thesis.

2.1 LPBF machines used

IN625 samples used for the study of the heat treatments and for the oxidation properties evaluation were produced with an EOSINT M270 Dual Mode machine. The study of the process parameters optimization of IN939 alloy was performed by means of a CONCEPT Mlab cusing R system. In Fig.26 both machines are shown while the technical data are reported in Table.15.

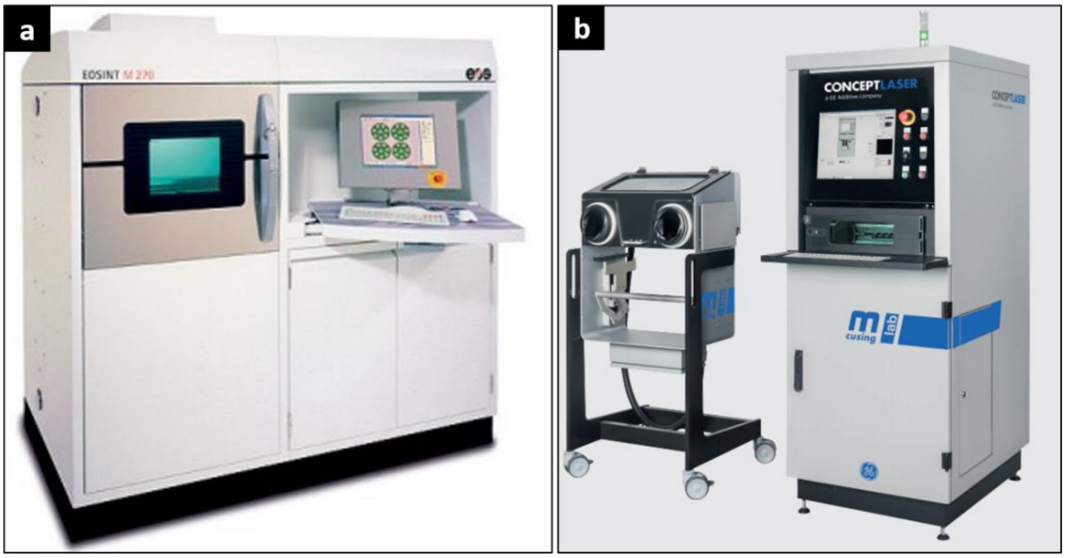

Figure 26: Images of (a) EOSINT M270 Dual mode [73] **and (b) CONCEPT Mlab cusing R machines** [74]

Table 15: Declared technical characteristics of EOSINT M270 Dual mode [73] and CONCEPT Mlab cusing R [74] machines

Machine	EOSINT M270 Dual mode	CONCEPT Mlab cusing R
Effective building volume (building platform included)	250x250x215 mm^3	90x90x80 mm^3
Laser type	Fibre laser 200 W	Fibre laser 100 W
Max laser scanning speed	7 m/s	7 m/s
Layer thickness (Material dependent)	20-100 µm	15-30 µm
Focus diameter	100-500 µm (variable)	approx. 50 µm
Power supply	32 A	1/N/PE AC 230 V, 16 A
Power consuption	max. 1.5 kW	max. 1.5 kW
Building platform temperature	40-80°C*	Room temperature

** EOSINT M270 Dual mode building platform can be heated up to the temperature of 200°C*

For the fabrication of IN625 and IN939 samples, the scanning strategy used is a stripe scanning strategy, with stripes width of 5 mm (typically used by EOS in their machines). This strategy utilizes a stripe pattern in order to melt a layer of powder. The stipes are melted by the laser beam and the distance between the center of two subsequent laser scan is known as hatching distance (**h_d**). Typically, it is used a hatching distance that allows an overlapping between two laser scans in order to avoid the formation of not melted areas (Fig.27 [75]). Then the next layer is melted rotating the stripes of 67° compared to the previous layer. An explicative illustration of the scanning strategy used for this thesis is reported in Fig.28.

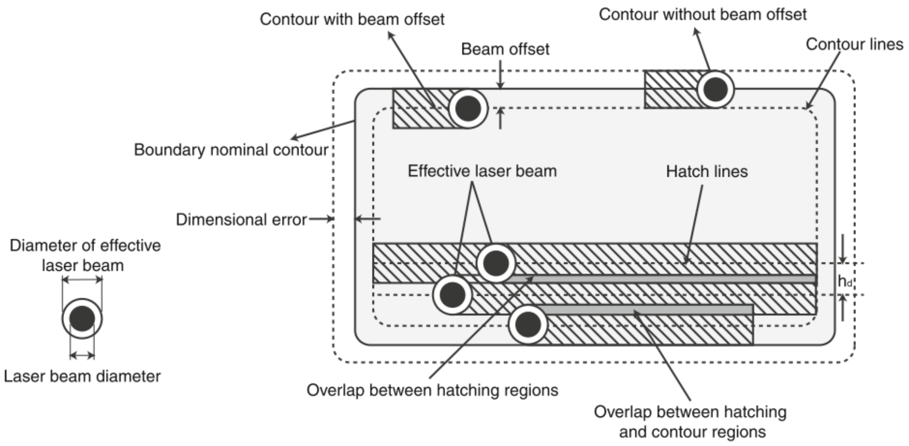

Figure 27: Representation of the laser tracks overlapping

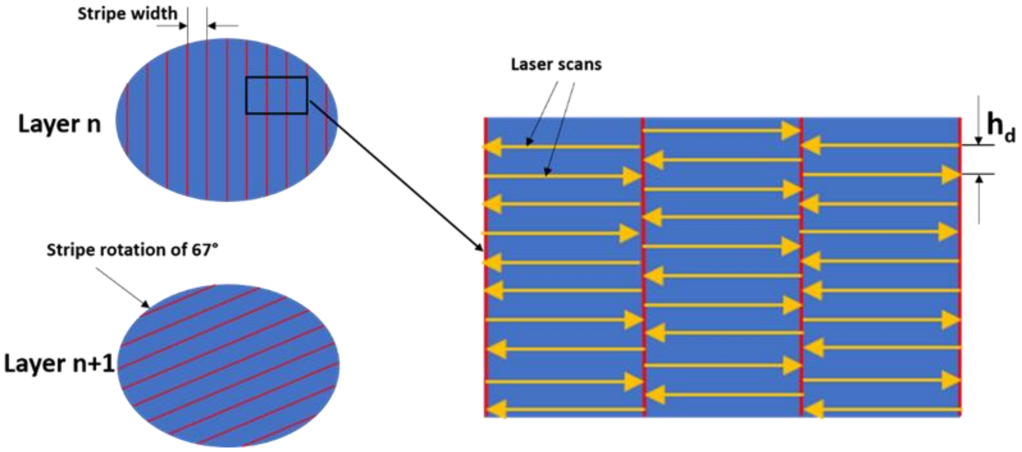

Figure 28: Representation of the scanning strategy applied in the samples building process for IN625 and IN939

In the case of IN625 samples, the parameters were already optimized for the EOSINT M270 in a previous work of the research group [64]. The parameter set applied for IN625 specimens' production are laser power (**P**) 195 W, hatching distance (**h_d**) 0.09 mm, scanning speed (**v**) 1200 mm/s and layer thickness (**t**) 0.02 mm.

For the IN939 different sets of parameters were used in order to find an optimum parameter set. For each sample, **P** and **t** were settled constant at 95 W and 0.02 mm respectively, using different values of **h_d** and **v**.

A first job was produced (j1 samples) with parameters that allow to explore a large volumetric energy density (VED, J/mm^3) range typically reported for Ni-based superalloys [24,50,76,77]. This first trial of process parameters optimization helps to identify a range of VED values suitable for the production of IN939 with low defects level. Then, it is possible to select the identified VED value regions performing a further more precise optimization. In fact, the VED approach is typically used to determine the process parameters window, avoiding lack of fusion and melt pool instability that caused the production of an high defected alloy, but since the VED alone is insufficient for determine the final defect content the single effect of others parameters, such as **h_d** and **v**, must be considered [49,78]. From the results of the first trial, it was selected a range of VED values which generated high densification level for the production of IN939 alloy. Therefore, different values of **h_d** and **v** were employed in order to generate specific VED values. Some parameter set was replicated in different jobs. The parameter set of each sample is reported in Table.16.

The VED values are calculated using the following equation [79,80]:

$$VED = \frac{P}{v * t * h_d} \quad (1)$$

Table 16: Parameter sets used in the optimization jobs of IN939 (j1, j2 and j3 indicate the job number)

Sample ID	P [W]	v [mm/s]	h_d [mm]	t [mm]	VED [J/mm^3]
1 j1	95	100	0.15	0.02	317
2 j1	95	200	0.09	0.02	264
3 j1	95	200	0.11	0.02	216
4 j1	95	200	0.13	0.02	183
5 j1	95	200	0.15	0.02	158
6 j1	95	400	0.05	0.02	238
7 j1	95	400	0.07	0.02	170
8 j1	95	400	0.09	0.02	132
9 j1	95	400	0.11	0.02	108
10 j1	95	400	0.13	0.02	91
11 j1	95	400	0.15	0.02	79
12 j1	95	600	0.05	0.02	158
13 j1	95	600	0.07	0.02	113
14 j1	95	600	0.09	0.02	88
15 j1	95	600	0.11	0.02	72
16 j1	95	800	0.05	0.02	119
17 j1	95	800	0.07	0.02	85
18 j1	95	800	0.09	0.02	66
12 j2	95	600	0.05	0.02	158
13 j2	95	600	0.07	0.02	113
14 j2	95	600	0.09	0.02	88
16 j2	95	800	0.05	0.02	119
17 j2	95	800	0.07	0.02	85
18 j2	95	800	0.09	0.02	66
19 j2	95	1000	0.03	0.02	158
20 j2	95	1000	0.05	0.02	95
21 j2	95	1000	0.07	0.02	68
22 j2	95	1000	0.09	0.02	53
23 j2	95	1200	0.03	0.02	132
24 j2	95	1200	0.05	0.02	79
25 j2	95	1200	0.07	0.02	57
26 j2	95	1200	0.09	0.02	44
27 j2	95	1400	0.02	0.02	170
28 j2	95	1400	0.03	0.02	113
29 j2	95	1400	0.05	0.02	68
30 j2	95	1400	0.07	0.02	48
31 j3	95	1400	0.09	0.02	38
32 j3	95	1600	0.02	0.02	148
33 j3	95	1600	0.03	0.02	99
34 j3	95	1600	0.05	0.02	59
35 j3	95	1600	0.07	0.02	42
36 j3	95	1600	0.09	0.02	33
37 j3	95	1800	0.02	0.02	132

38 j3	95	1800	0.03	0.02	88
39 j3	95	1800	0.05	0.02	53
40 j3	95	1800	0.07	0.02	38
41 j3	95	2000	0.02	0.02	119
42 j3	95	2000	0.03	0.02	79
43 j3	95	2000	0.05	0.02	48
44 j3	95	2000	0.07	0.02	34
45 j3	95	2200	0.02	0.02	108
46 j3	95	2200	0.03	0.02	72
47 j3	95	2200	0.05	0.02	43
48 j3	95	2200	0.07	0.02	31

2.2 Ni-based superalloy powder used

2.2.1 IN625 powders

For the IN625 samples production, a gas atomized IN625 powder, bought from EOS GmbH, was used. The powder possesses a particle size distribution characterized by D10 16 μm, D50 27 μm and D90 48 μm, and the nominal composition reported in the datasheet is shown in Table.17 [81]. The chemical composition satisfies the UNS N06625.

Table 17: IN625 nominal composition (EOS datasheet) [81]

Element	**min (wt%)**	**Max (wt%)**
Ni	58.00	Bal.
Cr	20.00	23.00
Mo	8.00	10.00
Nb	3.15	4.15
Fe	-	5.00
Ti	-	0.40
Al	-	0.40
Co	-	1.00
Si	-	0.50
Mn	-	0.50
C	-	0.10
Ta	-	0.05
P	-	0.015
S	-	0.015

2.2.2 IN939 powders

For the IN939 samples production, a gas atomized IN939 powder, bought from LPW (Carpenter), was used. The declared composition is reported in Table.18 [82].

Table 18: IN939 nominal composition (LPW datasheet) [82]

Element	min (wt%)	Max (wt%)
Ni	Bal.	Bal.
Cr	22.00	23.00
Co	18.50	19.50
Ta	1.90	3.20
Nb	-	1.00
Ti	1.30	4.20
Al	1.80	2.00
W	-	2.10
Si	0.20	0.90
C	0.10	0.20
B	-	0.01
Zr	-	0.10
S	-	0.005

2.3 Powder characterization

The IN625 powder was already characterized by the research group before the start of this work, so that characterization is not reported in this thesis.

The morphology of the powder of IN939 was studied using a scanning electron microscope (SEM) Phenom XL. For the morphology study the powder was placed on a SEM stab covered by a conductive adhesive.

In order to study the cross section of the powder, it was mounted in conductive resin, polished down to 1 µm with diamond suspension. The cross sections have been observed at an optical microscope (OM, Leica DMI 5000 M) at 200x magnification, and using 3455 particles the average porosity and the relative standard deviation were evaluated.

In order to reveal the powder microstructure, the polished cross sections have been chemically etched using the Kalling reagent n°2 (a solution composed of 5 g of $CuCl_2$, 100 ml of HCl and 100 ml of ethanol), and the images have been taken at the SEM Phenom XL.

A semi-quantitative determination of the chemical composition of the powder has been evaluated with energy dispersive X-ray spectroscopy (EDS) at the SEM Phenom XL, to validate the chemical composition of the datasheets.

The particle size distribution has been obtained using laser granulometry (Fritsch model Analysette 22 Compact) with powder ultrasonic treated and powder not treated.

The apparent density and flow rate of the powder have been analyzed using the Hall flowmeter test, following the ASTM B212 for the apparent density and the ASTM B213 for the flow rate.

2.4 Massive Metallographic samples preparation

2.4.1 IN625 metallographic samples

IN625 metallographic samples have been obtained cutting cubes (15x15x15 mm^3) fabricated with the EOS machine, in the As-Built condition and after heat treatments, using a precision cutting machine (Mecatome T210) equipped with a SiC cutting wheel. The cuttings have been performed parallel to the building direction (Z) in order to see the ZX plane and perpendicular to the building direction in order to see the XY plane.

The samples have been carefully polished using various SiC grinding papers, down to grid 2400, and then they have been polished down to 1 μm with diamond suspension. In the case of the samples used for the electron beam scattering diffraction (EBSD) analysis have been performed another step of polishing with OP-S suspension (colloidal silica, 0.04 μm). After polishing samples used for microstructure and phases identification have been etched using Kalling reagent n°2, which is often used for etching Ni-based superalloys [83–85]. Etching time was comprised between 30 sec and 3 minutes, based on the heat-treated condition.

2.4.1 IN939 metallographic samples

IN939 metallographic samples used in the parameter set optimization have been obtained cutting cylinders (height 12 mm and diameter 10 mm) fabricated with the CONCEPT machine, in the As-built condition, using a precision cutting machine (Mecatome T210) equipped with a SiC cutting wheel. The cuttings were performed parallel to the building direction (Z) in order to see the ZX plane.

A cube of as-cast IN939 has been cut in half with the same cutting machine.

The samples have been carefully polished using various grinding papers in SiC, down to grid 2400, and then they have been polished down to 1 μm with diamond suspension.

IN939 samples produced for the process optimization were observed before etching at 50x magnification and 11 photos were taken for each parameter set in order to evaluate porosity.

Some samples have been etched using Kalling reagent n°2. In this case, the etching time was comprised between 30 sec and 1 minute, based on the material condition.

2.5 Microstructural characterization and phases identification

2.5.1 Optical microscope (OM)

The IN939 gas atomized particles have been moulted and than the porosity content has been determined by means of the optical microscope (OM) Leica DMI 5000 M, with the procedure seen in the section 2.3.

The OM has been used also in the microstructural evaluation, after etching, for IN625 samples.

Moreover, the OM has been used on LPBF IN939 samples before etching in order to evaluate the defect content associated to the production parameters used. The details of the defect analysis are reported in section 2.X. Etched samples have been observed, evaluating the microstructure.

2.5.2 Scanning electron microscope (SEM)

Gas atomized powder shape, morphology, particles size and cross-sections as well as microstructure, secondary phases morphology and composition have been analyzed using different scanning electron microscopes (SEM) and field emission scanning electron microscopes (FESEM) equipped with energy dispersive X ray spectroscopy (EDS).

For IN625:

The texture and the orientation of the grains of IN625 after different annealing treatments (see 2.6.1) have been studied using electron beam scattering diffraction unit (Nordlys II detector - Oxford Instruments) during the works performed in Chalmers University (period of visiting PhD student).

Study of the Oxide cross sections have been studied with SEM and EDS, during the works performed in Chalmers University (period of visiting PhD student).

Scratch lines on the oxidized samples have been observed using SEM.

For IN939:

Cracking density of the IN939 samples has been evaluated through SEM (see 2.8.1)

The SEM have been used also in the study of the microstructure investigating the dendritic structures and the possible cracking mechanisms.

The following list contains all the SEMs used in this thesis:

- FEG-SEM, LEO 1550, equipped with EDS and EBSD;
- FEG-SEM, Zeiss SupraTM40, equipped with EDS;

SEM - Phenom XL, Phenom-World BV, Eindhoven, The Netherlands, equipped with EDS.

2.5.3 X-Ray Diffraction analysis (XRD)

X-ray diffraction (XRD) analysis has been performed using a XRD, PANalytical, Almeno, The Netherland system. The instrument uses a Bragg-Brentano configuration and a CuKα radiation.

Annealed IN625 samples and IN939 samples diffractograms have been taken one time for each sample, with **θ** range from 30° to 100°, step size of 0.013° and a counting time of 25 s per step.

For the oxidized samples of IN625 the conditions of the XRD analysis have been **θ** range from 15° to 100°, a step size of 0.013° and a counting time of 35 s per step. Each measure has been repeated 3 times.

The resulting XRD patterns have been analyzed in order to identify the phases present in the sample, using the X'pert Highscore software.

XRD patterns have been analyzed in order to obtain the interplanar distance (**d**) of the alloy crystal lattice using the Bragg's law, knowing the X-ray radiation wavelength (**λ**) and the peak position (**2θ**) [86]:

$$\boldsymbol{n\lambda = d_{h,k,l}\sin\theta} \tag{2}$$

$$\boldsymbol{d_{h,k,l} = \frac{n\lambda}{\sin\theta}} \tag{3}$$

With **n** integer.

It is possible to calculate the lattice parameters **a**, **b** and **c** using the $\boldsymbol{d_{h,k,l}}$ obtained and the Miller's indices using the following equation [86]:

$$\boldsymbol{\frac{1}{d_{h,k,l}} = \frac{h^2}{a^2} + \frac{k^2}{b^2} + \frac{l^2}{c^2}} \tag{4}$$

In the case of cubic lattice the three lattice parameters **a**, **b** and **c** are equal and the equation can be simplified as [86]:

$$\boldsymbol{a = d_{h,k,l}\sqrt{h^2 + k^2 + l^2}} \tag{5}$$

In the case of oxidized samples, in which more patterns are available, the Nelson-Riley method [87] has been used, in order to reach a more precise evaluation of the lattice constant. The method requires the calculation, for each peak of a phase, of the constant lattice, which have to be plotted versus a Nelson-Riley coefficient calculated, for that peak, with the following expression:

$$\boldsymbol{Nelson - Riley\ coeff. = \frac{1}{2}\left(\frac{\cos\theta^2}{\sin\theta} + \frac{\cos\theta^2}{\theta}\right)} \tag{6}$$

Using a linear fitting on the obtained graph, it is possible to obtain a good value of the lattice constant taking the intercept value of the lattice constant where the Nelson-Riley coefficient value is equal to 0. An example graph is reported in Fig.29.

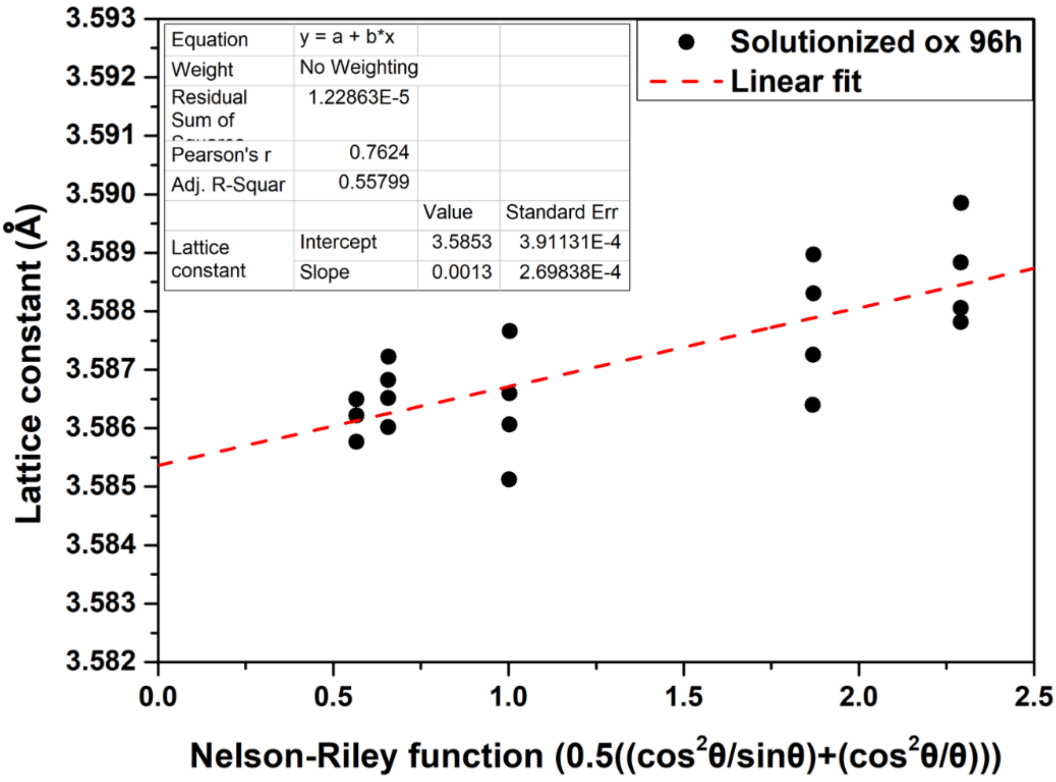

Figure 29: Example of the Nelson-Riley method used to determine the Lattice constant value of the alloy

2.6 Specific characterization performed on Annealing treatments of LPBF IN625

2.6.1 Heat treatments

In order to study the effects of commonly suggested annealing treatments for the traditionally wrought IN625 alloy, different heat treatments were performed on as-built LPBF IN625 alloy.

1) 870 °C for 1 hour: this heat treatment is usually applied for the stress relieving of the IN625 [11].

2) 980 °C for 1 hour: this heat treatment is usually suggested for the annealing treatment of the IN625 [11].

3) 1080 °C for 1 hour: according to the ASTM B443, the annealing temperature range of the IN625 is between 871 °C and 1092 °C. Since 870 °C and 980 °C are placed at the beginning and at the half of this range, a temperature near to the maximum value was selected.

4) 1150 °C for 2 hours: this is the common solution annealing treatment suggested for the IN625 [11].

5) 1030 °C 1 hour: after the analysis of the results of the previews conditions, an intermediate temperature between the 2 and 3 have been chosen in order to determine the temperature that trigger recrystallization after 1 hour.

In order to prevent microstructural evolution during the cooling, all the heat treated samples have been Water Quenched (WQ) at the end of the treatment [11].

All the performed heat treatments have been conducted in a muffle furnace in air.

2.6.2 Electron BackScatter Diffraction (EBSD) analysis

The Electron BackScatterd Diffraction analysis uses the diffraction pattern generated by electrons that interact with a crystal lattice. The diffraction pattern generated can assume different aspects, based on the lattice crystallographic orientation and the crystal composition. The diffraction pattern can be evaluated on really small areas of the sample (down to nanometric resolutions) using a fluorescent phosphor sensor placed near to the sample. Thanks to a database, the resulting pattern is identified, revealing for each point the lattice orientation and the eventual presence of other phases [88].

In order to perform the EBSD analysis, samples inside the SEM have been tilted by 70° and scanned with electron beam at 20 kV with, using a step size of 1–2 μm. For each sample have been analyzed an area of 500x750 μm^2.

The grain boundaries frequency has been evaluated, considering low angle grain boundaries for misorientation between adjacent grains $1° \leq \theta \leq 10°$, high angle grain boundaries for $\theta > 10°$ and twinning grain boundaries for $\theta = 60°$. This value is the typical misorientation θ for twinning grain boundary along (111) orientation [89].

2.6.3 Tensile tests

The IN625 tensile samples have been produced as oversized cylinders and then machined in order to reach the dimension of gauge length of 40 mm, reduced section of 51 mm and diameter of 8 mm following the ASTM E8M-09. For each selected condition have been tested three samples horizontally (XY samples) and three samples vertically (Z samples). The tensile specimens were tested by means of a Zwick-Roell BT1 - FR100 machine using a strain rate settled at 8.10^{-3} s^{-1}. Fig.30 schematically shows the orientation of the IN625 tensile samples along vertical and horizontal orientations.

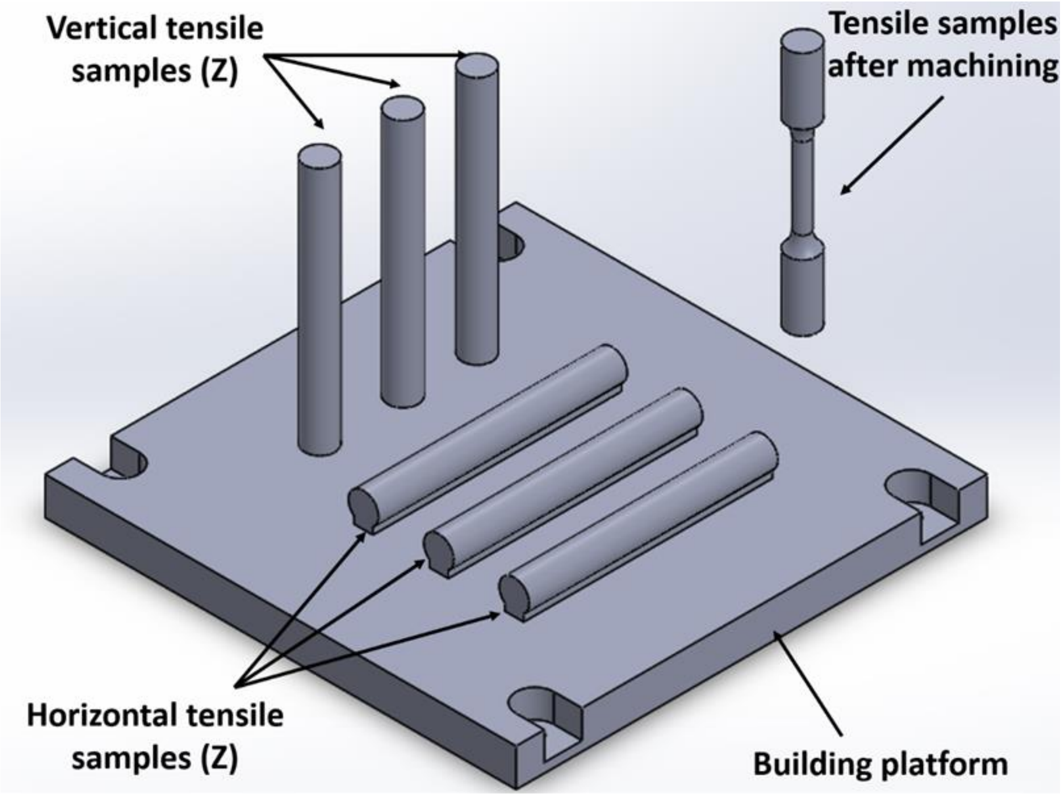

Figure 30: Schematic illustration of the building orientations of the IN625 tensile samples

2.6.4 Thermo-mechanical analysis (TMA)

The coefficient of thermal expansion (CTE) of IN625 as-built and solutionized in the temperature range of 100 – 1200°C has been evaluated using a TMA-SETSYS Evolution Setaram Instrument system.

Samples used in this analysis were parallelepipeds with height 10 mm and a square base 6x6 mm^2. The heating rate was settled at 2°C/min. The analysis has been conducted in Ar atmosphere.

2.7 Specific characterization performed on the study of oxidation property of IN625

2.7.1 Thermal gravimetric analysis (TGA)

This analysis has been conducted increasing linearly the temperature over the time, in order to check if there are different oxidation regimes in different temperature ranges.

For this purpose, the mass gain of IN625 in the as-built and solutionized states in the temperature range from 25 up to 1200°C has been evaluated using a Mettler Toledo 1600 TGA system. The heating rate has been settled at 10°C/min. The analysis has been conducted with an air flux of 50 ml/s.

The results have shown that that from ≈950 °C the oxidation behaviour of both as-built and solutionized IN625 changes.

2.7.2 IN625 oxidation samples preparation

For the oxidation study on IN625 have been prepared samples with dimensions of 8x30x20 mm^3. These samples have been removed from the building platform through EDM (electro discharge machining).

A sample set has been subjected to solution treatment (1150 °C 2h + water quench) (see 2.6.1) and the remaining samples have been left in the as built state.

All samples have been polished using SiC grinding paper down to grid 1200 on all the faces, removing all the surface roughness and the oxides formed during the solution treatment and carefully preserving the geometry.

After the oxidation treatments (see 2.7.3), the samples have been cut using a precision cutting machine equipped with Al_2O_3 cutting wheel, in order to obtain samples for different analysis, as shown in Fig.31.

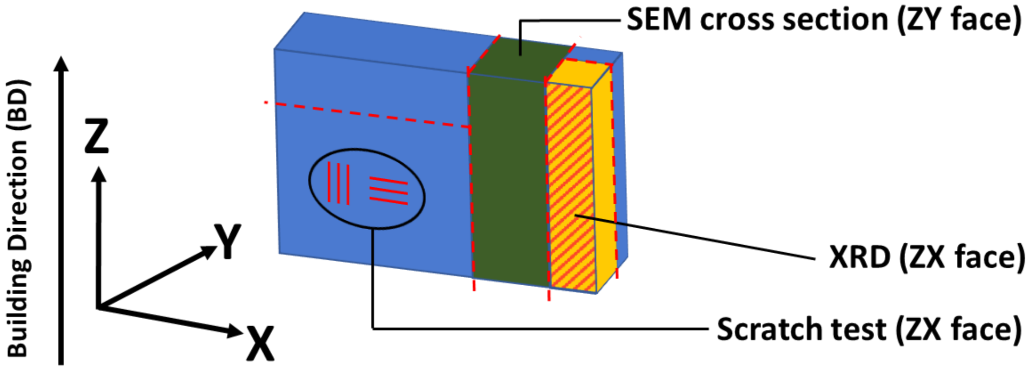

Figure 31: IN625 oxidation samples preparation

The samples obtained in this way have been used for XRD analysis (see 2.5.3), scratch test analysis (see 2.7.4) and for the cross-section analysis. Cross-section samples have been mounted in conductive resin and polished with grinding papers in SiC down to grid 2400, then they have been polished down to 1 µm with diamond suspension and with OP-S suspension down to 0.04 µm.

2.7.3 IN625 Oxidation treatment

In order to study the oxidation property of IN625, the samples have been oxidized in static air at the temperature of 900°C. All the samples have been put in an alumina crucible (Fig.32). After 8, 24, 48, 72 and 96 hours a sample has been quickly removed from the furnace, leaving the others inside. After that the removed sample have been air cooled and weighted on a precision scale (0.0001 g of sensibility) in order to evaluate the mass change after oxidation. The oxidation treatment at 900 °C was performed on the As Built and solutionized samples.

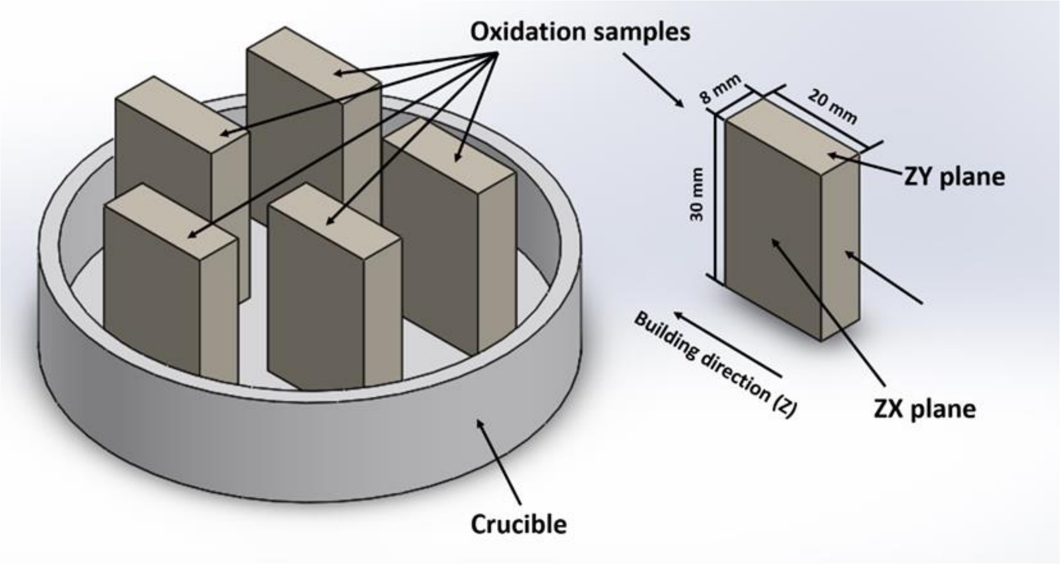

Figure 32: Oxidation samples preparation

2.7.4 Scratch test analysis

The oxide layer mechanical resistance has been evaluated through scratch tests carried out with a nano-indenter system (Hysitron TI 950 Triboindenter, Hysitron-Bruker, Minneapolis, MN, USA). The test has been conducted on IN625 in the as-built and solutionized states after 8h and 96h of oxidation treatment. The samples have been tested on the ZX plane with three scratch parallel to the building direction (BD) and three perpendicular to the BD, in order to highlight possible variations between direction. Each scratch test consists in an indenter the perform a scratch long 1 mm, where the indentation force is increased linearly from 0 mN to 250 mN.

During the indenter movement the lateral force needed to proceed in the scratch is recorded.

2.8 Specific characterization performed on LPBF IN939

2.8.1 Image analysis

The as-fabricated samples used for the parameter optimization have been prepared as described in section 2.4.2.

The total void content (that consider pores plus cracks) have been evaluated taking 10 pics at the OM at magnification 50x for each parameter set, for a total analyzed area of 27.3 mm^2, and analyzing them with ImageJ software. An example is reported in Fig.33.

In order to separate the pores and the cracks, the cracks have been manually removed by the OM images, giving the possibility to only consider the pores contribution (Fig.33c).

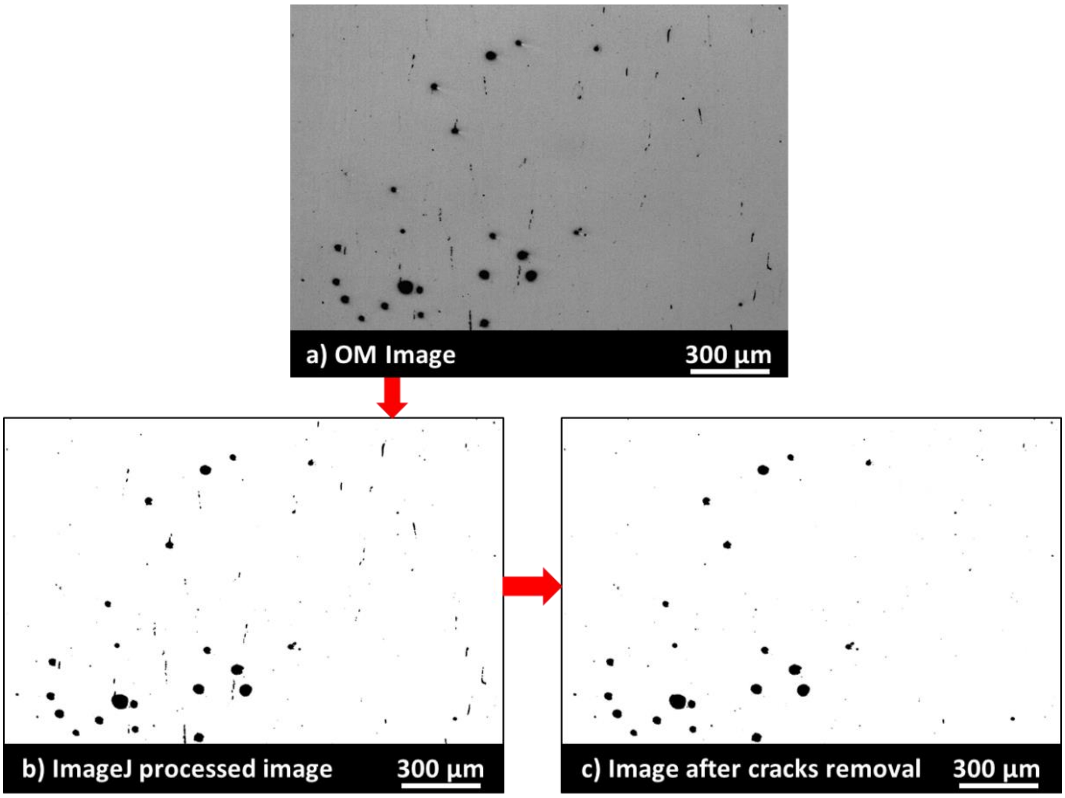

Figure 33: a) Original OM image, b) ImageJ processed image for the void content evaluation, c) hardly detectable cracks and d) image with removed cracks for the porosity evaluation

Since the cracks are very tight and sometimes difficult to be detected by OM analysis, the cracking density was determined by SEM analysis. This approach is typically reported for the characterization of LPBF Ni-based superalloys [69,70,90]. For the analysis, 10 SEM images were taken at 500x magnification, for each sample, and subsequently post processed using ImageJ analysis. The total area evaluated for each sample is 2.86 mm^2.

The cracks length have been approximated by the Feret diameter [90].

In this case the pores have been manually eliminated from the images. An example is reported in Fig.34.

As other authors in literature [69,70,90], the cracking density has been evaluated as mm/mm^2, dividing the total cracks length for each image for the analysed area.

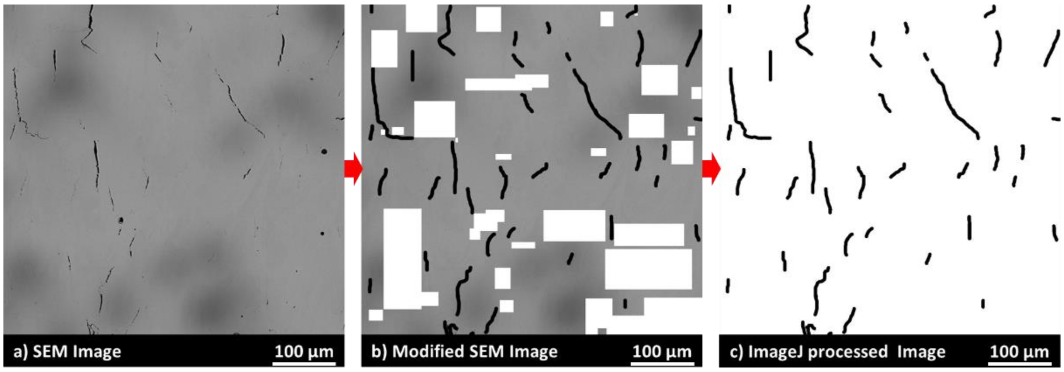

Figure 34: Example of crack density evaluation with a) starting SEM image, b) image with porosity removed and cracks highlighted and image analysed with ImageJ software

2.8.2 Hardness evaluation

The Brinell hardness has been evaluated on the LPBFed IN939 samples and on the as-cast IN939 using an Emco test M4U025.

The hardness test has been conducted using a spherical steel indenter with 2.5 mm of diameter and applying 62.5 kg of load.

For each sample 5 indentation have been performed.

Chapter 3

Results and discussion on IN625

This chapter contains the results of the analysis performed on the Ni-based alloy IN625 processed with LPBF technology by means of an EOSINT M270 Dual Mode system. The process parameters optimization, as well as part of the study of the heat treatments, were already published in previous works of the group [57,63,64,91].

Part of this work was performed during the visiting PhD student period at Chalmers University of Technology.

This section is focused on the study of the effects of the annealing heat treatments on the LPBF IN625 and the main results were already published [92]. This study includes:

1) The microstructure evaluation of as-built, three annealing heat treatment states and the standard solution heat treatment states of IN625.
2) The impact of the heat treatments on the texture evolution.

The mechanical properties (tensile properties and hardness) of the as-built and heat-treated conditions correlate to their microstructure and texture.

3.1 Annealing treatments

In order to evaluate the effects of the annealing treatments on the LPBF as-built IN625, the following heat treatments were performed:

1) 870 °C for 1 hour: this is the commonly suggested stress relieving treatment for the IN625 [11].

2) 980 °C for 1 hour: this is the commonly suggested annealing treatment for the IN625 [11].

3) 1080 °C for 1 hour: this temperature was chosen according to the ASTM B443, in which the annealing temperature range from 871 °C to 1092 °C.

4) 1150 °C for 2 hours: the commonly suggested solution annealing treatment for the IN625 [11].

5) 1030 °C 1 hour: based on the results of the above conditions this condition was added to study the texture evolution using an intermediate condition between the 2 and 3.

Water quenching (WQ) was performed on all the samples in order to study only the effects of the heat treatments, preventing further microstructural modifications during the cooling [11].

3.1.1 Microstructural evolution and mechanical properties

3.1.1.1 IN625 As-Built condition

As-Built Microstructure: Optical Microscope (OM)

The microstructure of the as-built state is shown in Fig.35. In the plane perpendicular to the building direction (XY plane) (Fig.35a) the laser scans tracks can be noticed, with a width up to 150 µm, as well as the grains that appear equiaxial with a diameter in a range from 5 to 100 µm. For LPBF IN625, a similar microstructure was observed by Kreitcberg et al. in their work [93].

Moving to the plane parallel to the building direction (ZX plane) (Fig.35b), it can be seen that the grains appear elongated along the Z-axis, which is a common feature for LPBF Ni superalloys [57,63,64,94].

Their length is between 5 and 400 µm, and they grow epitaxially through several layers.

On this plane, the laser tracks appear as melt pools, which possess a with up to 150 µm and a depth up to 50 µm. The variations from a layer to the previous one derived from the scanning strategy which applies a rotation of 67° between consecutive layer [57,63,93,95]. In Fig.35c a 3D reconstruction of the microstructure is reported.

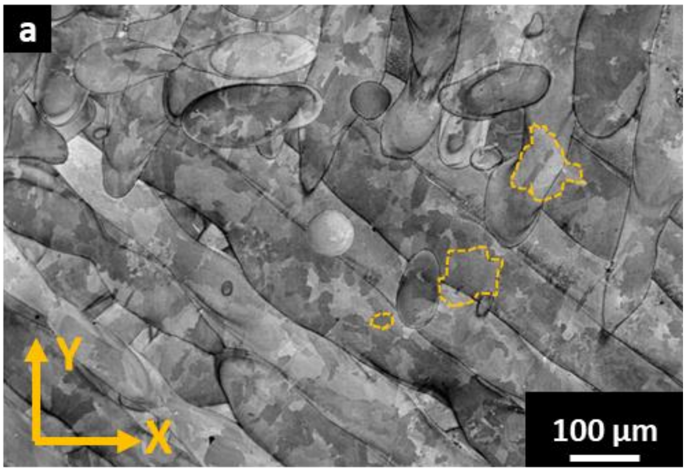

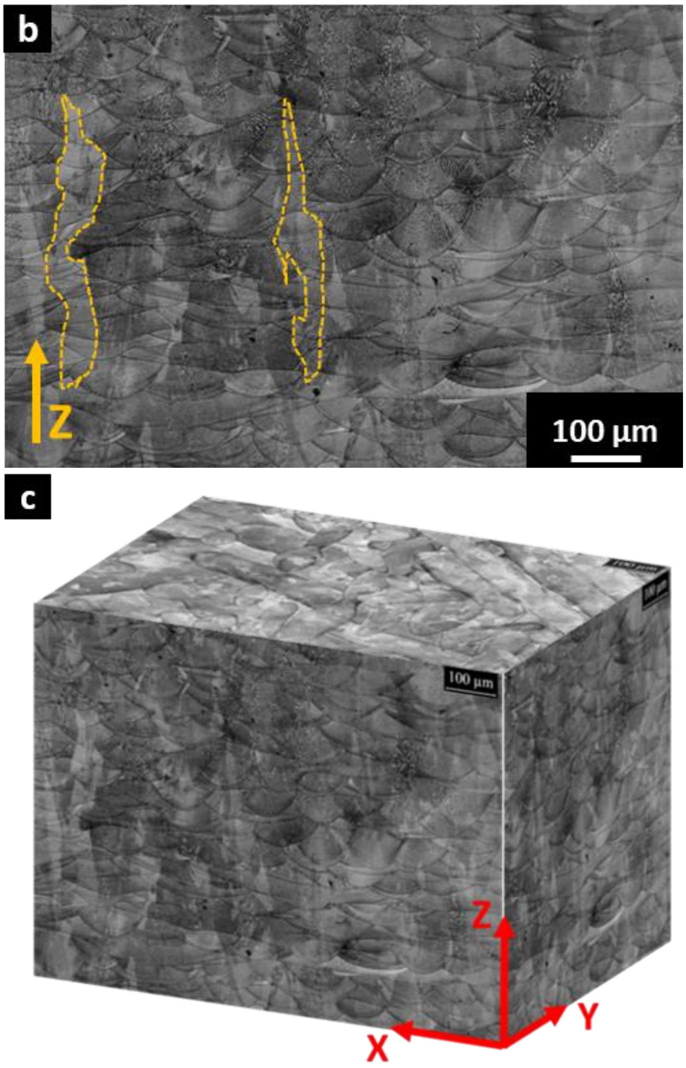

Figure 35: Etched (a) XY plane (b) ZX plane and (c) 3D reconstruction

As-Built Microstructure: Scanning Electronic Microscopy (SEM)

Fig.36 shows the SEM image of the ZX plane of the LPBF IN625 state. From the micrograph, it is possible to observe that the melt pools are composed of extremely fine dendritic structures.

These dendritic structures are organized in zones characterized by columnar shaped dendrites (yellow rectangle in Fig.36) and zones with cellular shaped dendrites (red rectangle in Fig.36). The switch between these two appearances can be correlated to the thermal flux direction during the solidification rate [55,96,97] as well as the re-melting of some portion of the alloy during the consolidation of an upper layer.

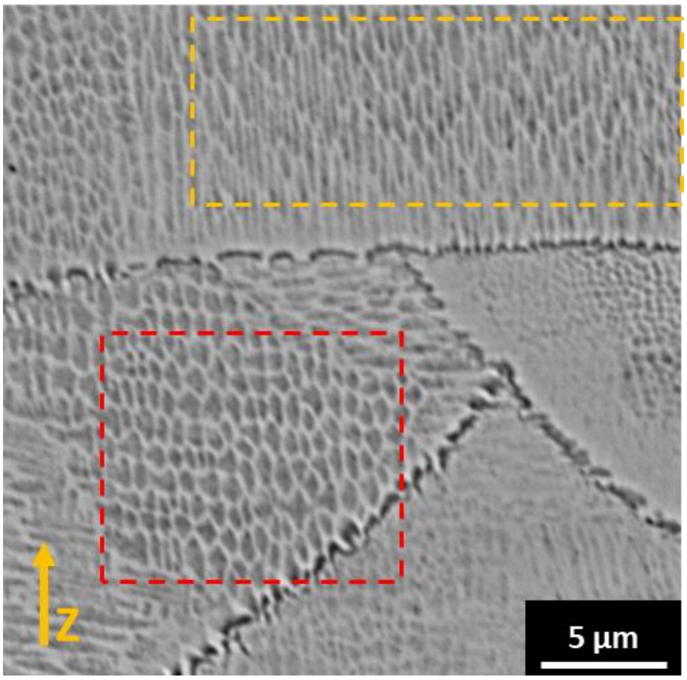

Figure 36: SEM micrographs on ZX plane

In the IN625, the dendrites present very fine structures, with width dimensions from 0.3 to 1 µm. Typically for estimating the cooling rate the secondary dendrites arm spacing (SDAS) is used. However, the Ni-based superalloys produced by LPBF, due to high cooling rate, do not show completely formed secondary dendrites, and therefore, the primary dendritic arm spacing (PDAS) is generally considered for the calculation [58]. Considering the PDAS, it is possible to estimate the cooling rate of the alloy during the solidification process using the equation:

$$\boldsymbol{PDAS = a * \varepsilon^{-b}} \qquad \textbf{(7)}$$

with $\boldsymbol{a}$ and **b** are material constants (for Ni-based superalloys $\boldsymbol{a}$ is 50µm, **b** is 1/3) [58].

During the work, it was evaluated an average value of 0.7 ± 0.3 µm, obtaining a cooling rate **ε** value around $3.5*10^5$ °C/s, which is extremely fast, explaining the absence of completely formed secondary dendritic structure. The magnitude of the estimated cooling rate is in line with the values reported in the literature [38,57,58].

Increasing the magnification using a FESEM, bright nanometric precipitates are revealed inside the dendrites (yellow arrows) as well as elongated phases in the interdendritic spaces (red arrows) (Fig.37a and b).

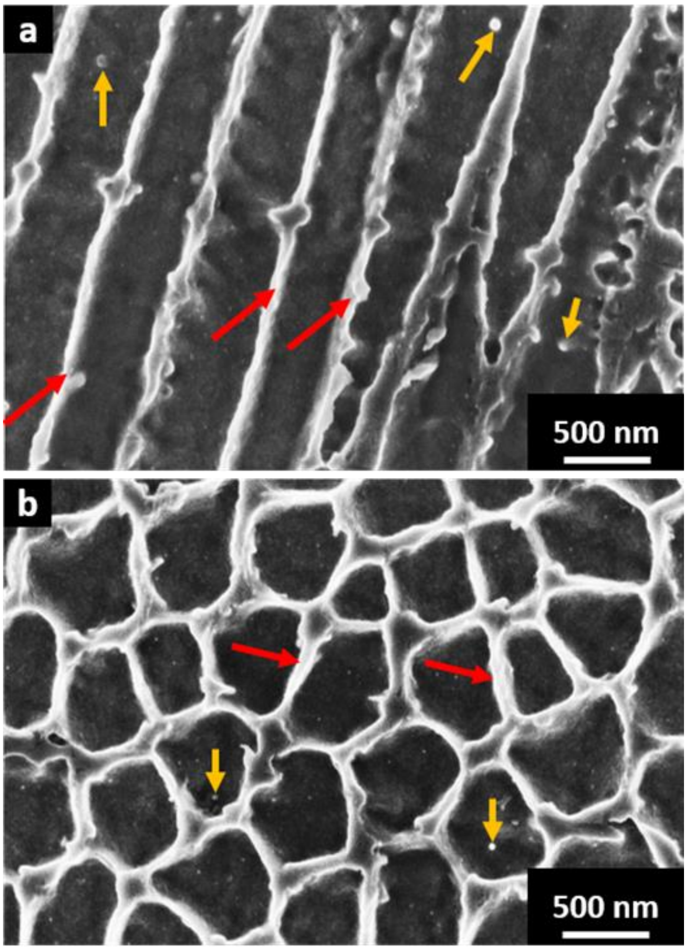

Figure 37: FESEM images of (a) columnar dendrites and (b) cellular dendrites [63]

TEM analysis performed in a previous work revealed that the nanometric precipitates are Nb-rich MC carbides formed by eutectic reaction during the solidification, with dimensions inferior to 100 nm, while the elongated phases are segregation of Nb and Mo [63].

In Ni-based superalloys, Nb and Mo solid solution reinforcer possess a strong segregation tendency, remaining entrapped within the interdendritic regions [3,98].

TEM also detected Nb-rich MC carbides due to eutectic reaction (**L** → **γ** + **MC**), but no laves phases were found. Their absence is probably due to the chemical composition of the IN625 powder used in this work.

In fact, it was reported that a high C/Nb ratio promotes the precipitation of Nb-rich **MC** carbides without formation of Laves phases, as can be seen in Fig.38, as well as a low concentration of Si and Fe reduce the Laves phase formation, while increasing the percentage of Nb ad C promote the carbides eutectic formation [3,16].

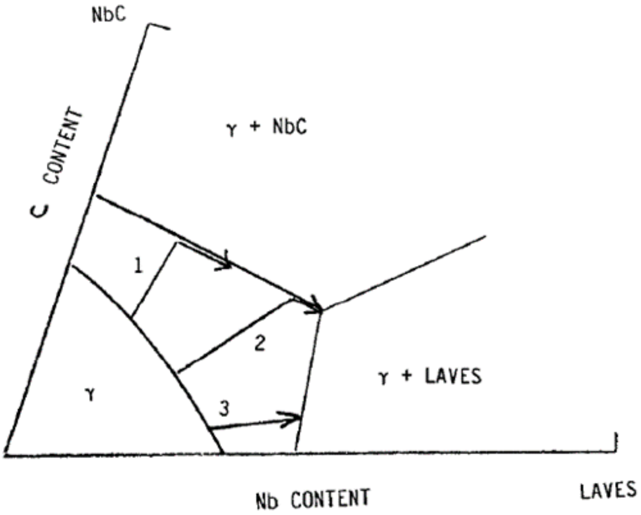

Figure 38: Solidification path based on Nb and C content [16]

As-Built Texture: Electron BackScatter Diffraction (EBSD) analysis

Further investigations were conducted performing EBSD analysis in collaboration with Chalmers University of Technologies. In Fig.39 EBSD maps on the as-built IN625 are reported for the XY and the ZX planes.

The grains on the XY planes are characterized by a strong texture, showing a preferred orientation along the 001 direction. This behaviour is well known for Ni-based superalloys produced by LPBF, where the <100> is the preferred crystallographic orientation during solidification [38,54].

The grains on the ZX planes do not possess any particular preferentially grain orientation: they appear elongated along the Z-axis as previously shown in the OM images.

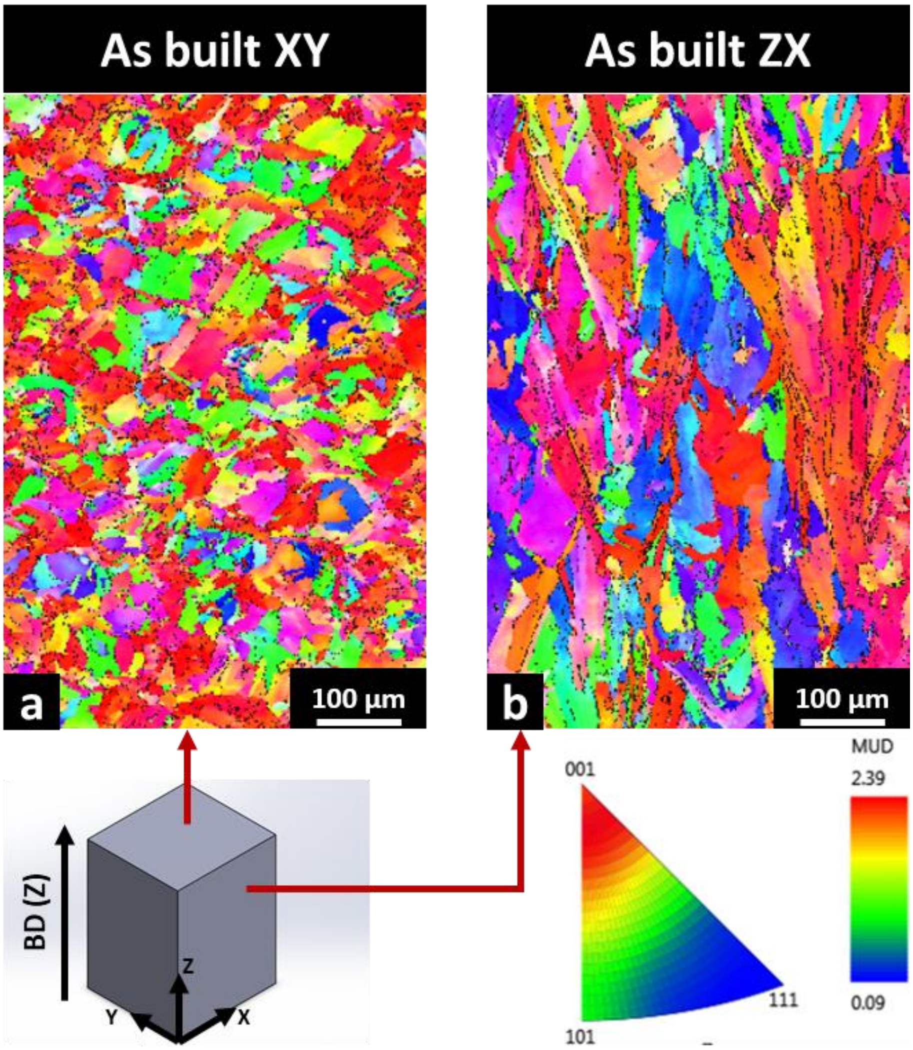

Figure 39: EBSD maps of as-built on XY and ZX planes

Moreover, the EBSD was also used to evaluate the grains boundaries misorientation angle for the XY plane (Fig.40) and for the ZX plane (Fig.41). For this work, grain boundaries have been classified in three categories: low angle grain boundaries (LAGB) for misorientation angles up to 10°, high angle grain boundaries (HAGB) for misorientation angles from 11° to 59° and twinning grain boundaries for 60° misorientation (TGB). The angle value 60° is based on the literature, indicating 60° as the typical misorientation value for twinning grain boundary along (111) orientation [89].

In the following images LAGB, HAGB and TGB are highlighted in white, black and yellow respectively. In Fig.40a can be noticed equiaxial grains with variable grain size, and that in some zone the smaller grains seem to be aligned, like following the laser scan tracks (white rectangles in Fig.40a). As can be seen in Fig.40b, inside the grains are present a huge amount of LAGB. These grain boundaries are probably caused by the presence of substructures formed by the presence of a large number of dislocations, created during the extremely rapid solidification and showed from the TEM analysis [24,63].

The amount of LAGB seems to be more concentrated in places where are present small grains, and less where there are larger grains, following also, in this case, the laser scan tracks.

The presence of LAGBs is reported in the literature also for others LPBF Ni-based superalloys [24,93,99].

The graph in Fig.40c shows the trend of the misorientation angles, pointing out that almost 50% of the grain boundaries had a value of misorientation of 2°.

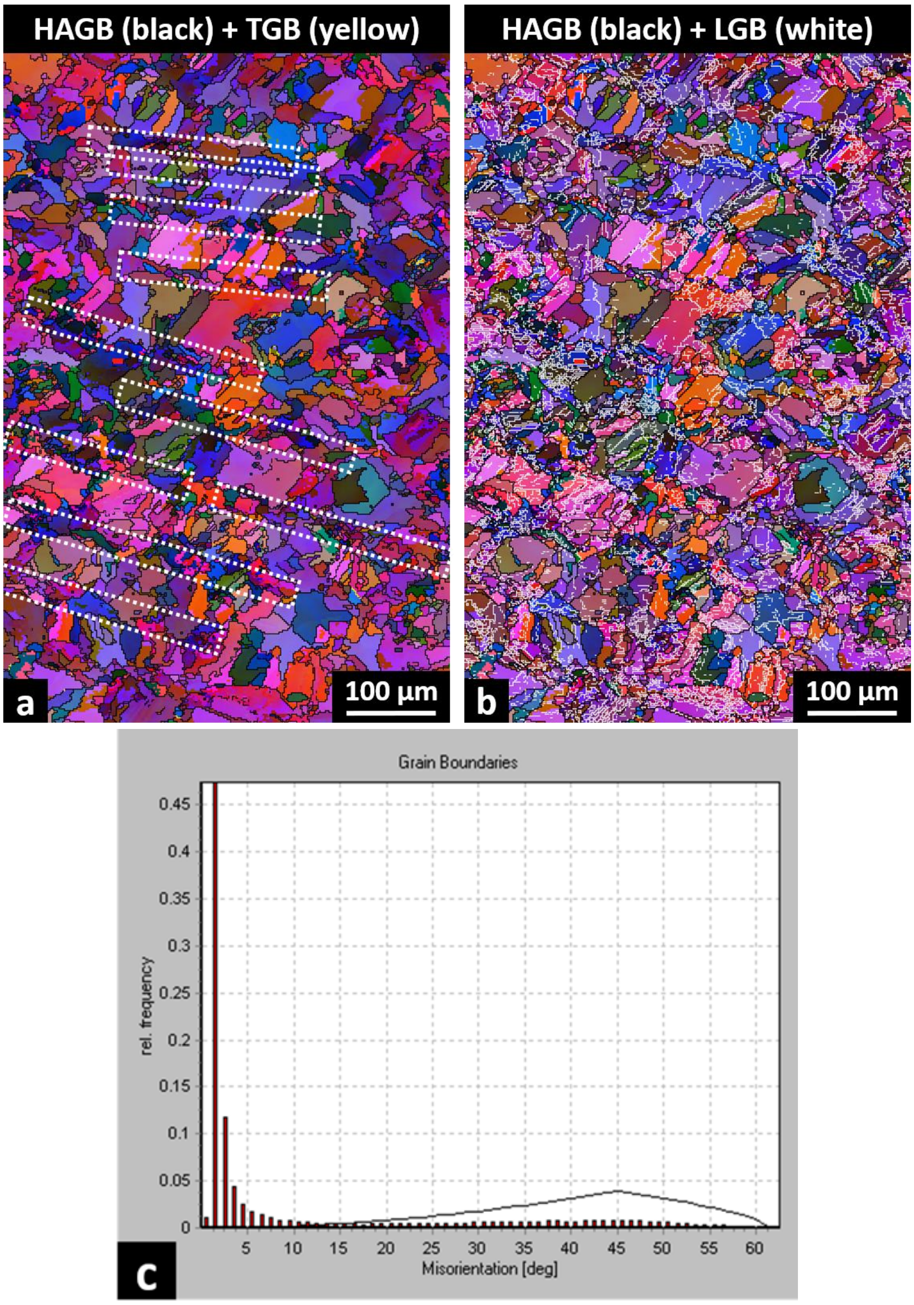

Figure 40: XY plane (a) HAGB in black, (b) LAGB in white and (c) frequency % of grain boundaries misorientation

The texture of the ZX plane displays elongated grains mostly longer than 100 µm as visible in Fig. 41a.

In Fig.41b the low angle grain boundaries are mostly uniformly distributed on the plane, without a particular pattern. Also for this plane, 2° have the most substantial misorientation angle fraction, reaching a value of 55%.

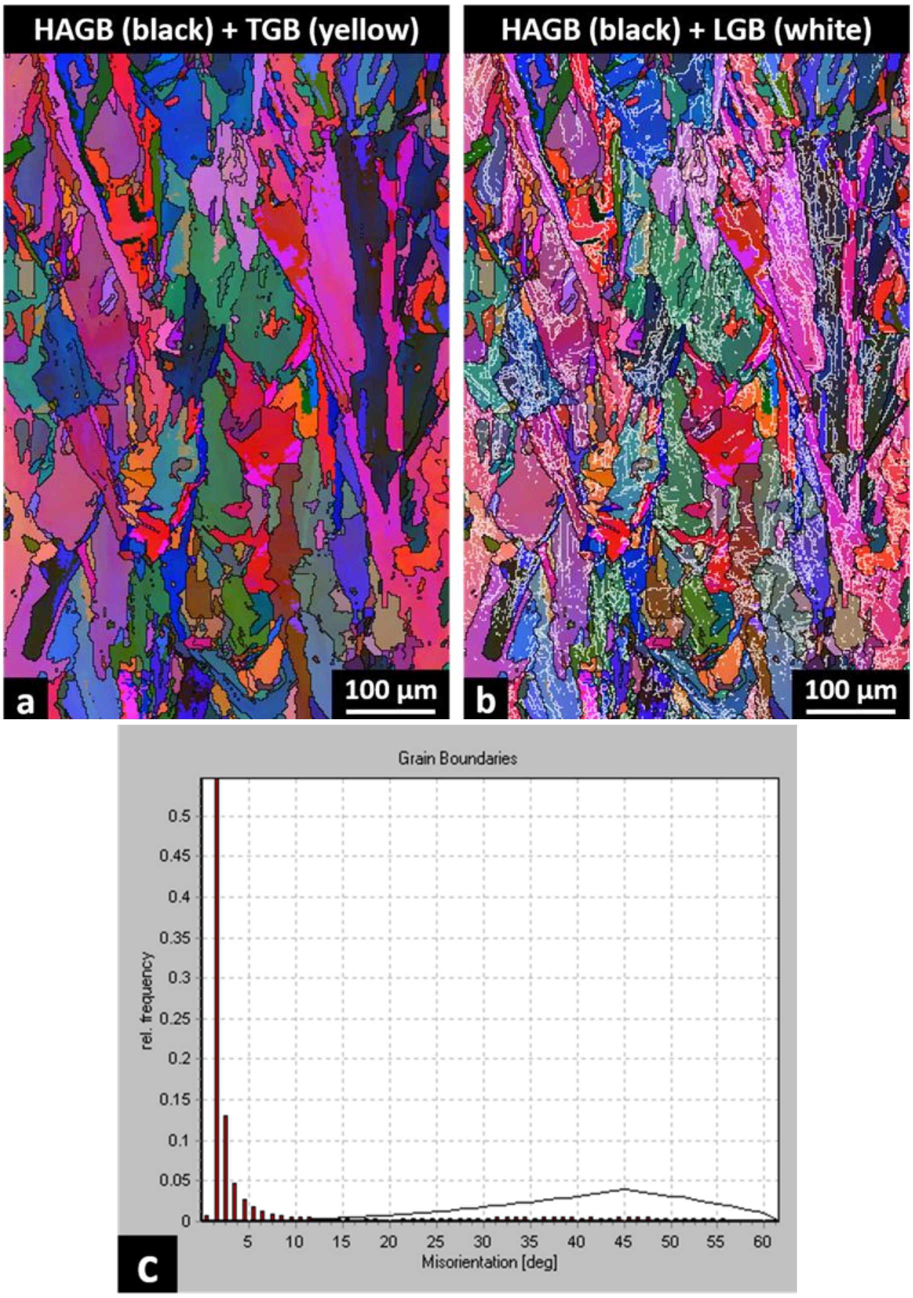

Figure 41: ZX plane (a) HAGB in black, (b) LAGB in white and (c) frequency % of grain boundaries misorientation

In Fig.42 a cumulative graph of the LAGB, HAGB and TGB content for both orientations is shown. For both orientations, the larger fraction of grain boundaries is composed by LAGB. This feature is particularly evident on the ZX plane, where 80% of the grain boundaries are LAGB. The difference in misorientation angle fraction between the two planes can be attributed to the higher number of grains in the XY plane, which increase the HAGB fraction at the expenses of the LAGB fraction.

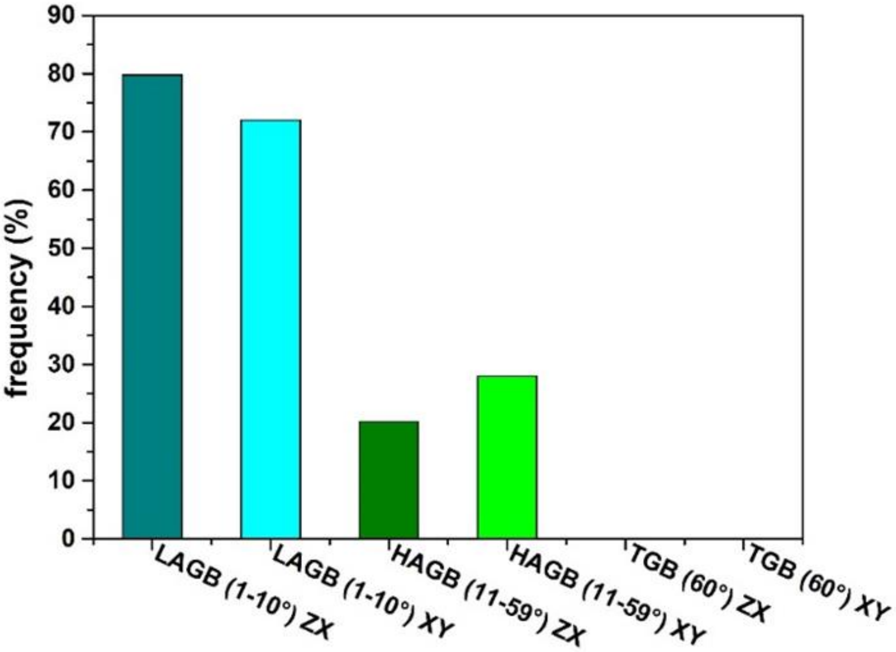

Figure 42: Comparison between the XY and ZX misorientation angle types frequency

As-Built Mechanical properties: tensile test

Fig.43 reports the stress-strain curves for the IN625 as-built samples built along the Z-axis and on the XY plane. The results are reported in Table.19 and compared with the literature on LPBF IN625 and IN625 processed by traditional processes. In Table.19 the tensile properties are reported as YS (yield strength), UTS (ultimate tensile strength) and El (elongation at break).

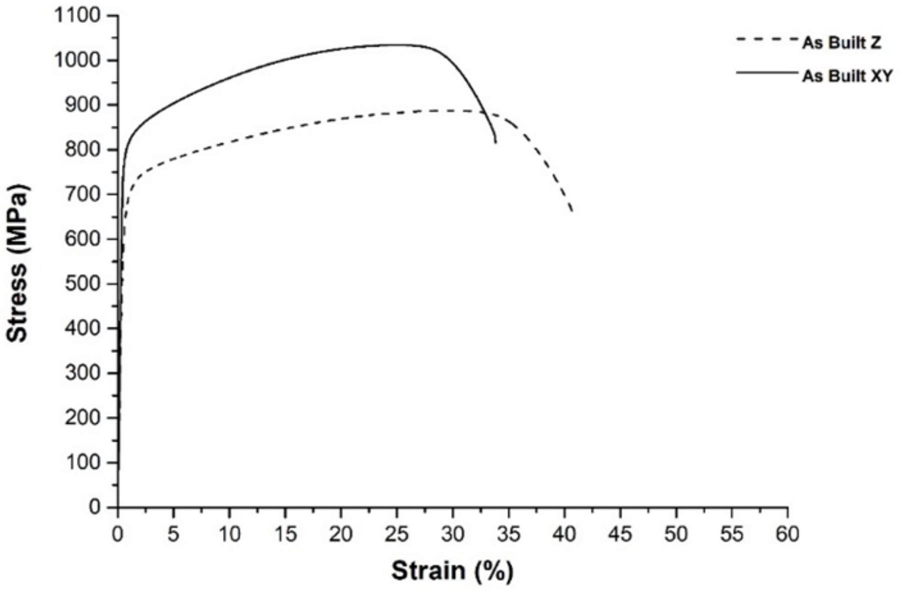

Figure 43: stress/strain curves for as-built IN625 tensile samples

Similarly to other authors [100,101] the horizontally grown as-built IN625 (XY) exhibits higher YS and UTS and lower ductility compared to the vertically built specimen (Z). This different behaviour is related to the strong anisotropy of the grains, which are elongated along the Z-axis. When the XY are strained the force is applied perpendicularly to the columnar grains, and, as seen in the EBSD map in Fig.41a, more HAGBs are available to block the dislocations path compared with the vertically orientated sample. Stroßner et al. [100] also suggest that in as-built the presence of the melt pool can be detrimental for the tensile properties of the vertically grown samples.

However, both XY and Z as-built IN625 samples meets the minimum requirement of the ASTM F3056-14 for LPBF IN625 standard, with YS and UTS values that are around the double compared to the minimum requirements values.

These values are similar to declared tensile properties of EOS for LPBF IN625, but with a reduced standard deviation, that can be attributed to the fact that in this work all the samples have been produced in the same build, while EOS probably produced the samples in multiple builds.

Few studies report the tensile properties of as-built LPBF IN625, because the final application requires post-processing such as stress relieving, annealing, solutioning or HIP treatments [99,102–105].

Wang et al. [106] tested as-built LPBF IN625 samples, but they obtained lower YS and UTS, with total El similar to this work. The variation between the data of this study and their data can be caused by the difference in building parameters used, as well as, the different powders and LPBF machine used.

Similar YS and UTS were obtained by Yadroitsev et al. [19], but with a considerably lower ductility, probably caused from a residual porosity reported as lower than 1 %, whereas in this study the porosity level is 0.064 ± 0.014%.

Compared to the commercially available IN625, LPBF as-built IN625 shows similar strengths of the as-rolled IN625 coupled with a higher El, and these properties are higher than the minimum requirement for the wrought condition of this alloy based on ASTM B443.

The extremely fine dendrites that compose the microstructure, coupled with the high dislocation content due to the particularly fast cooling and solidification rates can explain why the LPFB as-built exhibits high YS and UTS without the application of post-heat treatments.

Table 19: Comparative table of the tensile properties of as-built LPBF IN625 with the literature

IN625	YS (MPa)	UTS (MPa)	El (%)
This work			
as-built z	618 ± 33	891 ± 5	40.7 ± 0.5
as-built xy [63]	783 ± 23	1041 ± 36	33.1 ± 0.6
Other authors studies – Other specifications			
as-built xy [106]	642 ± 23	879 ± 2	30 ± 2
as-built z [81]	615 ± 50	900 ± 50	42 ± 5
as-built xy [81]	725 ± 50	990 ± 50	35 ± 5
as-built XY [19]	800 ± 20	1030 ± 50	8–10
as-built Z [19]	720 ± 3	1070 ± 60	8–10

Wrought IN625 [19]	517	930	40
As-rolled [18]	414 - 758	827 - 1103	30 – 36
Wrought IN625 grade 1*	>414	>827	>30
Wrought IN625 grade 2**	>276	>690	>30
LPBF ASTM F3056-14	275 (min.)	485 (min.)	30 (min.)

**ASTM B443 (minimum annealing temperature 871 °C)*

***ASTM B443 (minimum solution annealing temperature 1093 °C)*

The tensile fracture surfaces reported in Fig.44 have been studied using SEM microscopy. In Fig.44a the fracture appears as a ductile fracture, as can be deducted by the microvoids, formed during the rupture by coalescence and in same case already present as defects caused by residual porosity. Higher magnification of the micro dimples is shown in Fig.44b.

In some point (arrows in Fig.44c) can also be found some evidence of brittle fracture mode, maybe intergranular cleavage started by the Nb and Mo segregations.

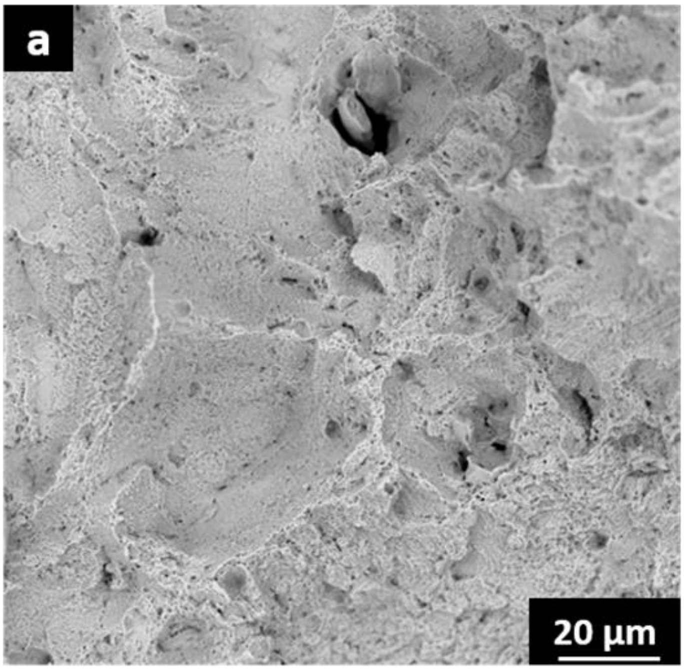

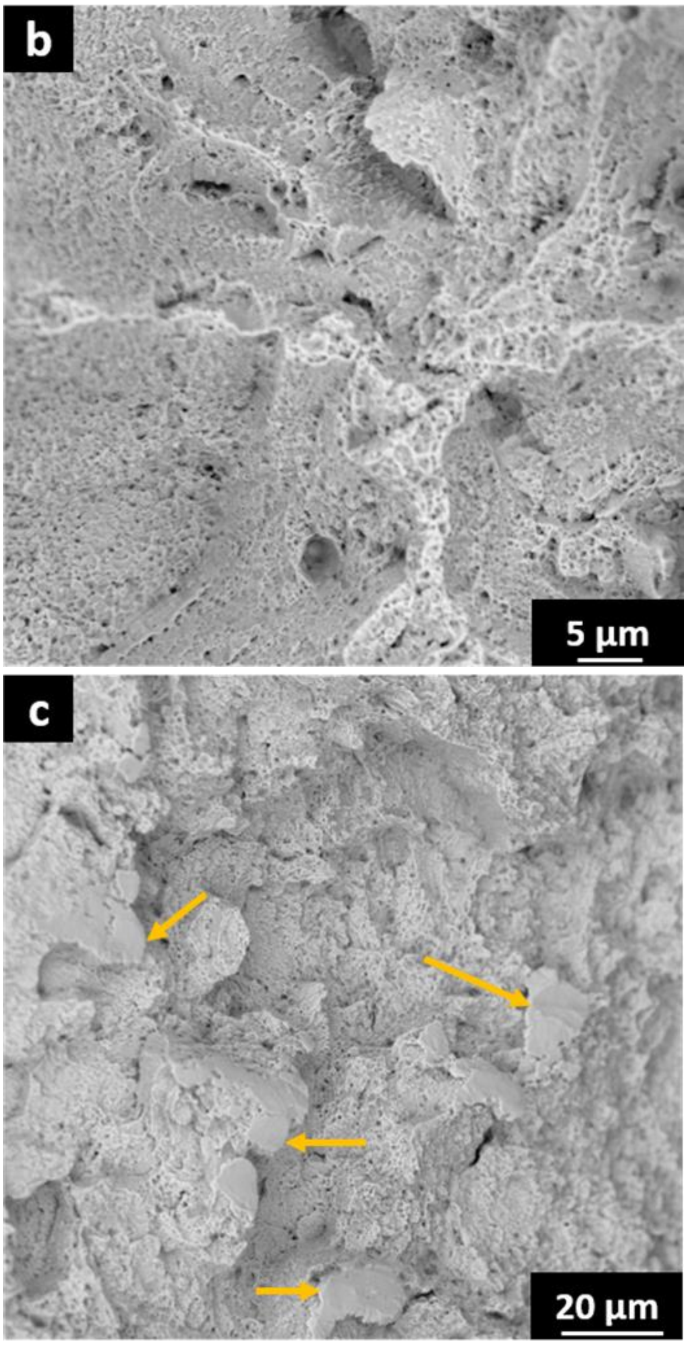

Figure 44: As-built IN625 fracture surface (a) micro voids, (b) micro-dimples and (c) portion of brittle fracture

3.1.1.2 IN625 stress relieved at 870 °C condition

Stress Relived 870 °C 1h Microstructure: Optical Microscope (OM)

The OM microstructure after stress relieving treatment at 870 °C for 1 hour can be seen in Fig.45. At the OM the microstructure appears similar to the as-built state, with visible melt pools on the ZX plane and long elongated grains aligned with the Z-axis.

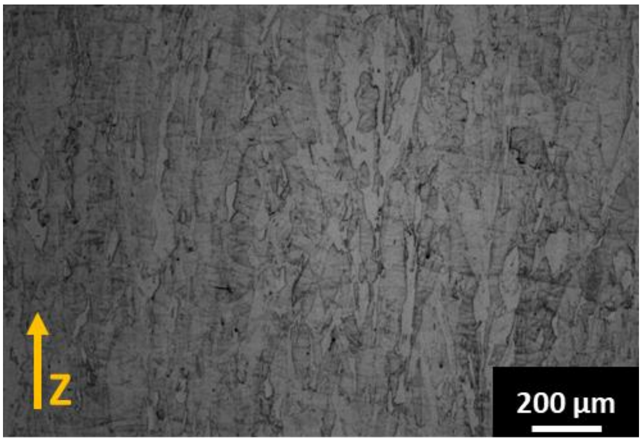

Figure 45: OM images of as-built IN625 after 870 °C 1h annealing

Stress Relived 870 °C 1h Microstructure: Scanning Electronic Microscopy (SEM)

At higher magnifications by SEM microscopy, the microstructure of the IN625 annealed at 870 °C for 1 hour shows a significant amount of precipitates, mostly concentrated on the melt pools contours and at the grain boundaries, as well as inside the grains in the interdendritic areas (Fig.46a). These precipitates appear in form of needles and plates, with average dimension inside the grains of 0.5±0.1 µm (Fig.46b yellow rounded) and up to 1.8 µm when located at the grain boundaries (Fig.46b, red arrows). The EDS analysis (Fig.47) performed on these precipitates revealed significant enrichment in Nb, coupled with the depletion of Cr and an almost unvaried Ni presence. Both shape and EDS point out that these precipitates are **δ** phase, that usually precipitates along the <111> direction and at the grain boundaries [94,107].

The **δ** presence in the alloy after this short treatment time at 870 °C is not normal according to the time-temperature-transformation (TTT) diagram of the wrought IN625 alloy [16]. This topic was also investigated in other studies [108,109], which detected faster precipitation of **δ** in LPBF IN625, caused by the presence of segregation with a high content of Nb. Also in our previous work [63] Nb segregation was found, explaining the accelerated precipitation kinetic of **δ**.

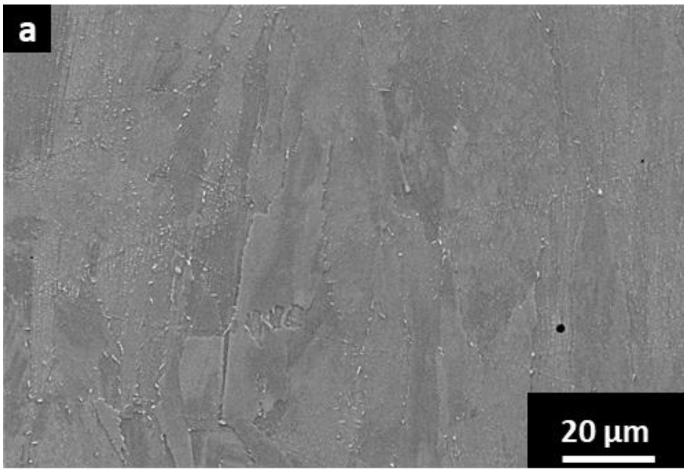

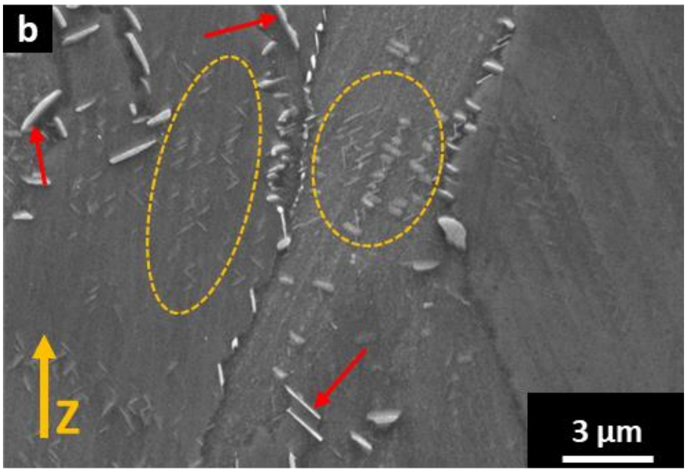

Figure 46: (a) SEM images of the annealed IN625 at 870 °C for 1 hour and (b) further magnified section at the grain boundaries

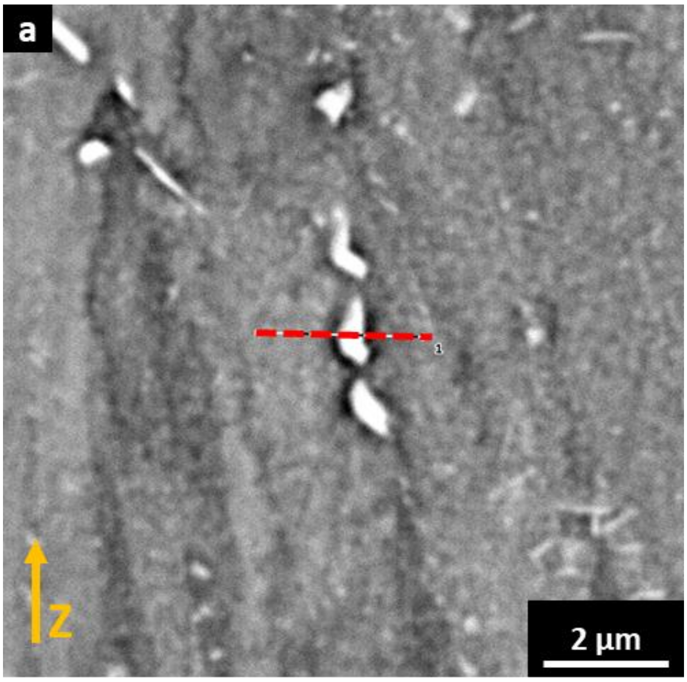

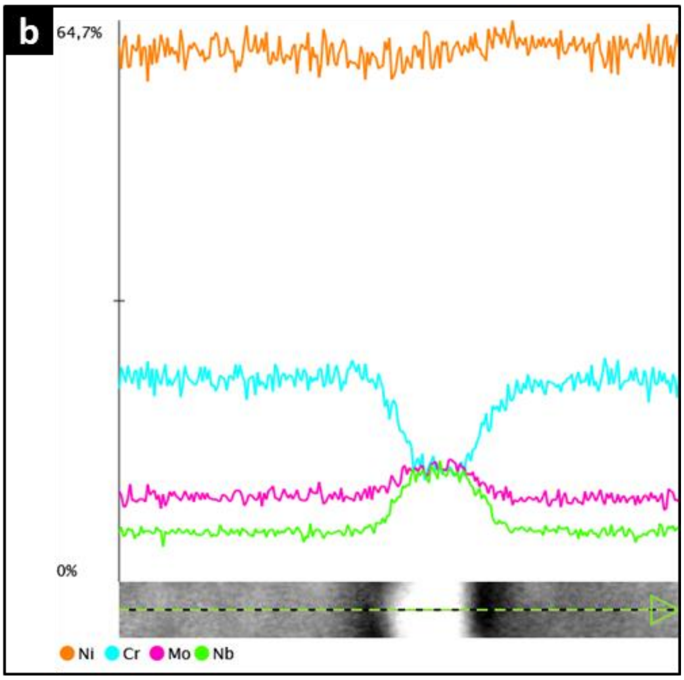

Figure 47: EDS analysis of δ phase

Taking a high magnification image of the alloy (Fig.48) the presence of the second type of precipitates is revealed. Those spherical nanometric phases are probably carbides, which could be the primary carbides already detected from FESEM and TEM in the as-built condition or secondary carbides formed during the heat treatment.

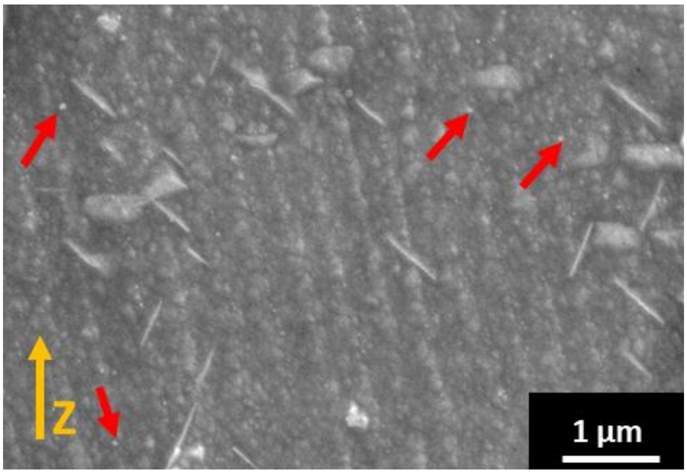

Figure 48: High magnification SEM images of the annealed IN625 at 870 °C, with carbides pointed out by the arrows

Stress Relived 870 °C 1h Texture: Electron BackScatter Diffraction (EBSD) analysis

In the EBSD map shown in Fig.49a the XY plane is characterized by the same strong texture already found in the as-built condition, with equiaxial grains orientated along the 001 direction, and long elongated grains aligned with the Z direction on the ZX plane as reported in Fig.49b, showing that the stress reliving treatment effects on the microstructure were circumscribed to the formation of the precipitates, with no impact on the features of the grain.

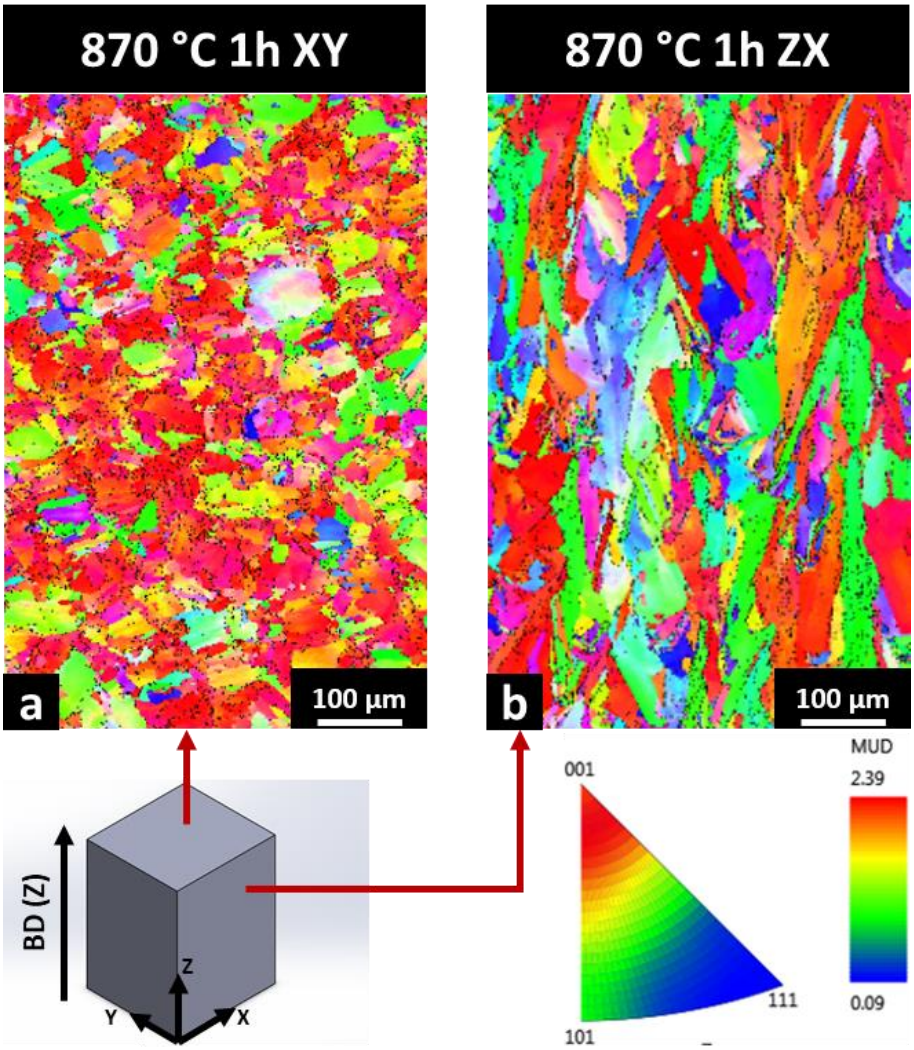

Figure 49: EBSD maps on the (a) XY and (b) ZX planes of the annealed IN265 at 870 °C

Analyzing the high angle grain boundaries of the XY plane in Fig.50a features similar to the as-built LPBF IN625 are found, as the equiaxial grains with variable grain size, zones that highlight the laser scan tracks with the presence of groups of aligned small grains with bigger grains between two lines (white rectangles in Fig.50a). Also the LAGB map (Fig.50b) appear similar to the as-built condition, as well as the misorientation angle graph in Fig.50c, which anyway show a 2° grain boundaries amount a little inferior to the as-built XY case, with a 40% occurrences.

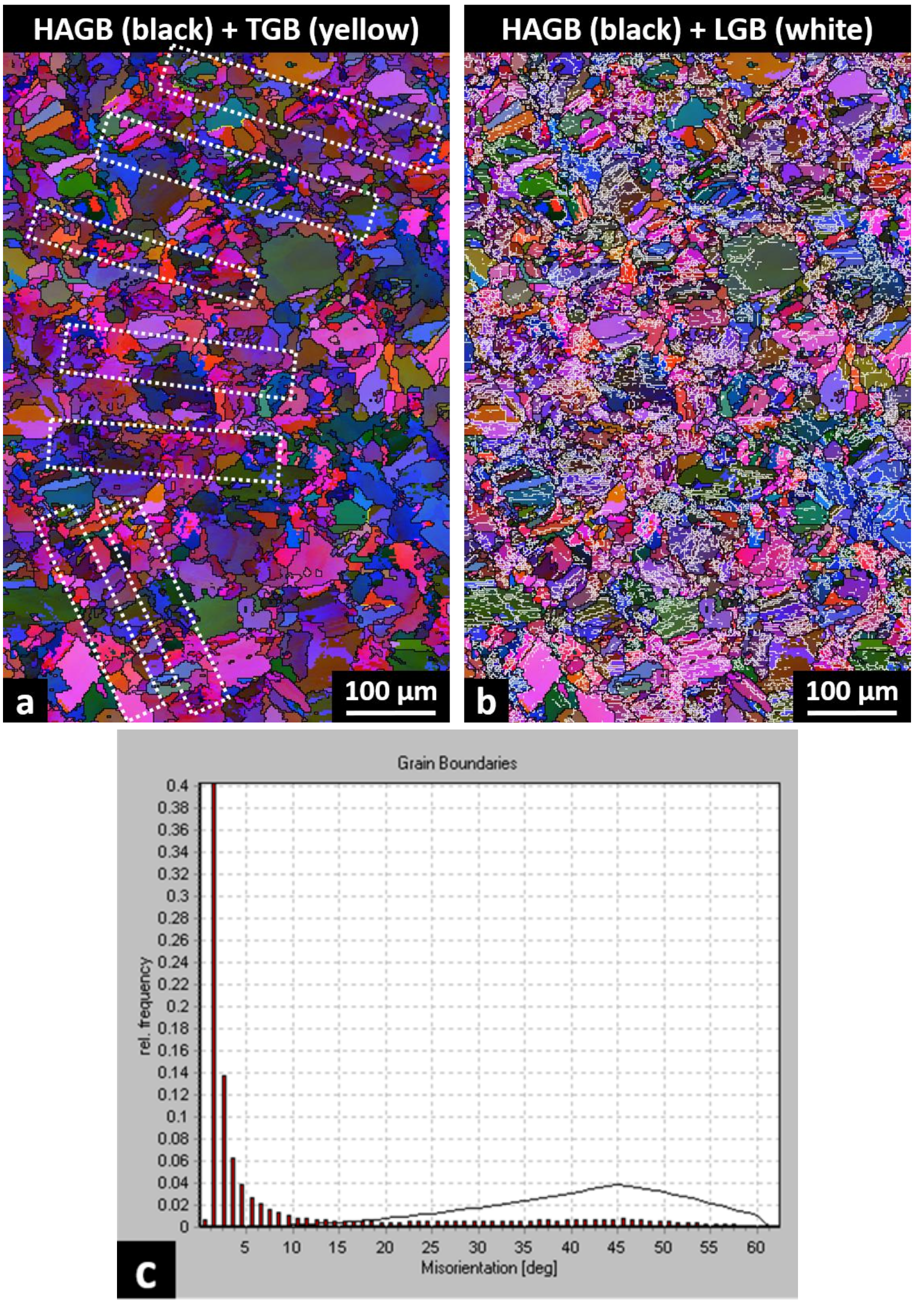

Figure 50: XY plane (a) HAGB in black, (b) LAGB in white and (c) frequency % of grain boundaries misorientation for the 870 °C 1 hour annealing

Also on the ZX plane, the findings are similar to the ZX as-built case (Fig.51a and b), with a lower 2° grains boundaries content (less than 50%) (Fig.51c).

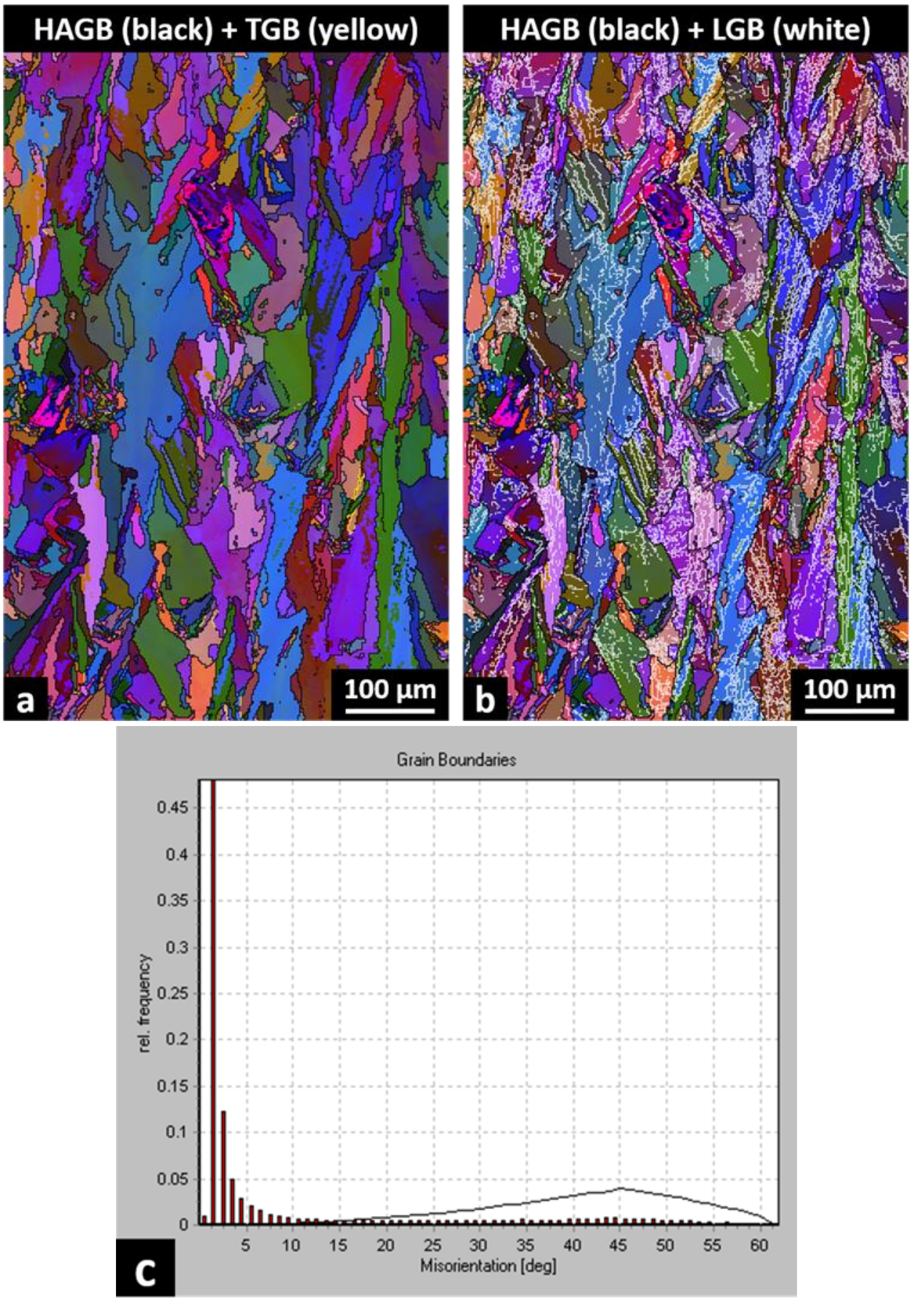

Figure 51: XY plane (a) HAGB in black, (b) LAGB in white and (c) frequency % of grain boundaries misorientation for the 870 °C 1 hour annealing

In Fig.52 can be noticed that also in this condition the greater fraction of grain boundaries is the LAGB. The difference from the as-built is the total value of the LAGB, which is slightly lower (around 75%) and with little diversity between the ZX and the XY planes.

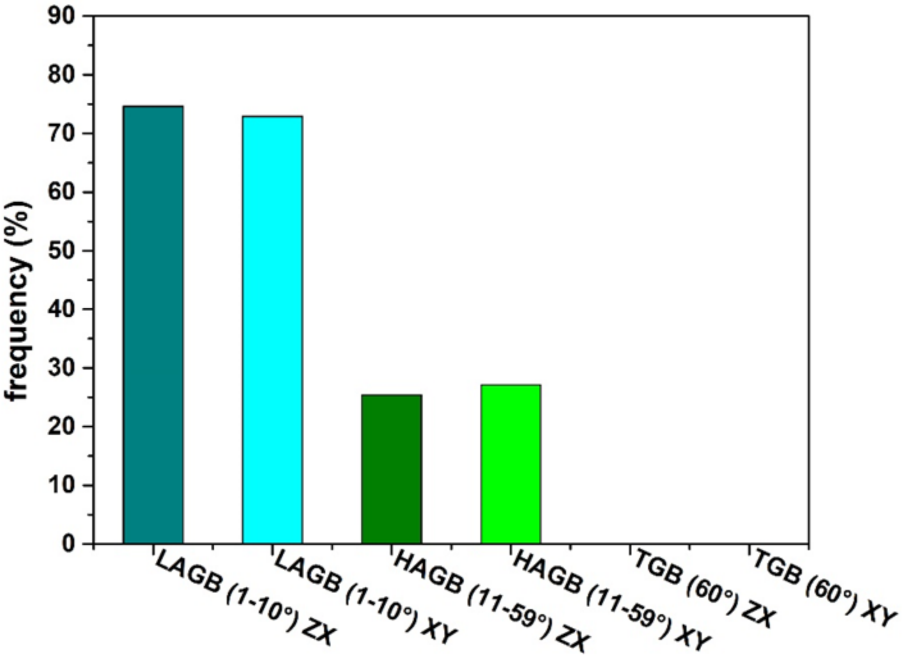

Figure 52: Comparison between the XY and ZX misorientation angle types frequency for the 870 °C annealed state

Stress Relived 870 °C 1h Mechanical properties: tensile test

The results of the tensile tests are reported in Fig.53 and Table.20.

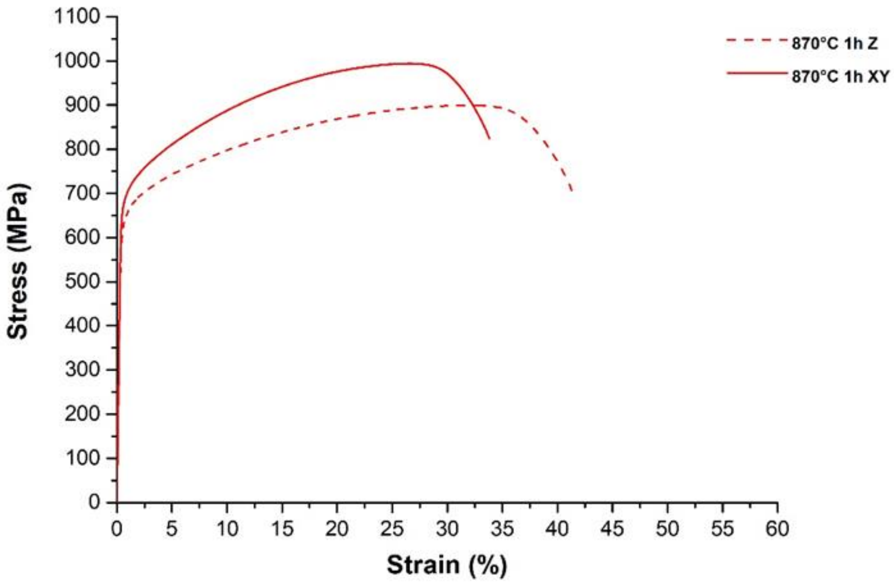

Figure 53: stress/strain curve for the 870 °C annealed IN625 tensile samples

Compared to the as-built condition there are no significant changes in the tensile properties for the Z samples, while for the XY samples that is a reduction of the YS, a contained lowering of the UTS and a little improvement of the total El. These properties deviation from the as-built state could be the result of the formation of the precipitates during the treatment, as well as, the partial stress reliving highlighted by the little reduction of the LAGB. Both samples conditions still maintain properties compatible with the as-rolled IN625 [18].

Table 20: Annealed at 870 °C 1 hour IN265 tensile properties

IN625	YS (MPa)	UTS (MPa)	El (%)
870 °C 1 hour XY	667 ± 3	996 ± 3	35.8 ± 1.8
870 °C 1 hour ZX	622 ± 6	900 ± 3	40.9 ± 1.7

The fracture appearance after the tensile tests (Fig.54a) shows a similar behaviour of the as-built condition, with dominant ductile fracture mode characterized by fine micro dimples (Fig.54b) and some evidence of brittle fracture mode (arrow in Fig.54c) probably caused by the intergranular **δ** precipitates or remaining segregations.

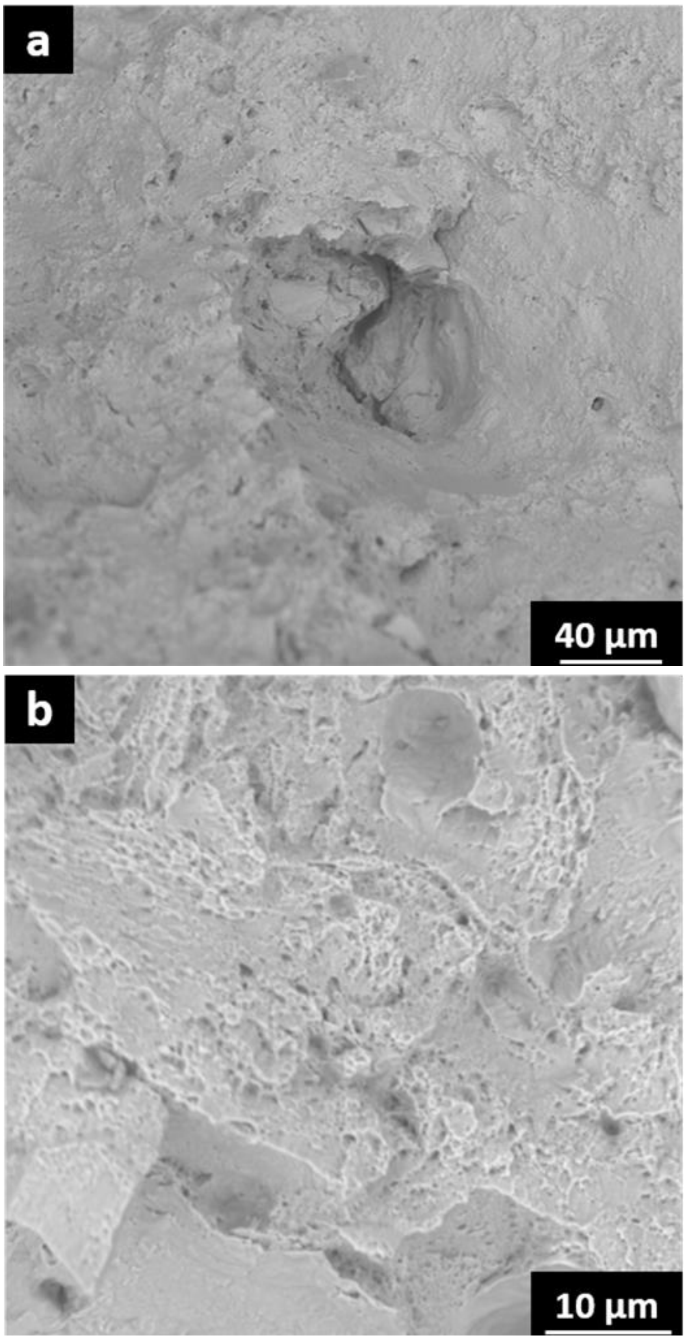

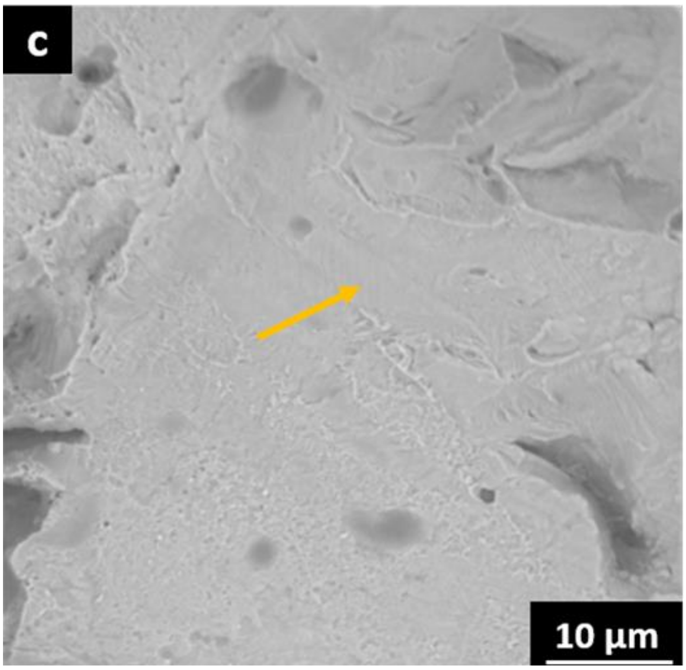

Figure 54: SEM images of the (a) 870 °C annealed IN625 fracture surface, (b) high magnification of the micro dimples and (c) high magnification of a brittle fracture area

3.1.1.3 IN625 Annealed at 980 °C condition

The annealing temperature of 980 °C for 1 hour is a common applied heat treatment on the commercially available wrought IN625 [11], but at this time there is little literature that evaluates the effects of this treatment on the LPBF IN625 [110].

Annealed 980 °C 1h Microstructure: Optical Microscope (OM)

As can be seen in Fig.55, the grain appearance of the alloy on the ZX plane is still characterized by long columnar grains aligned along the Z-axis, but the melt pools contours have disappeared.

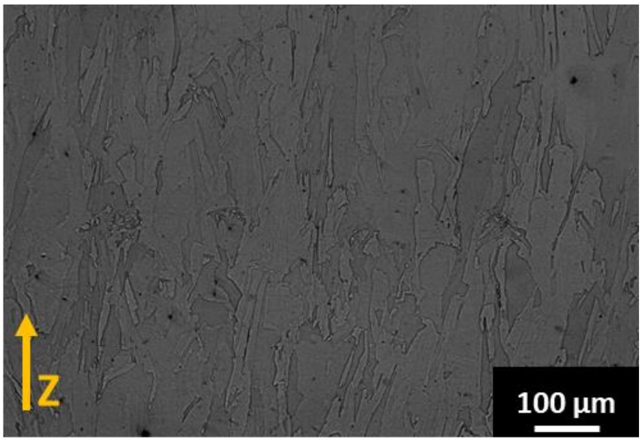

Figure 55: OM images of the 980 °C annealed LPBF IN625

Annealed 980 °C 1h Microstructure: Scanning Electronic Microscopy (SEM)

Further magnifications of the alloy are reported in the SEM images in Fig.56a and b. Compared to the 870 °C annealing, in this condition, there is no evidence of the large precipitation of **δ**. Few big precipitates can be located at the grain boundaries (Fig.56b, yellow arrow). The EDS performed on some of these precipitates (Fig.57) reported an enrichment in Nb and Mo, coupled with a depletion in Ni and Cr. Those findings allow to identify these phases as carbides, and their appearance is also in line with the TTT diagram of wrought IN625 [16]. Moreover, inside the grains nanometric carbides (Fig.56b, red arrows) can be spotted in the places where the segregations were located, and they probably have consumed the segregations in order to grow.

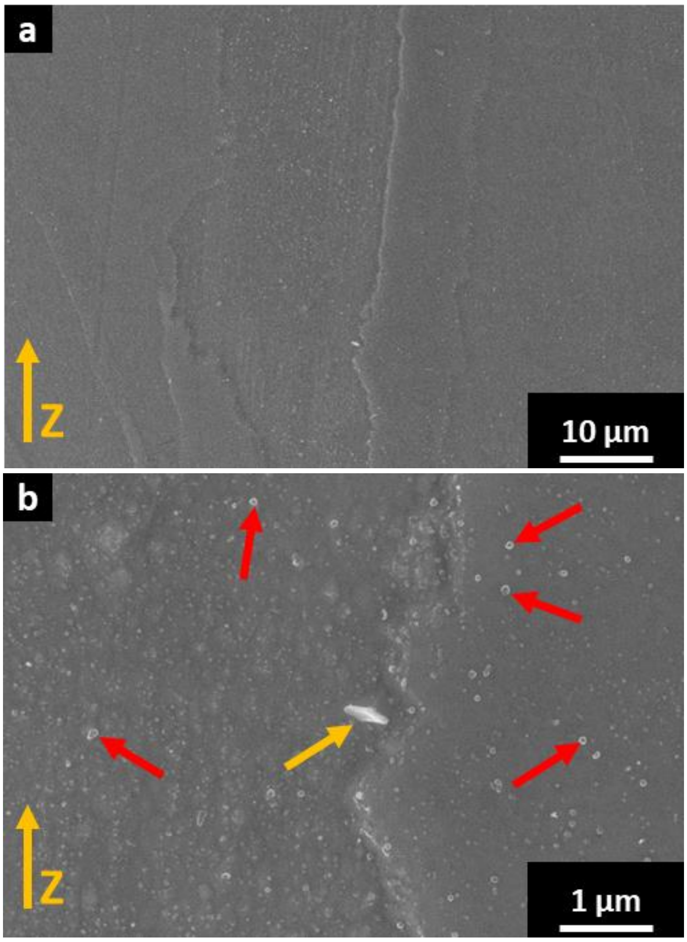

Figure 56: SEM images of (a) the 980 °C annealed IN625 and (b) magnification on a relatively large precipitate

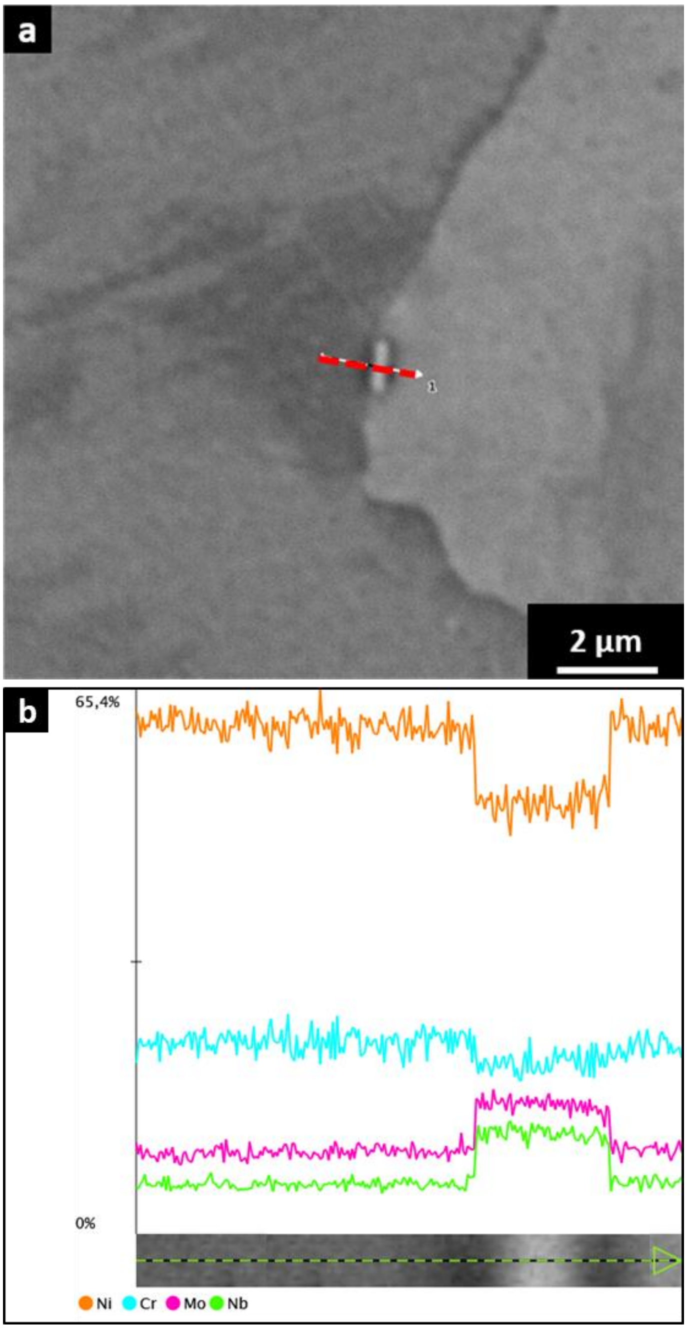

Figure 57: EDS lines performed on a big precipitate

Annealed 980 °C 1h Texture: Electron BackScatter Diffraction (EBSD) analysis

The EBSD map analysis on the XY plane (Fig.58a) still reveals the same texture reported for the as-built sample and for the 870 °C annealed condition, with equiaxial grains orientated along the 001 direction. The ZX face shows long elongated grains aligned with the Z direction, as seen in Fig.58b.

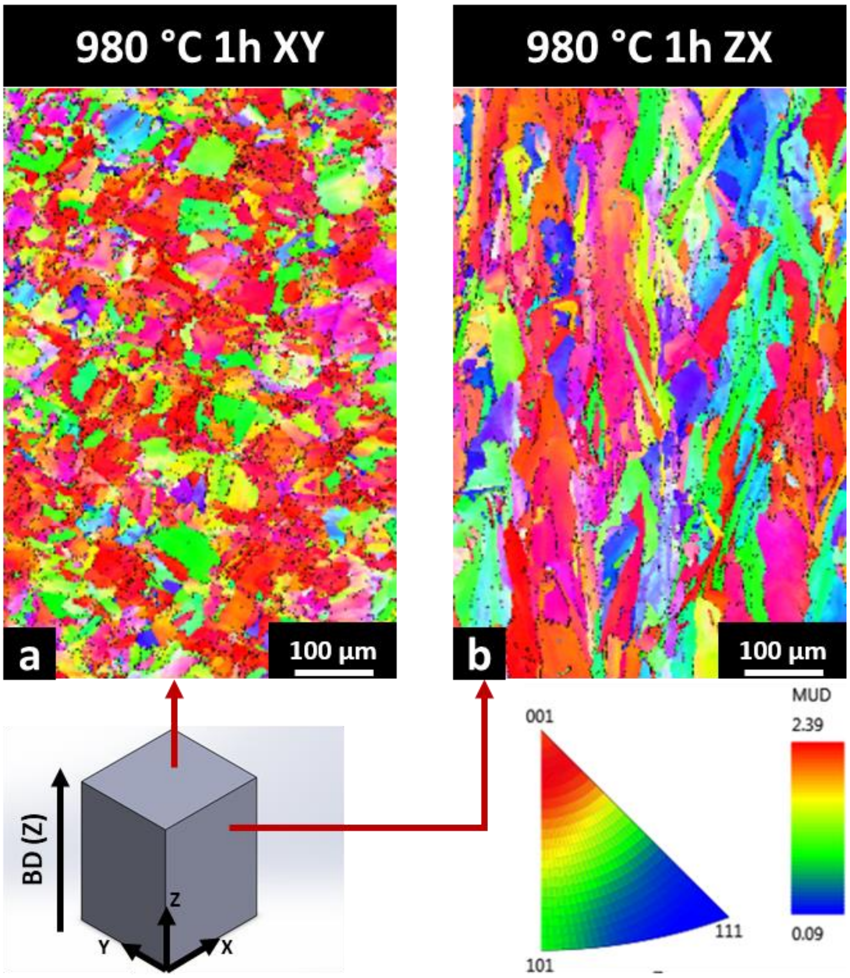

Figure 58: EBSD maps on the (a) XY and (b) ZX planes of the annealed IN265 at 980 °C

The HAGB map in Fig.59a found equiaxial grains with variable grain size, the presence of zones that remember the laser scan tracks passage (white rectangles in Fig.59a), as already seen in the as-built and 870 °C treated conditions. However, this time also a small amount of TGB (yellow, circled with red lines) appears, indicating a start in the recrystallization process. The LAGB map (Fig.59b) appear similar to the previous conditions, with a remarkable amount of LAGB concentrated in zones rich in small-sized grains, and the graph in Fig.59c results are very close to the results of the 870 °C annealed condition, with the same amount of 2° grain boundaries.

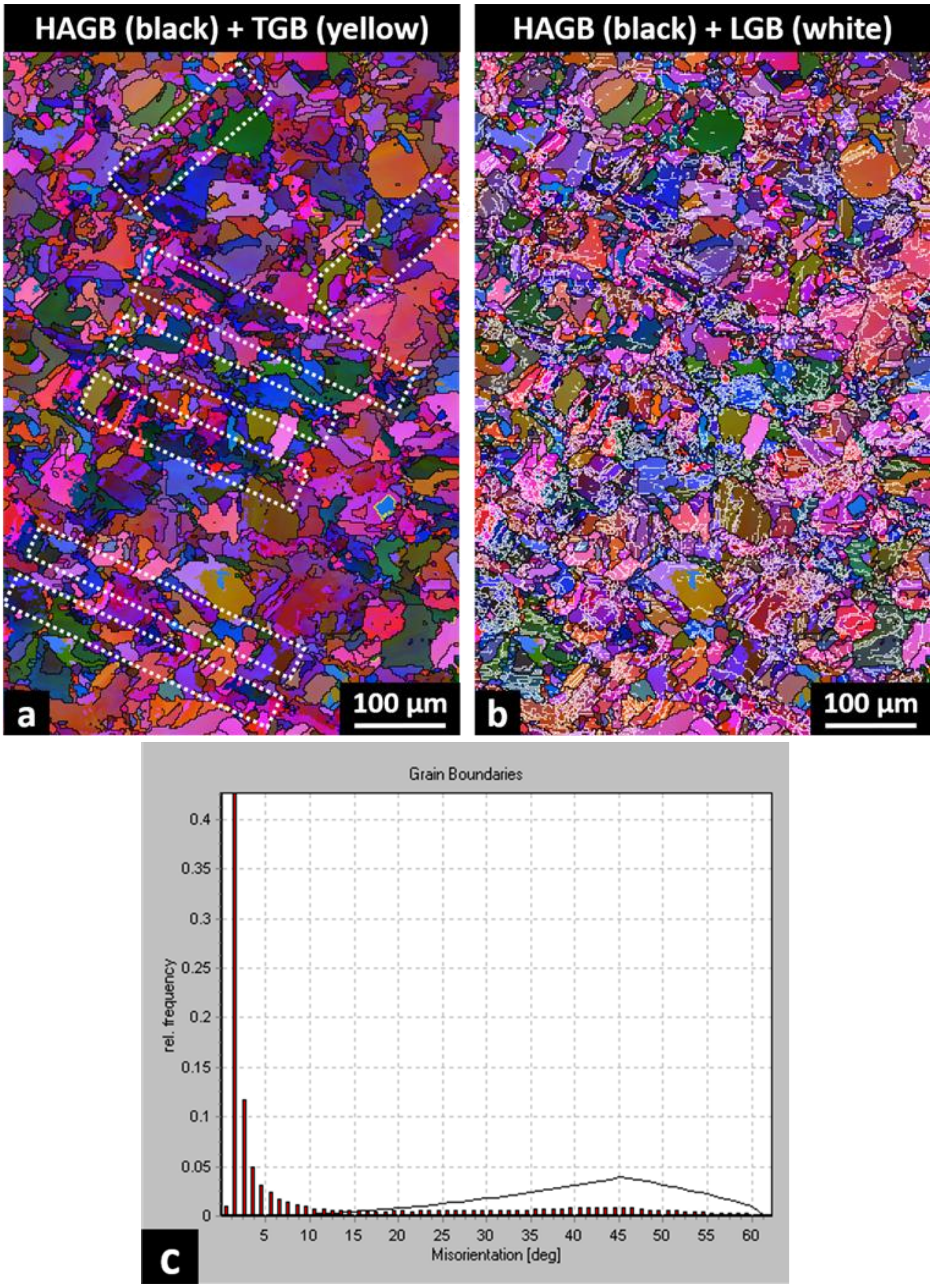

Figure 59: XY plane (a) HAGB in black, (b) LAGB in white and (c) frequency % of grain boundaries misorientation for the 980 °C 1 hour annealing

In the ZX face maps shown in Fig.60a and b the results are very similar to the 870 °C annealed state, with the exception of a TGB. The graph in Fig.60 report a situation with less than 50% of 2° grains boundaries content but does not detectthe TGB, maybe because its extension is too low for being noticed. However, the presence of TGB can indicate that increasing the annealing time at this temperature can lead to recrystallization.

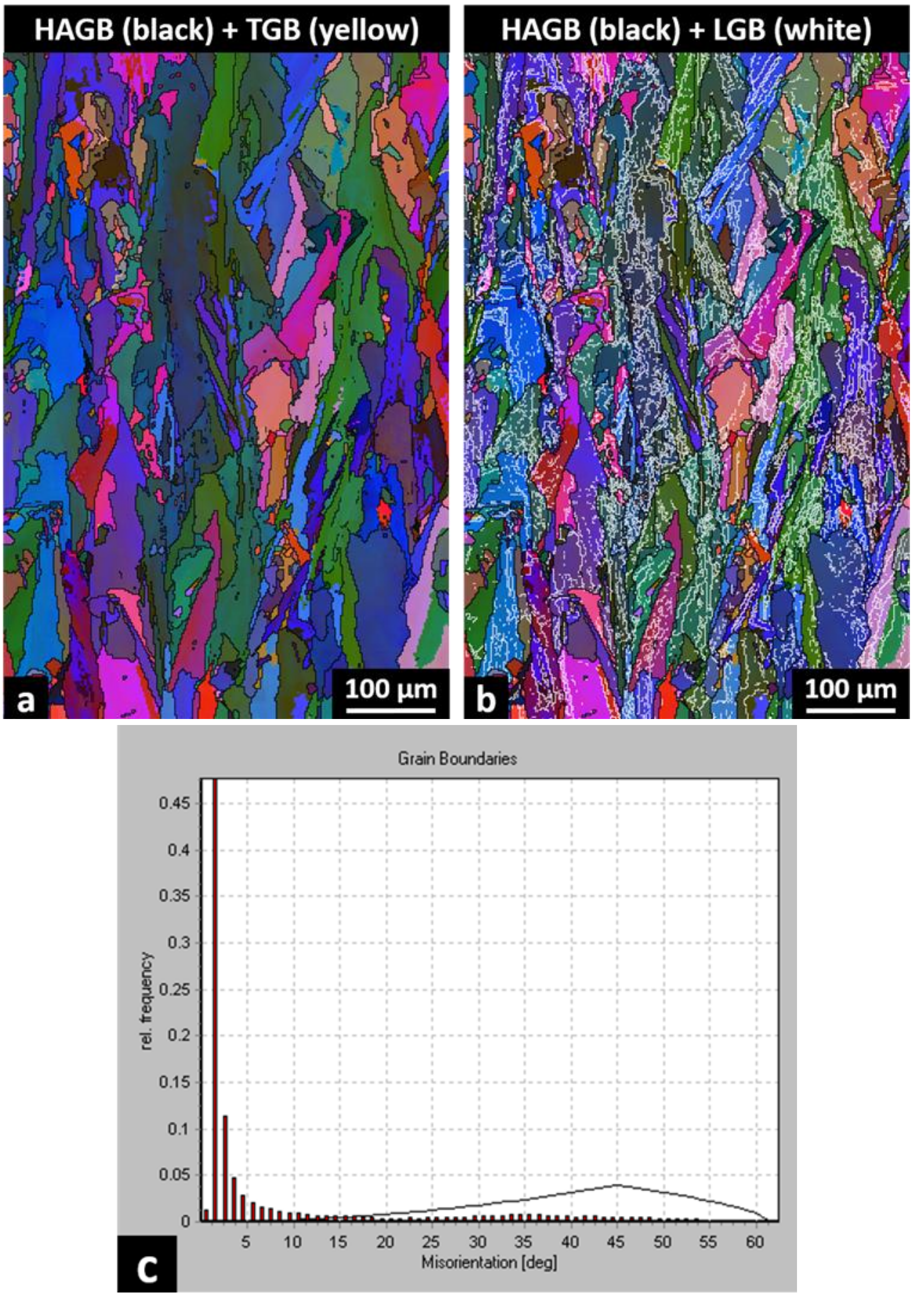

Figure 60: ZX plane (a) HAGB in black, (b) LAGB in white and (c) frequency % of grain boundaries misorientation for the 980 °C 1 hour annealing

The graph reported in Fig.61 confirms the uniformity with the 870 °C stress relived state, with really similar LAGB and HAGB fraction content, plus a minimal contribution of TGB for the XY plane.

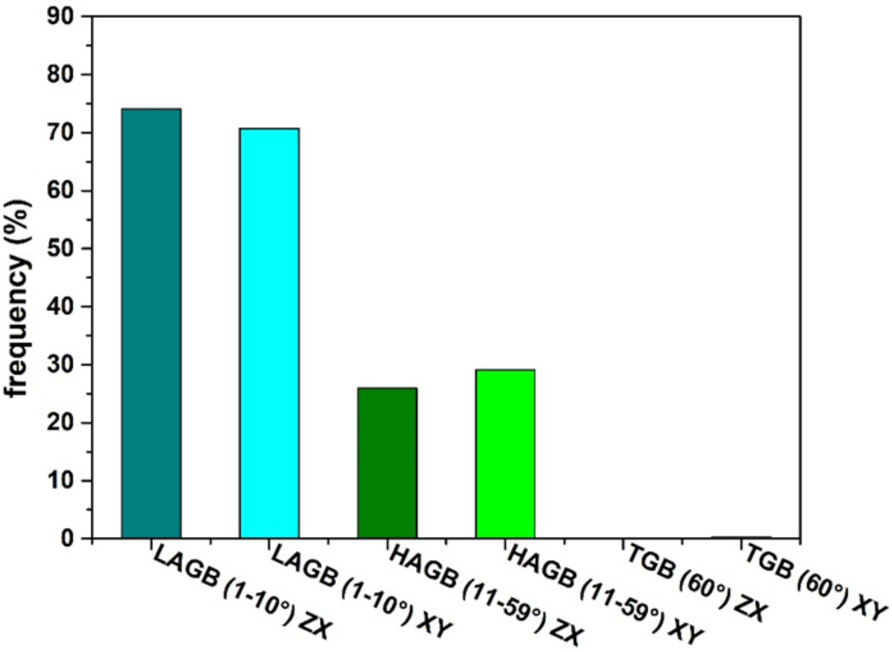

Figure 61: Comparison between the XY and ZX misorientation angle types frequency for the 980 °C annealed state

Annealed 980 °C 1h Mechanical properties: tensile test

The tensile properties of the 980 °C annealed state, reported by the stress-strain curve in Fig.62 and listen in Table.21 with a slight reduction of the YS and the UTS and a consistent improvement of the ductility for both XY and ZX samples compared with the tensile properties of as-built and stress relieved samples (870 °C for 1 hour) . The reduction in the stress resistance and the greater ductility are probably due to the strong reduction of segregations [110].

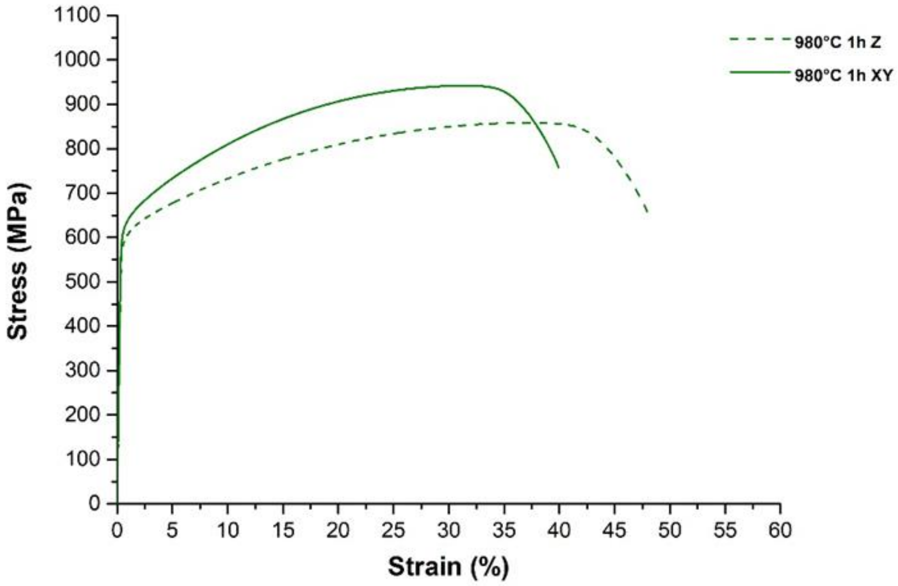

Figure 62: stress/strain curve for the 980 °C annealed IN625 tensile samples

Table 21: Annealed at 980 °C 1 hour IN265 tensile properties

IN625	YS (MPa)	UTS (MPa)	El (%)
980 °C 1 hour XY	612 ± 5	948 ± 8	39.8 ± 0.1
980 °C 1 hour ZX	579 ± 5	854 ± 4	47.6 ± 0.6

The fracture analysis (Fig.63a and b) revealed mostly ductile fracture, as pointed out by the micro dimples and the voids. Some little brittle fracture area is found, but is rare, probably provoked by the intergranular carbides or some defects already present in the as-built state.

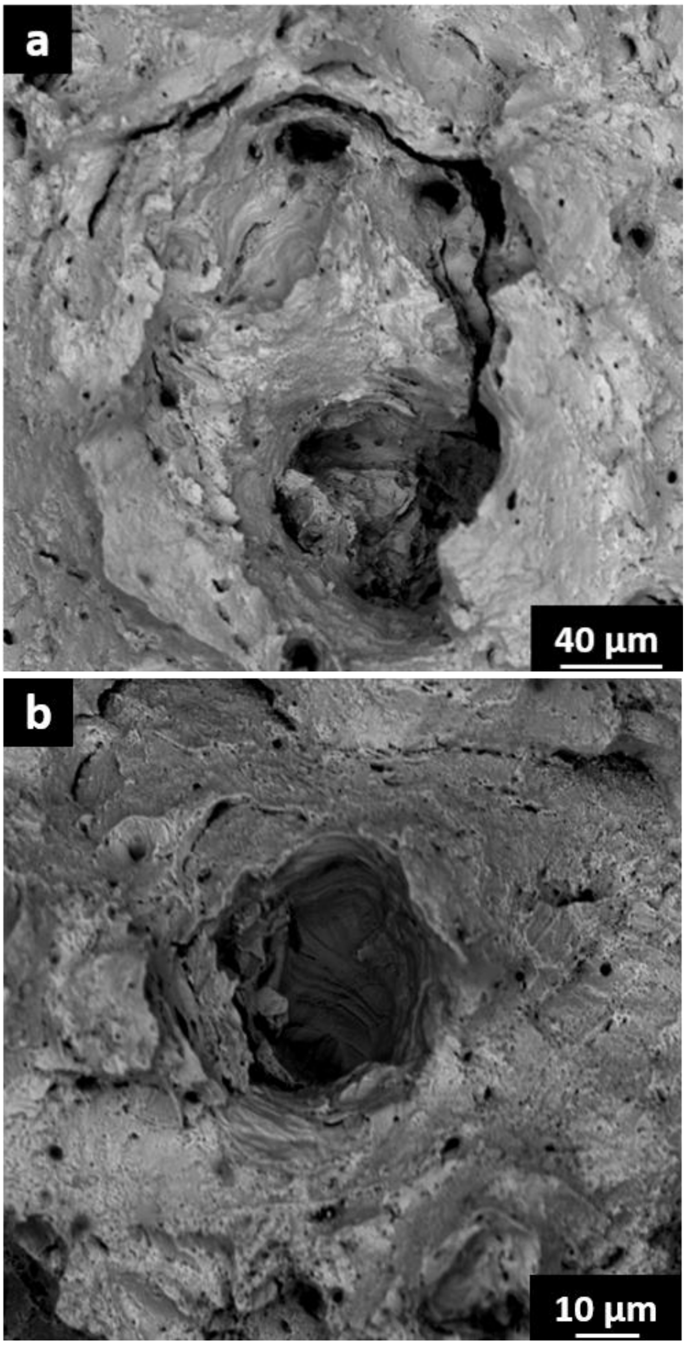

Figure 63: SEM images of the (a) 980 °C annealed IN625 fracture surface, (b) and higher magnification image

3.1.1.4 IN625 Annealed at 1080 °C condition

Annealed 1080 °C 1h Microstructure: Optical Microscope (OM)

The annealing temperature of 1080 °C for 1 hour resulted in evident recrystallization, as can be seen in the OM image in Fig.64. The grains have lost the elongated appearance, assuming and equiaxial shape, with dimension which can reach 120 µm. However, also small grains (circled in red) can be found in some positions. As effect of the recrystallization TGBs are appeared, clearly visible after the etching. Their presence is common in Ni-based superalloy after high-temperature treatments [111–113].

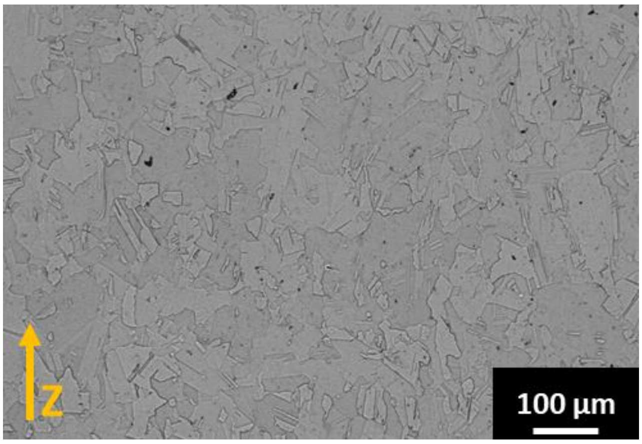

Figure 64: OM images of the 1080 °C annealed IN625

Annealed 1080 °C 1h Microstructure: Scanning Electronic Microscopy (SEM)

The SEM images (Fig.65a and b) display the presence of carbides, typically with size inferior to 1 µm (Fig.65b red arrows), probably formed by the growth of the MC carbides found in the as-built state or developed during the heat treatment. The dendritic structures are no more detected in this condition, pointing out the homogenization of the chemical composition.

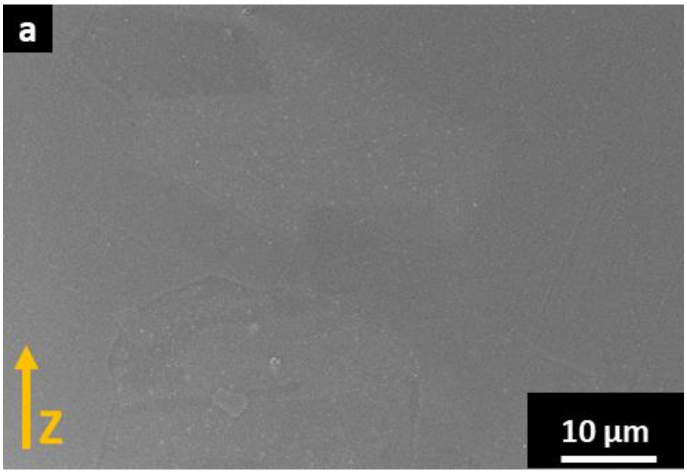

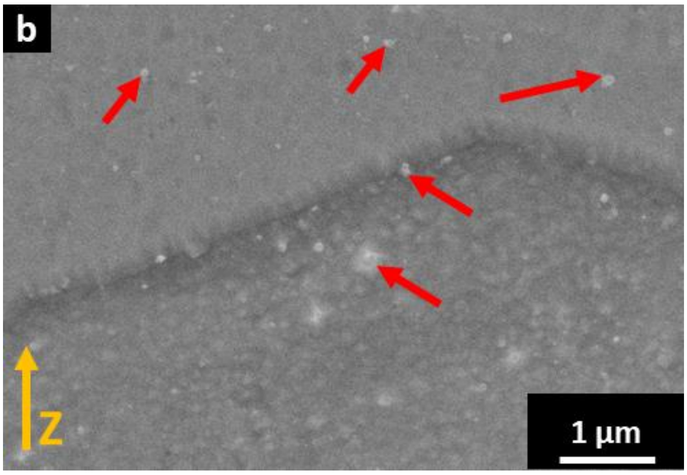

Figure 65: SEM images of the 1080 °C microstructure and carbides at (a) lower and (b) higher magnifications

Annealed 1080 °C 1h Texture: Electron BackScatter Diffraction (EBSD) analysis

The EBSD maps in Fig.66a show the effect on the recrystallization on the XY plane. The grains appear equiaxial and generally bigger compared to the previous conditions; however, some portion of the alloy still possess small grains groups aligned to form the laser scan track, indication that the recrystallization at this temperature for one hour is not sufficient to perform complete recrystallization. The ZX plane (Fig.66b) shows the absence of elongated grains and the dimensions of the grains are comparable with the XY plane.

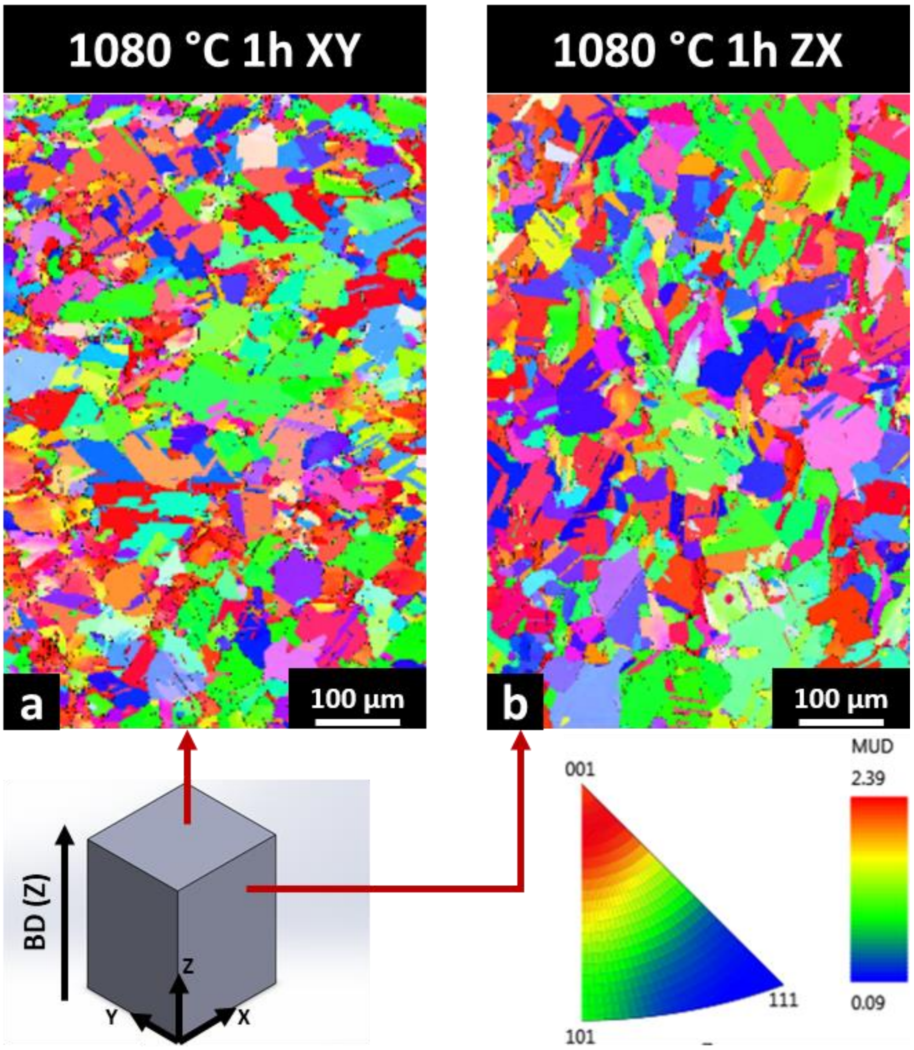

Figure 66: EBSD maps of the annealed 1080 °C IN625 on the (a) XY plane and (b) ZX plane

The EBSD map of the XY plane with the HAGB in Fig.67a reveals the TGB presence, mostly concentrated on the bigger grains: the portions characterized by the presence of small grains are instead decorated with the remaining LAGB (green surrounded in Fig.67b), indicating that these areas are not completely recrystallized. From the graph in Fig.67c can be seen that the LAGB content is significantly dropped down, while the HAGBs are increased in fraction, as well as, the TGBs at 60° that have become the dominant fraction with a value above the 30%.

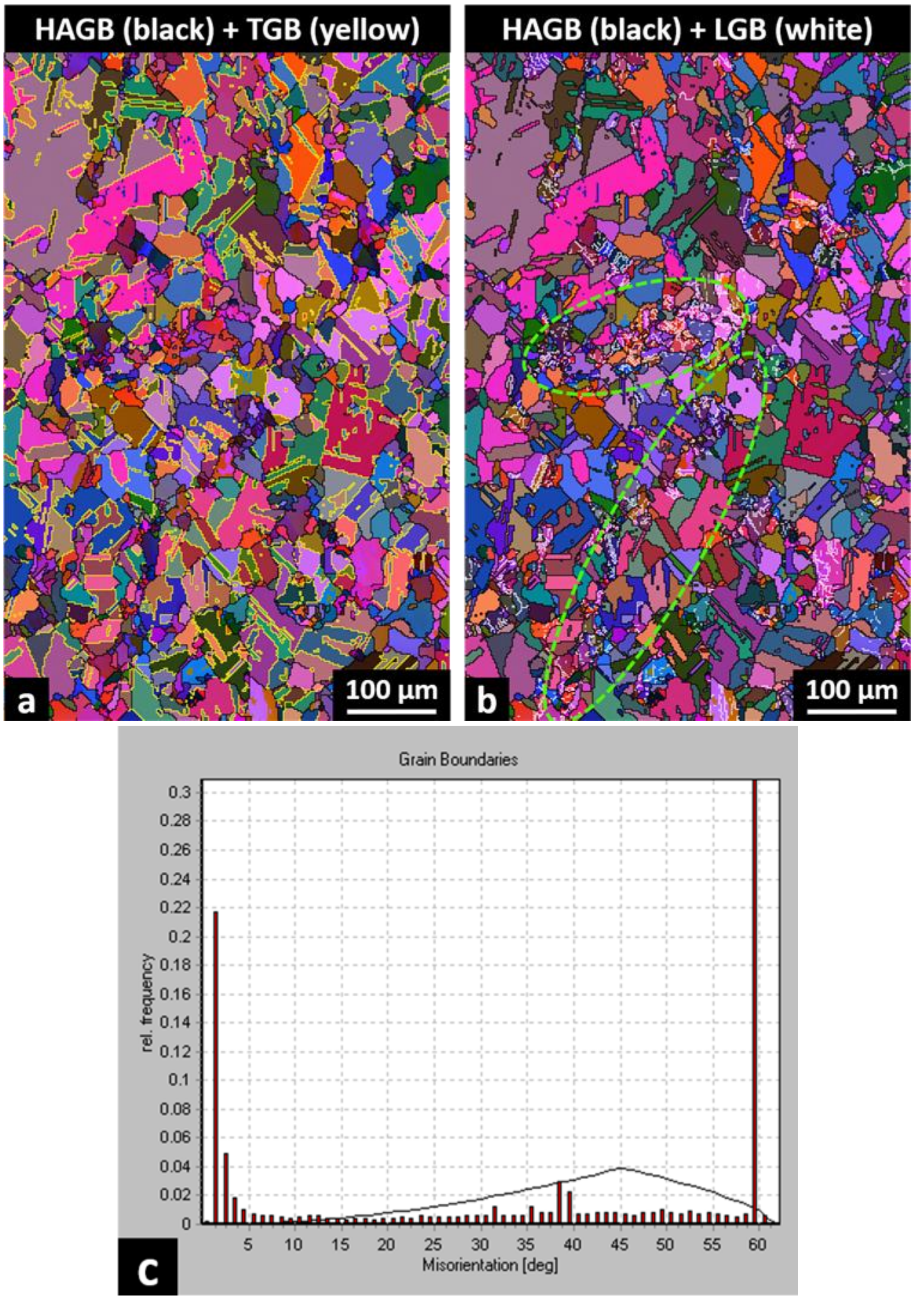

Figure 67: ZX plane (a) HAGB in black, (b) LAGB in white and (c) frequency % of grain boundaries misorientation for the 1080 °C 1 hour annealing

The EBSD maps performed on the ZX plane (Fig.68a and b) reveals also on this case the TGB presence and a small fraction of LAGB grouped in some areas. The graph in Fig.68c reports a fraction % of the different grain boundaries type simile to the one found in the XY plane. This can be easily noticed from the graph in Fig.69, where can be also seen that the total amount of LAGB and TGB are similar with values slightly above 30%.

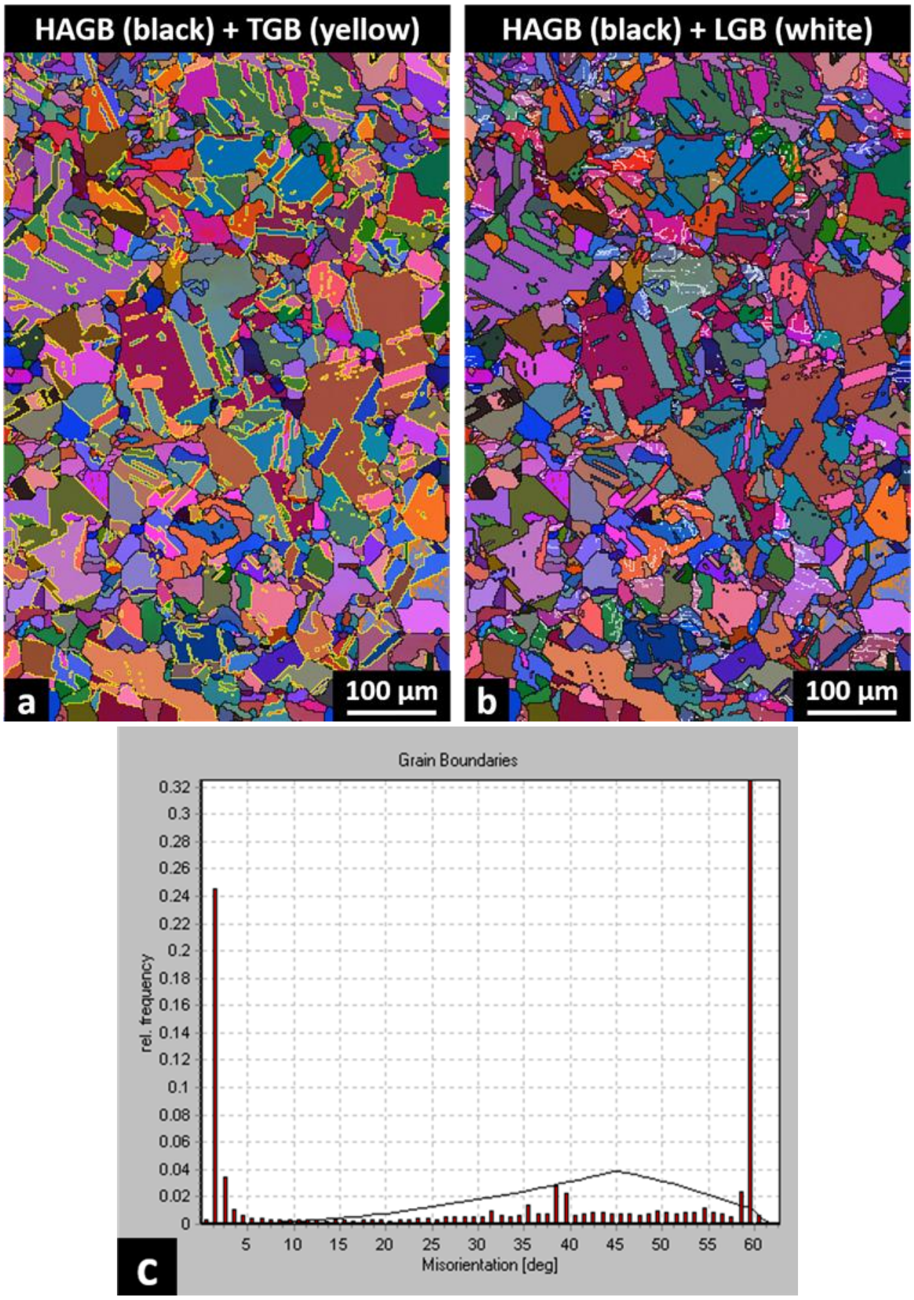

Figure 68: XY plane (a) HAGB in black, (b) LAGB in white and (c) frequency % of grain boundaries misorientation for the 1080 °C 1 hour annealing

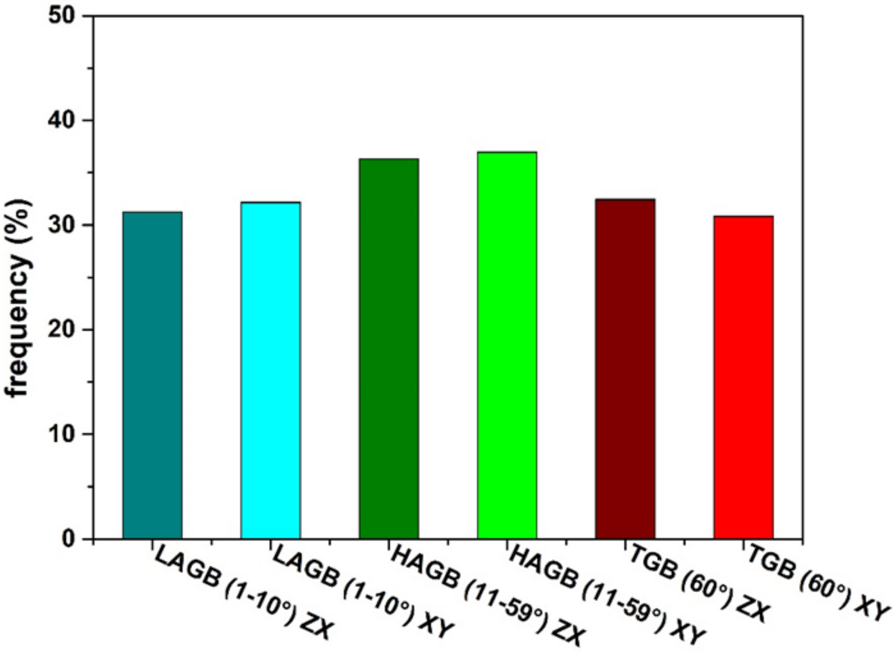

Figure 69: Comparison between the XY and ZX misorientation angle types frequency for the 1080 °C annealed state

Annealed 1080 °C 1h Mechanical properties: tensile test

Fig.70 and Table.22 summarize the tensile behaviour of the LPBF IN625 after the 1080 °C annealing treatment. Compared with the previous conditions the alloy shows a marked reduction of the YS (more pronounced for the XY samples) and of the UTS. The ductility, however, is increased, reaching 50%. The tensile properties of the Z and the XY samples are very similar due to the presence of equiaxed grains coupled with the TGB which help to reduce the anisotropy typical of the as-built state.

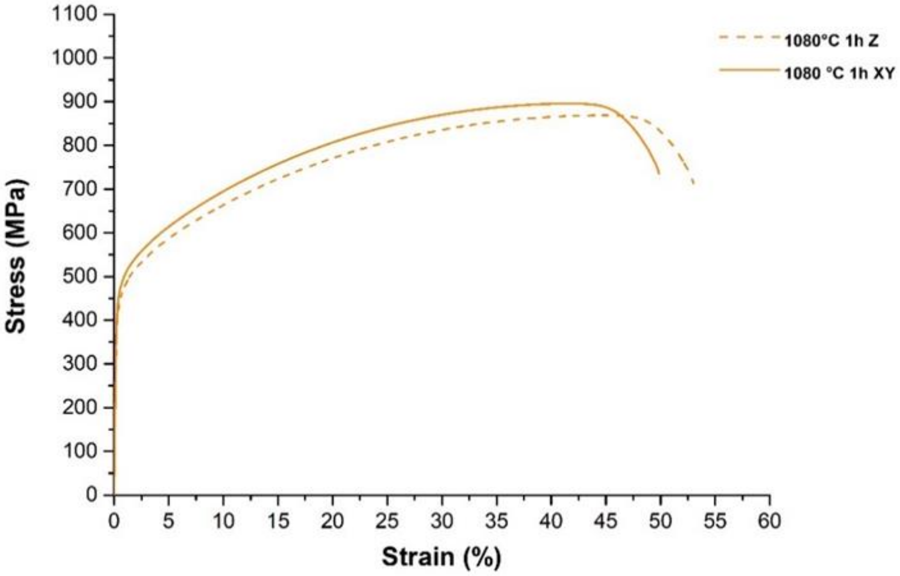

Figure 70: stress/strain curve for the 1080 °C annealed IN625 tensile samples

Table 22: Annealed at 1080 °C 1 hour IN265 tensile properties

IN625	YS (MPa)	UTS (MPa)	El (%)
1080 °C 1 hour XY	451 ± 1	896 ± 1	50.9 ± 1.5
1080 °C 1 hour ZX	430 ± 6	867 ± 2	52.8 ± 0.3

The fracture analysis (Fig.71a and b) revealed a complete ductile fracture, as pointed out by the micro dimples and the voids. At lower magnification some unmelted powders are detected, and they are probably the fracture starting point.

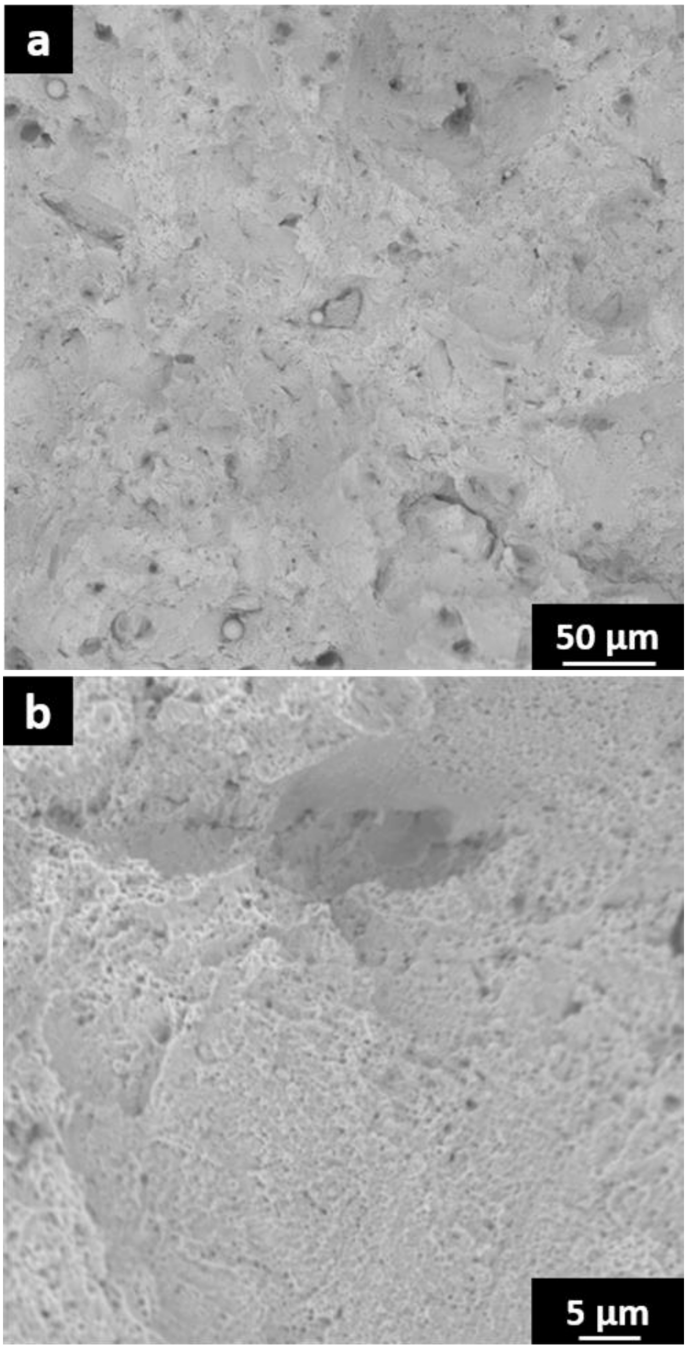

Figure 71: SEM images of the (a) 1080°C annealed IN625 fracture surface, (b) and higher magnification image

3.1.1.5 IN625 Solutionized condition

The solution treatment applied to the alloy resulted in a microstructure similar to the one seen for the annealing temperature of 1080 °C, with recrystallization leading to grains with equiaxial shape and twin grain boundaries formation. The grain dimension reached up to 140 µm, and also in this condition, there is the presence of small grains (Fig.72, red rounded).

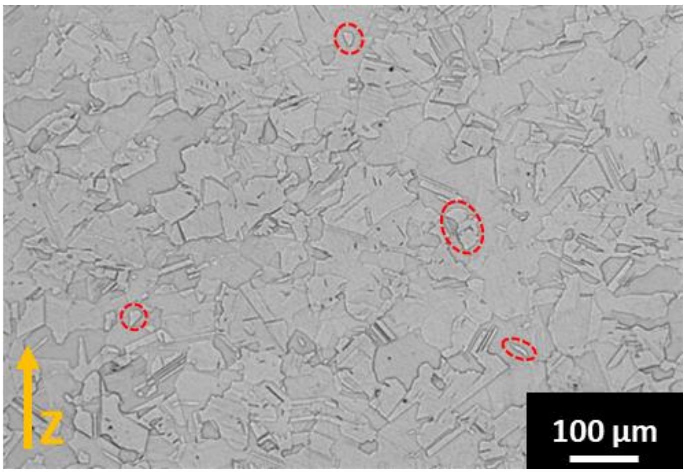

Figure 72: OM of the solutionized LPBF IN625 (1150 °C one hour)

Solutionized Microstructure: Scanning Electronic Microscopy (SEM)

SEM investigation (Fig.73a and b) did not found large carbides, but only very fine sub-micrometric carbides with dimension mainly comprised between 20 and 400 nm (Fig.73b, red arrows). Usually, the carbides with higher dimension are located in the grain boundaries. The TEM analysis performed in a previous work [63] identified these carbides as MC carbides rich in Nb and Mo. Other work in literature found the presence of micrometric carbides after solution at 1150 °C for 1 hour followed by air cooling [110] and the formation of $M_{23}C_6$ after recrystallization [95]. The differences with these works can be explained taking in account the differences in heat treatments performed (treatment time, temperature, cooling rate) and in the chemical composition of the powder used, which can lead to different precipitation paths [3,114].

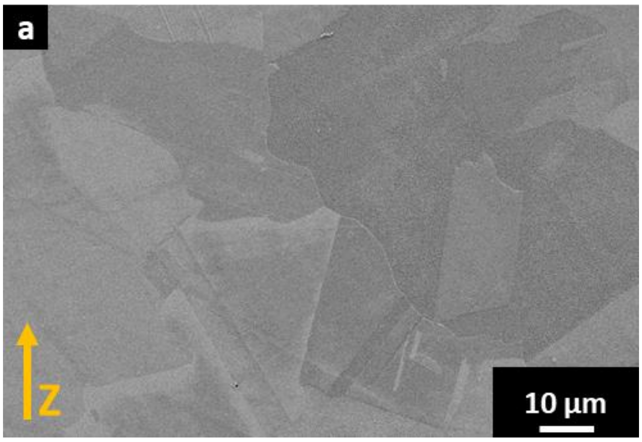

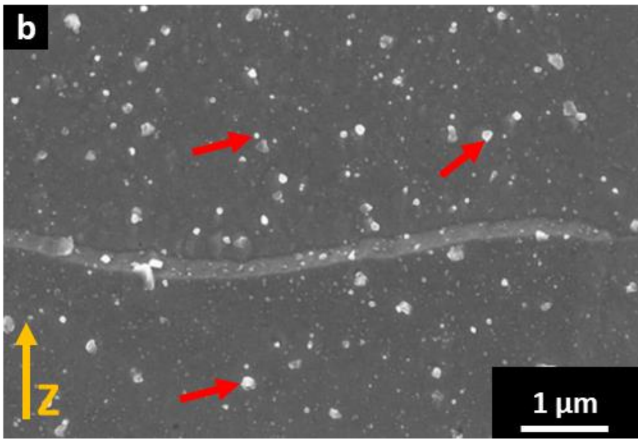

Figure 73: SEM images of the solutionized IN625 and (b) further magnified section at the grain boundary

Solutionized Texture: Electron BackScatter Diffraction (EBSD) analysis

The grain orientation of the XY plane in the maps in Fig.74 show equiassic grains, but this time there are no signs of the laser scan track, as well as in the ZX plane, indicating the complete occurrence of the recrystallization.

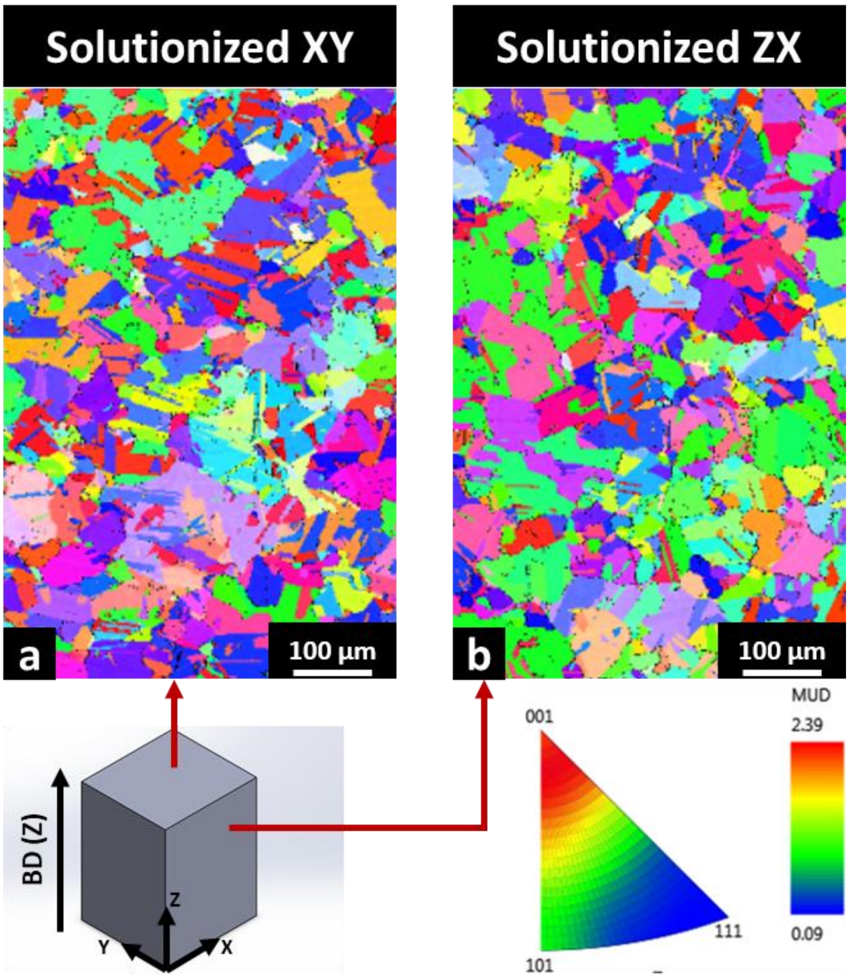

Figure 74: EBSD maps on the (a) XY and (b) ZX planes of the solutionized IN265

The XY plane HAGB map in Fig.75a shows the outstanding presence of TGB presence, well distributed on the plane. The LAGB instead are only present in some isolated spot. The graph in Fig.75c reports a fraction of TGB above 55%, with less than 1 % of LAGB.

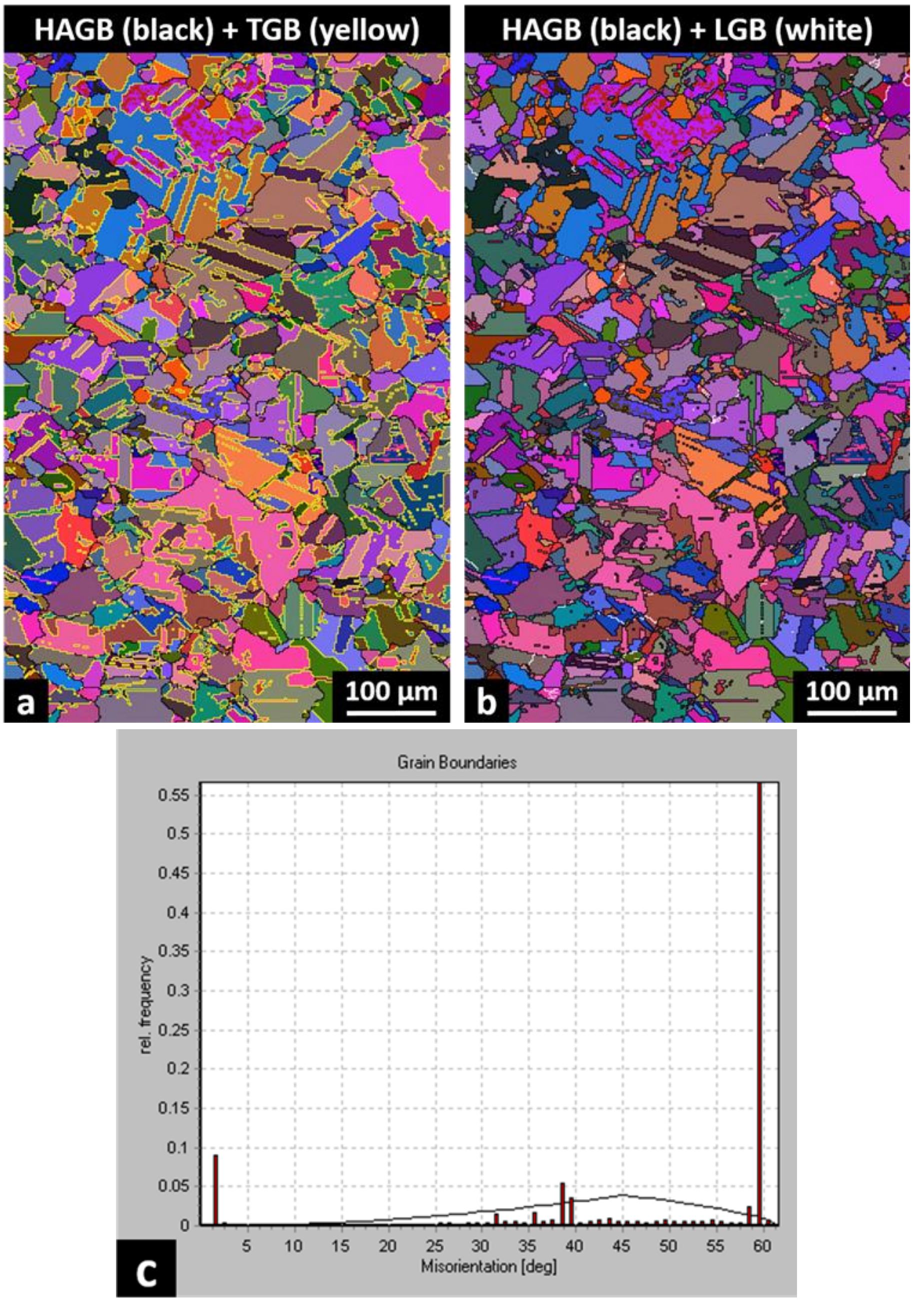

Figure 75: XY plane (a) HAGB in black, (b) LAGB in white and (c) frequency % of grain boundaries misorientation for the solutionized IN625

The findings on the ZX plane (Fig.76) are the same found in the XY plane, with minimal deviation between the two planes (Fig.77), showing the complete recrystallization of the alloy.

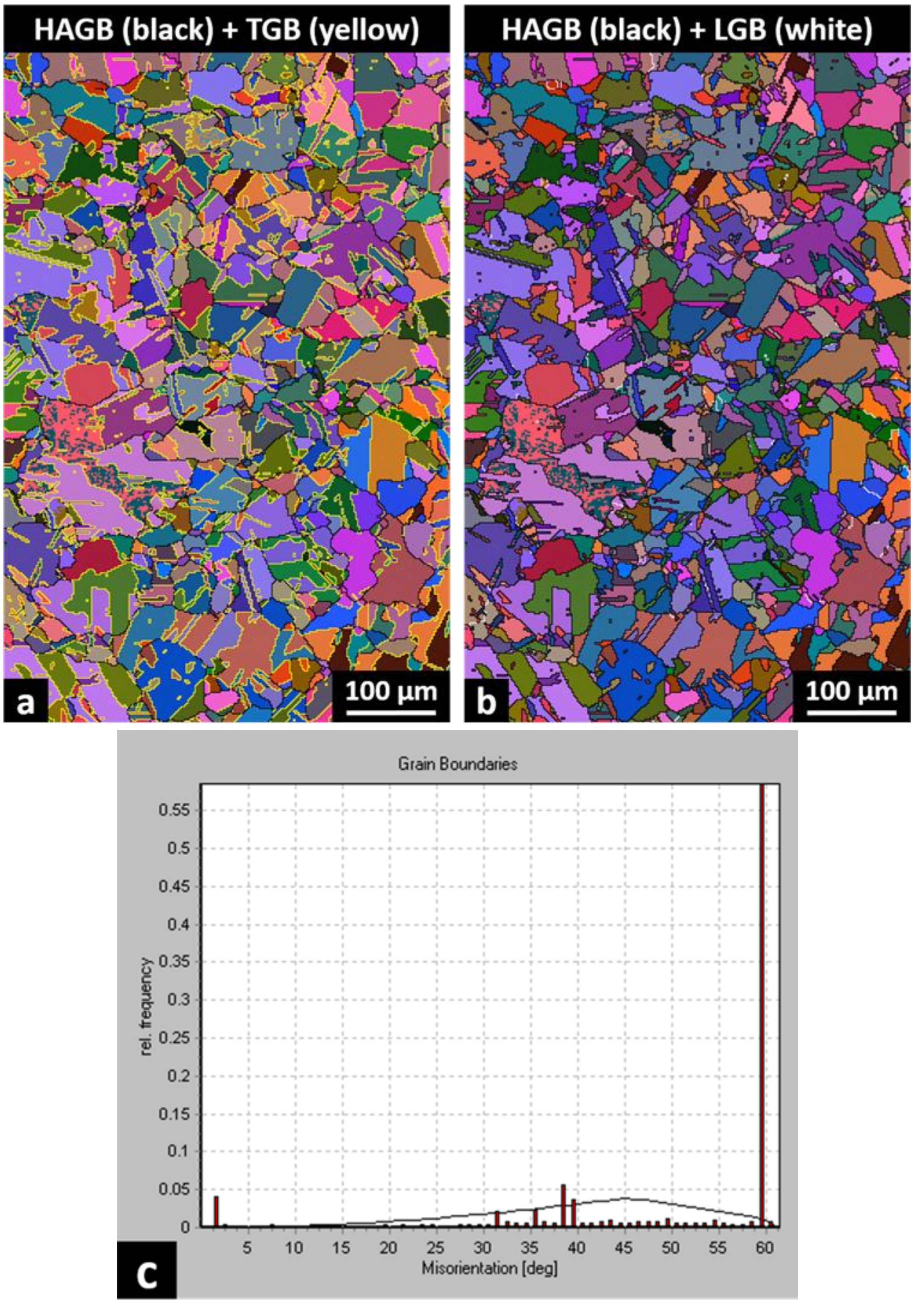

Figure 76: ZX plane (a) HAGB in black, (b) LAGB in white and (c) frequency % of grain boundaries misorientation for the solutionized IN625

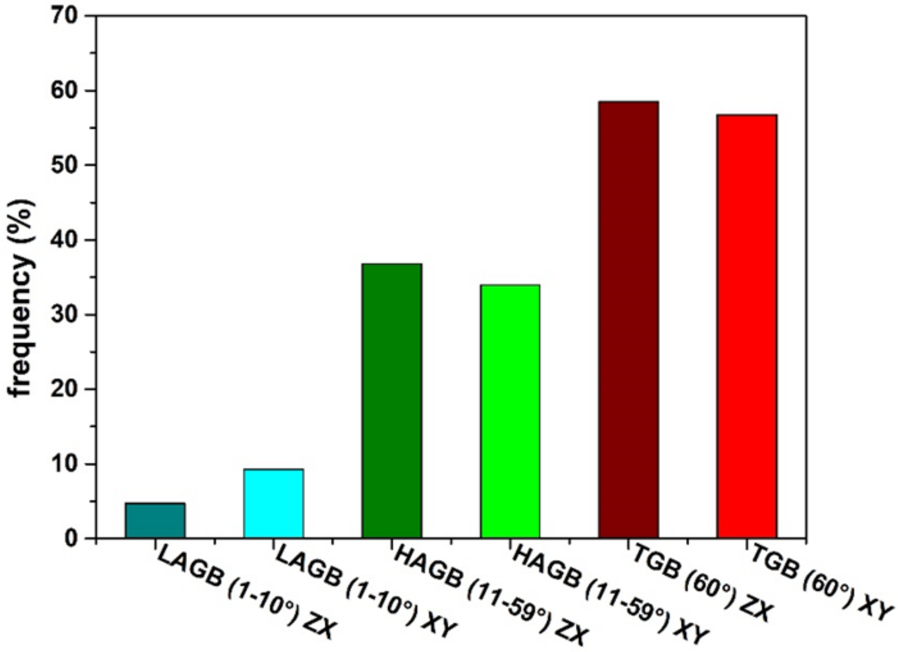

Figure 77: Comparison between the XY and ZX misorientation angle types frequency for the solutionized state

Solutionized Mechanical properties: tensile test

The tensile test results (Fig.78 and Table.23) confirm the loss of the anisotropy of the alloy, showing nearly identical properties for XY and ZX direction samples. The YS and UTS are the lowest of all the conditions seen until now, while the ductility is the highest. The reason behind this behaviour is probably the reduction the LAGB, as well as the small dimension and minimal concentration of secondary phases.

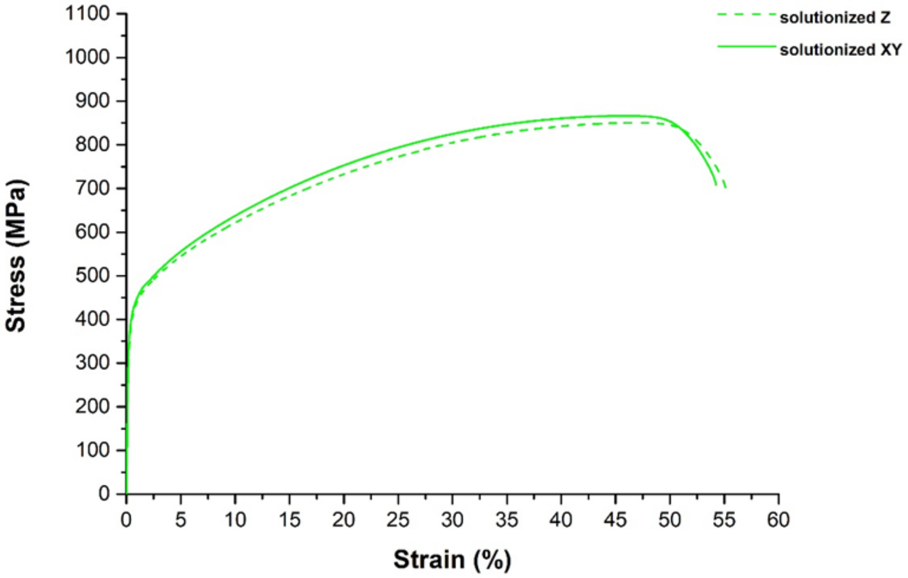

Figure 78: stress/strain curve for the solutionized IN625 tensile samples

Table 23: solutionized IN625 tensile properties

IN625	YS (MPa)	UTS (MPa)	El (%)
solutionized XY	396 ± 9	883 ± 15	54.9 ± 1.2
solutionized ZX	379 ± 9	851 ± 3	54.5 ± 1.1

As for the 1080 °C condition, the fracture is of the ductile type, as expected from a condition fully solutionized (Fig.79).

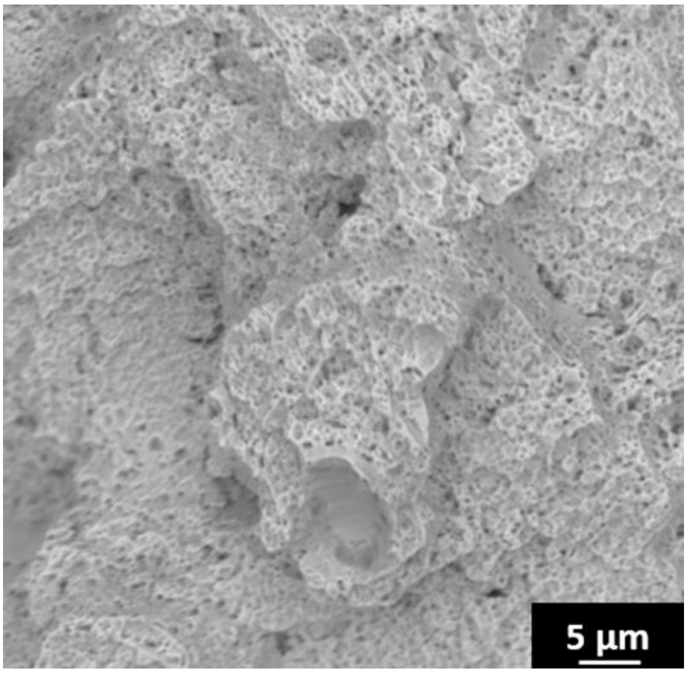

Figure 79: fracture surface of the solutionized sample

3.1.2 TMA analysis

In order to obtain a greater understanding of the phenomena that occurs during the various thermal exposures, a TMA analysis was performed on an LPBF as-built IN625 sample and for comparison also on a sample solutionized. The results of these analyses are reported in Fig.80. The first peak found on both conditions is the peak of the **γ''** phase (metastable Ni_3Nb coherent btc phase, disk-shaped formed on the {100} planes [2,3,11]), the reinforcing phase formed during the ageing treatments. It is possible to see that for the as-built sample the precipitation onset is located to lower temperature, and the overall peak is wider for the solutionized samples, indication of a greater precipitation range, probably due to the presence of Nb segregations in the as-built condition, which accelerate the γ'' formation thanks to the local increased of Nb concentration. On the other hand, the solutionized condition possesses a shorter precipitation range, located at higher temperature compared to the as-built. Moreover, at the end of the precipitation peak the true alpha value is consistently higher value compared with the as-built value, which can be explained with a greater impact of the precipitation on the microstructure: the as-built forms **γ''** consuming the Nb present in the segregations, meanwhile in the solutionized condition **γ''** precipitates using the Nb dissolved in the matrix (as better explained in the XRD section). The second peak is located near to the 870 °C annealing temperature. According to the TTT diagram of the IN625 at this temperature is stable the **δ** phase, which can be formed by the coalescence of the **γ''** or directly from the matrix. Interestingly the baseline curves show opposite directions for the two conditions of the alloy. This can be due to differences in the **γ''** content and distribution between the two states, as well as, the presence of the segregations and dendritic structures only in the as-built condition, that tend to be dissolved during precipitation and **δ** growth. This is the last noticeable peak for the solutionized sample. Moving on the as-built is found a peak centred at 980 °C, one of the annealing temperatures used in this study. Since this temperature was characterized by the absence of **δ**, so the peak is probably due to the dissolution of **δ** phase in the matrix. The last peak is located at the last annealing temperature used, 1080°C, pointing out that it is related to the recrystallization phenomenon. In order to check this theory a fourth annealing temperature, located at the initial part of the recrystallization peak was studies, 1030 °C for one hour.

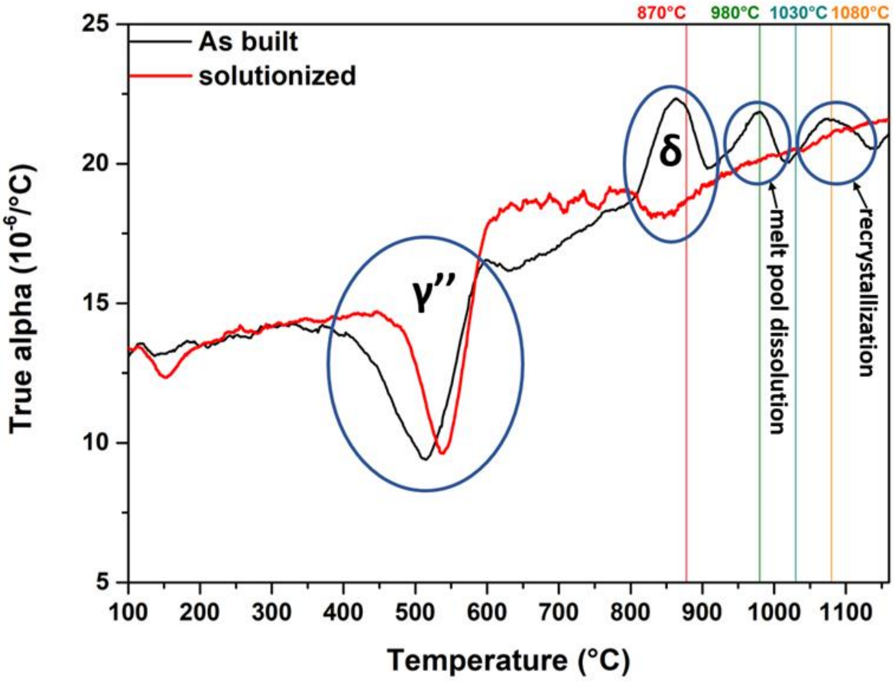

Figure 80: TMA results for the as-built and solutionized conditions

The EBSD maps in Fig.81 prove that the heat treatment at 1030 °C is enough to trigger the recrystallization of the microstructure, removing the elongated grains appearance from the ZX plane.

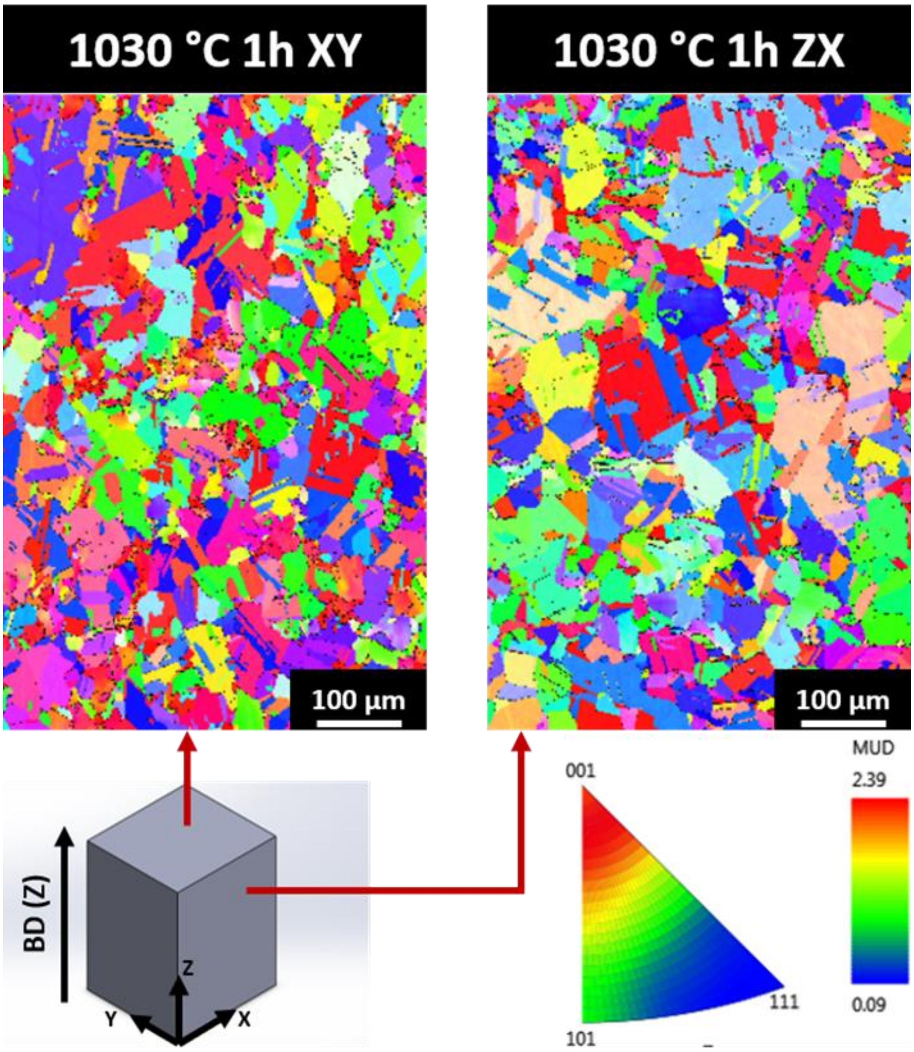

Figure 81: EBSD maps on the (a) XY and (b) ZX planes of the 1030 °C annealed IN265

The EBSD maps in Fig.82 and Fig.83 show that the grain boundaries result to be similar to the 1080 °C annealed IN625 (Fig.68 and Fig.69), with TGB formation and a drastic reduction of the LAGB (green rounded in Fig.82b), which the remains are located in correspondence of small grains that resemble the laser scan tracks. Both % fraction/ misorientation angle graphs (Fig.82c and Fig.83c) show that the 2° and 60° fractions are similar, with the exception of the ZX plane where the 2° content is lower than the 60° fraction of a 4 %.

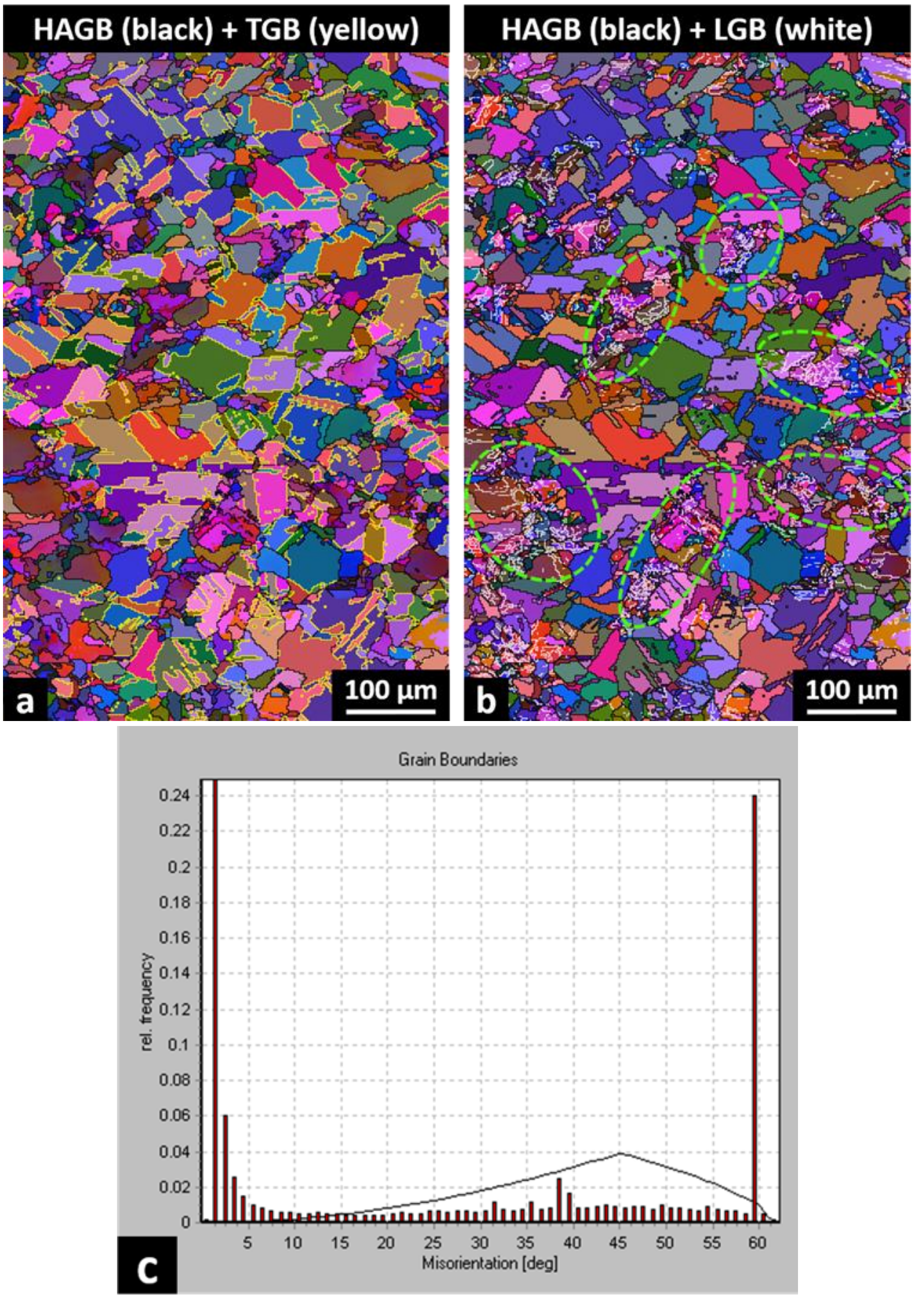

Figure 82: XY plane (a) HAGB in black, (b) LAGB in white and (c) frequency % of grain boundaries misorientation for the 1030 °C annealed IN625

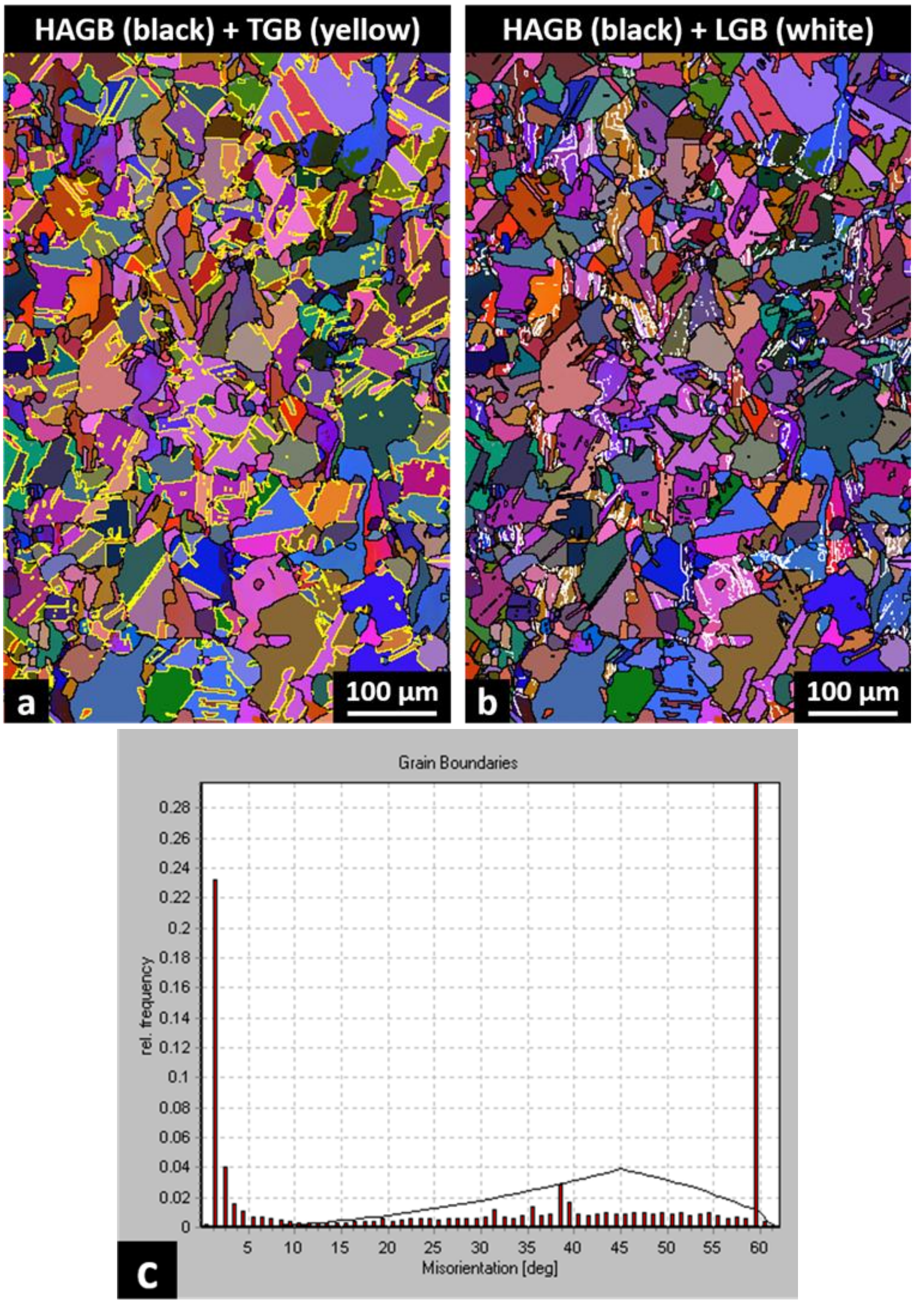

Figure 83: ZX plane (a) HAGB in black, (b) LAGB in white and (c) frequency % of grain boundaries misorientation for the 1030 °C annealed IN625

The graph in Fig.84 summarizes these results, pointing out that, differently from the 1080 °C annealed state, the total amount of LAGB is greater than the TGB content, indicating that the recrystallization level after 1 hour at 1030 °C is lower compared to the recrystallization level after 1 hour at 1080 °C.

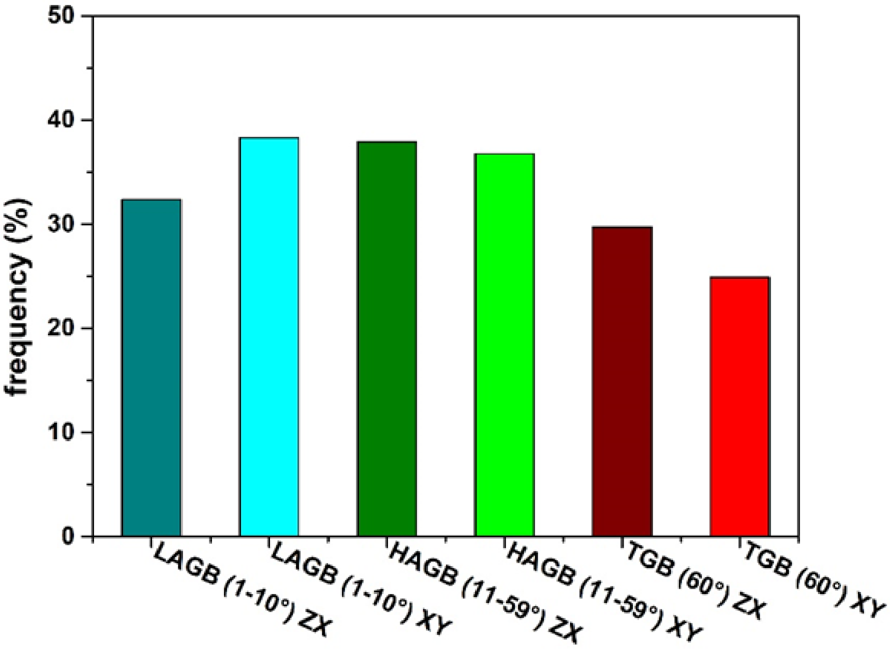

Figure 84: Comparison between the XY and ZX misorientation angle types frequency for the 1030 °C annealed IN625

3.1.3 XRD analysis

Analysing the XRD diffractograms obtained from the different conditions considered in this work, it is possible to evaluate the lattice constant of γ matrix of the IN625 alloy, in order to obtain data on the effects of the annealing treatments on its homogenization. This is because during the homogenization, the Nb and Mo dispersed in the alloy in form of segregations are dissolved in the matrix, increasing the lattice parameter, since they possess a greater atomic size than Ni. At the same time can also happen that precipitates like **γ''**, **δ** and carbides are formed during the high-temperature exposures, removing these elements from the matrix and reducing the lattice parameter [95,108]. In order to reduce the error in the lattice parameters evaluation, the Nelson-Riley method was applied [87,115].

The results of this analysis are reported in Fig.85. The first annealing temperature applied, 870 °C for 1 hour is characterized by a greater lattice constant compared with the as-built condition, indicating that the segregation dissolution effect on the lattice parameter is more important than the reduction caused by the carbides and **δ** phases precipitation. Raising the annealing temperature to 980 °C produced further increment in the lattice parameter, due to the δ dissolution, as well as, an increased segregations reduction. The increment continued also in the treatment at 1080 °C, due to the absence of dendritic structures and phases different from carbides, indicating greater homogenization.

However, the solutionized condition exhibited the maximum value of the lattice parameter, revealing a very homogeneous level of chemical composition, with the matrix and only sub-micrometric MC carbides, which requires temperature superior than 1200° C in order to be dissolved [3].

The value obtained for this condition, 3.607±0.002 Å is comparable to the value of the traditional solution annealed IN625 found by Rai et al., which is 3.609 Å [116].

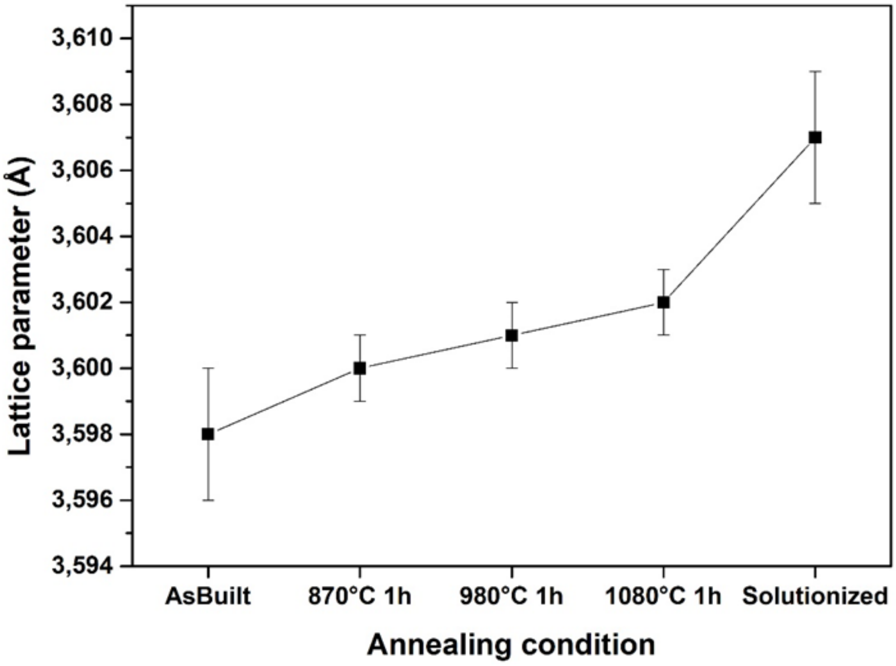

Figure 85: lattice parameter of the γ matrix in the LPBF IN625 alloy at different annealing conditions

3.1.4 Results summary of annealing treatments

The results on the study of heat treatments on LPBF IN625 revealed that the choice of the annealing temperature is critical for both resulting microstructure and mechanical properties.

The treatment at 870 °C promotes the **δ** phase precipitation and a small segregations dissolution. From the grains point of view, this treatment does not induce recrystallisation, but slightly reduces the LAGBs fraction.

Increasing the temperature to 980 °C does not cause the **δ** precipitation, in fact, only some carbides formation or growth occurs and it reduces the LAGBs content without producing appreciable recrystallization in the alloy.

1030 °C and 1080 °C annealing treatments allow partial recrystallization to occur, removing the grain texture and a big part of the LAGBs.

At the end the solution treatment was the one which led to complete recrystallization and homogenization of the alloy, removing almost completely the LAGBs and the segregation and secondary phases, except for the sub-micrometric carbides.

As reported in Fig.86, increasing the annealing temperature led to a slight reduction of LAGBs until 1030 °C, where the recrystallization begins. From that point, a large portion of LAGBs is removed and replaced with HAGBs and TGBs. The last category becomes largely dominant in the solutionized state, where there are almost no LAGBs left.

The effect on the increased annealing temperature on the mechanical properties, summarized in Fig.87 and Table.24 is the progressive reduction of the YS and of the UTS and the increment of the ductility. XY samples are characterized by higher resistance and lower ductility compared to the Z samples, but the increased annealing temperature led to a reduction of the anisotropy in the mechanical properties, as in the case of the solutionized samples that had nearly identical properties in both orientations. The as-built condition possesses YS and UTS compatible with other studies present in literature [19,81,106] in both the directions. The as-built, stress relived at 870 °C and the annealed at 980 °C conditions in both directions satisfy the requirement for the wrought grade 1 alloy, and all the conditions characterized in this work satisfy the requirement for the wrought grade 2 IN625 and the LPBF ASTM F3056-14.

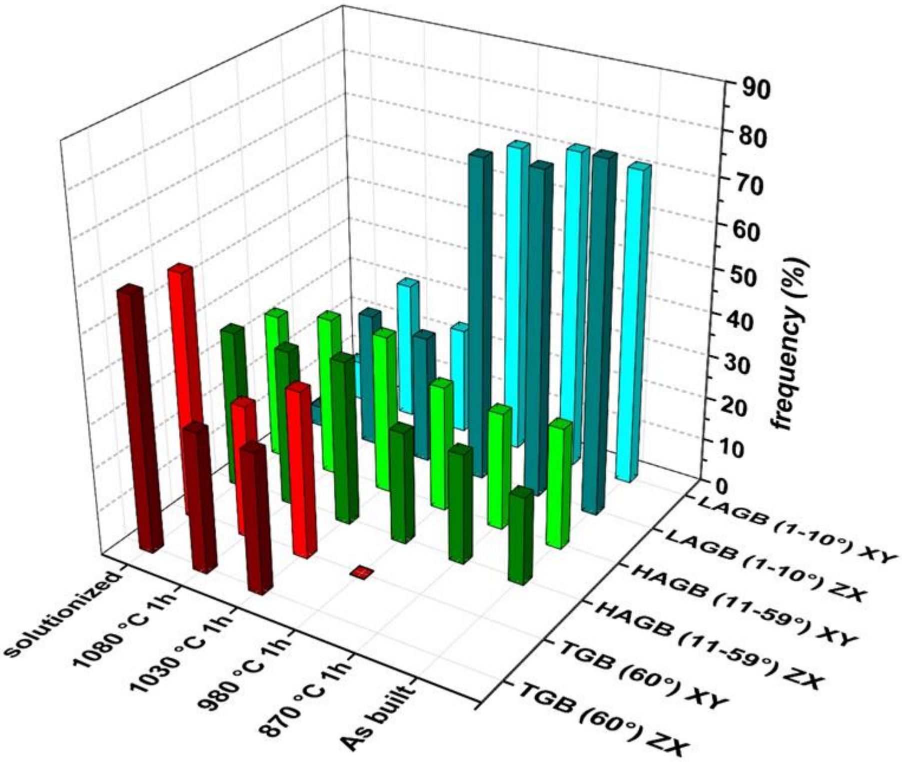

Figure 86: EBSD results on the grain boundary types fractions

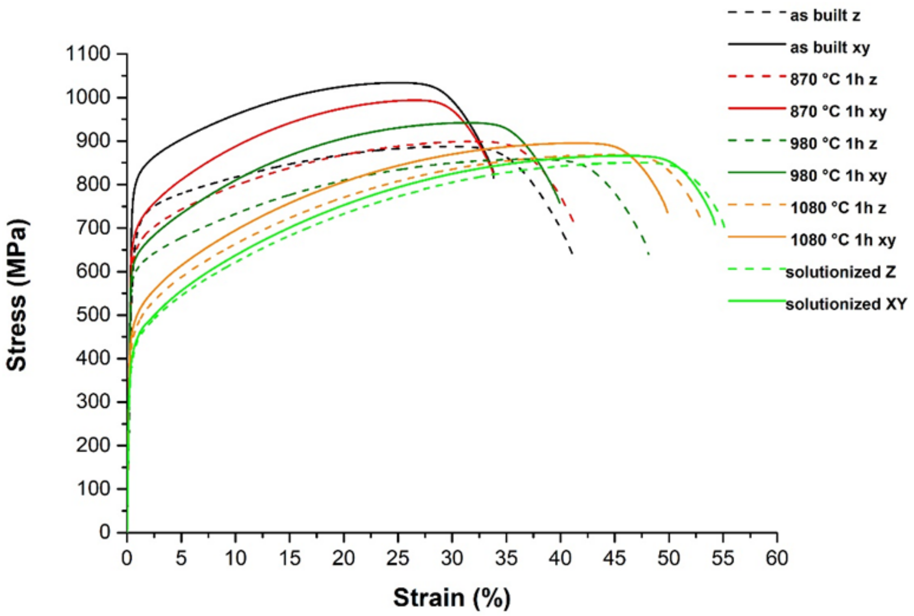

Figure 87: stress/strain curves of all the conditions

Table 24: Summarizing table of the mechanical properties of the annealed LPBF IN625

	YS (MPa)	UTS (MPa)	El (%)
	This work		
as-built XY [63]	783 ± 23	1041 ± 36	33.1 ± 0.6
as-built ZX [92]	618 ± 33	891 ± 5	40.7 ± 0.5
870 °C 1 hour XY [92]	667 ± 3	996 ± 3	35.8 ± 1.8
870 °C 1 hour ZX [92]	622 ± 6	900 ± 3	40.9 ± 1.7
980 °C 1 hour XY [92]	612 ± 5	948 ± 8	39.8 ± 0.1
980 °C 1 hour ZX [92]	579 ± 5	854 ± 4	47.6 ± 0.6
1080 °C 1 hour XY [92]	451 ± 1	896 ± 1	50.9 ± 1.5
1080 °C 1 hour ZX [92]	430 ± 6	867 ± 2	52.8 ± 0.3
solutionized XY [63]	396 ± 9	883 ± 15	54.9 ± 1.2
solutionized ZX [92]	379 ± 9	851 ± 3	54.5 ± 1.1
	Literature		
as-built xy [106]	642 ± 23	879 ± 2	30 ± 2
as-built z [81]	615 ± 50	900 ± 50	42 ± 5
as-built xy [81]	725 ± 50	990 ± 50	35 ± 5
as-built XY [19]	800 ± 20	1030 ± 50	8–10
as-built Z [19]	720 ± 3	1070 ± 60	8–10
Wrought IN625 [19]	517	930	40
As-rolled [18]	414 - 758	827 - 1103	30 – 36
Wrought IN625 grade 1*	>414	>827	>30
Wrought IN625 grade 2**	>276	>690	>30
LPBF ASTM F3056-14	275 (min.)	485 (min.)	30 (min.)

**ASTM B443 (minimum annealing temperature 871 °C)*

***ASTM B443 (minimum solution annealing temperature 1093 °C)*

3.2 IN625 Oxidation properties

Since IN625 alloy is characterized by excellent strength at high temperature including outstanding corrosion and oxidation resistance [63,64,93,110], it is often applied in harsh work conditions.

For this reason, the IN625 oxidation performance has been extensively investigated in the literature, for instance, for applications such as steam turbine and fuel cells (SOFC) [117–122].

However, LPBF IN625 possess a very particular microstructure out of equilibrium, and during thermal exposures it is subjected to different microstructure evolution compared to the IN625 processed by traditional technologies, which can lead to a different oxidation behaviour.

However, to the authors' knowledge, there is no literature about the oxidation properties for the LPBF produced IN625, but only some study on the corrosion properties [123,124].

In this work, the oxidation behaviour of the as-built and solution annealed LPBF IN625 conditions are compared.

At the beginning of this work an explorative thermal gravimetry analysis (TGA) in air was performed on both conditions, in order to identify possible different oxidation regimes. The results of the TGA are reported in Fig.88. Both conditions show a constant mass gain up to ≈950 °C, and after that temperature the mass gain is characterized by an acceleration. The as built sample shows a slightly greater mass gain compared to the solutionized specimen. In order to investigate the initial stage of the first oxidation regime, the temperature of 900 °C was selected.

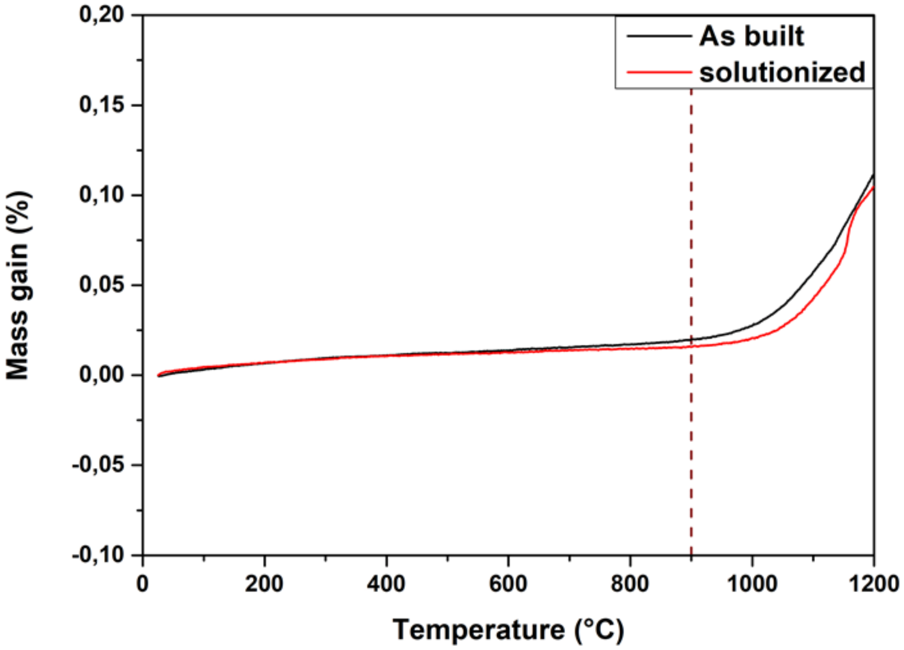

Figure 88: TGA on the LPBF as built and solutionized IN625

3.2.1 Mass gain over the time and oxide thickness evolution

Samples oxidized in air for different times showed mass gains (Fig. 89). The mass gain of the two conditions considered is almost the same in the initial part of the graph, up to 48 hours of oxidation. For the following oxidation times up to 96 hours the as built mass gain slows down, following a parabolic path, indicating that the oxide is passivating the alloy. Differently, the solutionized condition did not slow down the oxidation, revealing an almost constant increment in mass, and it did not seem to possess a protective oxide. The high deviations of the samples oxidized for 8 hours are due to the small mass gain of the samples, that was comparable with the scale sensibility.

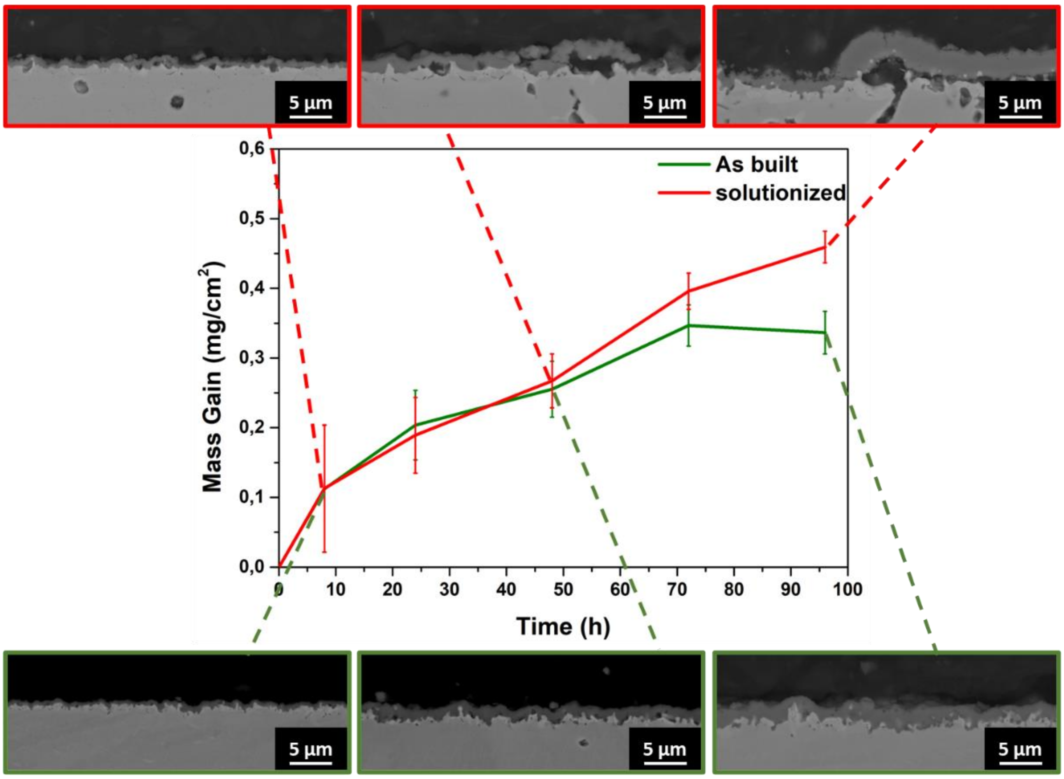

Figure 89: Mass gain evolution of as built and solutionized oxidized samples

Under the assumption of a compact, continuous and adherent oxide layer, it is possible to calculate the oxidation constant (**K$_P$**) of the as built and the solutionized conditions, approximating a parabolic behaviour, applying the following equation [125]:

$$\left(\frac{\Delta w}{A}\right)^2 = K_p * t \tag{8}$$

The equation term **Δw** represent the mass gain during the oxidation, **A** (cm^2) represent the external area of the sample and **t** (h) is the oxidation time [126].

The obtained **K$_P$** (mg^2*cm^{-4}*h^{-1}) is useful for the comparison of the two conditions, as already applied in the literature for IN625 alloy and other superalloys [125,127]. As reported in Fig.90, the solutionized condition is divided in two parts, due to the change of the behaviour after 48 hours. For this reason, two **K_p** are reported, one representative of the first oxidation stage and one for the second part. The resulting **K_p** are reported in Table.25 and compared with some result found in literature.

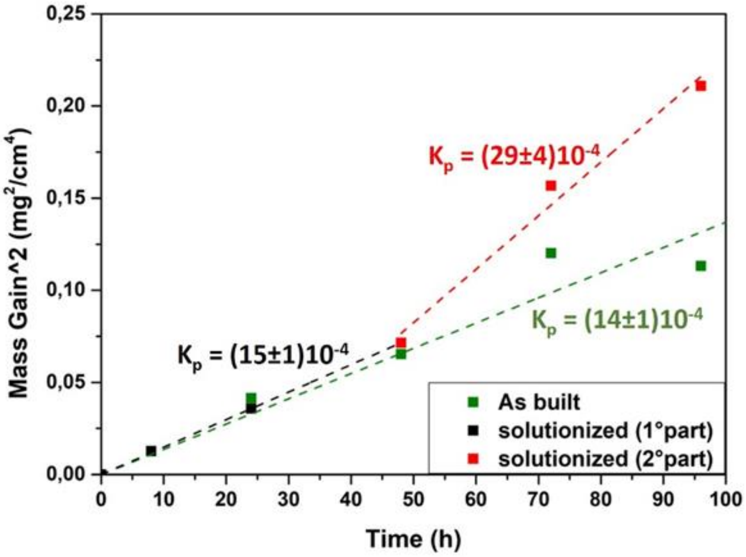

Figure 90: square mass gain of the oxidized as built and solutionized samples of LPBF IN625

Table 25: K_p of IN625 oxidized in air in this work and in literature

IN625 condition	Oxidation T [°C]	Oxidation type	K_p [mg^{2}cm^{-4}h^{-1}]
		This work	
LPBF as-built	900	Static furnace	(14±1)E-4
LPBF solutionized (1° stage)	900	Static furnace	(15±1)E-4
LPBF solutionized (2° stage)			(29±1)E-4
		Literature	
LMD (Hong)[128]	800	Cyclic oxidation	19.97E-2
Commercial (N'Dah)[122]	900	Cyclic oxidation	2E-3
Commercial (Buscail)[121]	900	TGA (air, 3% H_2O, 1.2 L/h)	1,15E-3

The **K_p** of the as built condition has a value of (14±1)E-4, similar to the first stage of the solutionized state, which possesses a **K_p** of (15±1)E-4. This value raises up to (29±1)E-4 for the solutionized condition, while remains constant for the as built condition. Hong et al. evaluated the **K_p** at lower temperature (800 °C) of Laser Metal Deposition (LMD) IN625, finding a value of 19.97E-2 [128], higher compared with the values obtained in this work at 900 °C. Since **K_p** value grows increasing the temperature due to the increased diffusivity [129], a lower **K_p** at higher temperature indicates that the oxidation performances of the IN625 conditions studied in this work are superior compared to LMD IN625, and also to conventional produced IN625 according to the works of N'Dah and Buscail, (Kp 2E-3 and 1,15E-3 respectively) obtained in similar conditions [121,122].

For the as built and solutionized conditions, the layer thickness evolution during the oxidation at 900 °C is reported in Fig.91. The behaviour of the oxide thickness follows the one found for the mass gain, with a similar increment up to 48 hours, followed by a small growth for the as built condition and a consistent increment for the solutionized state. It is easy to see that the standard deviation of the results tends to increase with the extension of the oxidation time, and for the solutionized samples the deviation is consistently higher compared to the as built condition. This is an indication of a less uniform oxide layer for the solutionized condition, as can be seen in Fig.91 and in Fig.92.

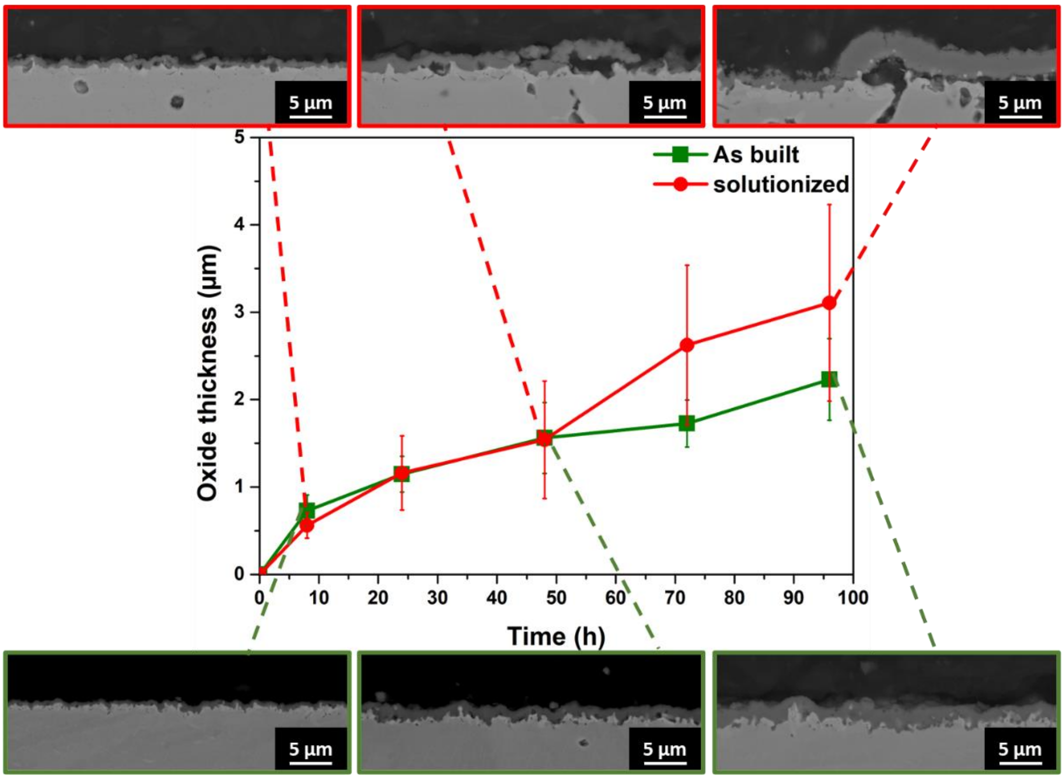

Figure 91: Oxide thickness evolution of as built and solutionized oxidized samples

Fig.92 shows that already after 8 hours of thermal exposure, it is possible to see some differences between the as built (Fig.92a) and the solutionized (Fig.92d) samples. As reported in Fig.91, both oxides are really thin, but the as built oxide shows an adherent, continuous oxide layer, meanwhile the solutionized sample oxide is bended in some point, forming voids between itself and the alloy. After 48 hours the as built (Fig.92b) oxide become thicker compared to 8 hours, but it is still continuous, with some cavities between the layer and the alloy, placed on the top of an intergranular oxidation. The solutionized oxide (Fig.92e) after 48 hours is characterized by an average thickness comparable with the 48 hours as built oxide, also having holes and cavities between the alloy and itself. The presence of these defects is the mainly cause of the high standard deviation in the graph in

Fig.91. Similar features are present after 96 hours of oxidation, with a thick uniform oxide layer for the as built (Fig.92c) and a more defective oxide for the solutionized condition (Fig.92f), with presence of cracks and some big void on the top of the alloy.

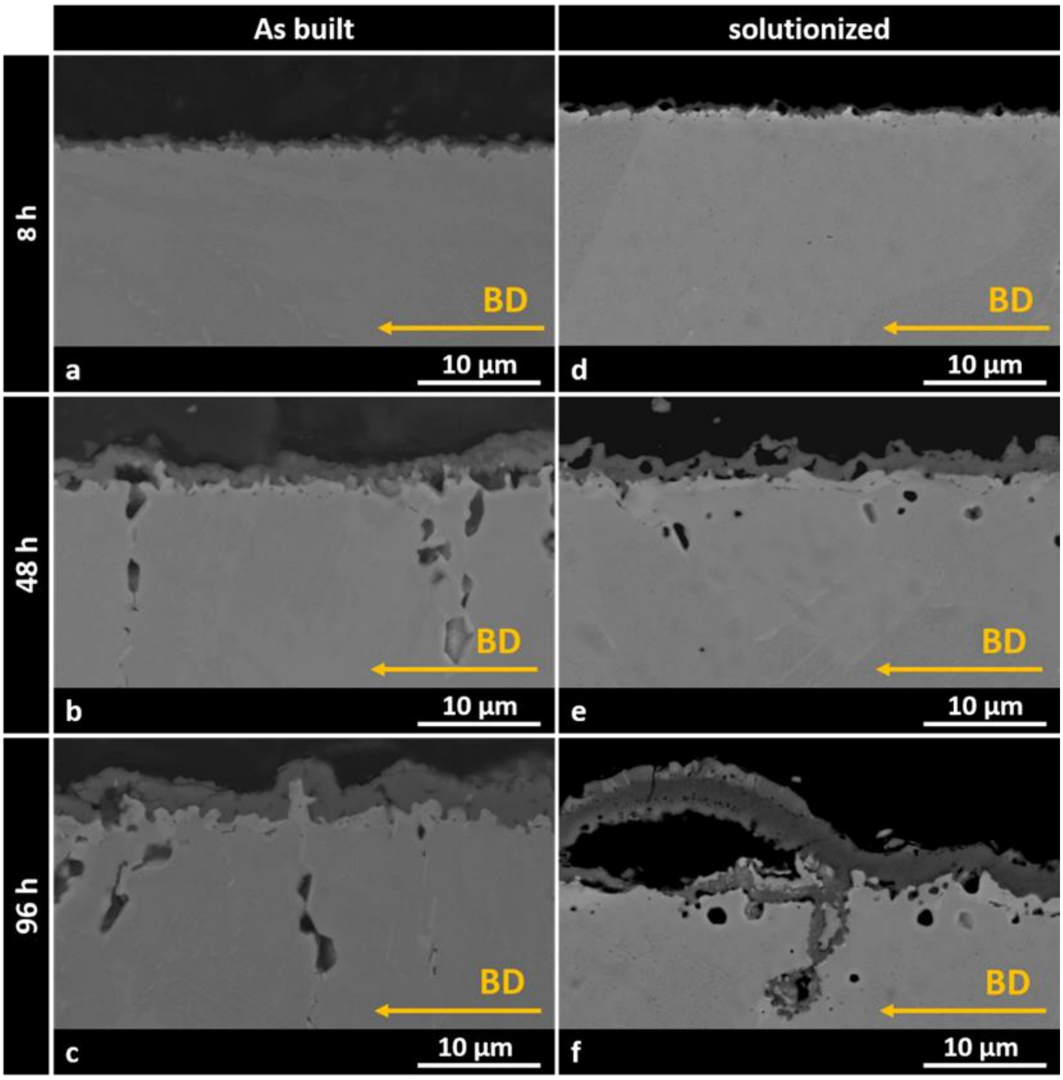

Figure 92: Cross sections of the oxidized as built IN625 after (a) 8h, (b) 48h, (c) 96h and the oxidized solutionized IN265 after (d) 8h, (e) 48h, (f) 96h

3.2.2 Cross section analysis

3.2.2.1 As Built oxidized for 8 hours condition

The oxide formed on the as built IN625 and the microstructure obtained after 8 hours of oxidation treatment are reported in Fig.93a and Fig.93b, respectively.

Fig.93a and Fig.93b have been taken at the same exact position at the same magnification, changing only the contrast. In this way Fig.93a, taken at low contrast, shows the oxide layer, meanwhile Fig.93b, taken at high contrast, reveals the microstructure of the alloy, but in this condition is not possible see the oxide layer.

The oxide layer in Fig.93a appears mostly compact and continuous, with a small hole, indicated by an orange arrow. Moreover, higher magnified image in Fig.93c reveals that the oxide maintains a good adhesion with the alloy, as suggested by the absence of holes between the oxide and the matrix. The XRD pattern in Fig.94 reveals the peaks of the oxide layer which is mainly composed of Cr_2O_3, typically formed for this alloy [117,121,122], together with a minor concentration of TiO_2. These findings are confirmed from the EDS maps reported in Fig.95, where Cr and O are concentrated in the oxide layer and the Ti concentration slightly increases in the oxide.

The EDS map also shows that at the oxide and alloy interface there is a lack of Cr, due to its migration inside the oxide layer. In the same position is present a Nb enrichment, caused by the lack of Cr in that part of the alloy. As reported in literature [130,131], the Nb solubility in Ni alloys increases when the Cr concentration decreases.

The enhanced solubility allows the Nb accumulation under the oxide layer, and this behaviour was already reported in literature by others authors for the traditional produced IN625 [121,130–132].

N'Dah et al. studied the cyclic oxidation at 900 °C of the IN625 alloy, but they performed the EDS map finding a Mo enrichment. The difference in our results can be caused by the different oxidation condition (cyclic vs. simple furnace oxidation) and also by the partial overlap of the Nb and Mo peaks in the EDS analysis, that make it difficult for the EDS to distinguish between Nb and Mo in some cases [132].

The Mo map in Fig.95 did not point out significant enrichments of Mo, confirming that in our case the enrichment is mostly in Nb.

The alloy microstructure under the oxide is characterized by elongated columnar grains aligned with the building direction, as seen in the previous sections and in literature for LPBF Ni alloys [57,63,64,94].

During the oxidation treatment, the thermal exposure allowed the precipitation of **δ**-phases, which appears as bright precipitates in SEM images in Fig 93a and 93c, located both inside the grains (yellow rounded) and along the grain boundaries paths. The **δ**-phases located in the grain boundaries (red arrows) possess a superior length compared to the intragranular **δ**. This is consistent with the findings of the previous sections, where the presence of segregations along grains boundaries [63] provide chemical elements for a major growth of these phases under thermal exposure. The majority of **δ**-phases at the grain boundaries were characterized by a length of around 3 μm.

It is possible to detect **δ** phases right under the oxide layer (Fig.93a and Fig.93c, green arrows), with dimension generally below 1 μm. They probably are formed thanks to the high Nb content caused by the Nb migration towards the oxide layer.

The precipitation of **δ** is also confirmed by the XRD diffractogram (Fig.94) and from the high Nb content found in the EDS maps where those precipitates are located.

Also in this case the **δ** phases precipitation is accelerated according to the TTT diagram for the wrought IN625, which is in accordance with other works on **δ** precipitation in LPBF IN625 [63,108,109].

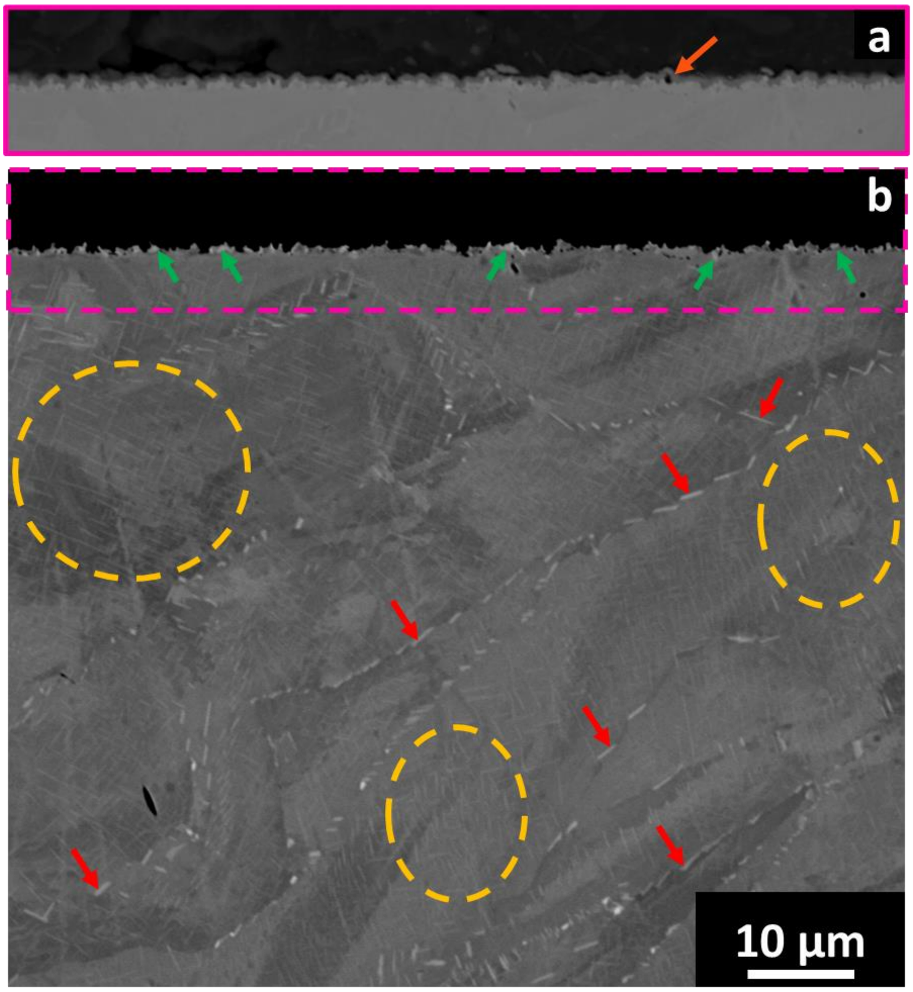

Figure 93: (a) low contrast SEM image of the LPBF as built IN625 oxide layer formed after 8h oxidation, (b) high contrast image in the same position made for highlight the alloy microstructure and (c) high magnification of the as built IN625 oxide layer after 8h oxidation

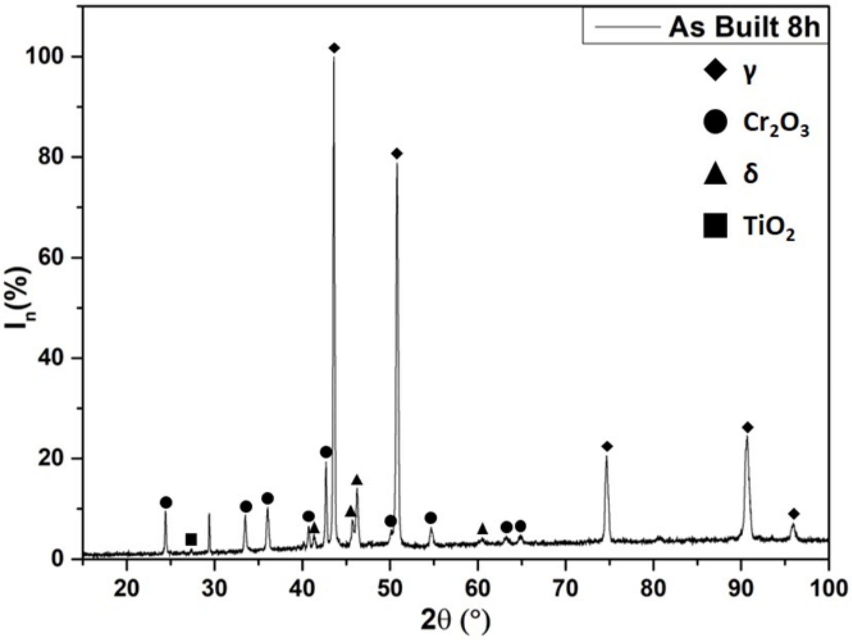

Figure 94: XRD diffractogram of 8 hours oxidized as built IN625

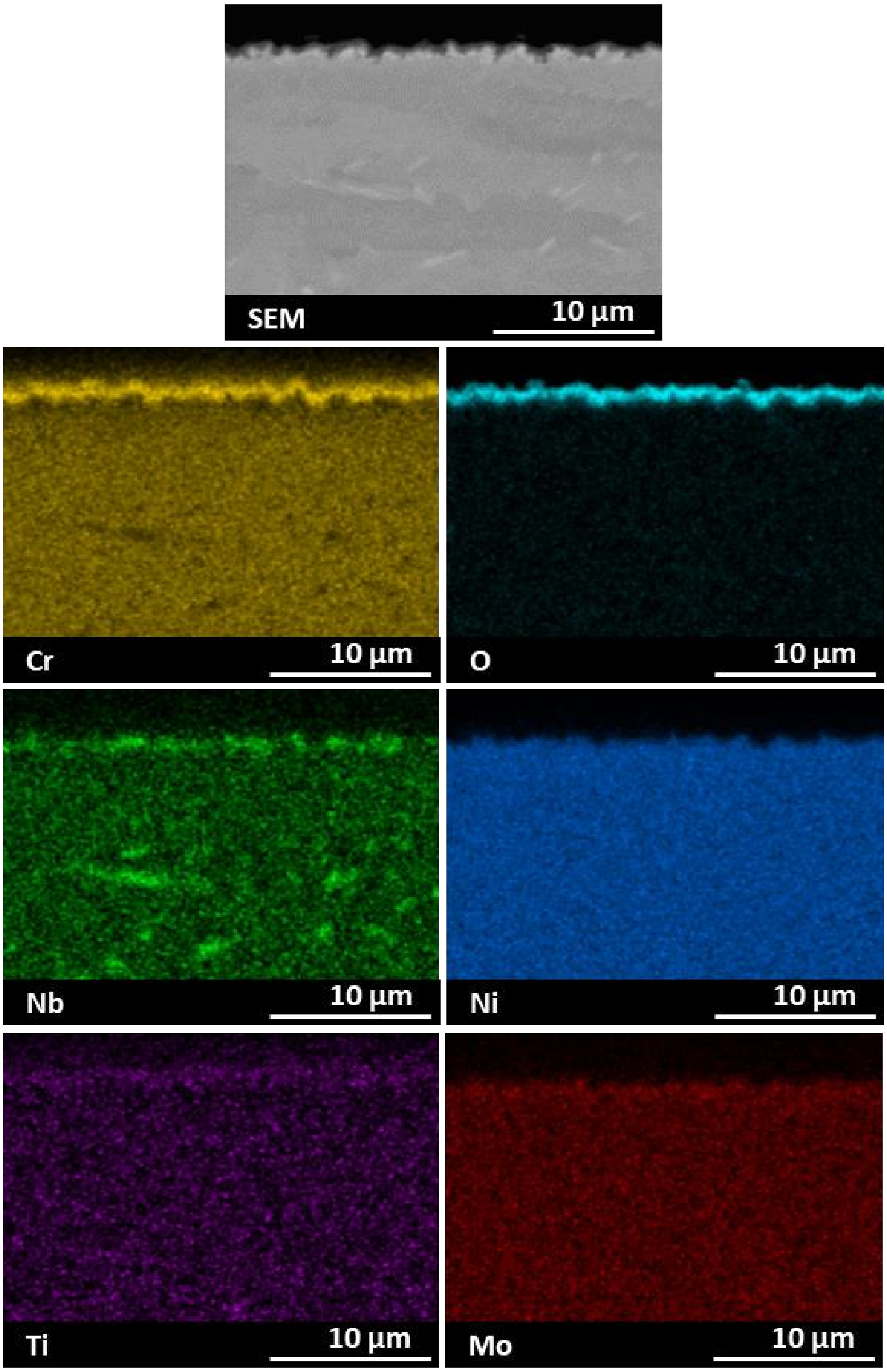

Figure 95: EDS map of 8 hours oxidized solutionized IN625

3.2.2.2 IN625 Solutionized oxidized for 8 hours condition

In Fig.96a the appearance of the oxide layer developed by the solutionized IN625 oxidized under thermal exposure for 8 hours is shown, while the microstructure is revealed in Fig.96b.

Fig.96a and Fig.96b have been taken in the same exact position at the same magnification, changing only the contrast. In this way Fig.96a, taken at low contrast, shows the oxide layer, meanwhile Fig.96b, taken at high contrast, reveals the microstructure of the alloy, but in this condition is not possible see the oxide layer.

The oxide layer thickness is comparable with the oxide of the as built condition after the same oxidation time. However, in this state the formed oxide possesses some differences. Initial appearances of internal oxidation are present (yellow arrows), as well as holes between the alloy surface and the oxide (orange arrows), better visible in Fig.96c.

From the peaks of the XRD pattern shown in Fig.97, the oxide layer composition is revealed to be Cr_2O_3, as in the case of the as built. However, in this case, the peaks of the TiO_2 are not detected, maybe because the concentration is below the sensibility limit of the instrument, typically around the 3 % in volume.

The EDS maps (Fig.98) confirmed the presence of Cr and O in the oxide layer, as well as a Ti enrichment, even if no TiO_2 was detected from the XRD, since the detection limit of the EDS analysis is usually around the 0.1% weight.

A layer of Nb enrichment right under the oxide layer is reported as well as for the as built state, and also in this condition it is possible detect some precipitate right under the oxide layer with dimension up to 2.5 μm (Fig.96a and Fig.96c, green arrows), probably formed thanks to the high Nb content caused by the Nb migration towards the oxide layer.

The microstructure possesses equiaxed grains, with the presence of twinning grain boundaries as seen in the previous sections.

δ-phases are present in the microstructure, located at the grain boundaries, and possess a length range of 0.5-3 μm (red arrows). The presence of **δ** is confirmed from the XRD analysis (Fig.97), with the intensity of the **δ** peaks between 40° and 50° inferior to the as built XRD.

The absence of **δ**-phases inside the grains is caused by the segregation dissolution after the solution treatment, because **δ**, according to the IN625 TTT diagram [11], need more than 8 hours at 900°C in order to precipitate. In the as-built condition the segregations act as nucleation point for **δ**, accelerating its formation.

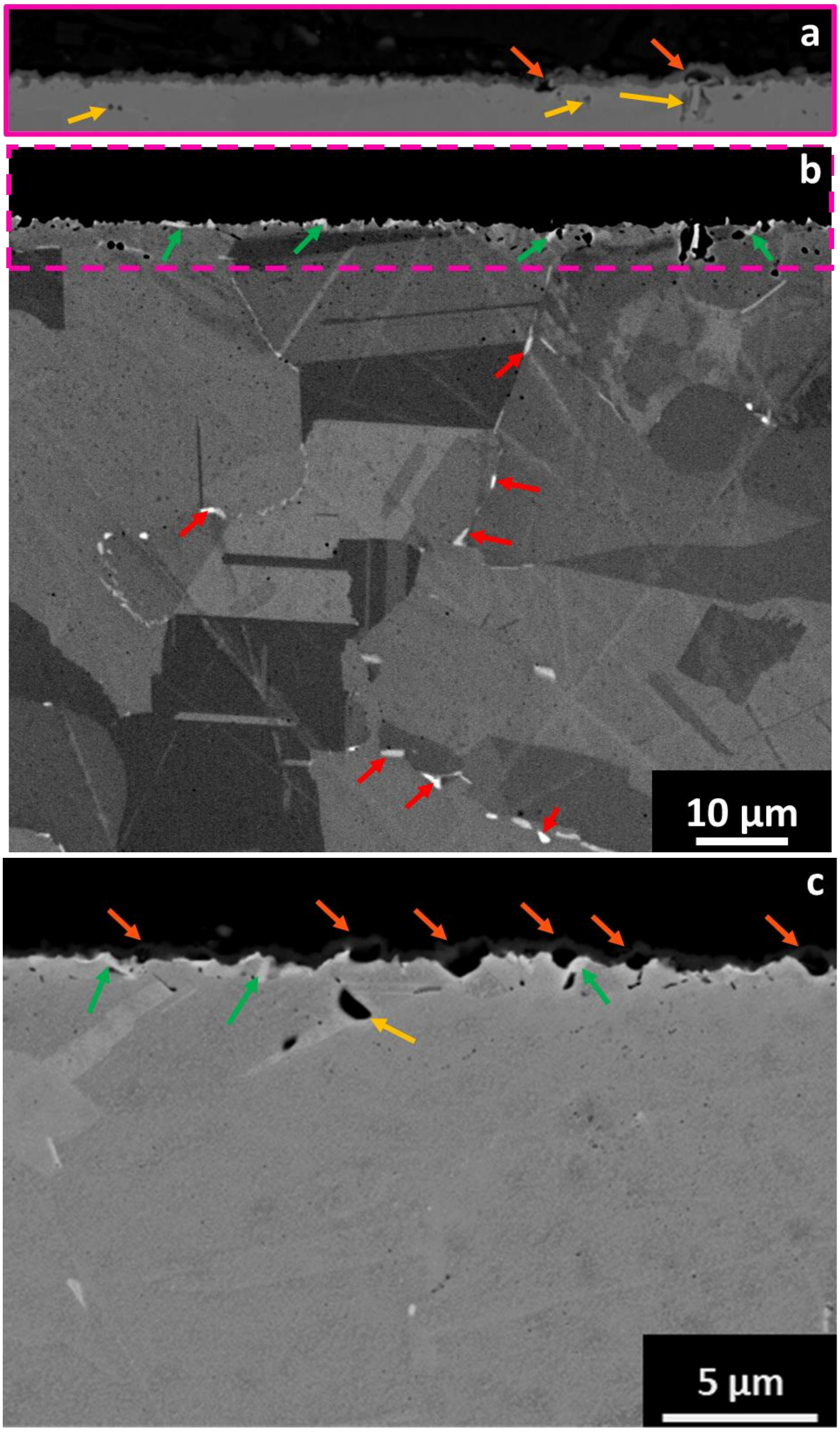

Figure 96: (a) low contrast SEM image of the solutionized IN625 oxide layer formed after 8h oxidation, (b) high contrast image in the same position made for highlight the alloy microstructure and (c) high magnification of the solutionized oxide layer after 8h oxidation

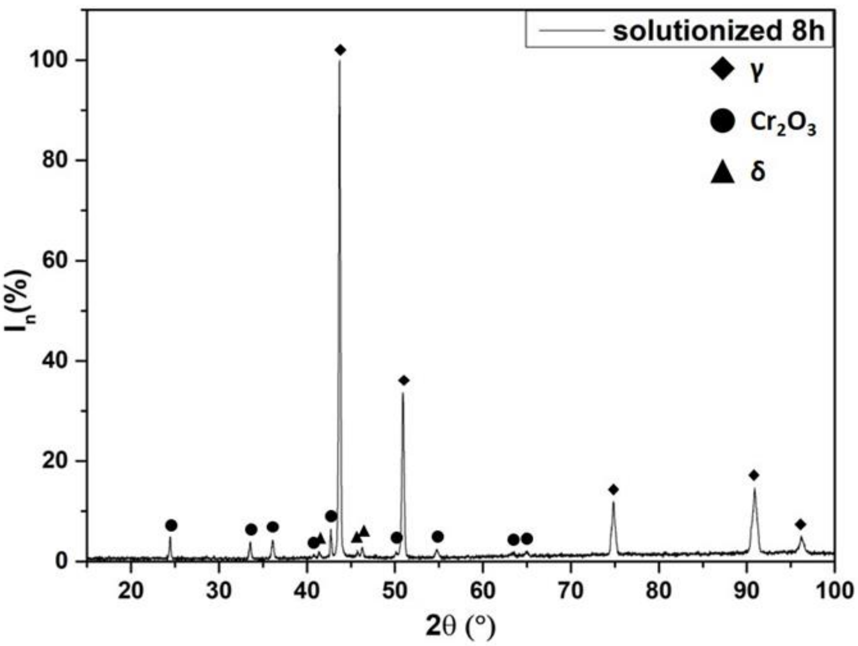

Figure 97: XRD diffractogram of 8 hours oxidized solutionized IN625

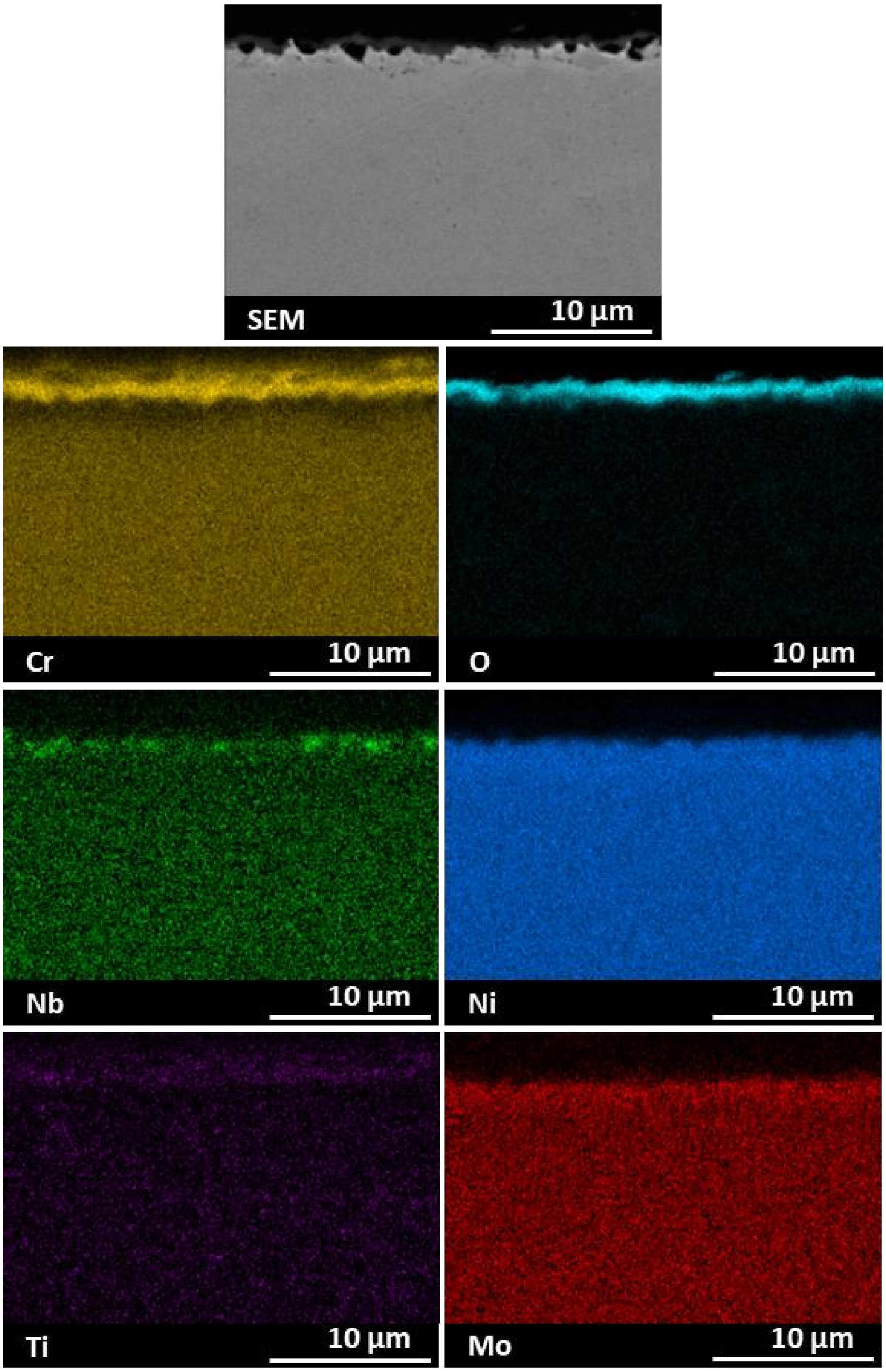

Figure 98: EDS map of 8 hours oxidized solutionized IN625

3.2.2.3 IN625 As Built oxidized for 96 hours condition

The aspect of the oxide layer and of the microstructural evolution of the as built LPBF IN625 are revealed in Fig.99a and Fig.99b respectively.

Fig.99a and Fig.99b have been taken at the same exact position at the same magnification, changing only the contrast. In this way Fig.99a, taken at low contrast, shows the oxide layer, meanwhile Fig.99b, taken at high contrast, reveals the microstructure of the alloy, but in this condition is not possible see the oxide layer.

The oxide shows a continuous and compact layer (Fig.99a and Fig.99c), without evident defects. Internal oxidation is present in this condition (yellow arrows in Fig.99b and Fig.99c), and follows the grain boundaries path for a length that can arrive up to 20 µm (Fig.99b). On the top of the internal oxidation, as can be seen in Fig.99c, the oxide layer becomes thicker. The XRD pattern in Fig.100 shows the peaks of Cr_2O_3 and TiO_2, as found in the previous section for the as built specimen oxidized for 8 hours.

The EDS maps in Fig.101 confirm the presence of Cr, O and Ti in the oxide layer and identifies the internal oxides as Ti and Al oxides. In the internal oxidation location, the EDS also detected the presence of the Nb, probably because of the precipitation at the grain boundaries. Moreover, right under the oxide layer the Nb-rich precipitates have become larger compared to the as-built oxidized 8 hours, reaching dimension up to 5 µm (green arrows in Fig.99b).

A last of results of the EDS analysis is the Mn enrichment of the oxide. In literature, N'dah et al. found Mn spinel inside the IN625 oxide after exposure at 1000 °C [122], as well as Garcia-Fresnillo et al. after 10000 hours at 750 °C [133]. The presence of Mn in the oxide is desirable especially above 1000 °C, because forming the spinel with Cr_2O_3 reduces the activity of the latter, retarding its evaporation [134].

The microstructure (Fig.99b) is still composed of columnar grains, with **δ**-phases scattered both inside the grains (yellow rounded) and at the grain boundaries (red arrows), with bigger dimensions in the latter case. The length of **δ** phase present dimensions similar to the same condition heat treated for 8 hours. However, the prolonged thermal exposure produced a higher concentration of **δ** phases.

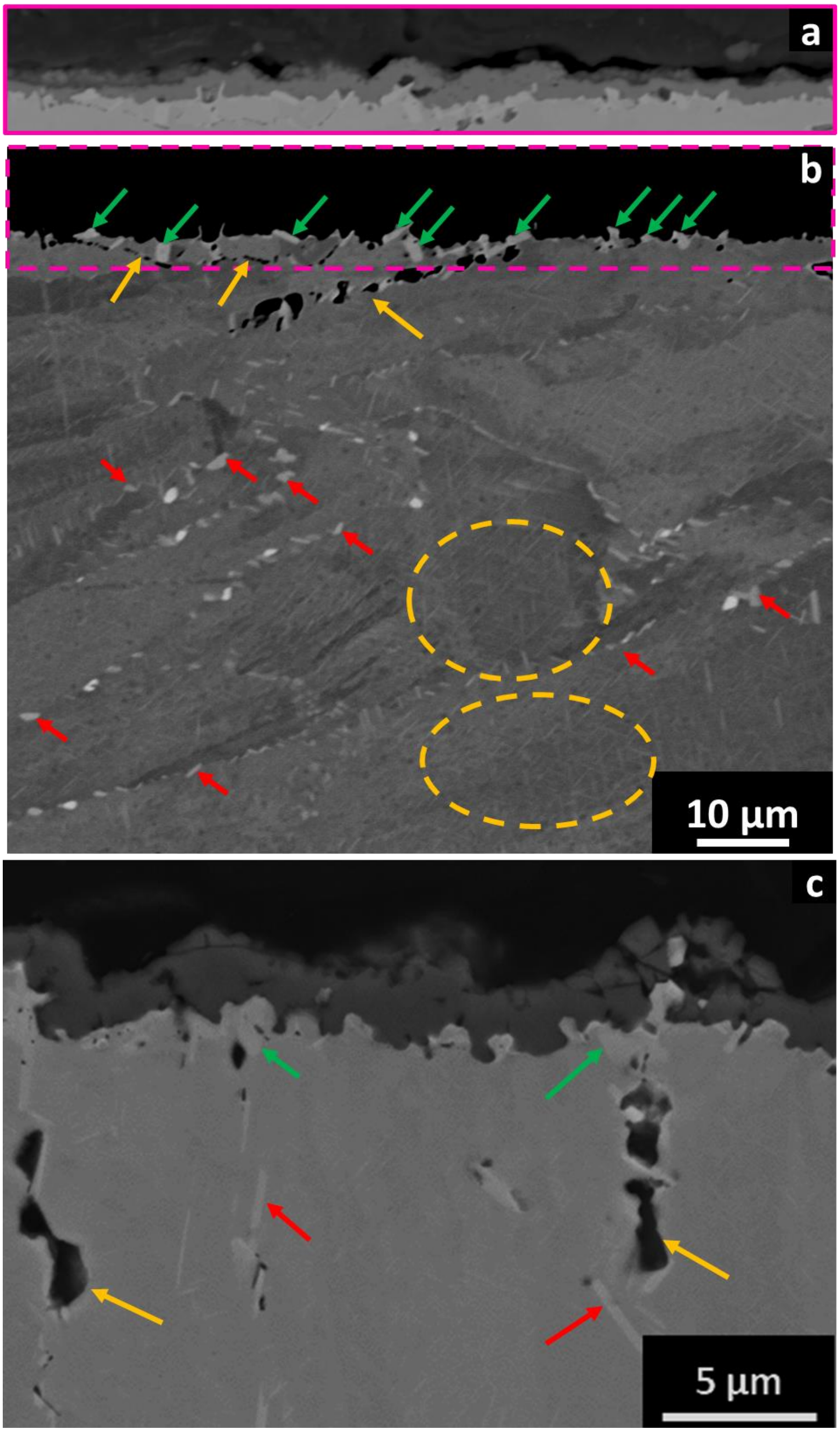

Figure 99: (a) low contrast SEM image of the as built IN625 oxide layer formed after 96h oxidation, (b) high contrast image in the same position made for highlight the alloy microstructure and (c) high magnification of the as built IN625 oxide layer after 96h oxidation

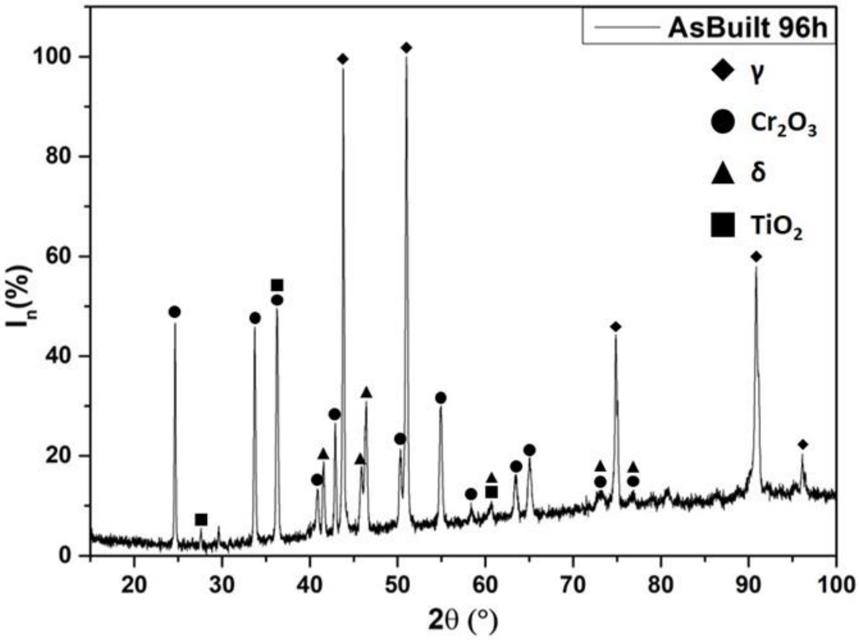

Figure 100: XRD diffractogram of 96 hours oxidized as built IN625

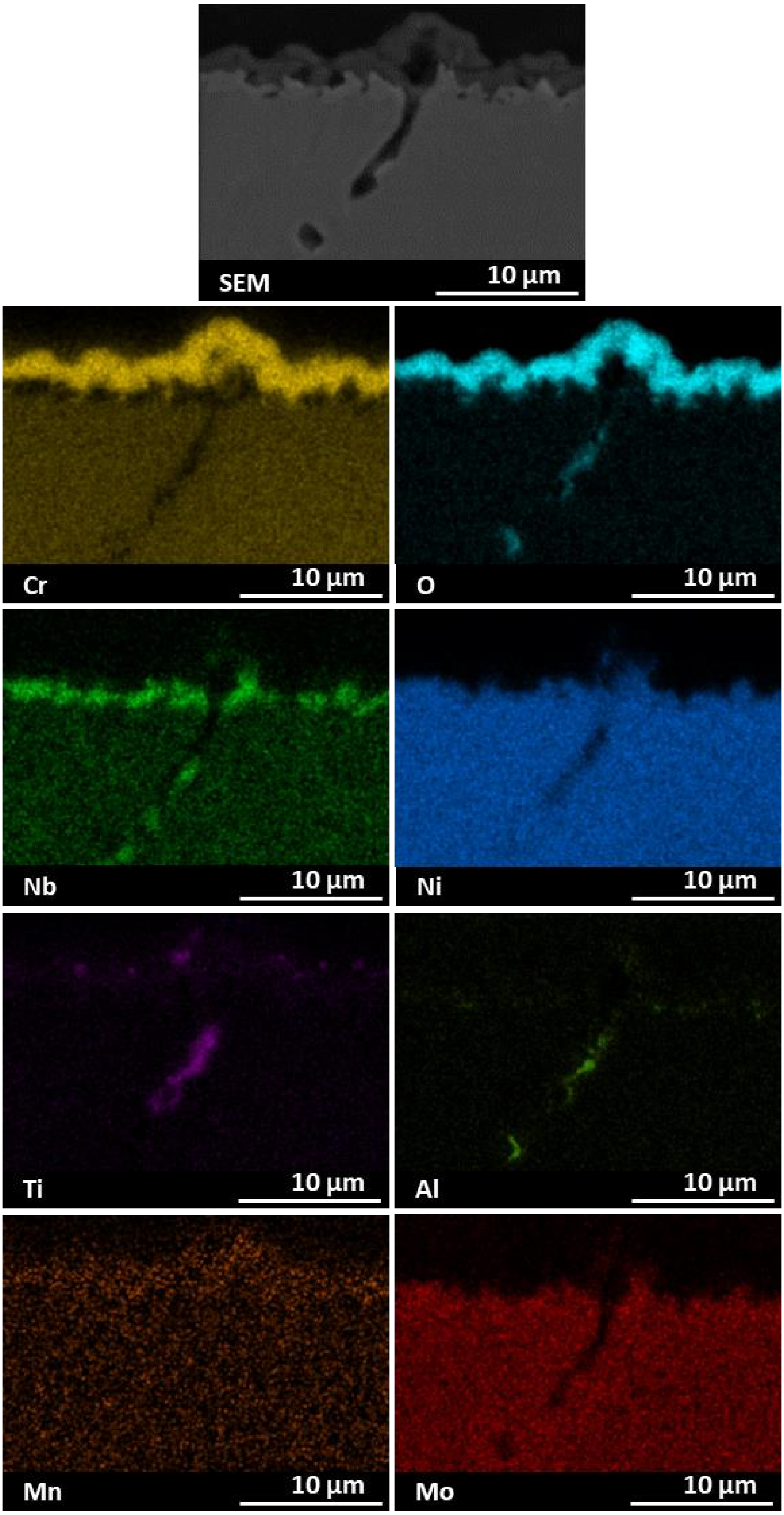

Figure 101: EDS map of 96 hours oxidized as built IN625

3.2.2.4 IN625 Solutionized oxidized for 96 hours condition

The appearance of the oxide layer developed by the solutionized IN625 oxidized for 96 hours and the microstructure of the alloy are displayed in Figure 102a and 102b, respectively.

Fig.102a and Fig.102b have been taken at the same exact position at the same magnification, changing only the contrast. In this way Fig.102a, taken at low contrast, shows the oxide layer, meanwhile Fig.102b, taken at high contrast, reveals the microstructure of the alloy, but in this condition is not possible see the oxide layer.

The oxide layer possesses cracks (orange arrows in Fig.102a, Fig.102d), holes at the interface between the oxide and the alloy (red circle in Fig.102c and Fig.102d) and non-uniform thickness (Fig.102c), which have a detrimental effect on the passivation effect of the oxide layer. The oxidation penetrates inside the alloy (yellow arrows in Fig.102b, Fig.102c and Fig.102d) for a length up to 50 μm following the GBs path and surrounding some grain (yellow arrows in Fig.102c).

The XRD pattern reported in Fig.103, makes it possible to determine the oxide layer composition, which is composed of Cr_2O_3, without TiO_2 peaks, probably because the amount is below the sensitivity of the analysis. Differently by the previous conditions, the XRD detect the presence of Nb_2O_5 and $NiCr_2O_4$ oxides, that will be deeply discussed later.

The EDS maps in Fig.104 shows a section in which the oxide is detached. The oxide layer contains Cr, O and Ti, as in the as built condition, and there are signals of the formation of a thin oxide layer on the exposed alloy (orange arrows).

The internal oxidation appears similar to the one found in the as built condition, with an enrichment in Ti and Al. The latter is present in some point of the lower part of the spalled oxide, probably incorporated when the oxide growth reached some internal oxidation hole located in the proximity of the alloy/oxide interface.

The Mn seems to be more concentrated in the oxide layer than inside the alloy. This result is the same observed for the as built condition.

After 96 hours of thermal exposures, the microstructure of the solutionized sample (Fig.102b and Fig.102c) is characterized by equiaxial grains, decorated by an important concentration of **δ** phase inside (yellow rounded) and between the grains (red arrows), where their length can arrive up to 25 μm.

As said for the solutionized condition oxidized for 8 hours, the segregations can nucleate **δ**, accelerating the precipitation, so removing the segregations with a solution treatment retard the precipitation of **δ**. In this condition, **δ** precipitates after more time, and can grow bigger compared to the as-built state, since the surrounding matrix possesses a higher content of Nb, thanks to the dissolution of the interdendritic areas and the segregations after the solutionizing treatment.

Also for this condition, there is an important concentration of large **δ** phases under the oxide layer, with dimension up to 8 μm (green arrows in Fig.102b, Fig.102d and red arrows in Fig.104, Nb map).

From Fig.102c can be observed that under the precipitates there is an alloy zone, long around 10 µm, with a low concentration of **δ** phases. This reduced precipitate content is probably caused by the reduction of the matrix Nb content caused by the migration at the alloy/oxide interface.

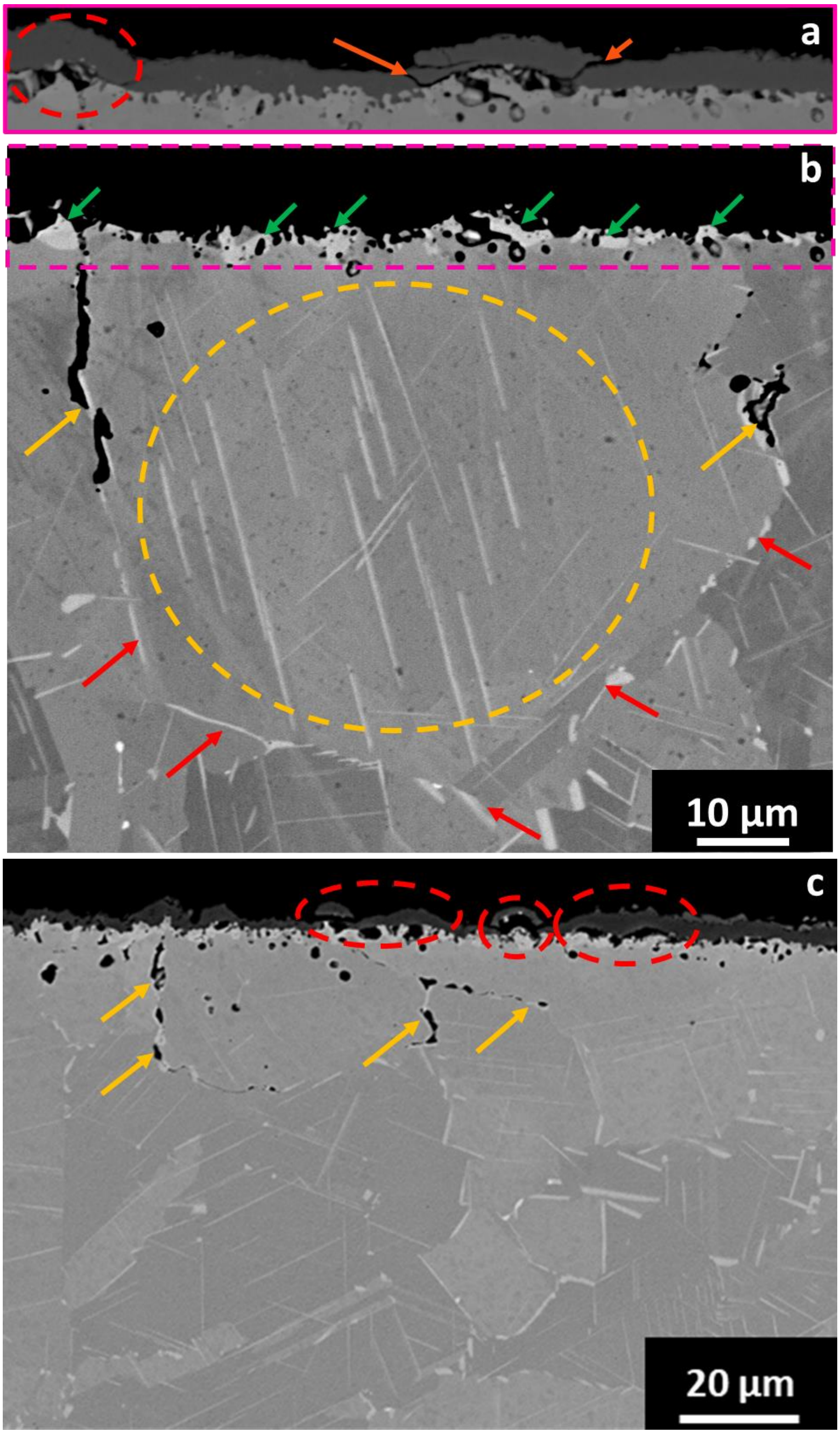

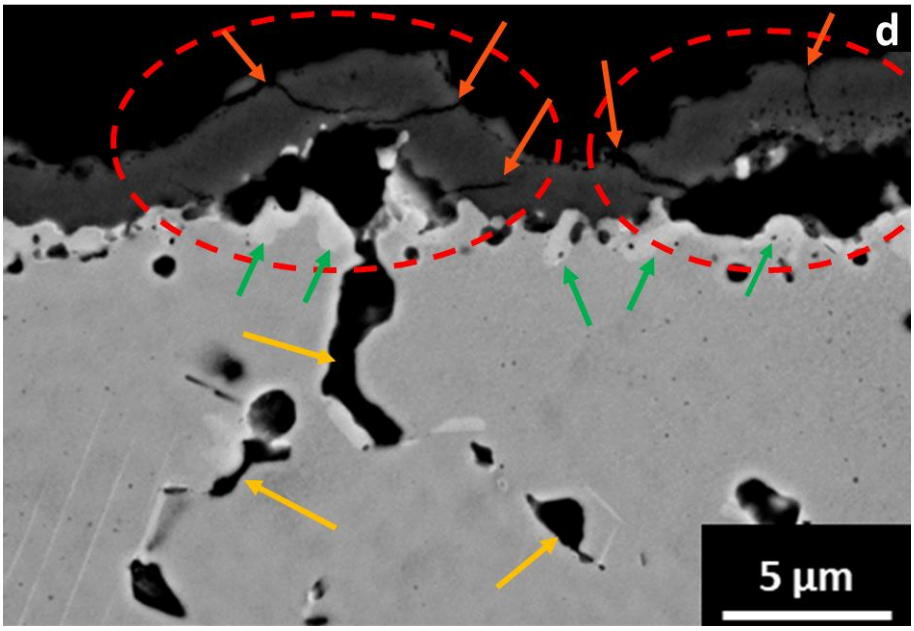

Figure 102: (a) low contrast SEM image of the solutionized IN625 oxide layer formed after 96h oxidation and (b) high contrast image in the same position made for highlight the alloy microstructure, (c) low magnification SEM image of the solutionized IN625 oxide layer after 96h oxidation and (d) high magnification SEM image of the solutionized IN625 oxide layer after 96h oxidation

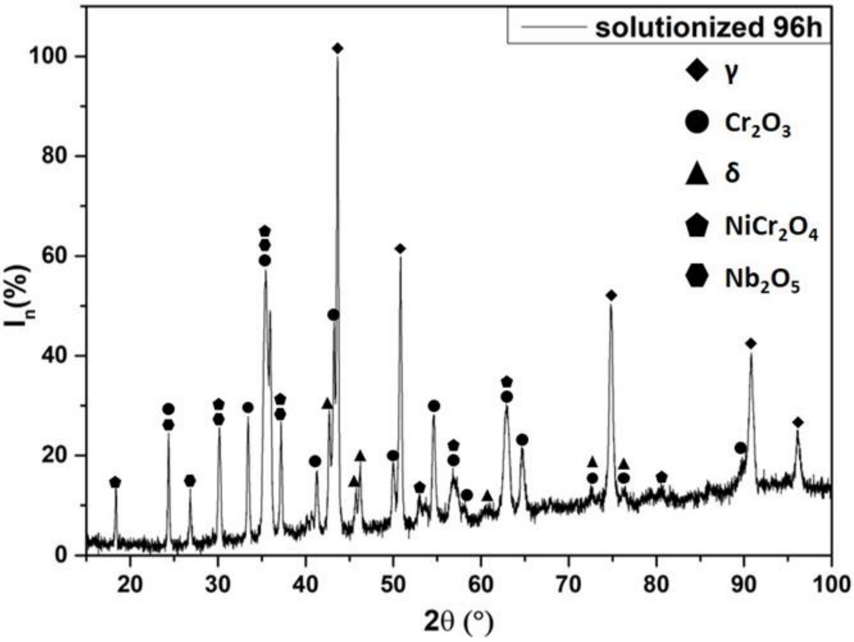

Figure 103: XRD diffractogram of 96 hours oxidized as built IN625

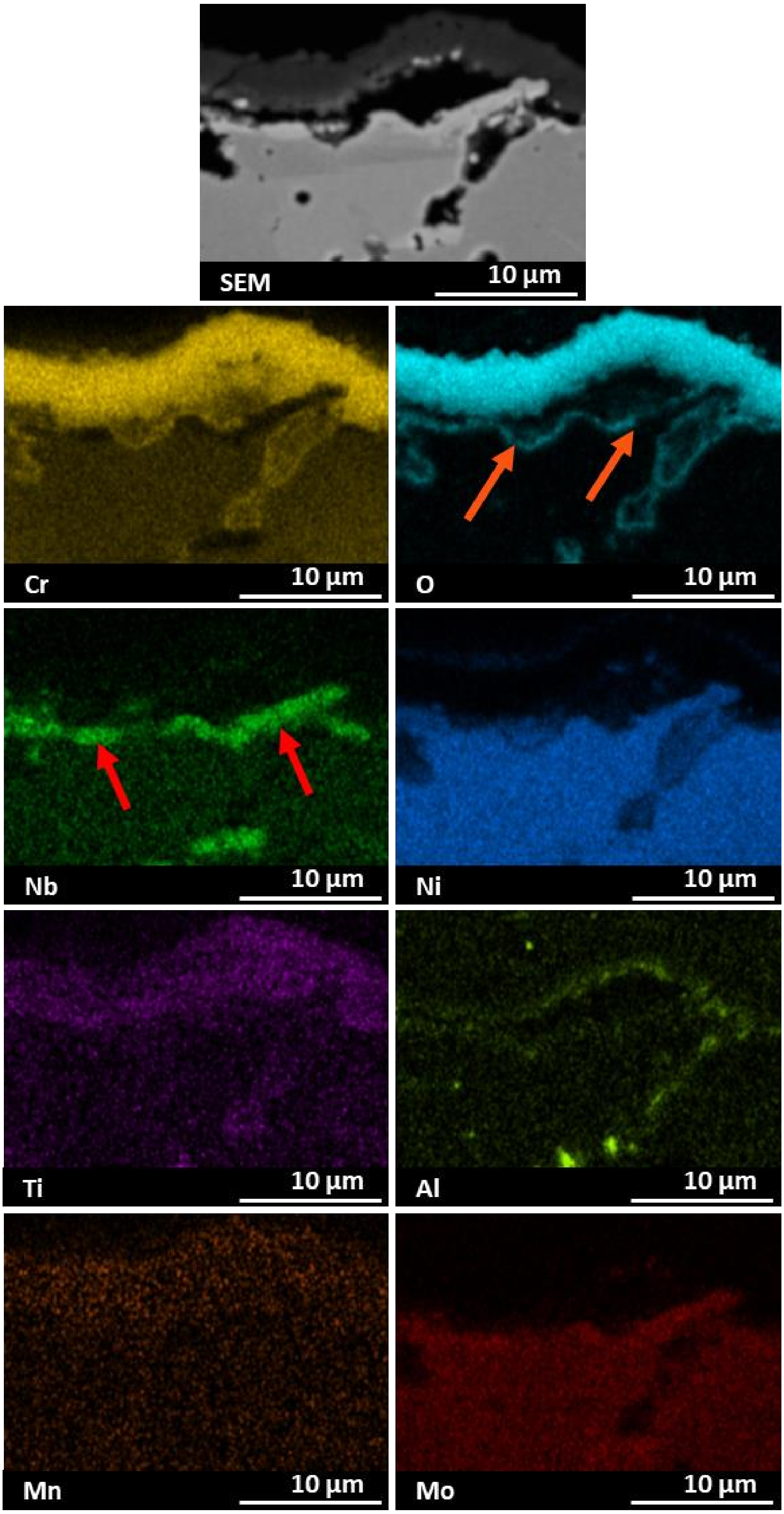

Figure 104: EDS map of 96 hours oxidized solutionized IN625

Only in this condition, there are portions of the oxide layer that possess a good adhesion with the alloy but also contains bright portions (red circle in Fig.105). The EDS maps performed on these sections (Fig.106) revealed an important presence of Ni and Nb, explaining the presence of peaks of Nb_2O_5 and $NiCr_2O_4$ in the XRD analysis.

It is interesting to observe that for these oxides (red circles in Fig.105), no cracks or ruptures in the oxide layer are detected, suggesting that they are not the cause of the reduced oxidation resistance of this alloy state.

The shape of these clusters is complementary to the shape of the underlying alloy and contain holes, indicating that they are probably created from the removal of portions of the alloy, then incorporated by the oxide layer.

This can explain the presence of the hole (internal oxidation already detected in the solutionized sample after 8h) as well as the high Nb content, developed in the interface with the oxide after the Cr consumption.

A possible formation mechanism of the mixed oxides is proposed in Fig.107. In the first step, a thin layer of oxide is developed on the alloy surface, with some defect such as spalling (Fig.107a).

Increasing the thermal exposure causes the growth of oxide layer, which starts to penetrate in the alloy consuming the grain boundaries and forming internal oxidation holes. The alloy located under the spalled oxide develop a new oxide layer (second step, Fig.107b).

Continuing this process eventually causes, in some location, the surrounding portion of the alloy by the internal oxidation, and the spalled oxide develops cracks that can lead to the spalled oxide rupture (Fig.107c).

The alloy portion surrounded by the oxide results in lack of Cr (used for the oxide layer formation) and enriched in Nb, as seen in the previous sections, and remains cut out from the diffusion of new Cr from the alloy below, because it is surrounded by oxide. From this point the alloy oxidation goes on, allowing the development of portion of Nb_2O_5 and $NiCr_2O_4$ oxides inside the main oxide layer of Cr_2O_3 (Fig 107d).

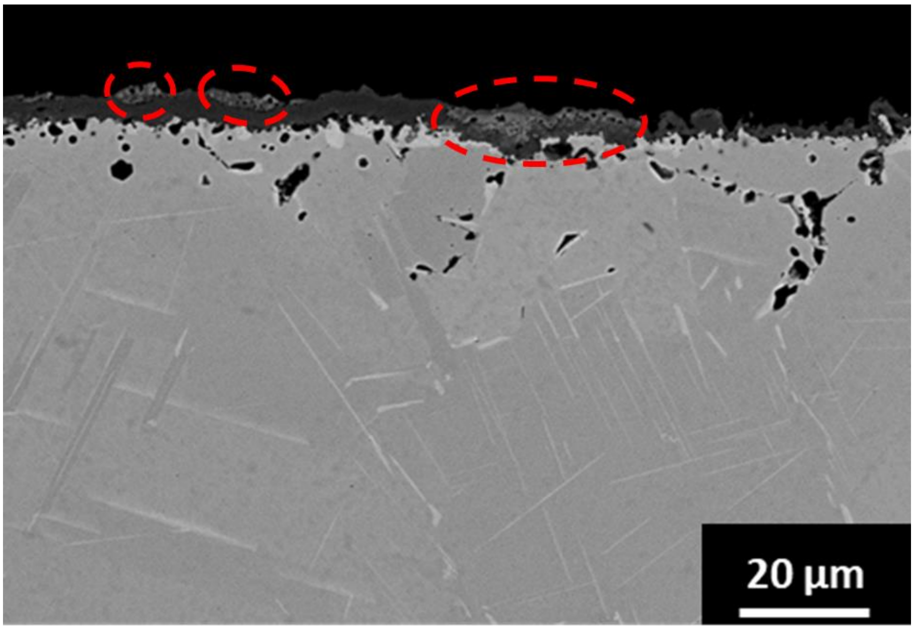

Figure 105: SEM image of the solutionized IN625 oxide layer after 96h oxidation with presence of $NiCr_2O_4$ and Nb_2O_5

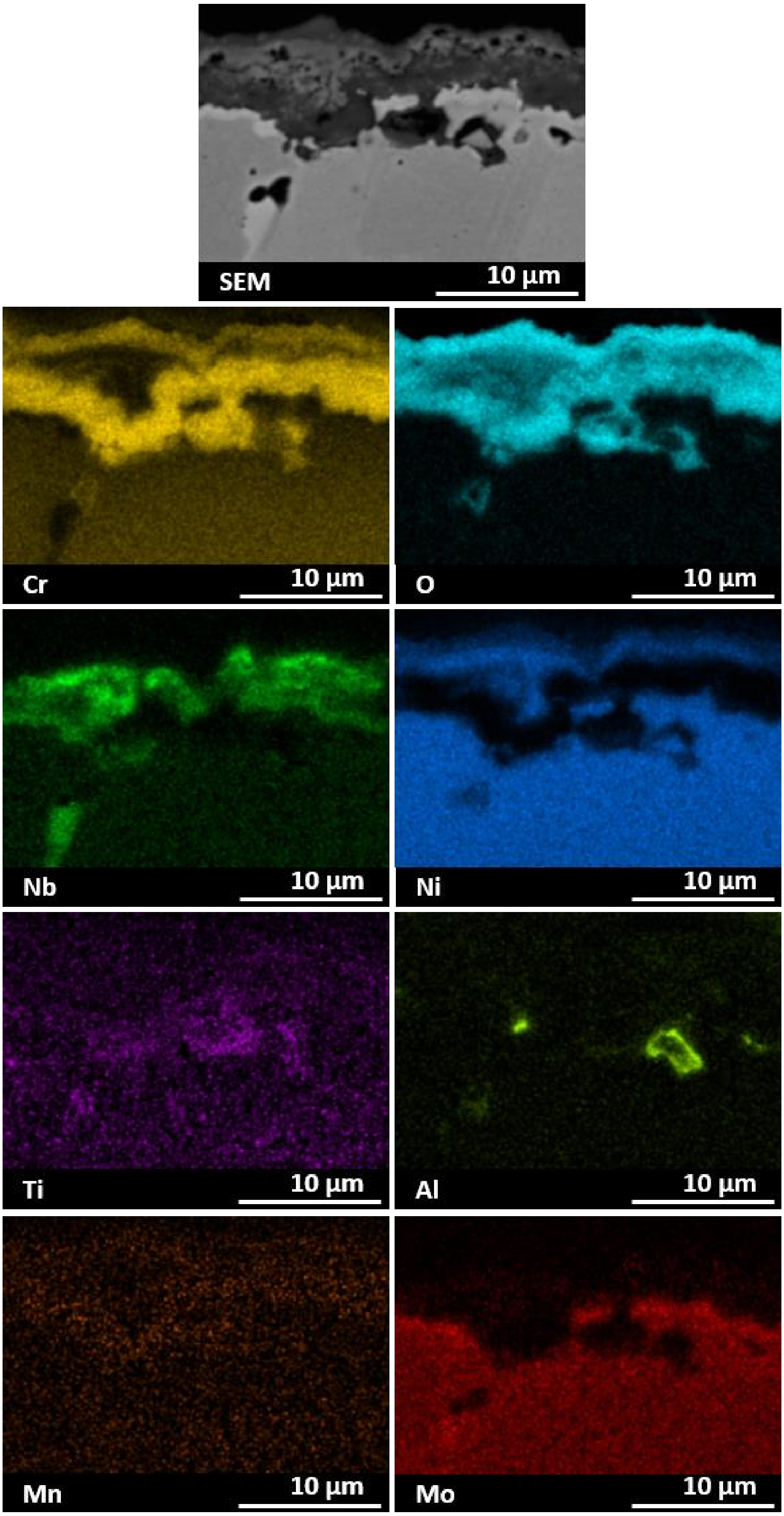

Figure 106: EDS map of 96 hours oxidized solutionized IN625 with presence of $NiCr_2O_4$ and Nb_2O_5

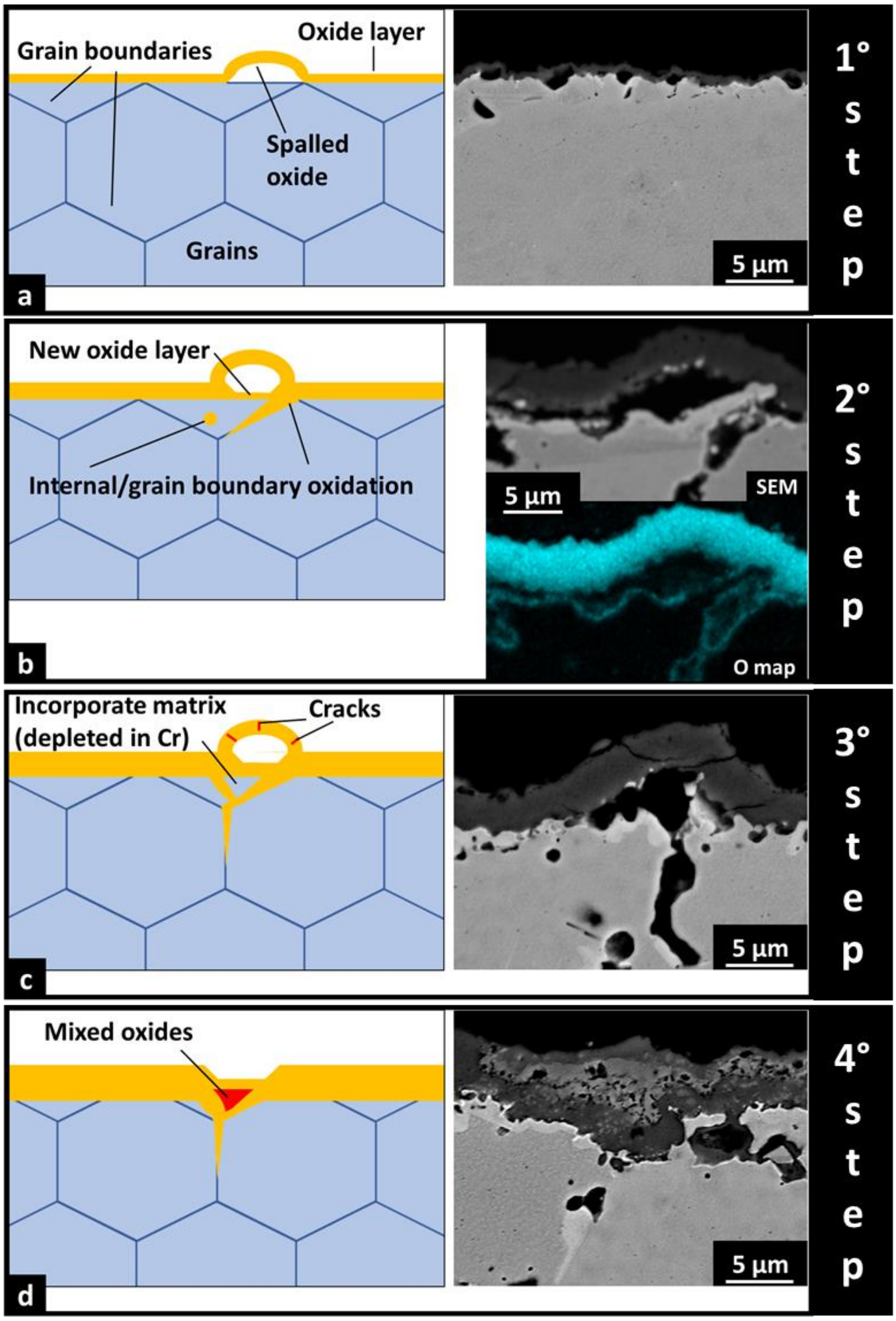

Figure 107: $NiCr_2O_4$ and Nb_2O_5 proposed formation mechanism

3.2.3 XRD analysis

Taking the austenitic matrix (γ phase) peaks position of the IN625 from the patterns in Fig.94, 97, 100 and 103, it is possible to calculate the lattice constant of the alloy after the oxidation treatments. The results of this analysis are summarized in Fig.108.

The data points located at 0 hours represent the as built and solutionized IN625 before the oxidation treatment. In this condition the as built possess an inferior lattice parameter compared with the solutionized condition, caused by the lower content in Nb dissolved in the γ phase, because is trapped in the segregations and interdendritic areas, which are dissolved after the solutionizing treatment.

After the oxidation for 8 hours the lattice constant value decreased for both as built and solutionized condition, but the drop is more consistent for the latter. After that the lattice constant did not seem to suffer from other variations when the oxidation time is increased.

The great homogeneity of the Nb in the solutionized condition led to a stronger depletion from the matrix during the migration at the interface and the precipitates nucleation and growth phenomena, causing a marked reduction of the lattice parameters compared to the as-built specimens. After the oxidation the contraction of the lattice parameter of the matrix is almost double for the solutionized condition compared to the as built sample, both after 8 hours and 96 hours.

It is possible that this behaviour leads to local stress accumulations, with a mechanism compatible with precipitation induced stress which lead to strain age cracking in other nickel alloys [49]. The presence of these stresses can explain the defects formation in the solutionized IN625, which cause the minor oxidation resistance.

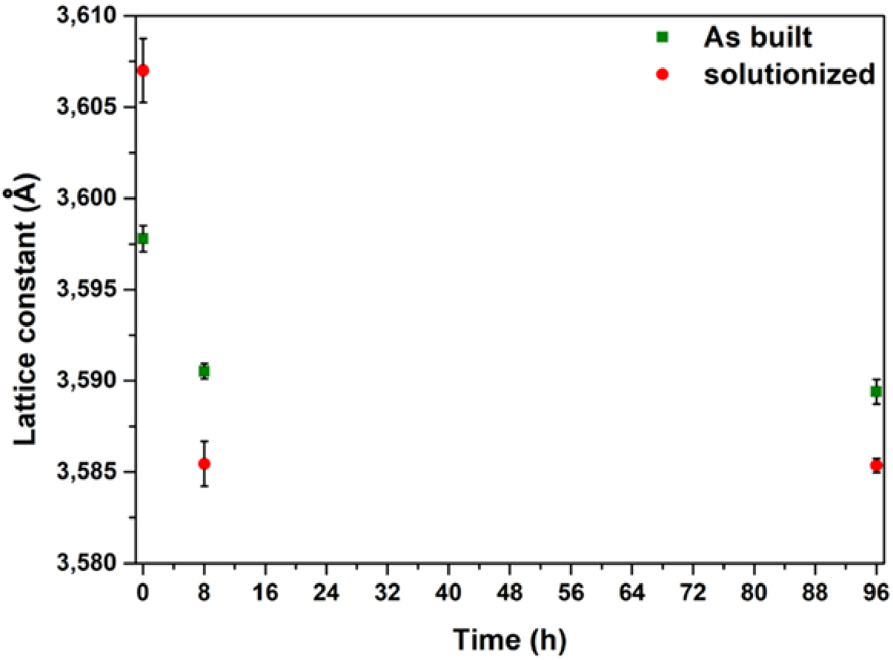

Figure 108: as-built and solutionized LPBF IN625 lattice parameter before and after oxidation at 900 °C for 8 and 96 hours

3.2.4 Scratch tests analysis

The mechanical behaviour of the oxide layer formed on the different samples has been investigated using the scratch test analysis.

The test consists in an indenter that performs a scratch 1 mm (1000 µm) long on the oxide. The indenter is subjected to a load, that increases linearly from 0 mN at the start of the scratch up to 250 mN at the end of the scratch.

During the indentation the lateral force needed by the indenter for moving is recorded.

For each condition, 3 scratch have been performed parallel to the building direction (par) and 3 have been performed perpendicular to the building direction (perp.). In Fig.109 the results of one parallel and one perpendicular test for each condition are reported in term of graphs, where the lateral force value is reported as function of the normal force applied to the indenter and the indenter position in the scratch (lateral displacement).

As can be noticed in the graphs in Fig.109, the later force value increases as the normal force increases, at first with a linear regime, than increases in a more marked way. The point where the first regime stops is associated with the moment in which the indenter has penetrated inside the oxide layer and reached the alloy. The normal force needed for reaching the alloy has been evaluated for each scratch and the results are reported in Table.26.

The as-built condition after 8 hours of oxidation shows just a slight difference between the parallel and perpendicular tests, reaching lower normal force values for the latter. This can be correlated to the anisotropy of the grain structure, that can be noticed also in the SEM images in Fig.110a and Fig.110b, where the grain boundaries are slightly highlighted by the oxide.

The solutionized condition after 8 hours of oxidation instead does not show differences between the scratch test orientations, probably because it possesses an equiaxial grain structure. The grain boundaries are slightly highlighted by the oxide also for this condition (Fig.110c and Fig.110d).

After 96 hours of oxidation, the as-built condition seems to lose the differences between the two test orientations. The normal force required to reach the alloy increases, since that the oxide thickness is increased compared to the 8 hours condition, reaching normal force values of around 200 mN for both the test directions. The grain boundaries, seen in the SEM images in Fig.110e and Fig.110f, are more highlighted by the oxide compared to the 8 hours condition.

The solutionized condition after 96 hours of oxidation does not show differences between the scratch test orientations, as for the 8 hours condition, but possesses a slightly lower resistance compared to the as-built condition oxidized for 96 hours, with normal force values below 190 mN. These slightly lower values can be caused by the presence of the mixed oxides or by the oxide defects present in this condition. However, the force needed to reach the alloy is not so different between the as-built and the solutionized condition, because in both cases, the oxide layer mainly contains Cr_2O_3. Since the oxide compositions are mainly similar, the mechanical resistances of the oxide layers are probably similar. The grain boundaries are evidently highlighted by the oxide also for this condition (Fig.110g and Fig.110h).

As can be noticed in Fig.110, no cracks or big oxide removals are present after the scratch test, indicating that the general adhesion of the oxide is mostly similar for all the conditions.

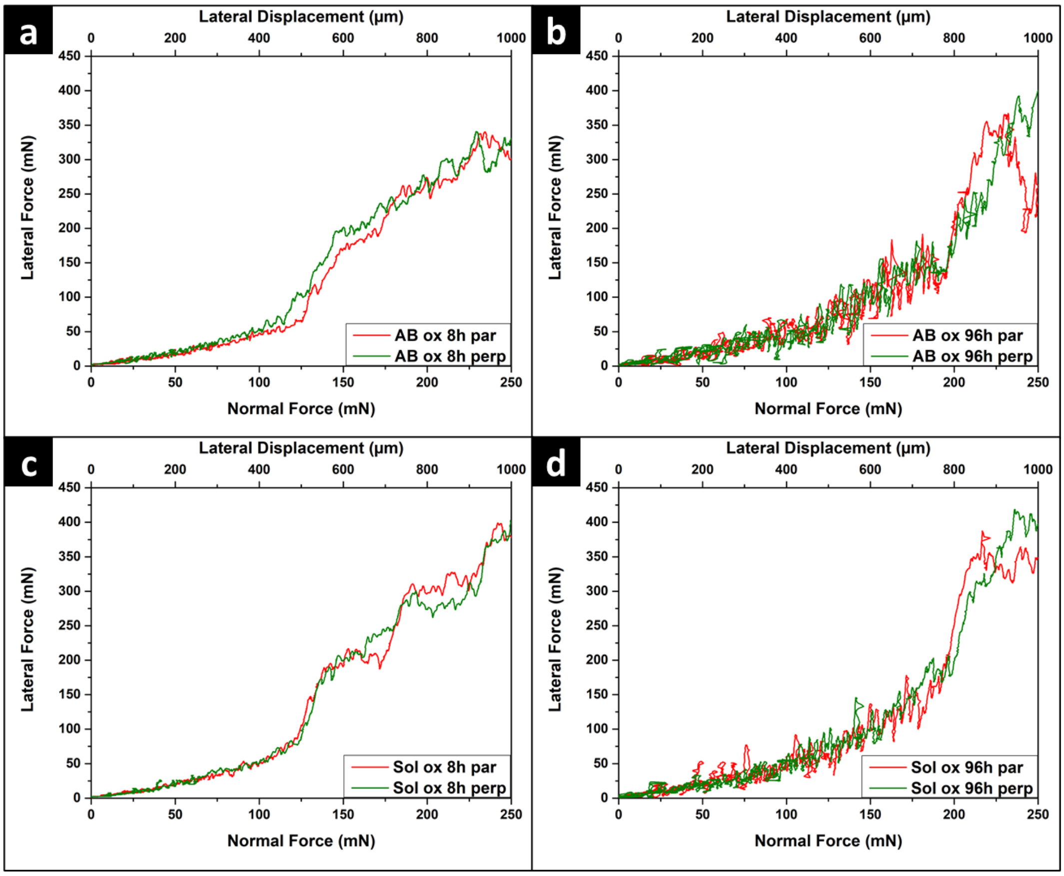

Figure 109: Lateral force versus normal force reported from scratch test of As Built 8h (a), As Built 96h (b), Sol 8h (c) and Sol 96h (d)

Table 26: Normal force needed to reach the alloy

Average Normal Force of scratch:	**As Built 8h**	**Sol 8h**	**As Built 96h**	**Sol 96h**
	Normal force (mN)	Normal force (mN)	Normal force (mN)	Normal force (mN)
Parallel	122±3	127±4	201±10	185±6
Perpendicular	115±2	125±5	202±14	188±10

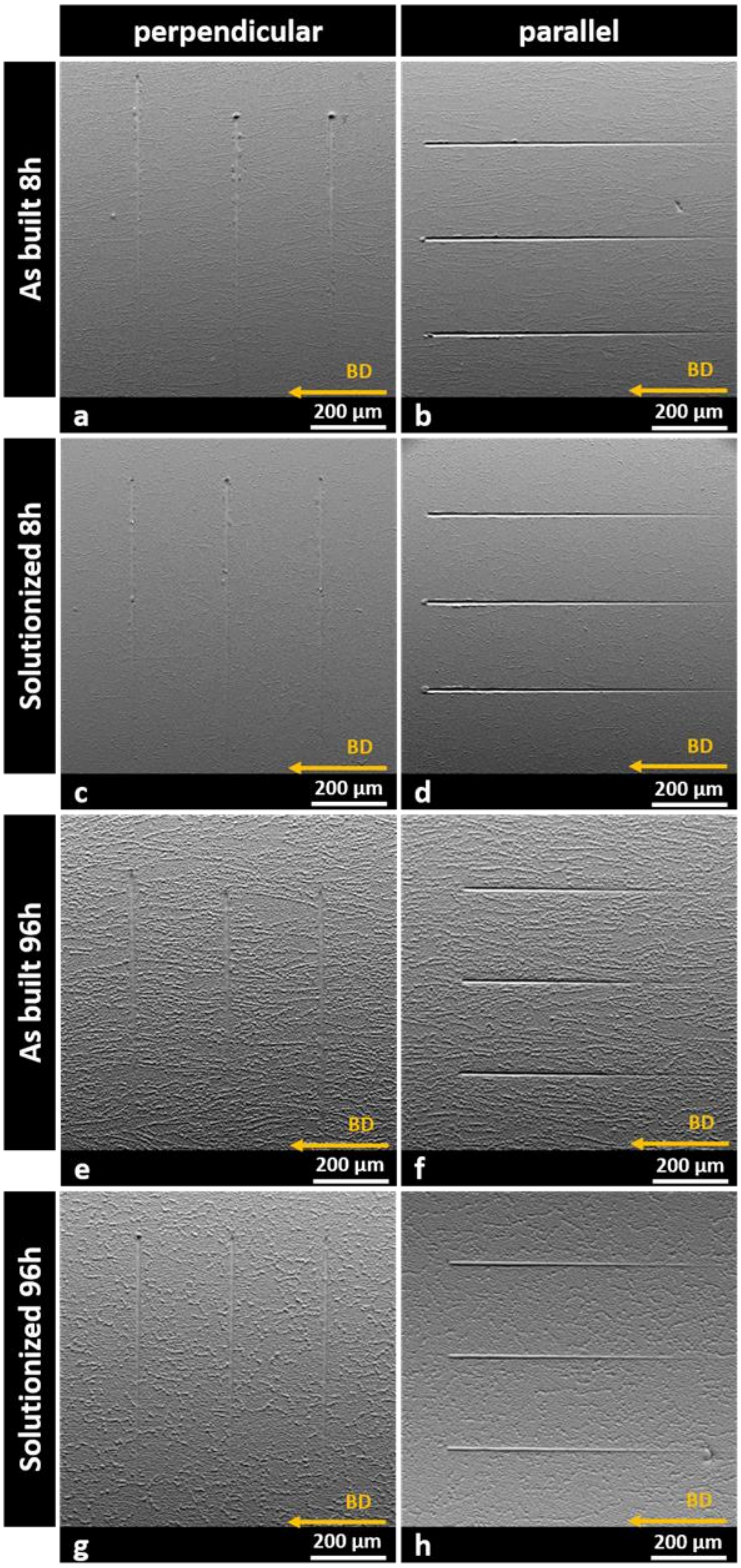

Figure 110: SEM images of scratch tests perpendicular to the BD of the As Built 8h (a), As Built 96h (e), Sol (c), Sol 96 (g) and parallel to the BD of As Built 8h (b), As Built 96h (f), Sol 8h (d) and Sol 96 (h)

3.2.5 Results summary of oxidation properties

After oxidation at 900 °C the as built condition have shown a greater oxidation resistance with respect to the solutionized state, thanks to the formation of a compact and continuous oxide layer that reduces the oxidation rate since from 8 hours of oxidation. The solutionized condition instead, shows evidences of spalling already after 8 hours, and an important defect content in the oxide layer increasing the oxidation time.

The microstructure of the as-built possesses segregations rich in Nb, absent in the solutionized condition, that accelerate the precipitation of δ phase and reduces its following growth compared to the solutionized case.

The segregation presence reduces the Nb content in the alloy matrix, that possesses a lower lattice constant in the as-built state and higher for the solutionized condition. This difference in the Nb dissolved in the matrix change the entity of the precipitation effect in the alloy, leading to a stronger reduction in the lattice constant for the solutionized condition. This fact can develop higher stresses in the alloy, explaining why the oxide start to possess defects after 8 hours already.

The developed oxide layer is composed for the most part of Cr_2O_3, with a contained presence of TiO_2 for both conditions.

Only the solutionized sample oxidized for 96 hours shows the presence of $NiCr_2O_4$ and Nb_2O_5, probably generated by an incorporation in the oxide layer caused by the bigger defect presence in the oxide compared to the as-built condition.

Little anisotropy in the oxide mechanical resistance of the as-built oxidized for 8 hours are detected, probably caused by the anisotropy in the grain structure. The solutionized sample oxidized for 8 hours instead shows isotropy in the oxide mechanical resistance, probably thanks to the equiaxial grain structure.

After 96 hours of oxidation both conditions show isotropy in the mechanical resistance of the oxide, since is become thicker and less influenced by the grain structure, but the solutionized condition possesses a slightly lower mechanical resistance, probably caused by the presence of defects in the oxide layer.

Chapter 4

Results and discussion on IN939

Inconel 939 is a Ni-based corrosion resistant superalloy typically used for blades and vanes in marine and land based gas turbines for continuous service up to around 850 °C [21,24,28] under load. This alloy can be used for higher temperatures with respect to the known Inconel 718 used up to around 650 °C under load.

There are very few studies concerning the characterization of Inconel 939 processed by LPBF [24,135]. Moreover, there are no studies regarding the effect of the process parameters on the densification of the alloy. This alloy is characterized by a reduced weldability due to high values of γ' formation elements within the alloy.

Therefore, this section concerns the process parameters optimization in order to obtain the parameters to generate dense components as well as the investigation of the microstructure of the as-built LPBF IN939 state with respect to the as-cast version.

Part of this work was present at the at the conference Material Science & Technology 2019 in Portland (Oregon, USA).

4.1 IN939 powder characterization

As can be observed in Fig.1, the morphology of the gas atomized IN939 particles is mostly spherical with smooth surface, as recommended for LPBF powder [41]. However, there are also some irregular particles, rough surfaces and presence of satellites particles as indicated in Fig.111 by the red circles, yellow circles and red arrows, respectively. The Hall flow test resulted in a flow time of 15.1±0.2 s and an apparent density of 4.29±0.01 g/cm^3.

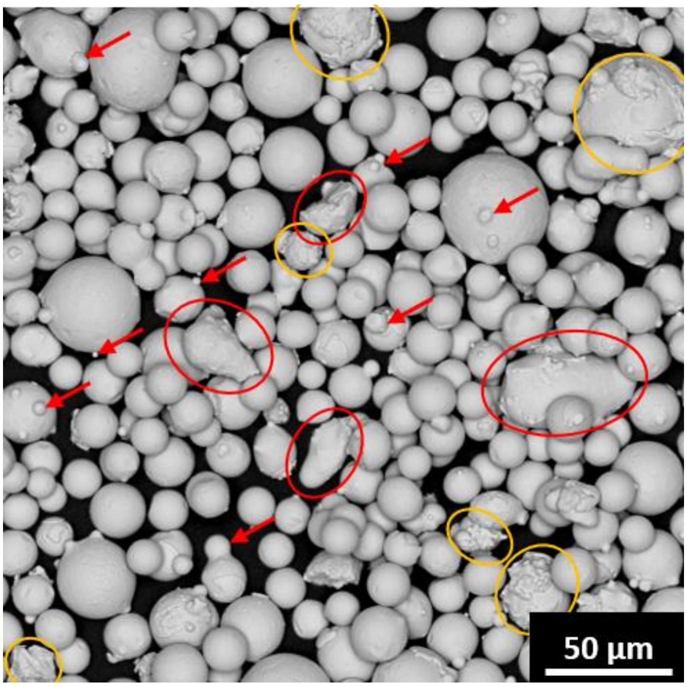

Figure 111: SEM image of the gas atomized IN939 powder used in this work. Particles with irregular shape are red rounded, particles with rough surface are yellow rounded and satellites are pointed out by red arrows

The laser granulometry was performed on the powders and the results are reported in Fig.112a revealing that the d10, d50 and d90 obtained from this analysis are 16.8, 26.1 and 40.7 µm, respectively. These results are very similar to the results obtained on the powder treated with ultrasonic vibration (Fig.112b)(d10, d50 and d90 are respectively 16.6, 25.5 and 40.0 µm), indicating that the particles do not tend to form big aggregates. Therefore, the majority of the particles had diameter inside the nominal dimension range (15 to 45 µm) stated by supplier company.

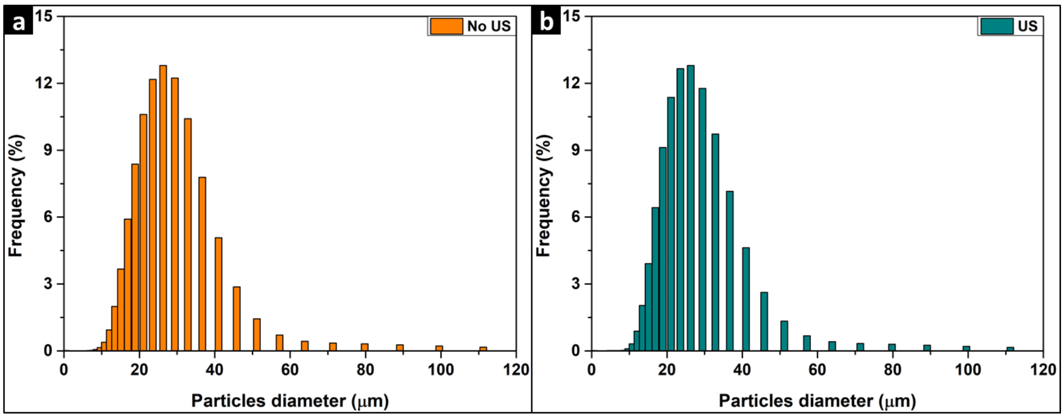

Figure 112: Particle size distribution of the gas atomized IN939 powder obtained by Laser granulometry.

In order to fully characterize the powder, also the cross section of the particles was observed. The powder appeared mostly dense, but it is possible to observe isolated particles with pores inside. The majority of these pores are spherical with dimensions below 1 µm, but some particles exhibit also irregular voids with size up to around 20 µm. These types of pores could be generated during the gas atomization process due to the entrapment of the gas within the particles. After performing image analysis on 3455 particles, the total porosity content of the powder was evaluated to be 0.4 ± 0.2 %. The common appearance of the powder cross section is shown in Fig.113.

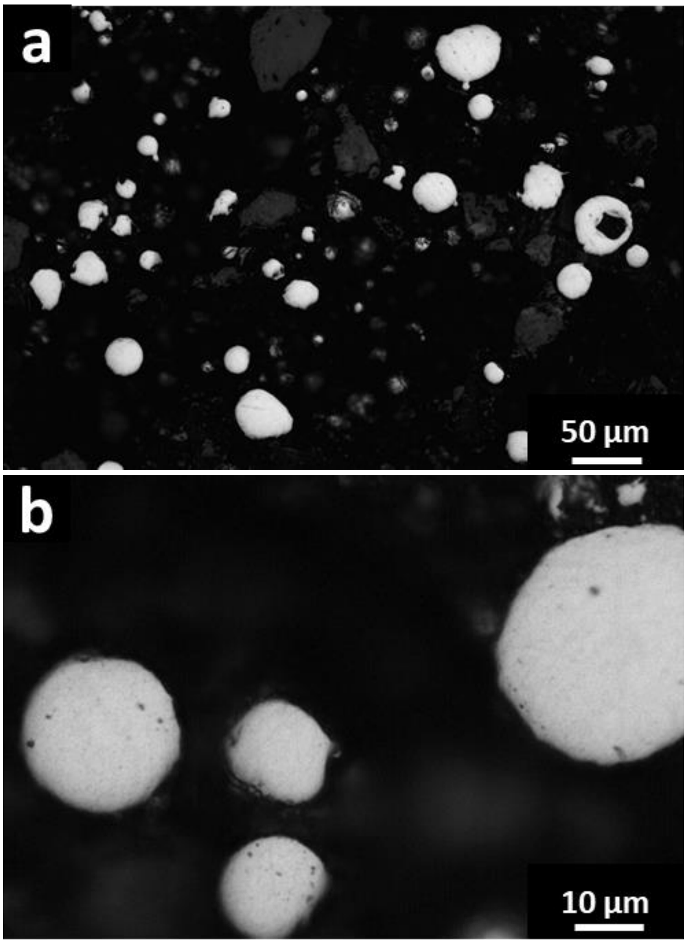

Figure 113: Optical image of the cross section of IN939 powder, with presence of some a) big and irregular and b) sub micrometric internal pores

Further observations on the particle cross sections were performed by SEM analysis, after chemical etching with Kalling reagent n°2. As showed in Fig.114, the particle is composed by a fine dendritic structure with dimension 1 ± 0.2 µm, bringing to a cooling rate of $1.04*10^5$ K/s using the formula applied in the previous chapter (eq. n°7, section 3.1.1.1), compatible with the typical cooling rate of gas atomization process (10^5 K/s) [137]. At higher magnifications, the black spots present were identified to be pores as well as cavities created by the chemical etching.

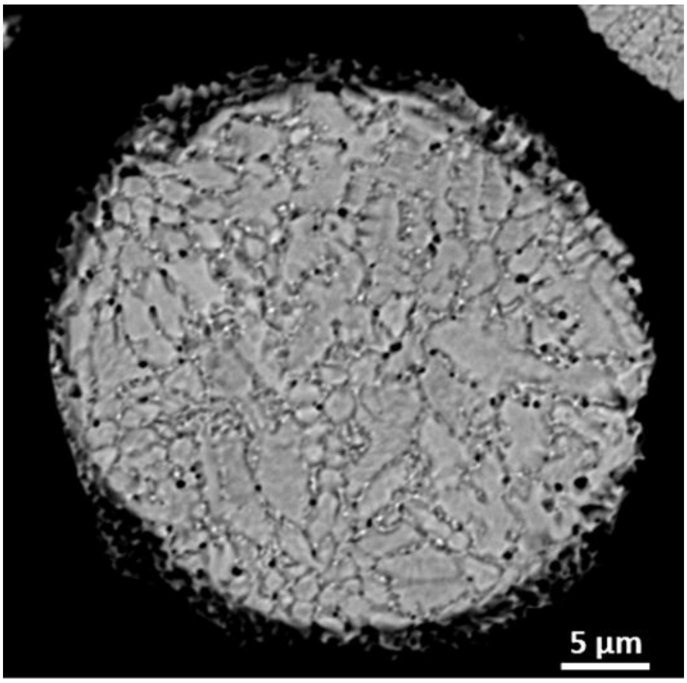

Figure 114: SEM image of the cross section of a IN939 particle etched with kalling reagent n°2

An EDS map was performed on the dendritic structures in order to understand how the chemical elements are located (Fig.115). According to the analysis, the dendritic core is rich in Ni, Cr, Co, Al and W while Nb, Ti and Ta tend to segregate in the interdendritic areas, also as reported for the as cast IN939 in the literature [20].

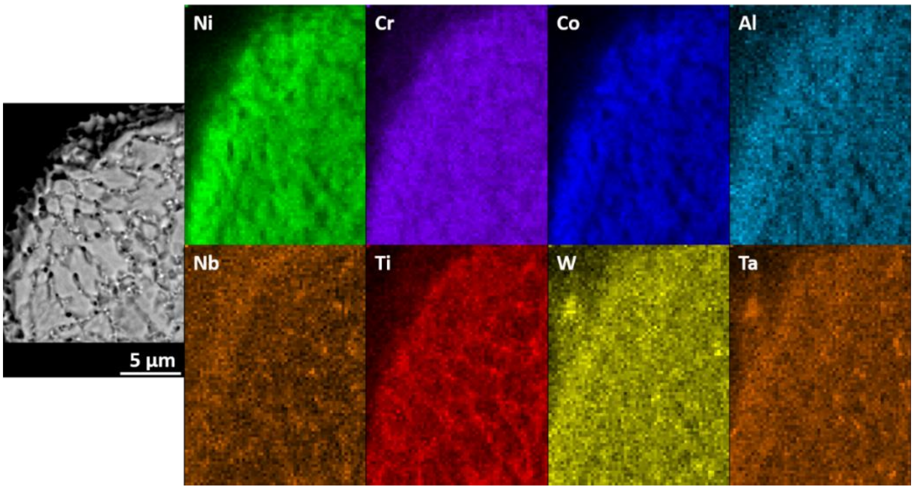

Figure 115: EDS map of a IN939 particle etched with kalling reagent n°2, which reveals the presence of Ni,Cr, Co, Al and W in the dendritic core and enrichment of Nb, Ti and Ta in the interdendritic areas

4.2 Process parameters optimization

The process parameters optimization was performed using a combination of different parameters, in order to provide different energy to melt the layer of loose powder. In order to select the parameters, the volumetric energy density (VED, J/mm^3) approach was employed. The VED formula is reported below:

$$\boldsymbol{VED = \frac{P}{v * t * h_d}} \tag{9}$$

Where **P** is the laser power in W, **v** is the scanning speed in mm/s, **t** is the powder layer thickness in mm and $\mathbf{h_d}$ is the etching distance in mm.

The range of VED values was selected considering the values reported in the literature for the Ni-based superalloys [50,76,77] including the LPBF IN939 alloy [24]. It should be noted that there are no published papers about the process parameters optimization on LPBF IN939 alloy. In fact, the papers on LPBF IN939 mainly focused on the mechanical characterization in the as-built and heat-treated states applying a precise set of process parameters [24,135].

Based on these investigations, it was initially selected a VED ranging from 65 to 320 J/mm^3. In order to obtain these VED values, it was selected hatching distance ($\mathbf{h_d}$) between 0.05 and 0.15 mm and the laser scanning speed (**v**) between 100 and 800 mm/s while the laser power (**P**, 95 W) and the powder layer thickness (**t**, 20 µm) were kept constant. The scanning strategy used was also fixed, applying a strategy that uses stripes with width of 5 mm and a rotation of 67° between each layer (see paragraph 2.1 for more details). The resulting VED values obtained by the combination of the different process parameters are listed in Table.27. The used parameters are marked in yellow.

Table 27: table of the resulting VED using different combination of h_d (unit mm) and v (unit mm/s). Combinations performed during the first job are marked in yellow. P = 95 W and t = 20 micron

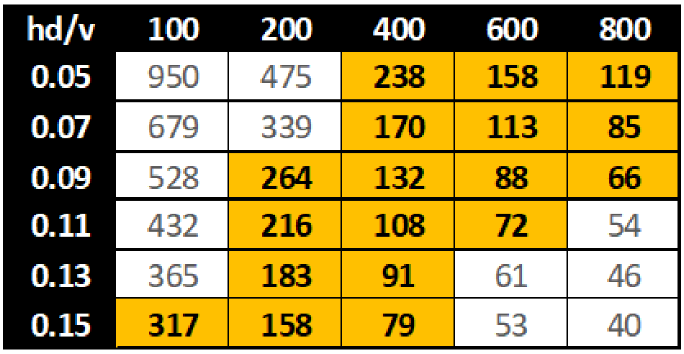

hd/v	100	200	400	600	800
0.05	950	475	**238**	**158**	**119**
0.07	679	339	**170**	**113**	**85**
0.09	528	**264**	**132**	**88**	**66**
0.11	432	**216**	**108**	**72**	54
0.13	365	**183**	**91**	61	46
0.15	**317**	**158**	**79**	53	40

Subsequently, the process parameters of the further jobs were assigned from the characterization of the first job. It is possible to notice that VED higher than 170 J/mm^3 have a negative impact on the densification of the IN939 samples, as can be seen in Fig.116a. Fig.116b shows the resulting void fraction of samples built with different $\mathbf{h_d}$ and **v**. From the graph, the void fraction decreases with the increment of v, indicating that lower energy input (lower VED values) can be positive for the densification of the alloy. Therefore, scanning speed higher than 600 mm/s should be employed.

Moreover, reducing the $\mathbf{h_d}$ helps to limit the voids. In fact, the reduction of $\mathbf{h_d}$ promotes a major overlapping between consecutive laser scans, reducing the risk of pores due to presence of unmelted areas. Therefore, it seems useful to employ **h_d** ≤ 0.09 mm.

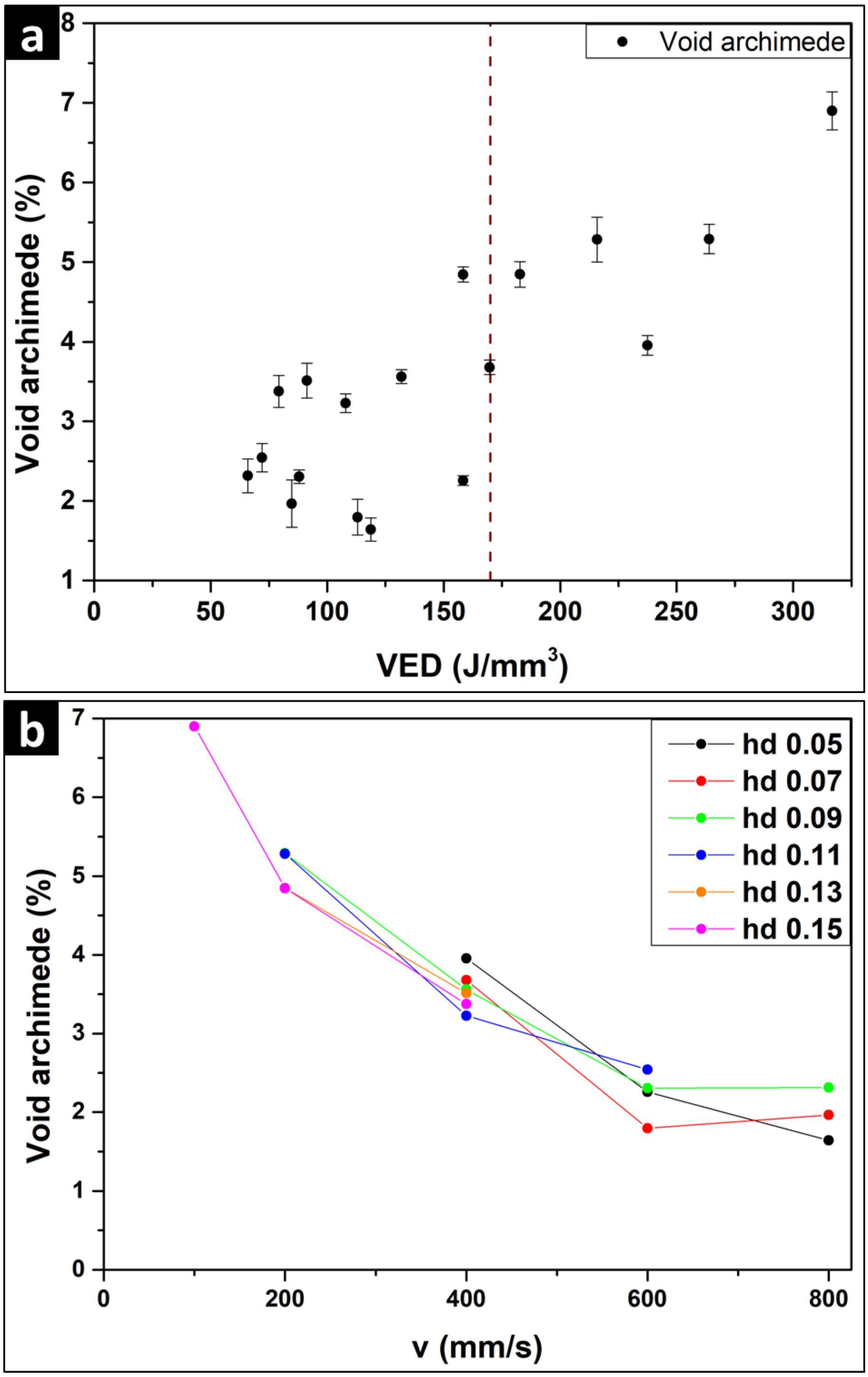

Figure 116: Void content of the 1° Job performed evaluated through Archimede density method in function of applied (a) VED, (b) h_d

Based on the results shown in Fig.6a and 6b, for the following trials, it was used VED from 30 to 170 J/mm^3, obtained using **h_d** between 0.02 and 0.09 mm and **v** between 600 and 2200 m/s, with constant **P** and **t.** The set of process parameters used together with their VED values are listed in Table.28.

Table 28: Table of the resulting VED using different combination of h_d and v for the trials performed after the first one. Only the VED values between 30 and 170 J/mm^3 were employed (highlighted by yellow).

hd/v	600	800	1000	1200	1400	1600	1800	2000	2200
0.02	396	297	238	198	170	148	132	119	108
0.03	264	198	158	132	113	99	88	79	72
0.05	158	119	95	79	68	59	53	48	43
0.07	113	85	68	57	48	42	38	34	31
0.09	88	66	53	44	38	33	29	26	24

Table.29 provides all the combination of process parameters used with the resulting level of void % (evaluated through Archimede method, that counts both porosity and cracks together), porosity % and cracks density (both evaluated with ImageJ analysis) and the hardness (Brinell).

Table 29: List of the parameter sets used for the production of each sample and resulting total void content obtained using Archimede density system, porosity content and crack density evaluated through Image J software and Birnell hardness . P = 95 W t= 20 micron are constant; (j1, j2, j3 indicate the job number).

Sample ID	v	hd	VED	Void archimede	Porosity ImageJ	Crack density	Hardness
	mm/s	mm	J/mm^3	%	%	mm/mm^2	HB
1 j1	100	0.15	317	6.90 ± 0.24	8.79 ± 1.24	0.65 ± 0.36	263 ± 6
2 j1	200	0.09	264	5.29 ± 0.18	8.35 ± 1.77	1.60 ± 0.62	256 ± 6
3 j1	200	0.11	216	5.28 ± 0.28	2.83 ± 2.04	3.51 ± 1.38	252 ± 8
4 j1	200	0.13	183	4.85 ± 0.16	3.54 ± 1.59	3.30 ± 0.44	253 ± 6
5 j1	200	0.15	158	4.84 ± 0.10	3.37 ± 15.8	4.22 ± 0.78	253 ± 11
6 j1	400	0.05	238	3.95 ± 0.13	2.54 ± 1.10	2.88 ± 0.56	273 ± 12
7 j1	400	0.07	170	3.68 ± 0.09	3.40 ± 0.99	2.58 ± 1.46	265 ± 2
8 j1	400	0.09	132	3.56 ± 0.09	3.39 ± 2.24	1.40 ± 0.90	268 ± 8
9 j1	400	0.11	108	3.23 ± 0.12	1.43 ± 0.34	1.36 ± 1.16	267 ± 3
10 j1	400	0.13	91	3.51 ± 0.22	1.74 ± 0.36	1.58 ± 0.74	265 ± 4
11 j1	400	0.15	79	3.37 ± 0.20	2.07 ± 0.36	5.90 ± 0.79	260 ± 3
12 j1	600	0.05	158	2.26 ± 0.06	0.57 ± 0.46	4.05 ± 1.10	289 ± 7
13 j1	600	0.07	113	1.80 ± 0.22	0.50 ± 0.17	3.89 ± 0.55	290 ± 3
14 j1	600	0.09	88	2.30 ± 0.09	0.92 ± 0.22	6.23 ± 0.70	275 ± 5
15 j1	600	0.11	72	2.54 ± 0.18	0.82 ± 0.14	2.09 ± 1.18	274 ± 4
16 j1	800	0.05	119	1.64 ± 0.15	0.53 ± 0.08	1.54 ± 0.86	310 ± 3
17 j1	800	0.07	85	1.97 ± 0.30	0.84 ± 0.14	2.98 ± 0.93	291 ± 2
18 j1	800	0.09	66	2.32 ± 0.21	0.81 ± 0.15	3.16 ± 1.33	280 ± 1
12 j2	600	0.05	158	1.50 ± 0.09	0.58 ± 0.21	3.36 ± 1.19	304 ± 5
13 j2	600	0.07	113	1.78 ± 0.05	0.78 ± 0.40	4.60 ± 1.25	290 ± 6
14 j2	600	0.09	88	1.89 ± 0.01	0.82 ± 0.27	5.97 ± 0.60	278 ± 4
16 j2	800	0.05	119	1.03 ± 0.03	0.28 ± 0.09	1.13 ± 0.52	315 ± 2
17 j2	800	0.07	85	1.42 ± 0.01	0.29 ± 0.13	2.83 ± 0.91	291 ± 6
18 j2	800	0.09	66	1.63 ± 0.02	0.36 ± 0.18	4.33 ± 1.08	288 ± 7
19 j2	1000	0.03	158	1.02 ± 0.01	0.14 ± 0.08	0.80 ± 0.56	316 ± 4

20 j2	1000	0.05	95	1.03 ± 0.05	0.21 ± 0.12	0.82 ± 0.57	314 ± 4
21 j2	1000	0.07	68	1.42 ± 0.01	0.21 ± 0.09	2.60 ± 1.08	305 ± 2
22 j2	1000	0.09	53	2.14 ± 0.02	1.83 ± 0.45	0.99 ± 0.68	296 ± 4
23 j2	1200	0.03	132	1.07 ± 0.02	0.17 ± 0.08	0.38 ± 0.12	319 ± 5
24 j2	1200	0.05	79	0.95 ± 0.02	0.17 ± 0.11	0.35 ± 0.33	323 ± 3
25 j2	1200	0.07	57	1.43 ± 0.07	3.06 ± 0.35	0.22 ± 0.20	310 ± 3
26 j2	1200	0.09	44	4.39 ± 0.03	18.41 ± 3.14	0.60 ± 0.23	246 ± 25
27 j2	1400	0.02	170	4.66 ± 0.02	12.59 ± 4.80	0.64 ± 0.33	238 ± 32
28 j2	1400	0.03	113	0.95 ± 0.03	0.35 ± 0.21	0.55 ± 0.24	325 ± 8
29 j2	1400	0.05	68	1.18 ± 0.03	0.96 ± 0.76	0.51 ± 0.24	321 ± 5
30 j2	1400	0.07	48	3.38 ± 0.04	10.33 ± 3.19	0.75 ± 0.42	268 ± 20
31 j3	1400	0.09	38	6.85 ± 0.02	12.51 ± 1.99	0.66 ± 0.44	211 ± 8
32 j3	1600	0.02	148	2.57 ± 0.02	5.25 ± 3.76	0.69 ± 0.60	276 ± 44
33 j3	1600	0.03	99	0.99 ± 0.03	0.53 ± 0.23	0.23 ± 0.11	326 ± 7
34 j3	1600	0.05	59	1.97 ± 0.03	1.40 ± 0.52	0.54 ± 0.23	308 ± 7
35 j3	1600	0.07	42	4.49 ± 0.01	7.60 ± 2.76	1.28 ± 0.31	252 ± 20
36 j3	1600	0.09	33	7.80 ± 0.05	17.65 ± 4.18	0.76 ± 0.38	183 ± 5
37 j3	1800	0.02	132	3.84 ± 0.03	8.20 ± 2.85	0.70 ± 0.31	262 ± 12
38 j3	1800	0.03	88	1.13 ± 0.03	0.67 ± 0.22	0.08 ± 0.02	324 ± 2
39 j3	1800	0.05	53	2.12 ± 0.03	3.28 ± 1.50	0.30 ± 0.12	297 ± 14
40 j3	1800	0.07	38	9.04 ± 0.01	19.51 ± 1.48	0.18 ± 0.08	188 ± 16
41 j3	2000	0.02	119	5.02 ± 0.04	9.82 ± 3.36	0.22 ± 0.14	220 ± 29
42 j3	2000	0.03	79	1.37 ± 0.04	1.29 ± 0.33	0.15 ± 0.14	326 ± 8
43 j3	2000	0.05	48	4.63 ± 0.04	7.26 ± 1.58	0.17 ± 0.05	271 ± 6
44 j3	2000	0.07	34	8.16 ± 0.02	23.33 ± 3.25	0.31 ± 0.21	161 ± 8
45 j3	2200	0.02	108	7.01 ± 0.03	15.40 ± 1.98	0.15 ± 0.06	207 ± 7
46 j3	2200	0.03	72	2.14 ± 0.02	3.59 ± 1.64	0.20 ± 0.13	301 ± 23
47 j3	2200	0.05	43	6.72 ± 0.03	12.96 ± 2.57	0.38 ± 0.17	237 ± 6
48 j3	2200	0.07	31	9.59 ± 0.04	41.55 ± 3.94	0.31 ± 0.16	139 ± 5

The void % of the samples was evaluated using two different methods, the Archimedes method and the ImageJ analisys (both considering pores and cracks). The results are reported in Fig.117. It can be noticed that the void content change drastically changing the evaluation method.

In the first part of the graphs (VED < 50) the Archimedes method reports a lower content of void compared to the ImageJ analysis. This can be explained by the presence of interconnected pores, that allow the entrance of water in the sample, misrepresenting the density evaluation. Instead the higher void content of Archimede for the samples with high density can be attributed to the presence of air trapped inside the cracks, which can reduce the value of the density [138]. Therefore, the void level obtained by analysing the OM micrographs using ImageJ is more representative of the effective densification level of the alloy.

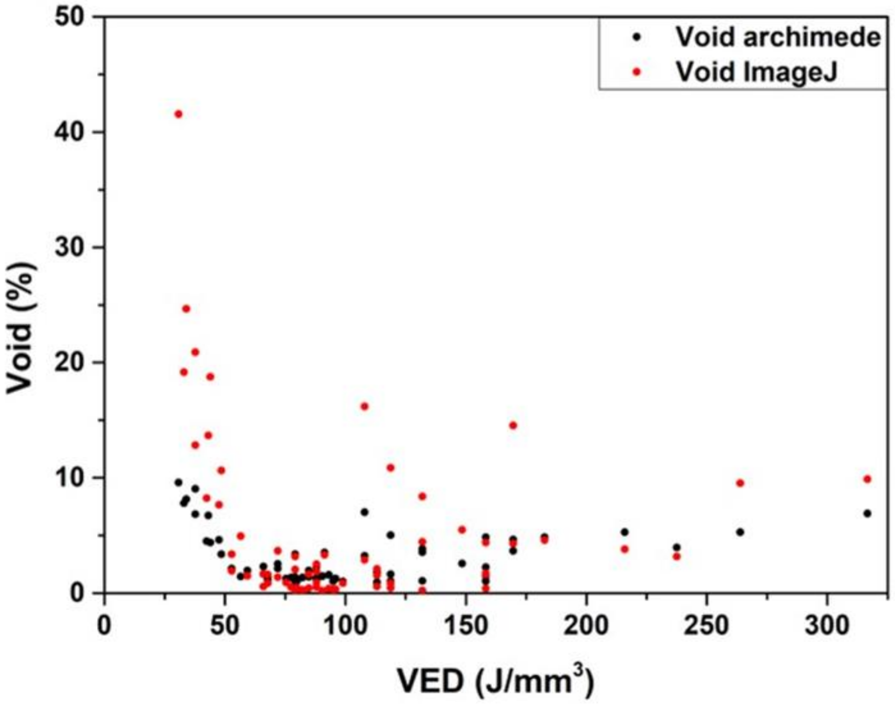

Figure 117: Void % content of the samples in function of the VED applied in the printing process, evaluated with Archimede method (black) and ImageJ analysis (red).

4.2.1 VED effects on porosity, cracking and hardness

The graph in Fig.118a shows how the applied VED influences the porosity content in the LPBF built IN939. It can be seen that the porosity level is low using VED range roughly between 50 and 160 J/mm^3. Samples built with VED below this range show a high content in porosity, from 7 up to 41.55 % (as reported in Fig. 118a). In this last case, it is possible to notice that the voids are probably caused by lack of fusion phenomena and balling effect due to the low energy given to the powder [39]. On the other hand, samples fabricated with VED higher than 160 J/mm^3, reveal high porosity level probably due to the occurrence of melt pool instability, hindering a complete spread of the melt on the substrate and trap bubble of the gas in the melt pool [139], leading to the formation of an important content of nearly-spherical pores (Fig.118b). The VED window between 50 and 160 J/mm^3 allows the production of samples with porosity level lower than 2% (0.14% at minimum), however, samples with similar or even equal VED are characterized by very different porosity content, probably because the same VED value can be obtained with multiple combination of **v** and **h$_d$**, and the effect of the single parameter (**v** and **h$_d$** in this work) on the melting process can produce different results. More in details, two samples built with the same VED having different parameters provide the same energy to the volume, but altering the way how the energy is delivered to the unit volume. For instance, a different hatching distance implies a different overlapping between subsequent laser scanning, thus influencing the melting and solidification process. The issues related to the limitation of the VED approach are already reported in literature [49,78].

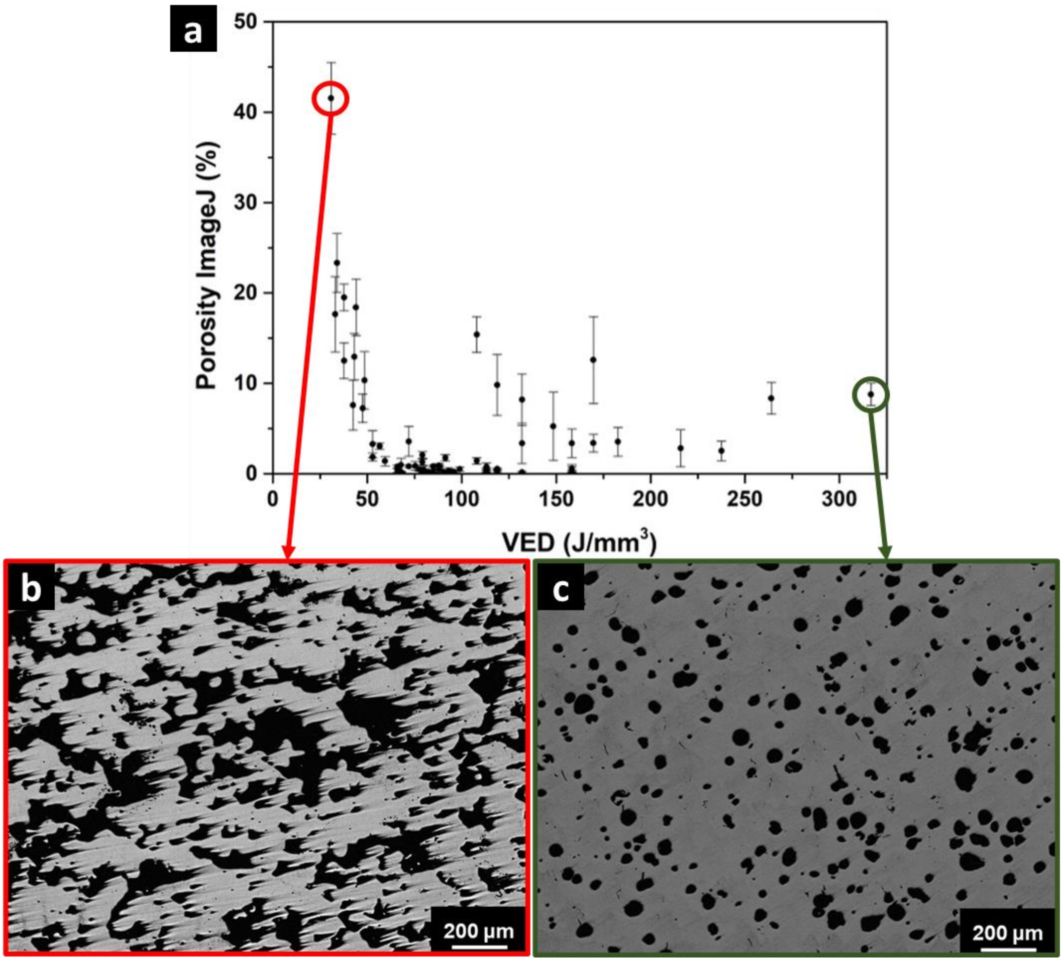

Figure 118: (a) Porosity content of the samples vs. the VED and examples of (b) sample built with low VED and (c) sample fabricated with high VED.

Fig.119 shows micrograph of samples built with the same VED vales using different process parameters. It can be noticed that in each row samples are characterized by the same VED, obtained with different parameter combinations, and the resulting porosity and cracks content are very different, pointing out situations with almost no cracks and very high concentration of porosity, high crack density and low porosity or both equally present. Considering this fact, it is important to study the effect of each parameter and not just the resulting VED. Therefore, the VED approach can be useful to determine a process parameters window that must be reduced by investigating the effect of each parameter. In fact, it is a useful approach in the preliminary part of this kind of studies in order to determine the VED window that avoid high defect formation due to the lack of densification and instability of the melt tracks [49,78].

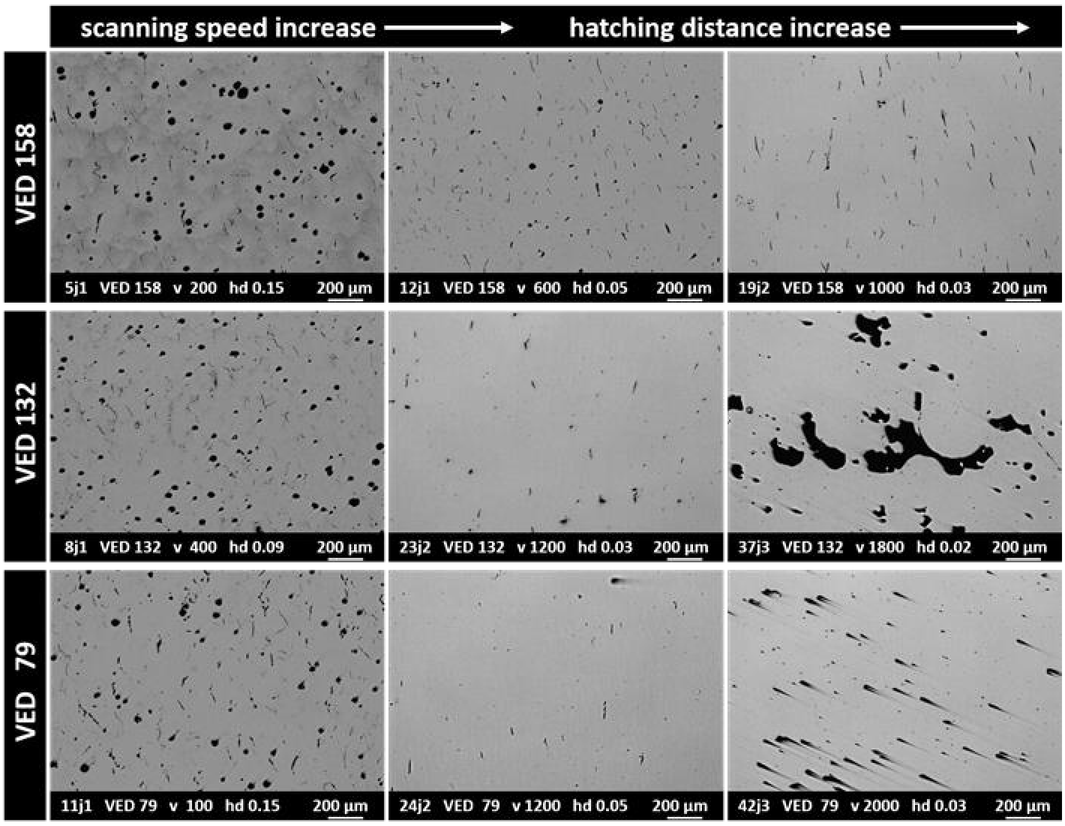

Figure 119: Optical images of LPBF built IN939. Samples in the same row are fabricated with equal VED, increasing both v and h_d moving to the right

From the crack density point of view, it is evident that there is not a clear trend if related with the VED utilized, since in the central part of the graph (Fig.120) there is a huge variability between samples produced with similar VED. This result confirms that the VED approach is limited, and cannot describe alone all the results [49,78].

Correlating this graph with the porosity content one (Fig.118a), it is possible to observe that samples with really high or really low VED possess generally less cracks, maybe due to the fact that their high porosity content permits a better stress accommodation, reducing the cracks occurrence. These aspects will be examined in detail in the next section (4.2.2).

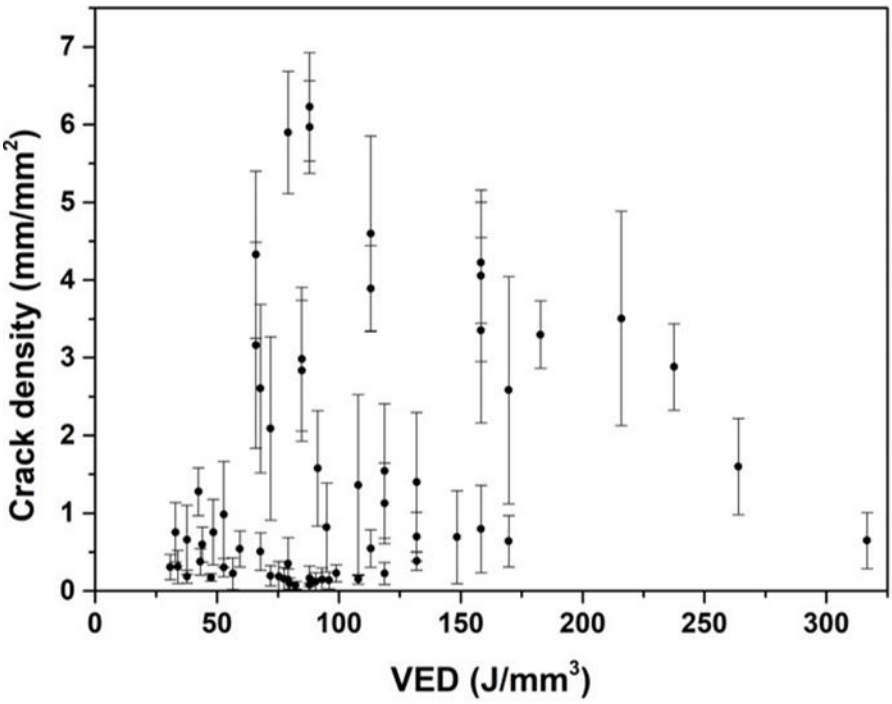

Figure 120: Cracking density of the samples vs. the VED

The hardness results (Fig.121) reveals a trend that is almost opposite compared to the porosity level, making clear that increased density enhance the hardness.

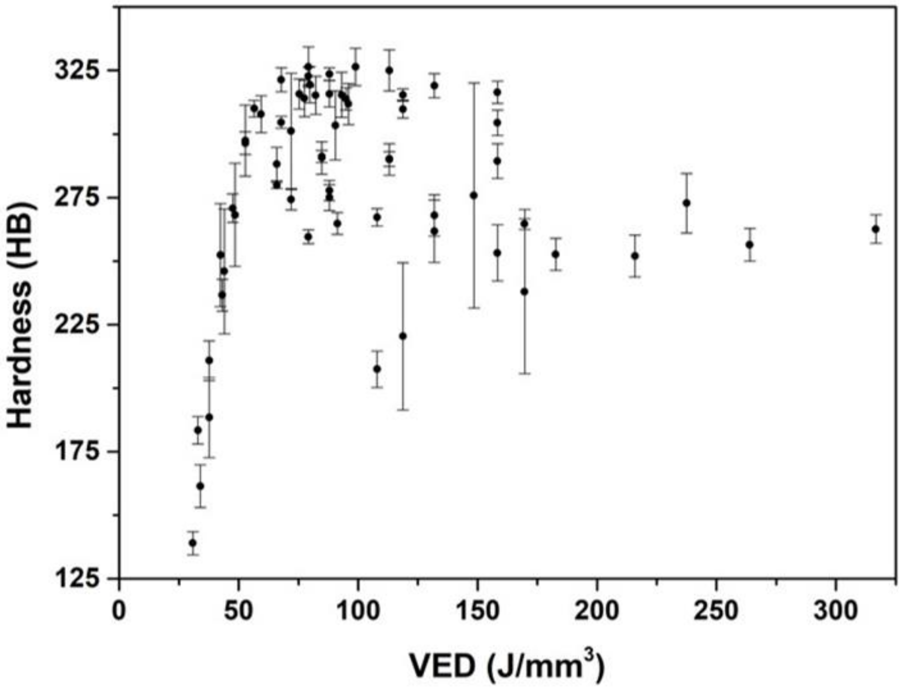

Figure 121: Hardness Brinell of the samples vs. the VED

4.2.2 Scanning speed and hatching distance effects

The porosity vs different scanning speed with the same **h**$_d$ is provided in Fig.122a and Fig.122b. Note that laser power and layer thickness are not taken into account since these parameters are constant for all the samples.

Fig. 122a shows that **v** of 600 and 800 mm/s allow to generate relative dense samples for a wide set of hatching distances (from 0.11 to 0.07 mm). For higher **v** (1000-1600 mm/s), it is still possible to obtain dense samples employing hatching distance from 0.05 to 0.03 mm, as better observable in the zoom in Fig.122b. Moreover, in order to obtain dense samples, 1800 mm/s associated with 0.03 mm still enables the formation of reduced porosity degree. For 2000-2200 mm/s also using **h**$_d$ of 0.03 mm the porosity starts increasing more rapidly. Finally, it is interesting to note that **h**$_d$ of 0.02 mm always generates increment of pores for all the range of scanning speed used, as reported in Fig.123. In fact, this extremely reduced **h**$_d$ probably involves too high overlapping between consecutive laser scanning, making the melt pools instable, thus involving the formation of large pores.

To sum up, all the scanning speed values associated with a specific hatching distance exhibit a range with reduced porosity level. For values superior or inferior to this range, the porosity tends to increase. For lower values, the energy supplier to the system is not sufficient to fully melt the powder generating lack of fusion, while for higher values the energy density it too high making the melt pools instable thus generating large pores. This mechanism is graphically summarized in Fig.124 reporting the trend for **h**$_d$ 0.07 mm that represents one the most marked porosity variations.

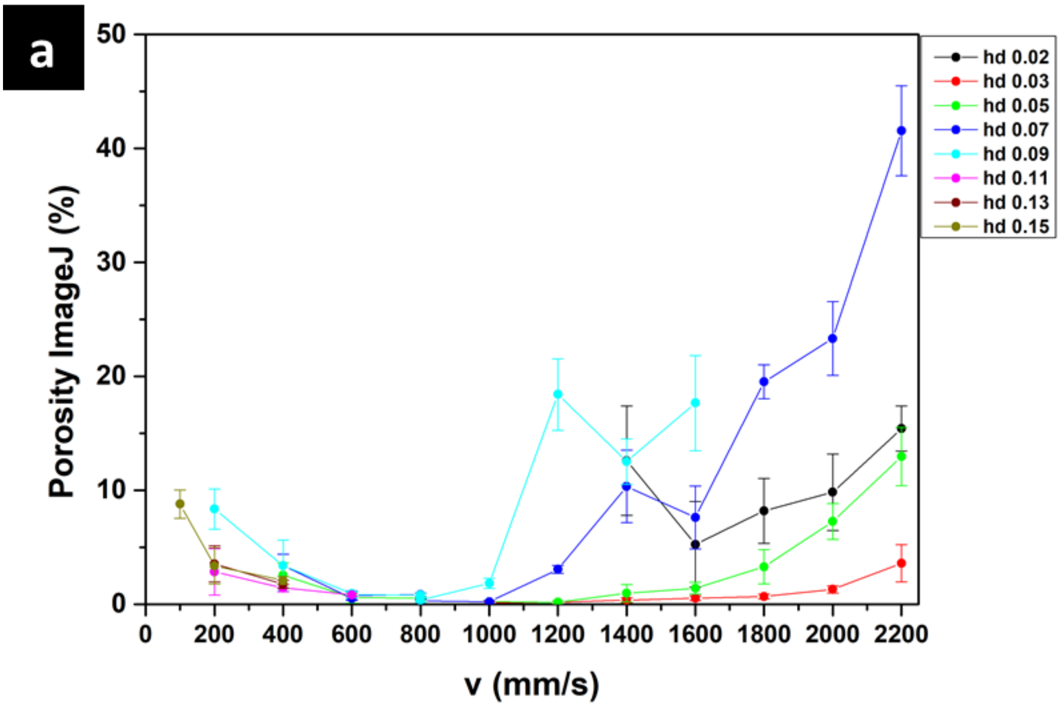

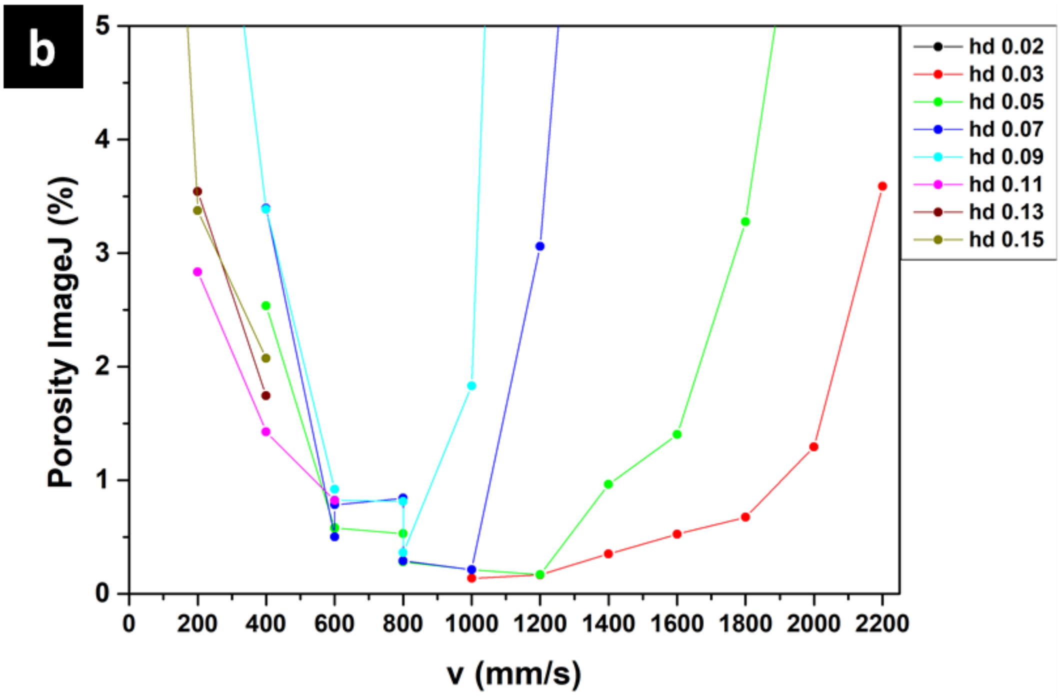

Figure 122: Porosity content of the samples vs. the laser scanning speed (v), a) total and b) zoomed below 5 % of porosity

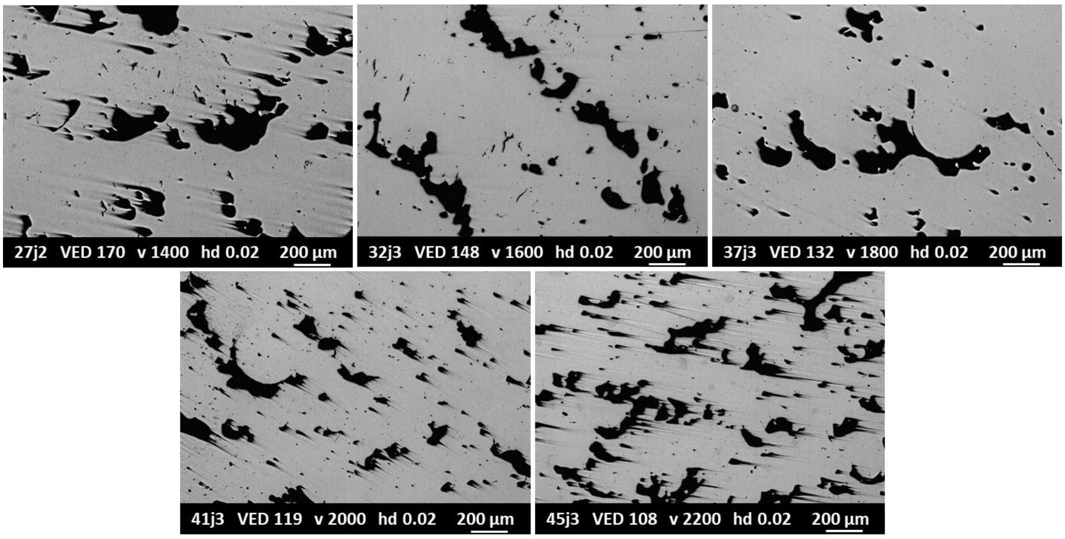

Figure 123: Optical images of IN939 samples printed using a hd value of 0.02 mm at different v

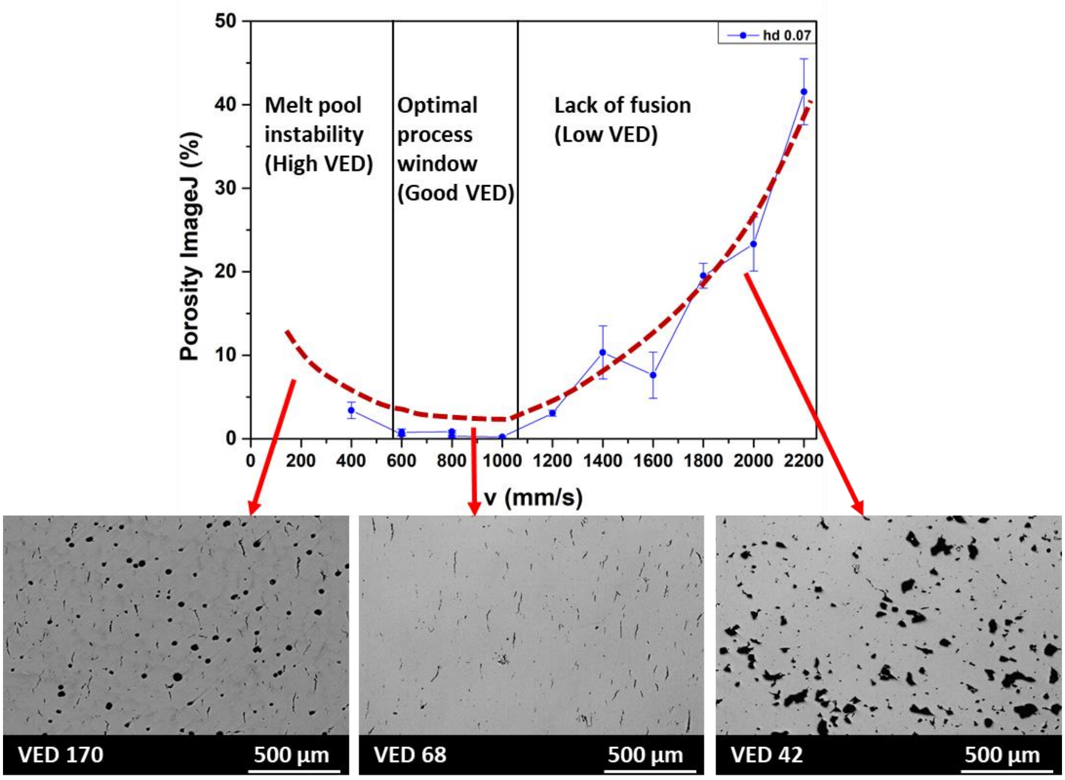

Figure 124: Representation of the v effect at a fixed h_d, with examples of porosity related to the high VED applied, good densification with moderate VED and poor densification for low VED

The crack density vs different **v** with the same $\mathbf{h_d}$ is shown in Fig.125a and Fig.125b.

It can be seen in Fig.125a that **v** up to 1000 mm/s are generally related to a crack density higher than 1 m/mm^2, with the exception of the sample built with **v** 100 m/s and $\mathbf{h_d}$ 0.15 mm due to the very large fraction of pores formed.

As reported in Fig.125b, $\mathbf{h_d}$ between 0.02 mm and 0.09 mm can provide crack density below 1 m/mm^2. Moreover, crack density below 0.6 mm/mm^2 are reported for all the v values higher than 1200 m/s, reaching the best densification level for $\mathbf{h_d}$ 0.03 mm and 0.05 mm. The $\mathbf{h_d}$ 0.02 mm shows really low crack density level, however, the samples content high porosity level.

To sum up, increasing the scanning speed generally reduces the crack density, in particular when coupled with low hatching distance values for **v** higher than 1200 m/s, as summarized in Fig.126. The reason of this behaviour is probably related to entity of the residual stress, precipitation formation and segregation presence, all linked to the thermal history of the LPBF processed alloy. A more detailed discussion of this topic is given in the section 4.3.

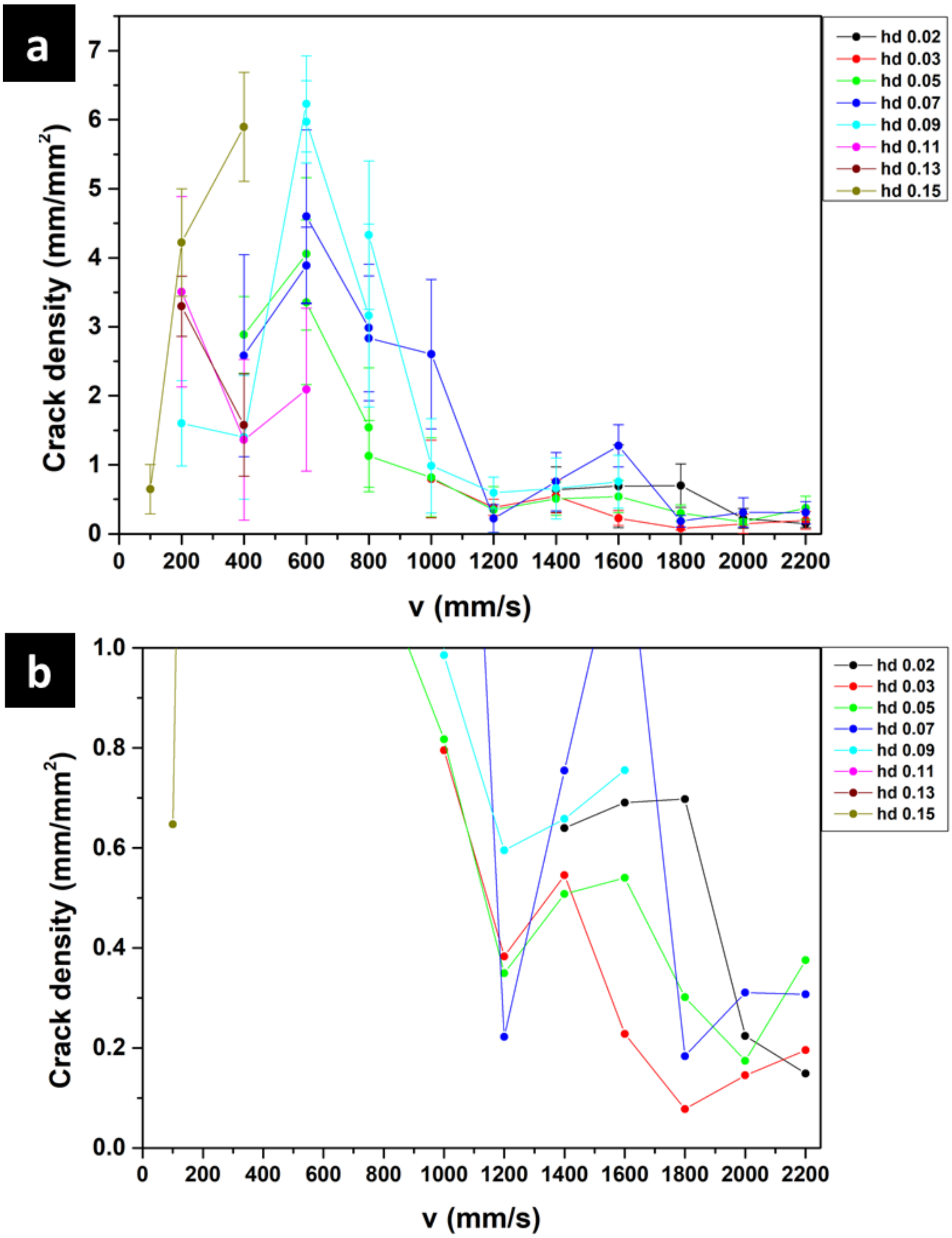

Figure 125: Cracking density of the samples vs. the laser scanning speed (v), a) total and b) zoomed below cracking density 1 m/mm^2

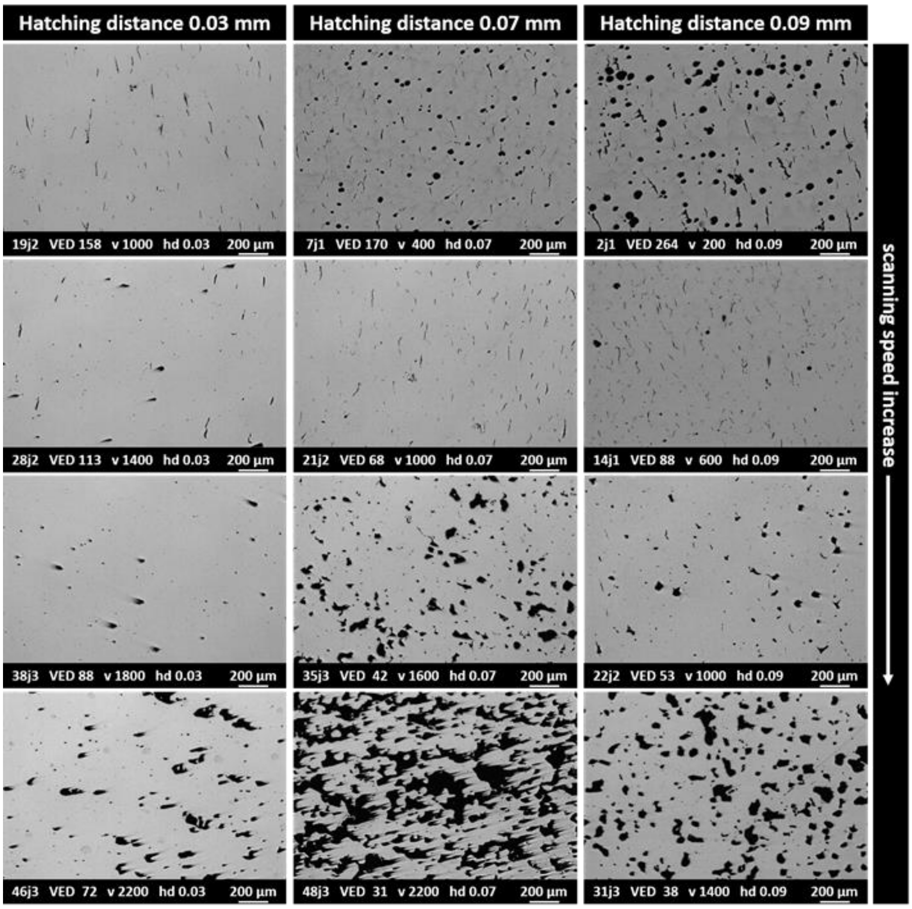

Figure 126: Optical images of LPBF printed IN939. Samples in the same column are printed with equal h_d, moving down in the columns the v is increased and the VED reduced

Fig.127 shows the hardness of the samples produced with different **v** having the same $\mathbf{h_d}$. Observing the trend for each $\mathbf{h_d}$, the hardness reaches a maximum to a certain value and then tends to decrease. The hardness reduction seems to correlate to the densification of the material, with the exception of the samples built with $\mathbf{h_d}$ 0.03 mm, that maintain similar hardness levels from **v** 1000 up to **v** 2000 mm/s even with the porosity content that only increases raising the **v**. However, the hardness values could be also correlated to the thermal history generated by the process parameters influencing the dendritic size and phases precipitation.

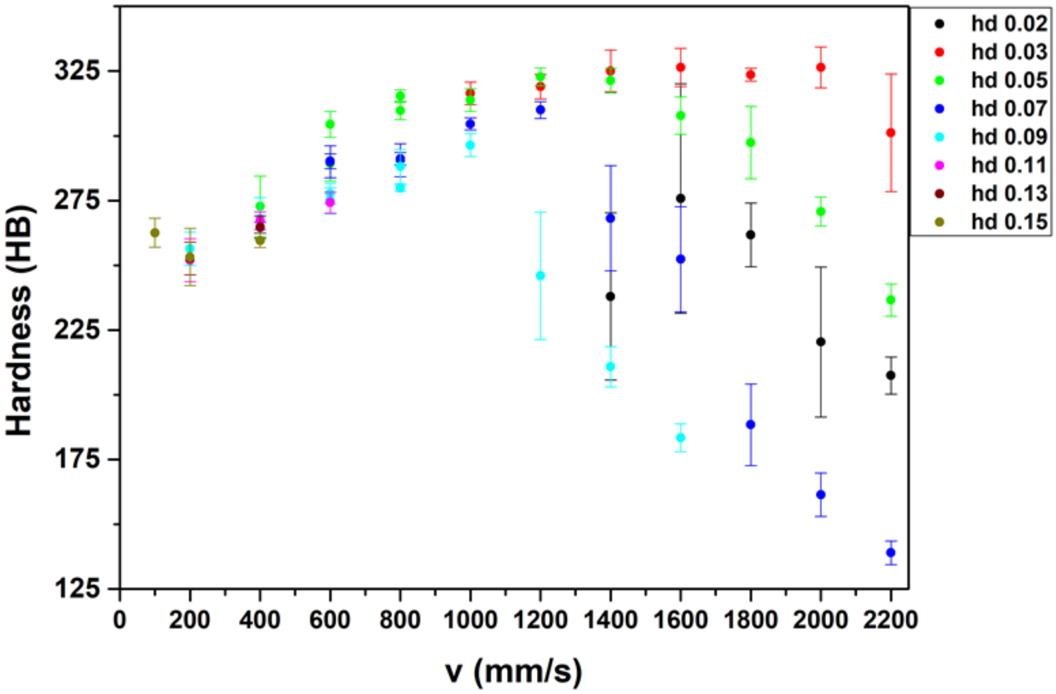

Figure 127: Hardness Brinell of the samples vs. the laser scanning speed (v)

4.2.3 Summary of the selected process parameters

Considering all the results discussed in this section, the discussion in the section 4.3 is focused on the microstructural evaluation of the sample 38 j3, because it is characterized by the lowest crack density among all the conditions and it exhibited a porosity of 0.67 ± 0.22 %, as well as the sample 19 j2, because it revealed the lowest porosity level (0.14 ± 0.08 %) with a medium content of cracks, allowing a good evaluation of the cracks features.

4.3 Microstructural evaluation of LPBF IN939

In this section the characterization of the microstructure is concentrated on the sample 38 j3 (**v** 1800 m/s, **h_d** 0.03 mm) and the sample 19 j2 (**v** 1800 m/s, **h_d** 0.03 mm).

The sample 38 j3 was chosen because it possesses the lowest crack density level obtained (0.08±0.02 mm/mm^2) and a contained porosity (0.67 ± 0.22 %). The sample was used for the microstructural evaluation.

The sample 19 j2 was chosen because possesses the lowest porosity content (0.14 ± 0.08 %) and a consistent number of cracks, making it perfect for the cracks evaluation. The cracking density for this sample is 0.80±0.56 mm/mm^2.

The ZX plane of the IN939 sample 38 j3, formed using LPBF technology, is revealed in Fig.128. The microstructure of the alloy is composed by elongated grains. These grains are characterized by a columnar shape, aligned along the building direction (Z-axis), with a maximum width of 100 µm and a height that also exceeds 500 µm in some case. This height is bigger than the powder layer, confirming that the grains grow epitaxially from a layer to another, as reported for other LPBF nickel-based superalloys, presenting a strong texture of the <100> direction, also found in the case of the IN625 in this thesis [38,54]. The presence of a texture can be observed using XRD analysis, as reported in Fig.129 for the both ZX plane and XY plane. In both cases, only the peaks of the matrix are present, with differences in the relative height due to the grains orientation. The chemical etching also highlighted the melt pool contours, that possess a variable width between each layer, because of the laser scan rotation of 67° between consecutive layers.

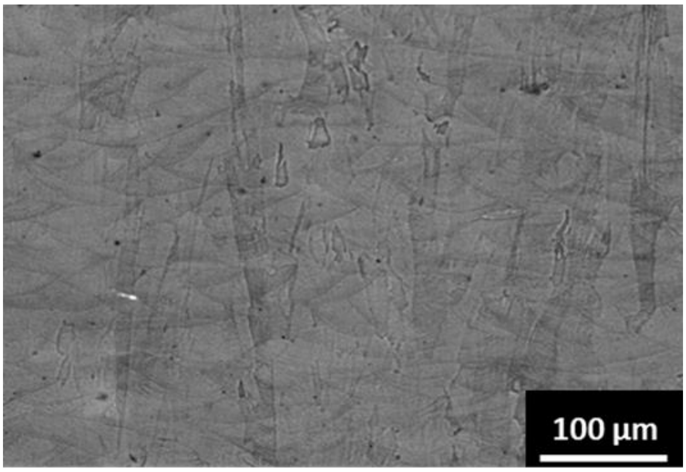

Figure 128: Optical microscopy image of the sample 38 j3, showed on the ZX plane, where columnar grains and melt pools are visible.

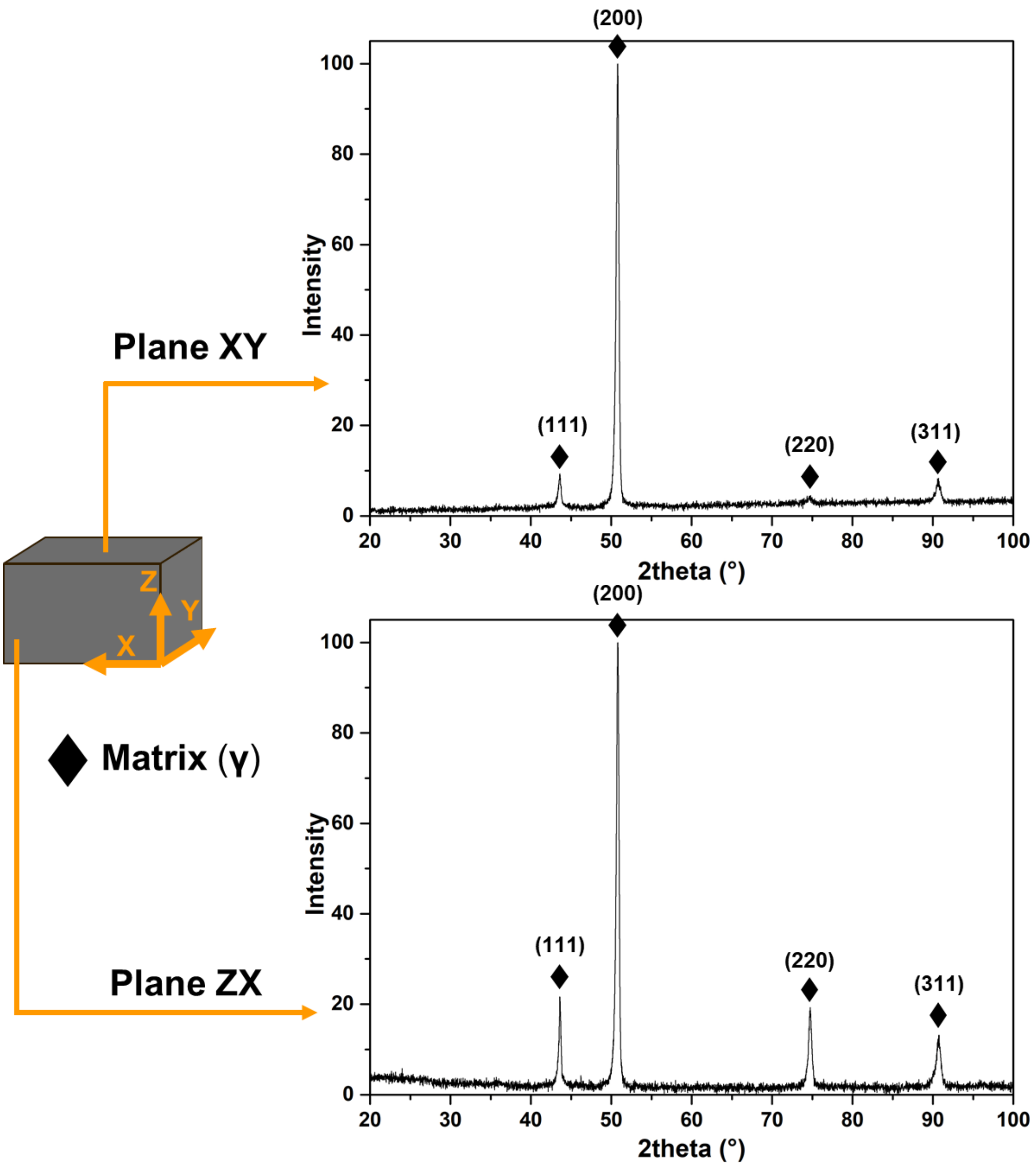

Figure 129: XRD patterns of LPBF IN939 performed on the ZX plane and on the XY plane.

Analysing more in depth the microstructure by SEM microscopy, it can be seen that the grains are composed by fine dendritic structures. These dendrites are organized in zones, some with columnar dendrites (yellow rectangle in Fig.130a, magnified in Fig.130b) and other with cellular dendrites (red rectangle in Fig.130a, magnified in Fig.130c). The dendrites are characterized by a characteristic dimension, the primary dendritic arm spacing (PDAS), that is the distance in µm between the centre of two adjacent dendrites. Using the following equation:

$$\boldsymbol{PDAS = a * \varepsilon^{-b}}$$

where **a** and **b** are constants with values 50 µm and 1/3 respectively for nickel-based alloys, it is possible to evaluate the solidification speed $\boldsymbol{\varepsilon}$ of the alloy [58]. The PDAS in this case was evaluated for the sample 38 j3 on 30 dendrites, obtaining a value of 0.35±0.08 μm, and the calculated solidification speed is $3.01*10^6$ °C/s. This value is compatible with the typical cooling rates of the LPBF process for the Ni-based superalloys [38,57,58].

Observing at high magnification the dendritic structures (Fig.130b, c), it is possible to observe the presence of nanometric precipitates in the interdendritic areas, with dimension below 100 nm. Their size is not enough for evaluate their composition using EDS, but they could be MC carbides or γ' [20]. Both these phases can be formed by eutectic reaction in superalloys [3]. This is because superalloys possess a solidification temperature range: during solidification the primary dendrites are formed at first, growing inside the liquid alloy. More the dendrites grow, more the remaining liquid results enriched in segregating elements [3], such as Ti, Nb and Ta. In this way the last liquid that solidify possesses an higher segregating elements content compared to the dendritic cores [3]. In the case of the LPBF produced alloy the repeated temperature cycling caused by the laser passages could also have an effect in the precipitation mechanism. From the images, it is clear that the large precipitates are along the interdendritic areas. In fact, these areas enriched in segregated elements can accelerate the phases formation [63,108,109].

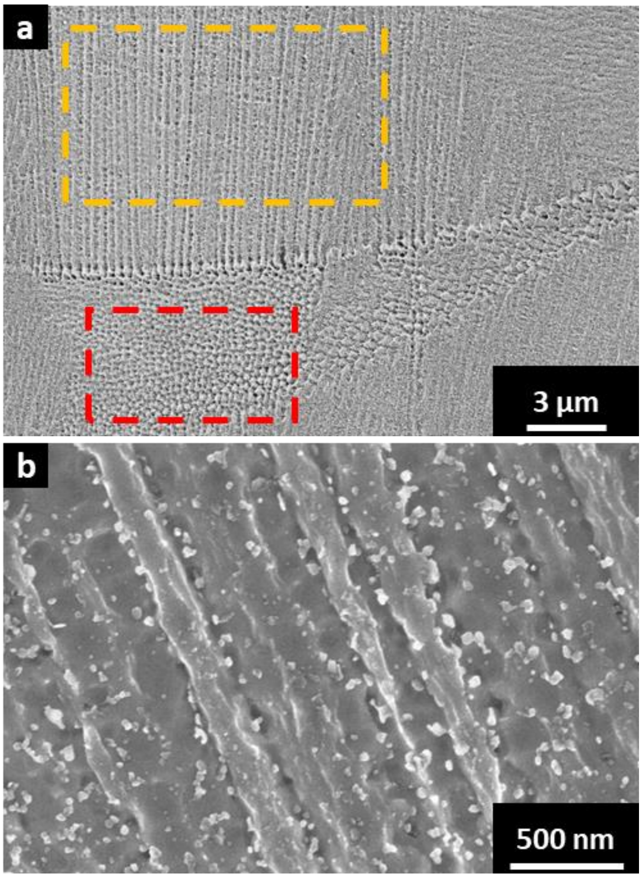

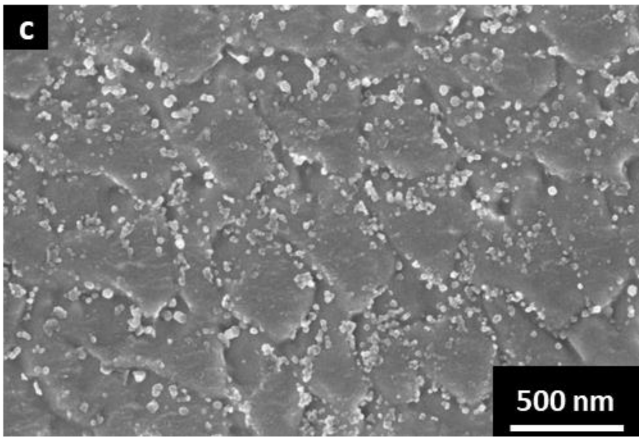

Figure 130: a) SEM images of the sample 38 j3 of IN939 with focus on the dendrites b) columnar, c) and cellular zones

As anticipated previously, in order to characterize the cracks in the LPBF alloy, the sample 19 j2 was examined, since it is characterized by a consistent number of cracks. From Fig.131, it is possible to notice that the cracks are vertically orientated, following the grain boundaries, in accordance to the findings of other authors for crack susceptible Ni-superalloy produced by LPBF [35,51,52,69,70]. A common factor in all the cases are residual stresses generated by the LPBF process, accumulated layer by layer due to fact that the contraction of the solidified alloy during the cooling is limited by the underling alloy as well as the thermal expansion of the alloy right under the melt pool is limited by the cooler alloy below [43,62]. The crack presence has been explained with different cracking mechanisms in literature.

For the case of the IN738LC Rickenbacher et al. identified the cracks origin in the solidification or liquation cracking mechanism since no precipitates were present in the cracks location, caused by the repeated melting coupled with the high stress developed by the LPBF process [71].

Wang and Carter found that the cracks are located on high angle grain boundaries in the alloy CM247LC, and after detecting the presence of carbides proposed ductility dip cracking as cracking mechanism [48,72].

Also Tomus et al. related the cracks formation to the precipitation of intergranular carbides, that coupled with the cyclic thermal stress can act as crack starting points. Moreover, it found that lowering the alloy content of Si and C reduces the cracking development [51].

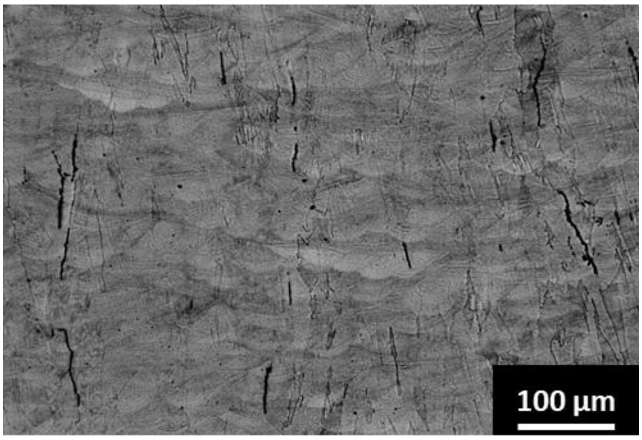

Figure 131: Optical image of multiple cracks on the ZX plane in the etched IN939 19 j2 sample

In order to understand the reasons of the crack formation in the IN939, the internal part of some cracks has been analysed at high magnification (Fig.132). Form the images, it is clear that the internal surfaces of the cracks are decorated with a large number of nanometric precipitates, that can explain the crack formation. They appear bright in the backscattered SEM image (Fig.132b), that may be an indication of carbides rich in heavy element such as Nb. Their size is too small for accurately determine their chemical composition. However, it is possible to infer that the high concentration of nanometric phases along the grain boundaries contribute to form the cracks within the material.

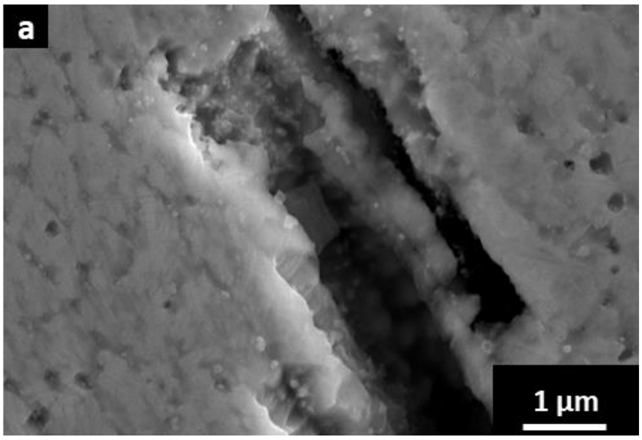

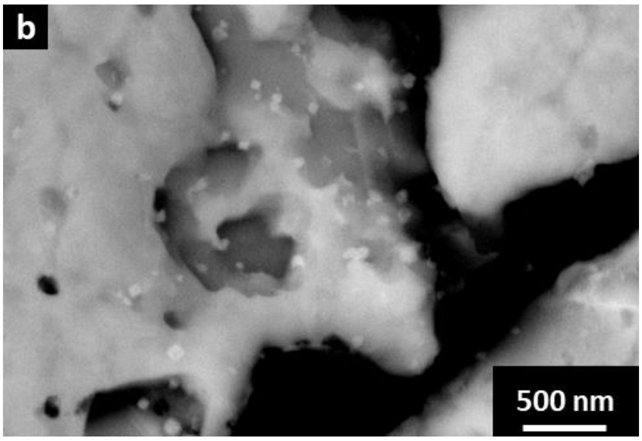

Figure 132: High magnification (a) secondary electron SEM image and (b) backscattered SEM image

In order to have an idea of the composition of the phases present in the cracks, an EDS line (Fig.133a, b) has been performed on some cracks, analysing points in which a little bridge between the two surfaces of the crack are present. The analysis pointed out enrichment of Ti, Si, Nb and C on these bridge zones, indicating the possible presence of carbides. According to literature, MC carbides, such as TiC and NbC can precipitate in the cast IN939 for high solidification speed [20], and this kind of carbides can lead to ductility deep cracking and, as well as γ', are associated to eutectic reactions which can lead to liquation cracking during weldment [26].

Moreover, the repeated heating that the alloy experiences during the production process can cause the precipitation of γ', which is associated to a stress development during precipitation, making this alloy possibly subject to strain age cracking [49].

In order to accurately determine the process responsible of the cracking, future studies will be performed.

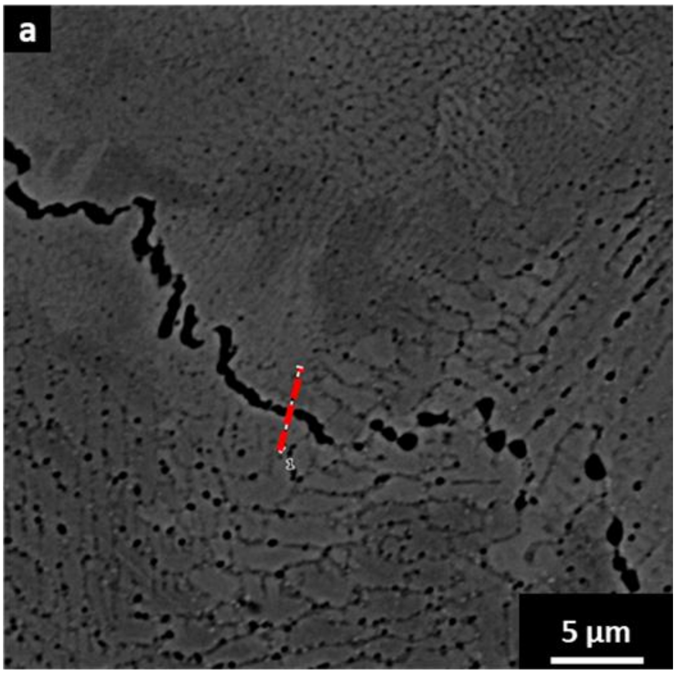

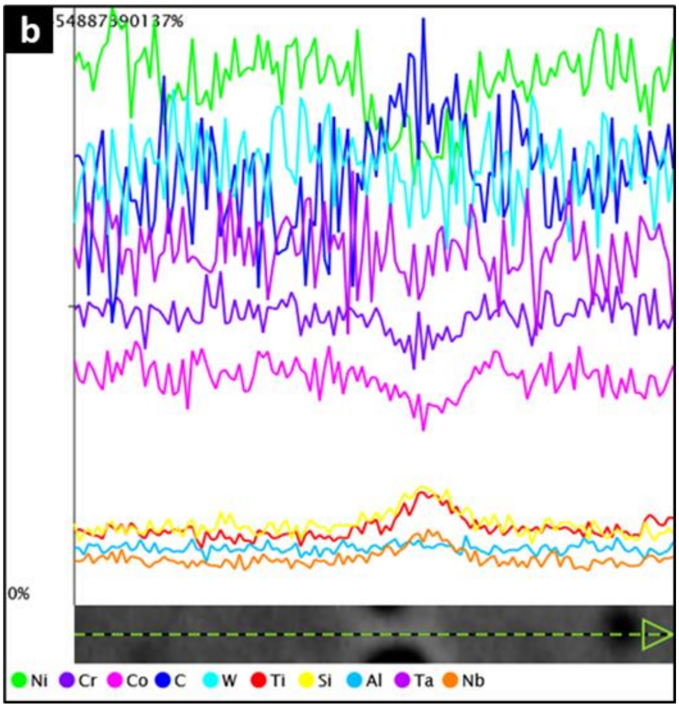

Figure 133: EDS line analysis of a crack in the LPBF produced IN939

Therefore, the cracking mechanisms could be attributed to the nanometric phases along the grain boundaries together with the high residual stresses. These phases could be generated during the LPBF process or by thermal cycling during its production.

4.4 Microstructural evaluation of as-cast IN939

The as cast alloy is characterized by a very different microstructure compared to the LPBF produced alloy. In the un-etched condition (Fig.134a) precipitates are already visible. The performing of the etching makes evident the dendritic structure (Fig.134b), with dendrites that possess a PDAS of 112 ± 35 μm, around 300 times bigger of the LPBF case, that can be related to a solidification rate around 0.3 °C/s according to the literature [140,141], which is slower that LPBF cooling rate evaluated (3.01*10^6 °C/s).

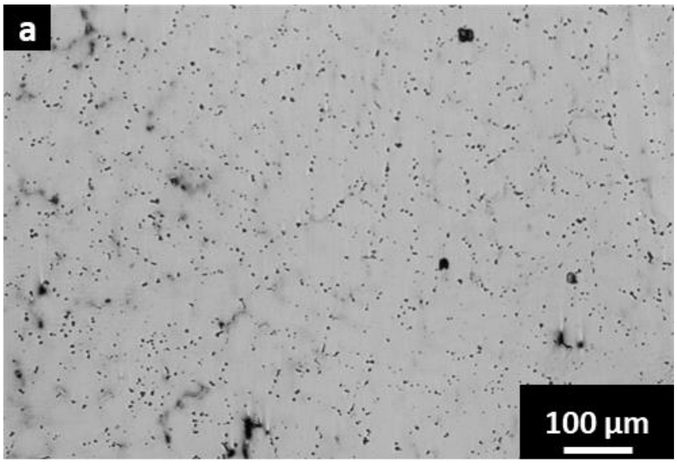

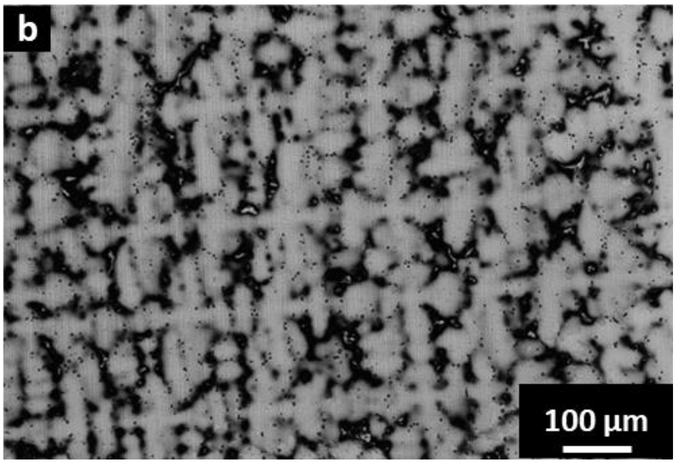

Figure 134: Optical microscope images of the as cast IN939 a) before and b) after chemical etching

The SEM investigation allowed the identification of different phases inside the as-cast microstructure.

In Fig.135 an island of precipitates is present, and from the morphology, according to the literature, these islands can be eutectic regions of **γ/γ’** [26,142], often observed in the as cast condition [20].

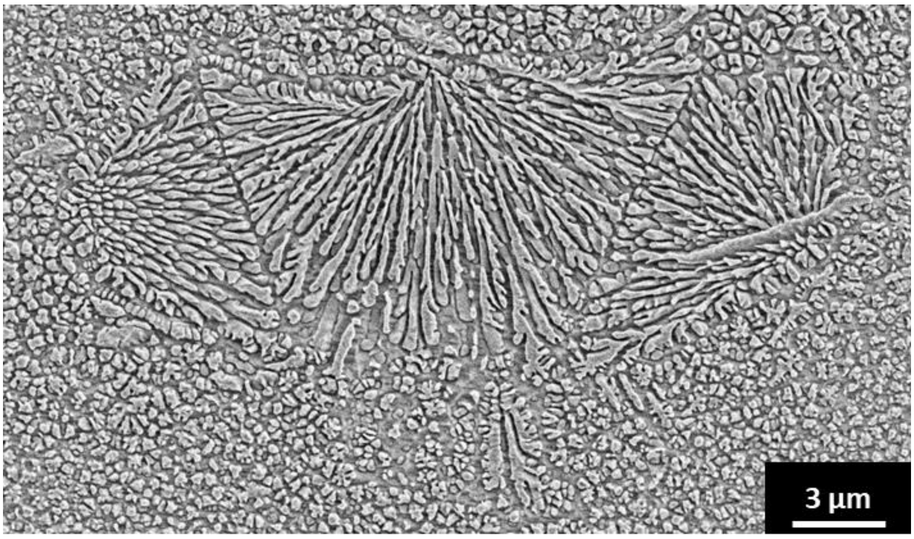

Figure 135: SEM image of the γ/γ’ eutectic region

Another phase observed is an elongated precipitate, with a width up to 10 µm and a length up to 100 µm (Fig.136a). The EDS in Fig.136b reports an increment in both Ni and Ti, without variation in the C content, and these findings point out that probably this precipitate is the **η** (Ni_3Ti) phase, which is a detrimental phase commonly found in the as-cast IN939 and that have to be eliminated using a solution treatment [20,143].

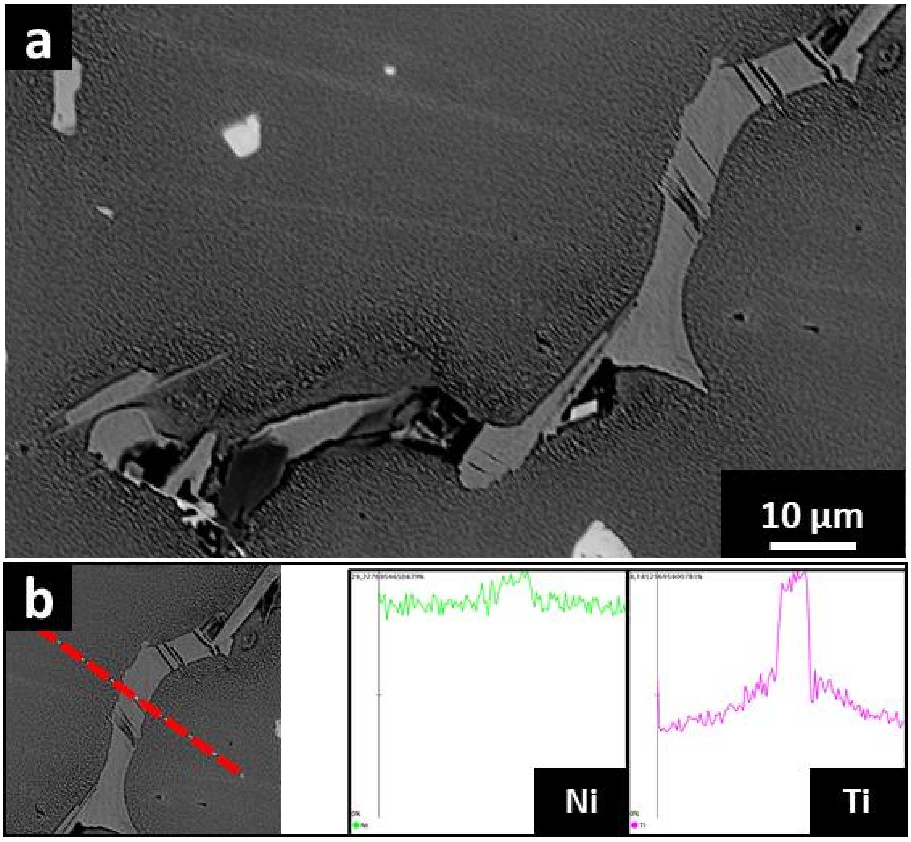

Figure 136: (a) SEM image of and (b) EDS analysis of the η phase

The last phase identified in the as-cast IN939 are carbides, with diameter up to 10 µm. They can be categorized in two types of carbides: with irregular shape or with regular shape.

The carbides with irregular shape result rich in Ti, Ta, Nb, Si and C, as reported in the EDS in Fig.137a, and are probably mixed carbides of the MC and/or M_6C types [20].

The regular shaped carbides (Fig.137b) possess a core, regular shaped also, rich in Ti and C with an Al content in line with the γ matrix, surrounded by a shell rich of Ti, Ta, Nb, Si and C, suggesting that the internal part is probably a MC-type TiC carbide, used as nucleation point for other mixed carbide of the MC and/or M_6C types.

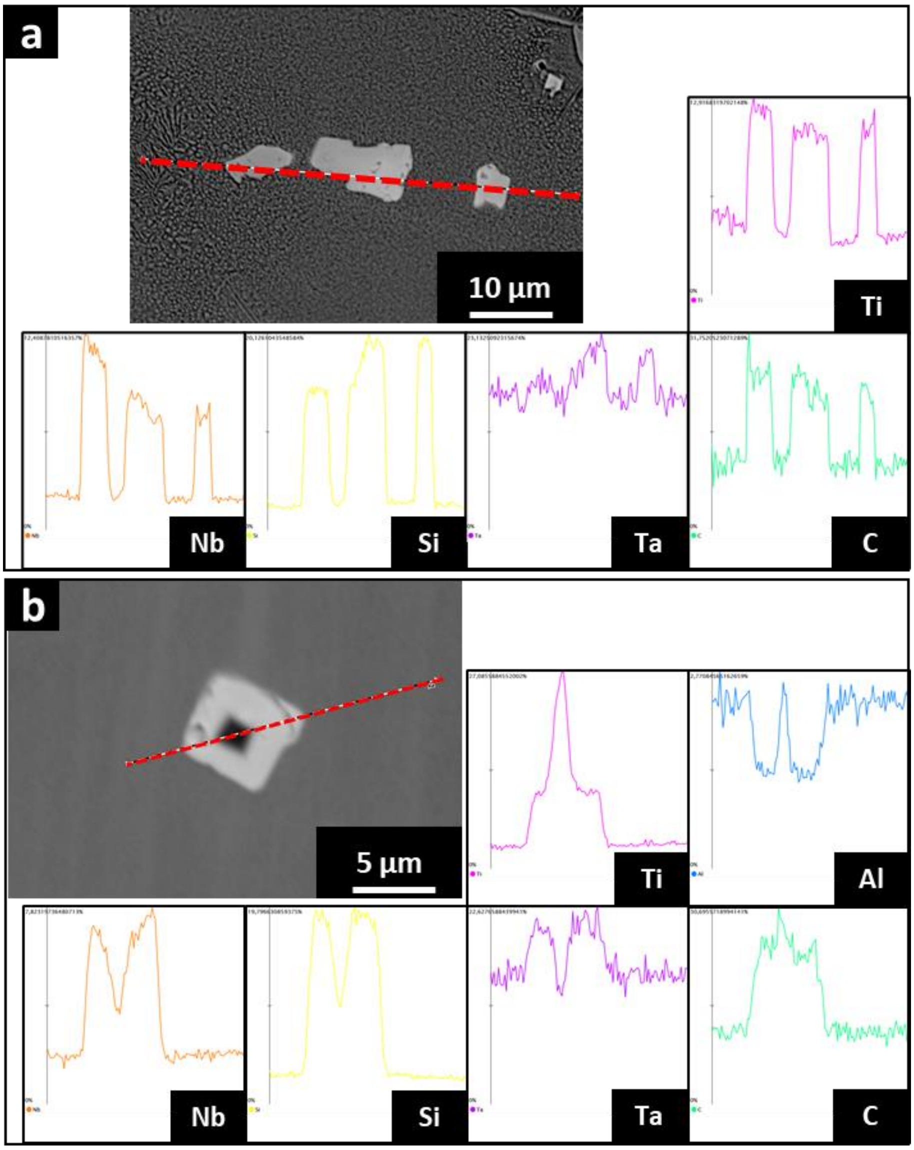

Figure 137: SEM image and EDS analysis of (a) irregular shaped carbides and (b) regular shaped carbides

4.5 Hardness comparison between as-cast and LPBF IN939

The Brinell hardness of the as-cast IN939 is 308±9 HB.

The value of as-cast IN939 is compared to the LPBF IN939 in Figure 138. The hardness is lower compared to samples produced with LPBF using a low $\mathbf{h_d}$, high $\mathbf{v}$ and with a densification level higher than 99 %. The high hardness level of these samples can be related to the low defects content, as well as the fine microstructure given by the LPBF process, as reported by many works in the literature [54,61,100,101,144,145].

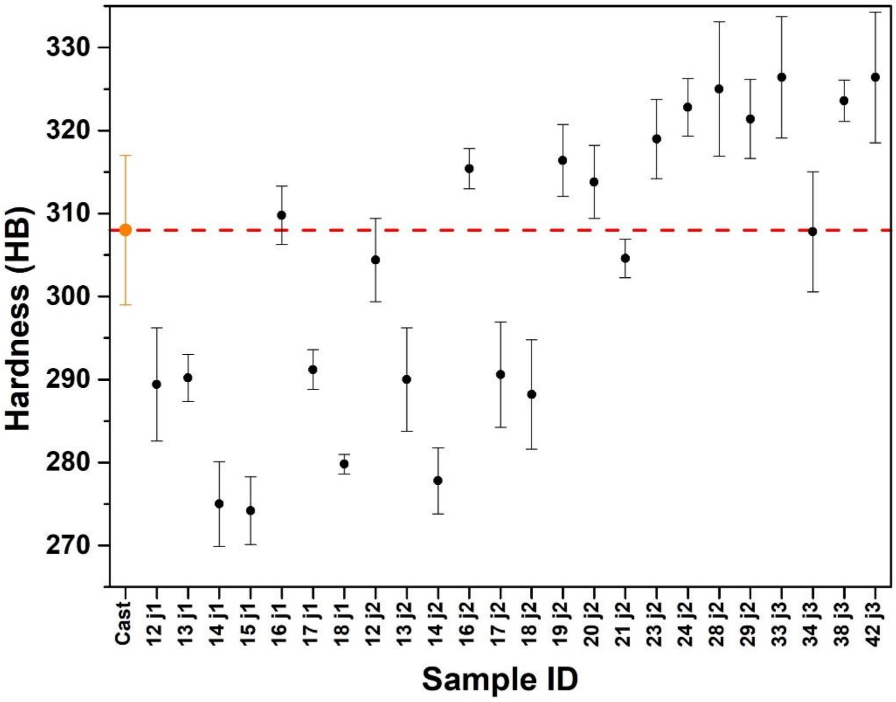

Figure 138: Hardness Brinell values of the LPBF sample printed with porosity level < 1 % and harness level of the as cast sample (red line)

4.6 Results summary of process parameters optimization for IN939

The performed work proved that the production of the LPBF IN939 with extremely limited crack content and high densification level is possible.

The VED approach is useful for identify the limits where lack of fusion (low VED) and melt pool instability (high VED) do not allow a good densification of the powder.

However, since both crack density and porosity content of the built samples using the same VED, but with a different combination of parameters can be different, only study the VED effect it is not enough for fully understand how to reduce the defects formation.

Investigating the effect of the singular parameter, increasing the **v** at a fixed $\mathbf{h_d}$ initially reduces the porosity reaching a minimum porosity level for intermediate **v**. Afterwards, higher **v** increased porosity. This is because of the lowering of the VED linked to the **v** increase, generating no complete melting.

The densification level for a fixed **v** increases lowering the value of $\mathbf{h_d}$, until a limit value of 0.03 mm. Below this level samples start to develop a consistent number of big irregular pores, probably caused by severe melt pool instability, probably due to a too marked overlapping between consecutive laser scan.

The crack density can be reduced increasing the **v** due to less energy delivered to the material, and therefore, less thermal stresses. Also employing low $\mathbf{h_d}$ values results beneficial in the cracks mitigation, probably because allows the use of high **v** without raising too much the resulting VED.

The LPBF built IN939 alloy is characterized by columnar grains and sub-micrometric dendrites and nanometric phases mainly dispersed in the interdentritic areas.

The cracks are aligned along the building direction, located at the grain boundaries and present in the internal surfaces nanometric precipitates that can have a crucial role in the crack formation.

The as-cast microstructure is characterized by a dendritic structure with dendrites dimension higher than 100 μm, resulted by a consistently lower cooling rate compared to the LPBF process. In the microstructure are present segregations of eutectic **γ/γ’**, elongated **η** phases long up to 100 μm and carbides with dimension up to 10 μm.

Chapter 5

Overall conclusions and future works

In this thesis work, two Ni-based superalloys, the IN625 and the IN939 were built by LPBF process.

The IN625 is easy to process with LPBF technology, and it was used for two studies.

One is the study of the standard annealing treatments effect on the LPBF produced IN625 microstructure, texture and mechanical properties.

The results indicate that the choice of the annealing temperature is critical for both microstructural features and mechanical properties.

From the phases point of view, the stress reliving at 870 °C causes the δ precipitation and a partial dissolution of the segregations. The annealing at 980 °C does not induce the δ formation but promotes carbides growth. Higher temperatures treatments remove all the phases with the exception of carbides.

The grain structure of the as-built remains almost unaltered up to heat treatments at 980 °C while for higher temperatures 1030 °C and 1080 °C partial recrystallization occurs with a marker reduction of the LAGB content and a consistent TGB formation. The solutioning treatment (1150 °C 2 h) allows a complete recrystallization, removing almost all the LAGB and developing a huge fraction of TGB.

The mechanical properties of the as-built state are different between samples built horizontally or vertically, with higher YS and UTS and lower El for the horizontal samples. The anisotropy is progressively reduced increasing the heat treatment temperature, with a reduction of YS and UTS and increment of El. Finally, the solution treatment completely removes the anisotropy and maximizes the El.

All the heat-treated conditions, satisfy the minimal requirements contained in the ASTM B443 for the grade 1 (stress reliving and annealing) and 2 (solution annealing) wrought IN625.

In the future can be interesting to characterize the precipitates formed using TEM analysis and to evaluate the effect of the different grain boundaries misorientation on the precipitation during thermal exposure.

The second study performed on the LPBF produced IN625 was the evaluation of the oxidation resistance at 900 °C in air of the as-built condition and the effect of the solution treatment.

The results show that in both cases the oxide layer formed is mainly composed by Cr_2O_3 and the alloy under it develops at the interface a Nb-rich layer that causes the precipitation of δ phase.

The as-built condition possesses a greater oxidation resistance compared to the solutionized condition, thanks to its compact and continuous oxide layer.

On the other hands, the oxide layer formed on the solutionized condition show evidence of defect and spalling already after oxidation times of 8 hours. These defects reduce the oxidation resistance of the alloy, and in some points cause the incorporation of portions of the alloy in the oxide, resulting in mixed oxide formation.

The differences in the oxidation resistance can be caused by the different precipitation mechanism present in the two conditions, faster but more contained for the as-built and slower but more marked in the solutionized condition, leading to bigger stresses at the alloy/oxide interface.

In the future can be interesting to study more deeply the effect of the Nb-rich layer on the oxidation mechanism and evaluate the oxidation performance of both the conditions for longer thermal exposures ($\geq$ 1000 hours).

At last, IN939 is a γ' reinforced superalloy that inherits more challenge for the LPBF process since it can develop cracks during the production.

Nowadays, no works on the process optimization were found in literature. Therefore, the aim of this work was to find a suitable process parameter set that minimizes the porosity and cracks content.

The performed work proves that it is possible to obtain samples of LPBF IN939 with a limited crack content and a high densification level.

The results show that the VED approach is useful to understand when lack of fusion (at low VED) and melt pool instability (at high VED) can happen, but it is not enough for completely understand the defects formation mechanism.

Increasing the **v** at a fixed $\mathbf{h_d}$ initially increases the densification level, reaching a minimum at intermediate **v**. Further **v** increments reduce the VED value, preventing a good consolidation of the alloy.

Reduction in the $\mathbf{h_d}$ increases the densification, down to 0.03 mm. Further reductions result in a really poor densification because of strong melt pool instability.

The crack density can be limited raising the **v**, probably because have a beneficial effect on the thermal stress development.

Reducing the $\mathbf{h_d}$ values reduces crack density, probably because with a low value allows the use of elevated $\mathbf{v}$ resulting in VED greater that the lack of fusion limit.

In the end, low $\mathbf{h_d}$ is beneficial for reduction of both porosity and crack contents, meanwhile a moderate $\mathbf{v}$ produces samples with really low porosity and a medium crack density and elevated $\mathbf{v}$ produces samples with an extremely low crack density but an increased porosity.

The as-built IN939 is characterized by columnar grains and extremely fine dendritic structures, with the interdendritic areas mainly decorated with nanometric precipitates.

The cracks are located at the grain boundaries, parallel to the building direction. The cracking mechanisms is probably related to the nanometric precipitates present in the crack internal surfaces together with high residual stress.

In the future can be interesting to evaluate the mechanical properties of the material that was developed with our process parameters optimization as well as its response to heat treatments. Since this alloy needs a complex four stage heat treatment in order to reach optimal mechanical properties at high temperature, the response of the material to the standard heat treatment procedure and an eventual heat treatment optimization is required for the LPBF IN939.

In addition, it will be interesting to study, using TEM, the nanometric precipitates formed in the as-built condition and determine their role in the cracking mechanism.

Morover, another important topic will be the investigation of the effect of HIP, as post processing, for further reduction of the residual porosity and crack content of this alloy thus contemporary evaluating the effect of HIP on the microstructure and mechanical properties.

References

[1] B. Geddes, H. Leon, X. Huang, Superalloys Alloying and Performance, 2009. www.asminternational.orgwww.asminternational.org.

[2] M.J. Donachie, S.J. Donachie, Superalloys A Technical Guide, 2002. doi:10.1361/stgs2002p001.

[3] S.D.K. John N.DuPont, John C. Lippold, Welding Metallurgy and Weldability of Nickel-base Alloys, 2009.

[4] I.A. Choudhury, Machinability of nickel-base super alloys : a general review, J. Mater. Process. Technol. 77 (1998) 278–284.

[5] F.C. Campbell, Manufacturing Technology for aerospace structural materials, Elsevier, 2006.

[6] R. Abbaschian, L. Abbaschian, R.E. Reed-Hill, Physical Metallurgy Principles, Fourth, CENGAGE Learning, 2012.

[7] X. Xing, X. Di, B. Wang, The effect of post-weld heat treatment temperature on the microstructure of Inconel 625 deposited metal, J. Alloys Compd. 593 (2014) 110–116. doi:10.1016/j.jallcom.2013.12.224.

[8] R.C. Reed, The Superalloys, 2006.

[9] I.J. Moore, M.G. Burke, E.J. Palmiere, Modelling the nucleation, growth and coarsening kinetics of γ'' (D0 22) precipitates in the Ni-base Alloy 625, Acta Mater. 119 (2016) 157–166. doi:10.1016/j.actamat.2016.08.027.

[10] L.M. Suave, J. Cormier, P. Villechaise, A. Soula, Z. Hervier, D. Bertheau, J. Laigo, Microstructural evolutions during thermal aging of alloy 625: Impact of temperature and forming process, Metall. Mater. Trans. A Phys. Metall. Mater. Sci. 45 (2014) 2963–2982. doi:10.1007/s11661-014-2256-7.

[11] H. Chandler, Heat Treater ' s Guide: Practices and Procedures for Nonferrous Alloys, 1996.

[12] H.L. Eiselstein, D.J. Tillack, The Invention and Definition of Alloy 625, (2012) 1–14. doi:10.7449/1991/superalloys_1991_1_14.

[13] V. Shankar, M. Valsan, K.B.S. Rao, S.L. Mannan, Effects of temperature and strain rate on tensile properties and activation energy for dynamic strain aging in alloy 625, Metall. Mater. Trans. A Phys. Metall. Mater. Sci.

35 A (2004) 3129–3139. doi:10.1007/s11661-004-0057-0.

[14] L.E. Shoemaker, Alloys 625 and 725: Trends in properties and applications, 6th Int. Symp. Superalloys 718, 625, 706 Deriv. (2005) 409–418. doi:10.7449/2005/Superalloys_2005_409_418.

[15] Y. Kawahara, Application of high temperature corrosion-resistant materials and coatings under severe corrosive environment in waste-to-energy boilers, J. Therm. Spray Technol. 16 (2007) 202–213. doi:10.1007/s11666-006-9012-5.

[16] S. FLOREEN, G. FUCHS, W. YANG, the Metallurgy of Alloy-625, Superalloys. (1994) 13–37. doi:10.7449/1994/Superalloys_1994_13_37.

[17] C. Hong, D. Gu, D. Dai, M. Alkhayat, W. Urban, P. Yuan, S. Cao, A. Gasser, A. Weisheit, I. Kelbassa, M. Zhong, R. Poprawe, Laser additive manufacturing of ultrafine TiC particle reinforced Inconel 625 based composite parts: Tailored microstructures and enhanced performance, Mater. Sci. Eng. A. 635 (2015) 118–128. doi:10.1016/j.msea.2015.03.043.

[18] S.M. Corporation, Inconel Alloy 625, Www.Specialmetals.Com. 625 (2013) 1–28. doi:SMC-066.

[19] I. Yadroitsev, L. Thivillon, P. Bertrand, I. Smurov, Strategy of manufacturing components with designed internal structure by selective laser melting of metallic powder, Appl. Surf. Sci. 254 (2007) 980–983. doi:10.1016/j.apsusc.2007.08.046.

[20] T.B. Gibbons, R. Stickler, IN939: Metallurgy, Properties and Performance, High Temp. Alloy. Gas Turbines. (1982) 369–393.

[21] M.R. Jahangiri, M. Abedini, Effect of long time service exposure on microstructure and mechanical properties of gas turbine vanes made of IN939 alloy, Mater. Des. 64 (2014) 588–600. doi:10.1016/j.matdes.2014.08.035.

[22] M.A. González Albarrán, D.I. Martínez, E. Díaz, J.C. Díaz, I. Guzman, E. Saucedo, A.M. Guzman, Effect of preweld heat treatment on the microstructure of heat-affected zone (HAZ) and weldability of Inconel 939 superalloy, J. Mater. Eng. Perform. 23 (2014) 1125–1130. doi:10.1007/s11665-013-0704-y.

[23] J. Zhu, A. Wise, T. Nuhfer, G.R. Holcomb, P.D. Jablonski, S. Sridhar, D.E. Laughlin, High-temperature-oxidation-induced ordered structure in Inconel 939 superalloy exposed to oxy-combustion environments, Mater. Sci. Eng. A. 566 (2013) 134–142. doi:10.1016/j.msea.2012.12.074.

[24] P. Kanagarajah, F. Brenne, T. Niendorf, H.J. Maier, Inconel 939 processed by selective laser melting: Effect of microstructure and temperature on the mechanical properties under static and cyclic loading, Mater. Sci. Eng. A. 588 (2013) 188–195. doi:10.1016/j.msea.2013.09.025.

[25] M.A. González, D.I. Martínez, A. Pérez, H. Guajardo, Microstructural rejuvenation through non-conventional heat treatments of an inconel 939 superalloy, Mater. Res. Soc. Symp. Proc. 1372 (2012) 89–96. doi:10.1557/opl.2012.114.

[26] M.A. González, D.I. Martínez, A. Pérez, H. Guajardo, A. Garza, Microstructural response to heat affected zone cracking of prewelding heat-treated Inconel 939 superalloy, Mater. Charact. 62 (2011) 1116–1123. doi:10.1016/j.matchar.2011.09.006.

[27] Z. Mišković, M. Jovanović, M. Gligić, B. Lukić, Microstructural investigation of IN 939 superalloy, Vacuum. 43 (1992) 709–711. doi:10.1016/0042-207X(92)90115-D.

[28] K.M. Delargy, S.W.K. Shaw, G.D.W. Smith, Effects of heat treatment on mechanical properties of high-chromium nickel-base superalloy IN 939, Mater. Sci. Technol. 2 (1986).

[29] G. Sjöberg, D. Imamovic, J. Gabel, O. Caballero, J.W. Brooks, J. Ferté, A. Lugan, Evaluation of the IN 939 Alloy for Large Aircraft Engine Structures, Technology. (2004) 441–450.

[30] Z. Prevorovsky, J. Krofta, J. Kober, NDT in additive manufacturing of metals, NDT Prog. 2017 - 9th Int. Work. NDT Progress, Proc. 2017-Octob (2017) 75–84. doi:10.1016/j.actamat.2016.07.019.

[31] M. Yakout, M.A. Elbestawi, S.C. Veldhuis, A review of metal additive manufacturing technologies, Solid State Phenom. 278 SSP (2018) 1–14. doi:10.4028/www.scientific.net/SSP.278.1.

[32] W. Zhang, A. De, A. Wilson-Heid, A.M. Beese, J.W. Elmer, J.S. Zuback, T. Mukherjee, J.O. Milewski, T. DebRoy, H.L. Wei, Additive manufacturing of metallic components – Process, structure and properties, Prog. Mater. Sci. 92 (2017) 112–224. doi:10.1016/j.pmatsci.2017.10.001.

[33] A. Katz-Demyanetz, V. V. Popov, A. Kovalevsky, D. Safranchik, A. Koptyug, Powder-bed additive manufacturing for aerospace application: Techniques, metallic and metal/ceramic composite materials and trends, Manuf. Rev. 6 (2019) 5. doi:10.1051/mfreview/2019003.

[34] D.D. Gu, W. Meiners, K. Wissenbach, R. Poprawe, Laser additive manufacturing of metallic components, 57 (2013) 133–164. doi:10.1179/1743280411Y.0000000014.

[35] S. Catchpole-Smith, N. Aboulkhair, L. Parry, C. Tuck, I.A. Ashcroft, A. Clare, Fractal scan strategies for selective laser melting of ‘unweldable’ nickel superalloys, Addit. Manuf. 15 (2017) 113–122. doi:10.1016/j.addma.2017.02.002.

[36] Y.M. Arısoy, L.E. Criales, T. Özel, B. Lane, S. Moylan, A. Donmez, Influence of scan strategy and process parameters on microstructure and its optimization in additively manufactured nickel alloy 625 via laser powder bed fusion, Int. J. Adv. Manuf. Technol. 90 (2017) 1393–1417. doi:10.1007/s00170-016-9429-z.

[37] A. Anam, J.J.S. Dilip, D. Pal, B. Stucker, Effect of Scan Pattern on the Microstructural Evolution of Inconel 625 during Selective Laser Melting, Int. Solid Free. Fabr. Symp. – An Addit. Manuf. Conf. (2014) 363–376. doi:10.13140/2.1.1256.6089.

[38] L.N. Carter, C. Martin, P.J. Withers, M.M. Attallah, The influence of the laser scan strategy on grain structure and cracking behaviour in SLM powder-bed fabricated nickel superalloy, J. Alloys Compd. 615 (2014) 338–347. doi:10.1016/j.jallcom.2014.06.172.

[39] X. Zhang, C.J. Yocom, B. Mao, Y. Liao, Microstructure evolution during selective laser melting of metallic materials: A review, J. Laser Appl. 31 (2019) 031201. doi:10.2351/1.5085206.

[40] J.L. Bartlett, X. Li, An overview of residual stresses in metal powder bed fusion, Addit. Manuf. 27 (2019) 131–149. doi:10.1016/j.addma.2019.02.020.

[41] A. Popovich, V. Sufiiarov, Metal Powder Additive Manufacturing, Intech. i (2016) 13. doi:http://dx.doi.org/10.5772/63337.

[42] A.B. Spierings, M. Voegtlin, T. Bauer, K. Wegener, Powder flowability characterisation methodology for powder-bed-based metal additive manufacturing, Prog. Addit. Manuf. 1 (2016) 9–20. doi:10.1007/s40964-

015-0001-4.

[43] J.H. Tan, W.L.E. Wong, K.W. Dalgarno, An overview of powder granulometry on feedstock and part performance in the selective laser melting process, Addit. Manuf. 18 (2017) 228–255. doi:10.1016/j.addma.2017.10.011.

[44] Y. Lu, S. Wu, Y. Gan, T. Huang, C. Yang, L. Junjie, J. Lin, Study on the microstructure, mechanical property and residual stress of SLM Inconel-718 alloy manufactured by differing island scanning strategy, Opt. Laser Technol. 75 (2015) 197–206. doi:10.1016/j.optlastec.2015.07.009.

[45] M.M. Attallah, R. Jennings, X. Wang, L.N. Carter, Additive manufacturing of Ni-based superalloys: The outstanding issues, MRS Bull. 41 (2016) 758–764. doi:10.1557/mrs.2016.211.

[46] G.A. Young, T.E. Capobianco, M.A. Penik, B.W. Morris, J.J. McGee, The mechanism of ductility dip cracking in nickel-chromium alloys, Weld. J. (Miami, Fla). 87 (2008).

[47] L.N. Carter, K. Essa, M.M. Attallah, Optimisation of selective laser melting for a high temperature Ni-superalloy, Rapid Prototyp. J. 21 (2015) 423–432. doi:10.1108/RPJ-06-2013-0063.

[48] X. Wang, L.N. Carter, B. Pang, M.M. Attallah, M.H. Loretto, Microstructure and yield strength of SLM-fabricated CM247LC Ni-Superalloy, Acta Mater. 128 (2017) 87–95. doi:10.1016/j.actamat.2017.02.007.

[49] L.N. Carter, M.M. Attallah, R.C. Reed, Laser Powder Bed Fabrication of Nickel-Base Superalloys: Influence of Parameters; Characterisation, Quantification and Mitigation of Cracking, Superalloys 2012. (2012) 577–586. doi:10.1002/9781118516430.ch64.

[50] Q. Han, K. Vanmeensel, H. Fan, M.L. Montero-Sistiaga, B. Van Hooreweder, R. Setchi, R. Mertens, S.L. Evans, S. Yang, Laser powder bed fusion of Hastelloy X: Effects of hot isostatic pressing and the hot cracking mechanism, Mater. Sci. Eng. A. 732 (2018) 228–239. doi:10.1016/j.msea.2018.07.008.

[51] D. Tomus, P.A. Rometsch, M. Heilmaier, X. Wu, Effect of minor alloying elements on crack-formation characteristics of Hastelloy-X manufactured by selective laser melting, Addit. Manuf. 16 (2017) 65–72. doi:10.1016/j.addma.2017.05.006.

[52] N.J. Harrison, I. Todd, K. Mumtaz, Reduction of micro-cracking in nickel superalloys processed by Selective Laser Melting: A fundamental alloy design approach, Acta Mater. 94 (2015) 59–68. doi:10.1016/j.actamat.2015.04.035.

[53] V.A. Popovich, E. V. Borisov, A.A. Popovich, V.S. Sufiiarov, D. V. Masaylo, L. Alzina, Functionally graded Inconel 718 processed by additive manufacturing: Crystallographic texture, anisotropy of microstructure and mechanical properties, Mater. Des. 114 (2017) 441–449. doi:10.1016/j.matdes.2016.10.075.

[54] E. Chlebus, K. Gruber, B. Kuźnicka, J. Kurzac, T. Kurzynowski, Effect of heat treatment on the microstructure and mechanical properties of Inconel 718 processed by selective laser melting, Mater. Sci. Eng. A. 639 (2015) 647–655. doi:10.1016/j.msea.2015.05.035.

[55] D. Deng, R.L. Peng, H. Brodin, J. Moverare, Microstructure and mechanical properties of Inconel 718 produced by selective laser melting: Sample orientation dependence and effects of post heat treatments, Mater.

Sci. Eng. A. 713 (2018) 294–306. doi:10.1016/j.msea.2017.12.043.

[56] D. Gu, Q. Shi, K. Lin, L. Xi, Microstructure and performance evolution and underlying thermal mechanisms of Ni-based parts fabricated by selective laser melting, Addit. Manuf. 22 (2018) 265–278. doi:10.1016/j.addma.2018.05.019.

[57] G. Marchese, E. Bassini, M. Calandri, E.P. Ambrosio, F. Calignano, M. Lorusso, D. Manfredi, M. Pavese, S. Biamino, P. Fino, Microstructural investigation of as-fabricated and heat-treated Inconel 625 and Inconel 718 fabricated by direct metal laser sintering: contribution of Politecnico di Torino and Istituto Italiano di Tecnologia (IIT) di Torino, Met. Powder Rep. 71 (2016) 273–278. doi:10.1016/j.mprp.2016.06.002.

[58] S. Li, Q. Wei, Y. Shi, Z. Zhu, D. Zhang, Microstructure Characteristics of Inconel 625 Superalloy Manufactured by Selective Laser Melting, J. Mater. Sci. Technol. 31 (2015) 946–952. doi:10.1016/j.jmst.2014.09.020.

[59] D. Zhang, Z. Feng, C. Wang, W. Wang, Z. Liu, W. Niu, Comparison of microstructures and mechanical properties of Inconel 718 alloy processed by selective laser melting and casting, Mater. Sci. Eng. A. 724 (2018) 357–367. doi:10.1016/j.msea.2018.03.073.

[60] G. Marchese, G. Basile, E. Bassini, A. Aversa, M. Lombardi, D. Ugues, P. Fino, S. Biamino, Study of the microstructure and cracking mechanisms of hastelloy X produced by laser powder bed fusion, Materials (Basel). 11 (2018). doi:10.3390/ma11010106.

[61] D. Zhang, W. Niu, X. Cao, Z. Liu, Effect of standard heat treatment on the microstructure and mechanical properties of selective laser melting manufactured Inconel 718 superalloy, Mater. Sci. Eng. A. 644 (2015) 32–40. doi:10.1016/j.msea.2015.06.021.

[62] T. DebRoy, H.L. Wei, J.S. Zuback, T. Mukherjee, J.W. Elmer, J.O. Milewski, A.M. Beese, A. Wilson-Heid, A. De, W. Zhang, Additive manufacturing of metallic components – Process, structure and properties, Prog. Mater. Sci. 92 (2018) 112–224. doi:10.1016/j.pmatsci.2017.10.001.

[63] G. Marchese, M. Lorusso, S. Parizia, E. Bassini, J.W. Lee, F. Calignano, D. Manfredi, M. Terner, H.U. Hong, D. Ugues, M. Lombardi, S. Biamino, Influence of heat treatments on microstructure evolution and mechanical properties of Inconel 625 processed by laser powder bed fusion, Mater. Sci. Eng. A. 729 (2018) 64–75. doi:10.1016/j.msea.2018.05.044.

[64] G. Marchese, X. Garmendia Colera, F. Calignano, M. Lorusso, S. Biamino, P. Minetola, D. Manfredi, Characterization and Comparison of Inconel 625 Processed by Selective Laser Melting and Laser Metal Deposition, Adv. Eng. Mater. 19 (2017) 1–9. doi:10.1002/adem.201600635.

[65] P. Karimi, T. Raza, J. Andersson, L.E. Svensson, Influence of laser exposure time and point distance on 75-μm-thick layer of selective laser melted Alloy 718, Int. J. Adv. Manuf. Technol. 94 (2018) 2199–2207. doi:10.1007/s00170-017-1019-1.

[66] E. Malekipour, H. El-Mounayri, Common defects and contributing parameters in powder bed fusion AM process and their classification for online monitoring and control: a review, Int. J. Adv. Manuf. Technol. 95 (2018) 527–550. doi:10.1007/s00170-017-1172-6.

[67] T. Mukherjee, H.L. Wei, A. De, T. DebRoy, Heat and fluid flow in additive manufacturing – Part II: Powder bed fusion of stainless steel, and titanium, nickel and aluminum base alloys, Comput. Mater. Sci. 150 (2018) 369–380. doi:10.1016/j.commatsci.2018.04.027.

[68] Q. Jia, D. Gu, Selective laser melting additive manufacturing of Inconel 718 superalloy parts: Densification, microstructure and properties, J. Alloys Compd. 585 (2014) 713–721. doi:10.1016/j.jallcom.2013.09.171.

[69] N. Kalentics, N. Sohrabi, H.G. Tabasi, S. Griffiths, J. Jhabvala, C. Leinenbach, A. Burn, R.E. Logé, Healing cracks in selective laser melting by 3D laser shock peening, Addit. Manuf. 30 (2019) 100881. doi:10.1016/j.addma.2019.100881.

[70] M. Cloots, P.J. Uggowitzer, K. Wegener, Investigations on the microstructure and crack formation of IN738LC samples processed by selective laser melting using Gaussian and doughnut profiles, Mater. Des. 89 (2016) 770–784. doi:10.1016/j.matdes.2015.10.027.

[71] L. Rickenbacher, T. Etter, S. Hövel, K. Wegener, High temperature material properties of IN738LC processed by selective laser melting (SLM) technology, Rapid Prototyp. J. 19 (2013) 282–290. doi:10.1108/13552541311323281.

[72] X. Wang, N. Read, L.N. Carter, R.M. Ward, M.M. Attallah, Defect formation and its mitigation in selective laser melting of high γ′ Ni-base superalloys, Proc. Int. Symp. Superalloys. 2016-Janua (2016) 351–358. doi:10.1002/9781119075646.ch38.

[73] EOS, TD_M270_Dental-Package_10-15_en, 2015.

[74] Conceptlaser, Mlab cusing R Metal laser melting system, (2016).

[75] F. Calignano, D. Manfredi, E.P. Ambrosio, L. Iuliano, P. Fino, Influence of process parameters on surface roughness of aluminum parts produced by DMLS, Int. J. Adv. Manuf. Technol. 67 (2013) 2743–2751. doi:10.1007/s00170-012-4688-9.

[76] J.P. Choi, G.H. Shin, S. Yang, D.Y. Yang, J.S. Lee, M. Brochu, J.H. Yu, Densification and microstructural investigation of Inconel 718 parts fabricated by selective laser melting, Powder Technol. 310 (2017) 60–66. doi:10.1016/j.powtec.2017.01.030.

[77] K.S. Sidhu, J. Shi, V.K. Vasudevan, S.R. Mannava, Residual Stress Enhancement in 3D Printed Inconel 718 Superalloy Treated by Ultrasonic Nano-Crystal Surface Modification, ASME 2017 12th Int. Manuf. Sci. Eng. Conf. Collocated with JSME/ASME 2017 6th Int. Conf. Mater. Process. (2017) V002T01A013-V002T01A013. doi:10.1115/MSEC2017-2918.

[78] U. Scipioni Bertoli, A.J. Wolfer, M.J. Matthews, J.P.R. Delplanque, J.M. Schoenung, On the limitations of Volumetric Energy Density as a design parameter for Selective Laser Melting, Mater. Des. 113 (2017) 331–340. doi:10.1016/j.matdes.2016.10.037.

[79] J. Li, Z. Wei, B. Zhou, Y. Wu, S. Chen, 90W-7Ni-3Fe Fabricated by Selective Laser Melting, (2019) 1–15.

[80] R. Li, H. Chen, C. Chen, H. Zhu, M. Wang, T. Yuan, B. Song, Selective Laser Melting of Gas Atomized Al–3.02Mg–0.2Sc–0.1Zr Alloy Powder: Microstructure and Mechanical Properties, Adv. Eng. Mater. 21 (2019) 1–15. doi:10.1002/adem.201800650.

[81] EOS GmbH - Electro Optical Systems, Material data sheet EOS NickelAlloy IN625 Material data sheet Technical data, 49 (2015) 1–6.

[82] LPW Technology, PowderRange Metal powders from LPW, (2017) 7. http://www.lpwtechnology.com/wp-content/uploads/2016/11/LPW-Powders-Brochure-2017.pdf.

[83] G.F. Vander Voort, Metallography Of Superalloys, Ind. Heat. (2003) 40–43. doi:10.1017/S1431927604883442.

[84] K. Small, D. Englehart, T. Christman, Etching Specialty Alloys, Adv. Mater. Process. (2008) 32–37. https://www.google.co.kr/%5Cnpapers3://publication/uuid/7B149A4D-2255-4F6E-A331-EFE5F5D70DE7.

[85] G.F. Vander Voort, E.P. Manilova, Metallographic techniques for superalloys, Microsc. Microanal. 10 (2004) 690–691. doi:10.1017/S1431927604883442.

[86] B. Fultz, J.M. Howe, Transmission electron microscopy and diffractometry of materials, Transm. Electron Microsc. Diffractometry Mater. (2008) 1–758. doi:10.1007/978-3-540-73886-2.

[87] J.B. Nelson, D.P. Riley, An experimental investigation of extrapolation methods in the derivation of accurate unit-cell dimensions of crystals, Proc. Phys. Soc. 57 (1945) 160–177. doi:10.1088/0959-5309/57/3/302.

[88] No Title, (n.d.). http://www.ebsd.com/.

[89] C. Blochwitz, W. Tirschler, Twin boundaries as crack nucleation sites, 41 (2005) 32–41. doi:10.1002/crat.200410305.

[90] L.N. Carter, X. Wang, N. Read, R. Khan, M. Aristizabal, K. Essa, M.M. Attallah, Process optimisation of selective laser melting using energy density model for nickel based superalloys, Mater. Sci. Technol. 0836 (2016) 1–5. doi:10.1179/1743284715Y.0000000108.

[91] G. Marchese, S. Parizia, E. Bassini, L. Massimo, D. Manfredi, F. Calignano, M. Lombardi, D. Ugues, S. Biamino, Effect of Prolonged Heat Treatments on Mechanical Properties of Inconel 625 Processed by Laser Powder Bed Fusion, Eur. Int. Powder Metall. Congr. Exhib. Eur. Powder Metall. Assoc. (2017).

[92] G. Marchese, S. Parizia, M. Rashidi, A. Saboori, D. Manfredi, D. Ugues, M. Lombardi, E. Hryha, S. Biamino, The role of texturing and microstructure evolution on the tensile behavior of heat-treated Inconel 625 produced via laser powder bed fusion, Mater. Sci. Eng. A. 769 (2019) 138500. doi:10.1016/j.msea.2019.138500.

[93] A. Kreitcberg, V. Brailovski, S. Turenne, Effect of heat treatment and hot isostatic pressing on the microstructure and mechanical properties of Inconel 625 alloy processed by laser powder bed fusion, Mater. Sci. Eng. A. 689 (2017) 1–10. doi:10.1016/j.msea.2017.02.038.

[94] M. Pröbstle, S. Neumeier, J. Hopfenmüller, L.P. Freund, T. Niendorf, D. Schwarze, M. Göken, Superior creep strength of a nickel-based superalloy produced by selective laser melting, Mater. Sci. Eng. A. 674 (2016) 299–307. doi:10.1016/j.msea.2016.07.061.

[95] A. Kreitcberg, V. Brailovski, S. Turenne, Elevated temperature mechanical behavior of IN625 alloy processed by laser powder-bed fusion, Mater. Sci. Eng. A. 700 (2017) 540–553. doi:10.1016/j.msea.2017.06.045.

[96] B. Zhang, G. Bi, S. Nai, C.N. Sun, J. Wei, Microhardness and microstructure evolution of TiB2 reinforced Inconel 625/TiB2 composite produced by selective laser melting, Opt. Laser Technol. 80 (2016) 186–195. doi:10.1016/j.optlastec.2016.01.010.

[97] F. Zhang, L.E. Levine, A.J. Allen, C.E. Campbell, E.A. Lass, S. Cheruvathur, M.R. Stoudt, M.E. Williams, Y. Idell, Homogenization kinetics of a nickel-based superalloy produced by powder bed fusion laser sintering, Scr. Mater. 131 (2017) 98–102. doi:10.1016/j.scriptamat.2016.12.037.

[98] J.N. Dupont, Solidification of an alloy 625 Weld Overlay, Metall. Mater.

Trans. A Phys. Metall. Mater. Sci. 27 (1996) 3612–3620. doi:10.1007/BF02595452.

[99] K. Amato, Comparison of Microstructures and Properties for a Ni-Base Superalloy (Alloy 625) Fabricated by Electron Beam Melting, J. Mater. Sci. Res. 1 (2012) p3. doi:10.5539/jmsr.v1n2p3.

[100] J. Strößner, M. Terock, U. Glatzel, Mechanical and Microstructural Investigation of Nickel-Based Superalloy IN718 Manufactured by Selective Laser Melting (SLM), Adv. Eng. Mater. 17 (2015) 1099–1105. doi:10.1002/adem.201500158.

[101] T. Trosch, J. Strößner, R. Völkl, U. Glatzel, Microstructure and mechanical properties of selective laser melted Inconel 718 compared to forging and casting, Mater. Lett. 164 (2016) 428–431. doi:10.1016/j.matlet.2015.10.136.

[102] C.U. Brown, G. Jacob, M. Stoudt, S. Moylan, J. Slotwinski, A. Donmez, Interlaboratory Study for Nickel Alloy 625 Made by Laser Powder Bed Fusion to Quantify Mechanical Property Variability, J. Mater. Eng. Perform. 25 (2016) 3390–3397. doi:10.1007/s11665-016-2169-2.

[103] D.B. Witkin, T. V. Albright, D.N. Patel, Empirical Approach to Understanding the Fatigue Behavior of Metals Made Using Additive Manufacturing, Metall. Mater. Trans. A Phys. Metall. Mater. Sci. 47 (2016) 3823–3836. doi:10.1007/s11661-016-3501-z.

[104] H. Hack, R. Link, E. Knudsen, B. Baker, S. Olig, Mechanical properties of additive manufactured nickel alloy 625, Addit. Manuf. 14 (2017) 105–115. doi:10.1016/j.addma.2017.02.004.

[105] J.R. Poulin, V. Brailovski, P. Terriault, Long fatigue crack propagation behavior of Inconel 625 processed by laser powder bed fusion: Influence of build orientation and post-processing conditions, Int. J. Fatigue. 116 (2018) 634–647. doi:10.1016/j.ijfatigue.2018.07.008.

[106] P. Wang, B. Zhang, C.C. Tan, S. Raghavan, Y.-F. Lim, C.-N. Sun, J. Wei, D. Chi, Microstructural characteristics and mechanical properties of carbon nanotube reinforced Inconel 625 parts fabricated by selective laser melting, Mater. Des. 112 (2016) 290–299. doi:10.1016/j.matdes.2016.09.080.

[107] E.A. Lass, M.R. Stoudt, M.B. Katz, M.E. Williams, Precipitation and dissolution of δ and γ″ during heat treatment of a laser powder-bed fusion produced Ni-based superalloy, Scr. Mater. 154 (2018) 83–86. doi:10.1016/j.scriptamat.2018.05.025.

[108] F. Zhang, L.E. Levine, A.J. Allen, M.R. Stoudt, G. Lindwall, E.A. Lass, M.E. Williams, Y. Idell, C.E. Campbell, Effect of heat treatment on the microstructural evolution of a nickel-based superalloy additive-manufactured by laser powder bed fusion, Acta Mater. 152 (2018) 200–214. doi:10.1016/j.actamat.2018.03.017.

[109] M.R. Stoudt, E.A. Lass, D.S. Ng, M.E. Williams, F. Zhang, C.E. Campbell, G. Lindwall, L.E. Levine, The Influence of Annealing Temperature and Time on the Formation of δ-Phase in Additively-Manufactured Inconel 625, Metall. Mater. Trans. A Phys. Metall. Mater. Sci. 49 (2018) 3028–3037. doi:10.1007/s11661-018-4643-y.

[110] C. Li, R. White, X.Y. Fang, M. Weaver, Y.B. Guo, Microstructure Evolution Characteristics of Inconel 625 Alloy from Selective Laser Melting to Heat Treatment, Mater. Sci. Eng. A. (2017). doi:10.1016/j.msea.2017.08.058.

[111] S. Holland, X. Wang, X.Y. Fang, Y.B. Guo, F. Yan, L. Li, Grain boundary

network evolution in Inconel 718 from selective laser melting to heat treatment, Mater. Sci. Eng. A. 725 (2018) 406–418. doi:10.1016/j.msea.2018.04.045.

[112] Y.S.J. Yoo, T.A. Book, M.D. Sangid, J. Kacher, Identifying strain localization and dislocation processes in fatigued Inconel 718 manufactured from selective laser melting, Mater. Sci. Eng. A. 724 (2018) 444–451. doi:10.1016/j.msea.2018.03.127.

[113] F. Geiger, K. Kunze, T. Etter, Tailoring the texture of IN738LC processed by selective laser melting (SLM) by specific scanning strategies, Mater. Sci. Eng. A. 661 (2016) 240–246. doi:10.1016/j.msea.2016.03.036.

[114] Z.R. Khayat, T.A. Palmer, Impact of iron composition on the properties of an additively manufactured solid solution strengthened nickel base alloy, Mater. Sci. Eng. A. 718 (2018) 123–134. doi:10.1016/j.msea.2018.01.112.

[115] B. Fultz, J. Howe, Diffraction and the X-Ray Powder, n.d. doi:10.1007/978-3-642-29761-8.

[116] S.K. Rai, A. Kumar, V. Shankar, T. Jayakumar, K.B.S. Rao, B. Raj, Characterization of microstructures in Inconel 625 using X-ray diffraction peak broadening and lattice parameter measurements, Scr. Mater. 51 (2004) 59–63. doi:10.1016/j.scriptamat.2004.03.017.

[117] K.H. Chang, S.M. Chen, T.K. Yeh, J.J. Kai, Effect of dissolved oxygen content on the oxide structure of Alloy 625 in supercritical water environments at 700°C, Corros. Sci. 81 (2014) 21–26. doi:10.1016/j.corsci.2013.11.034.

[118] M.Y. Xiao, Study on the Corrosion Behaviour of Nickel-Base Alloy 625 in Landfill Leachate Treated by Supercritical Water Oxidation, Adv. Mater. Res. 908 (2014) 93–97. doi:10.4028/www.scientific.net/amr.908.93.

[119] P. Huczkowski, W. Lehnert, H.H. Angermann, A. Chyrkin, R. Pillai, D. Grüner, E. Hejrani, W.J. Quadakkers, Effect of gas flow rate on oxidation behaviour of alloy 625 in wet air in the temperature range 900–1000 °C, Mater. Corros. 68 (2017) 159–170. doi:10.1002/maco.201608831.

[120] A. Vesel, A. Drenik, K. Elersic, M. Mozetic, J. Kovac, T. Gyergyek, J. Stockel, J. Varju, R. Panek, M. Balat-Pichelin, Oxidation of Inconel 625 superalloy upon treatment with oxygen or hydrogen plasma at high temperature, Appl. Surf. Sci. 305 (2014) 674–682. doi:10.1016/j.apsusc.2014.03.160.

[121] H. Buscail, R. Rolland, C. Issartel, F. Rabaste, F. Riffard, L. Aranda, M. Vilasi, Effects of water vapour on the oxidation of a nickel-base 625 alloy between 900 and 1,100 °C, J. Mater. Sci. 46 (2011) 5903–5915. doi:10.1007/s10853-011-5544-2.

[122] E. N’dah, M.P. Hierro, K. Borrero, F.J. Pérez, Study of the cyclic oxidation resistance of superalloy IN-625: Lifetime predicted by COSP-modelling program, Oxid. Met. 68 (2007) 9–21. doi:10.1007/s11085-006-9048-4.

[123] M. Cabrini, S. Lorenzi, C. Testa, T. Pastore, F. Brevi, S. Biamino, P. Fino, D. Manfredi, G. Marchese, F. Calignano, F. Scenini, Evaluation of Corrosion Resistance of Alloy 625 Obtained by Laser Powder Bed Fusion, J. Electrochem. Soc. 166 (2019) C3399–C3408. doi:10.1149/2.0471911jes.

[124] M. Cabrini, S. Lorenzi, C. Testa, F. Brevi, S. Biamino, P. Fino, D. Manfredi, G. Marchese, F. Calignano, T. Pastore, Microstructure and selective corrosion of alloy 625 obtained by means of laser powder bed fusion, Materials (Basel). 12 (2019) 1–11. doi:10.3390/ma12111742.

[125] M. Calandri, D. Manfredi, F. Calignano, E.P. Ambrosio, S. Biamino, R.

Lupoi, D. Ugues, Solution Treatment Study of Inconel 718 Produced by SLM Additive Technique in View of the Oxidation Resistance, Adv. Eng. Mater. (2018) 1–16. doi:10.1002/adem.201800351.

[126] H.A. Miley, THEORY OF OXIDATION AND TARNISHING OF METALS. I. The linear, parabolic and logarith, J. Electrochem. Soc. 81 (1942) 391–411.

[127] L. Kumar, R. Venkataramani, M. Sundararaman, P. Mukhopadhyay, S.P. Garg, Studies on the oxidation behavior of inconel 625 between 873 and 1523 K, Oxid. Met. 45 (1996) 221–244. doi:10.1007/BF01046827.

[128] C. Hong, D. Gu, D. Dai, S. Cao, M. Alkhayat, Q. Jia, A. Gasser, A. Weisheit, I. Kelbassa, M. Zhong, R. Poprawe, High-temperature oxidation performance and its mechanism of TiC/Inconel 625 composites prepared by laser metal deposition additive manufacturing, J. Laser Appl. 27 (2014) S17005. doi:10.2351/1.4898647.

[129] B. He, G. Xu, M. Zhou, Q. Yuan, Effect of Oxidation Temperature on the Oxidation Process of Silicon-Containing Steel, Metals (Basel). 6 (2016) 137. doi:10.3390/met6060137.

[130] A. Chyrkin, P. Huczkowski, V. Shemet, L. Singheiser, W.J. Quadakkers, Predicting subsurface enrichment/depletion processes during high-temperature oxidation of alloy 625 thin foils, 18th Int. Corros. Congr. 2011. 2 (2011) 1–11.

[131] A. Chyrkin, P. Huczkowski, V. Shemet, L. Singheiser, W.J. Quadakkers, Sub-scale depletion and enrichment processes during high temperature oxidation of the nickel base alloy 625 in the temperature range 900-1000 °c, Oxid. Met. 75 (2011) 143–166. doi:10.1007/s11085-010-9225-3.

[132] D.M. Gorman, R.L. Higginson, H. Du, G. McColvin, A.T. Fry, R.C. Thomson, Microstructural analysis of IN617 and IN625 oxidised in the presence of steam for use in ultra-supercritical power plant, Oxid. Met. 79 (2013) 553–566. doi:10.1007/s11085-012-9342-2.

[133] L. Garcia-Fresnillo, A. Chyrkin, C. Böhme, J. Barnikel, F. Schmitz, W.J. Quadakkers, Oxidation behaviour and microstructural stability of alloy 625 during long-term exposure in steam, J. Mater. Sci. 49 (2014) 6127–6142. doi:10.1007/s10853-014-8344-7.

[134] G.R. Holcomb, D.E. Alman, Effect of manganese addition on reactive evaporation of chromium in Ni-Cr alloys, J. Mater. Eng. Perform. 15 (2006) 394–398. doi:10.1361/105994906X117170.

[135] W. Philpott, M.A.E. Jepson, R.C. Thomson, Comparison of the effects of a conventional heat treatment between cast and selective laser melted IN939 alloy, Adv. Mater. Technol. Foss. Power Plants - Proc. from 8th Int. Conf. (2016).

[136] A.T. Sutton, C.S. Kriewall, M.C. Leu, J.W. Newkirk, Powder characterisation techniques and effects of powder characteristics on part properties in powder-bed fusion processes, Virtual Phys. Prototyp. 12 (2017) 3–29. doi:10.1080/17452759.2016.1250605.

[137] N.A. Yefimov, Handbook of Non-Ferrous Metal Powders, Second Edition, Elsevier, 2019.

[138] J.A. Slotwinski, E.J. Garboczi, Porosity of additive manufacturing parts for process monitoring, AIP Conf. Proc. 1581 33 (2014) 1197–1204. doi:10.1063/1.4864957.

[139] L.E. Criales, Y.M. Arısoy, B. Lane, S. Moylan, A. Donmez, T. Özel, Laser powder bed fusion of nickel alloy 625: Experimental investigations of

effects of process parameters on melt pool size and shape with spatter analysis, Int. J. Mach. Tools Manuf. 121 (2017) 22–36. doi:10.1016/j.ijmachtools.2017.03.004.

[140] B. Gao, Y. Sui, H. Wang, C. Zou, Z. Wei, R. Wang, Y. Sun, Effects of Cooling Rate on the Solidification and Microstructure of Nickel-Based Superalloy GTD222, Materials (Basel). 12 (2019) 1920. doi:10.3390/ma12121920.

[141] X. Shi, S. Duan, W. Yang, H. Guo, J. Guo, Solidification and segregation behaviors of superalloy IN718 at a slow cooling ratess, Materials (Basel). 11 (2018) 1–15. doi:10.3390/ma11122398.

[142] M.T. Jovanović, Z. Miškovic, B. Lukić, Microstructure and stress-rupture life of polycrystal, directionally solidified, and single crystal castings of nickel-based IN 939 superalloy, Mater. Charact. 40 (1998) 261–268.

[143] S.W.K. Shaw, Response of in-939 To Process Variations., (1980) 275–284.

[144] K.N. Amato, S.M. Gaytan, L.E. Murr, E. Martinez, P.W. Shindo, J. Hernandez, S. Collins, F. Medina, Microstructures and mechanical behavior of Inconel 718 fabricated by selective laser melting, Acta Mater. 60 (2012) 2229–2239. doi:10.1016/j.actamat.2011.12.032.

[145] Z. Wang, K. Guan, M. Gao, X. Li, X. Chen, X. Zeng, The microstructure and mechanical properties of deposited-IN718 by selective laser melting, J. Alloys Compd. 513 (2012) 518–523. doi:10.1016/j.jallcom.2011.10.107.